Design of adjustable tuned mass dampers employing nonlinear elements

A Thesis submitted to the University of Sheffield

for the degree of Doctor of Philosophy in the Faculty of Engineering

by

Ning Tang

Department of Mechanical Engineering

University of Sheffield

July 2017

Abstract

The work focuses on the design of the Tuned Mass Damper (TMD), targeted multi-mode, multi-directional vibrations of mechanical structures occurring over a wide temperature ranges. Extension of the target frequency range is achieved by making the devices adjustable, using components with nonlinear load-deflection behaviour. Two nonlinear components that are new in TMD design are studied, namely elastomeric O-rings and Tangled Metal Wire (TMW) particles. Evaluation of the performance of these devices on a typical engineering structure is carried out, and the feasibility of the proposed devices demonstrated.

For the O-ring TMD, analytical models are developed to describe the load-deflection behaviour of the O-ring. An existing model for axial compression is improved while new models are established for shear and rocking deformations. Validation of the models is carried out using a specifically designed vibration test. Numerical models, aiming to estimate the elasticity of the O-rings with irregular cross-sectional shape, are developed and validated by comparison with the experimental results.

The TMW particles seeks to address high temperature applications. The strong compression-dependent stiffness of these particles provides the basis for an adjustable TMD. Although there is some variation in the stiffness and damping for different collections of particles with similar physical properties, uniformity increases after several test runs. According to the assumptions of the equivalence of the TMW materials and the hyperelastic solid, a semi-empirical analytical model is developed and validated using experimental results.

A novel design optimisation algorithm, based on the complex power approach,

developed to provide an alternative route for the TMD involving nonlinear elements. The proposed route, involving the use of the a numerical, evolutionary search method, is finally applied to the design of a nonlinear TMD.

Acknowledgements

I owe sincere and earnest thankfulness to my supervisor, Dr Jem Rongong and Prof Neil Sims, for the the endless help and support throughout the PhD process. They have shared their interesting ideas throughout my researches. I am also grateful to Dr Charles Lord for valuable discussions about the Finite Element modelling of many interesting structures and materials.

I would also thank to the other group members (and others in the office) for stimulating talks and providing vast amounts of moral support. Special thanks go to Kartik and Haval for interesting conversations about all teaching and researching topics.

My sincere thanks also goes to both Dave Webster and Les Morton, for offering me support on the experiments setting up and specimen preparation. Without their support, it would not be possible in getting experimental works done.

Finally, I am truly indebted and thankful to my parents, to support my studying in the University of Sheffield.

List of publications from this work

Conferences:

[1] Tang, N., J. A. Rongong, and G. R. Tomlinson. "Nonlinear behaviour of tangled metal wire particle dampers." *International Conference on Structural Engineering Dynamics*, Lagos, Portugal, 2015.

[2] Tang, N., N. Sims, and J. Rongong. "Modelling of an adjustable TMD incorporating an elastomeric O-ring." *17th International Conference on Experimental Mechanics*, Rhodes, Greece, July 2016.

[3] Lord, C., Tang, N., and Rongong, J.. "Damping of metallic wool with embedded rigid body motion amplifiers." *6th European Conference on Structural Control*, Sheffield, United Kingdom, July 2016.

[4] Tang, N., Rongong, J., Lord, C., and Sims, N. "Experimental investigation and modeling of dynamic performance of wave springs." *11th International Conference on Advances in Experimental Mechanics*, Exeter, United Kingdom, September 2016.

Contents

List of Figures

List of Tables

Chapter 1

Introduction

1.1 Background

Lightweight structures subject to rigid body motion are generally desirable from application and cost perspectives. However, these structures are usually more susceptible to damage. Additionally, metals and composites typically used in these structures have low damping [9], increasing the likelihood of vibration problems. Vibration induced dynamic forcing can be much higher than the static load that a structure carries and can therefore induce failure. To mitigate any unexpected dynamic response, damping techniques, including Tuned Mass Dampers (TMDs), are sometimes used.

A classic TMD, as shown in Figure 1.1, is an oscillator that is attached to a vibrating structure. The concept of the TMD is to transfer energy from the vibrating host structure to a connected oscillator where it is dissipated. TMDs are popular as they are highly effective in reducing resonant vibrations when suitably optimised [10]. The performance of classic TMDs is not well defined for broadband vibration of structures with large numbers of modes and motion in multiple directions. While individual devices can be added to target given modes, the overall mass of the system might increase considerably if more than a few modes are considered.

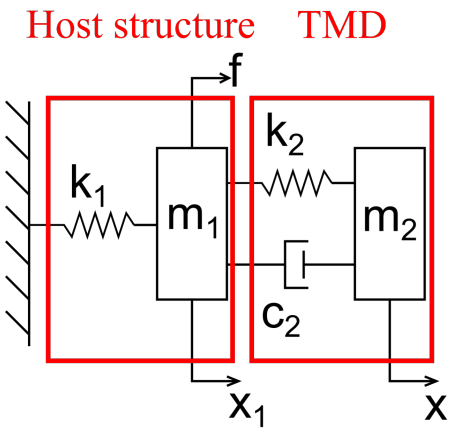

Figure 1.1: Schematic model of a TMD

1.1.1 Passive nonlinear TMD

To broaden the working frequency range of a TMD, the smart elements with nonlinear stiffness and damping may be employed. For such materials, the stiffness, and hence, frequency-altering mechanics is relative simple and the overall weight is low, while the nonlinearity, for example strain-dependent stiffness, may also bring out unwanted multiple harmonics. One selected approach t is to incorporate variable stiffness elements, such as elastomeric O-rings made from a viscoelastic polymer such as nitrile or natural rubber. Elastomeric materials are of interest not only because of their appropriate elasticity and energy loss levels but because they are viscoelastic materials, the hysteretic properties of these polymers are well understood. The elastomeric polymers (also called rubber-like polymers) are complex agglomerates of long, intertwined, thread-like molecules [11]. Damping of these materials comes from the relaxation and recovery of the molecular chains. At molecular level, the chains, which can be linear or branched, wriggle and writhe depending on the amount of the thermal energy present. An increase in temperature induces greater movement in the molecules and, at a continuum level, therefore results in softening. Cross-links between molecules tend to restrain this motion resulting in an increase in stiffness. To overcome this problem, elastomeric O-rings have been introduced. O-rings with different static compression

provide different stiffness due to geometric and material nonlinearity. Nevertheless, there has been limited research to establish models that describe the dynamic load-deflection behaviour of O-rings, or, therefore to model a TMD incorporating O-rings.

Since polymeric material is sensitive to temperature, a TMD incorporating O-rings may lose its effectiveness at high temperature. In this case, a Tangled Metal Wire (TMW) material, also called 'metal rubber' or 'metal mesh', could be employed as the elastic and damping components of the TMD. TMW is a porous material formed by compressing helical wires together in a mould. For TMW in bulk form, the damping mechanism is dominated by hysteresis through dry friction generated by the contact between neighbouring wire coils [12]. Some loss also occurs from plastic deformation within the wires and at contact points [13]. The behaviour of TMW is nonlinear with strain amplitude [14]. When the static compression is low, the response of TMW is dominated by the compression of free coils. At this stage, the stiffness is nearly constant and the damping is relatively low. As the strain amplitude increases, sliding occurs between neighbouring coils and considerable energy is dissipated through friction. Increased static loading delays the onset of slip, and under very high compression TMW tends to lock up [15].

The classic TMD is designed based on the facts that 1) most of the energy transfers to the secondary system when the resonance frequency of the TMD is close to that of the host structure; 2) two invariant points always exist for the receptance of the host structure in a SDOF-TMD system when the resonance frequency is fixed. The optimal damping tends to be achieved when the two resonance peaks of this system are of the same height. It is interesting to note that these two resonances merge into one when the damping is high as the energy transfer between the two systems is blocked by the high damping. Therefore, a suitable level of damping can balance the energy transfer and dissipation of the secondary system and achieve the best performance of vibration suppression of the host structure.

1.2 Motivation of the work

For many flexible structures including plates, panels and shells, many material damping strategies, such as constrained layer dampers and viscoelastic polymer isolators, have been used successfully. These classic damping technologies are less effective for structures where the dynamic strains, in comparison to the vibration level, are very low or are localised to inaccessible regions, for example, a stiff boring bar that supporting the cutting tools during machining the deep holes. This being the case, it is worthwhile to develop a novel tuned mass damper, as a low-cost and reliable energy dissipation device.

In the work reported here, two different nonlinear elements, elastomeric O-rings and TMW particles, were selected. Performance of the O-rings when subjected to different factors such as static compressions, dynamic strains and frequencies have been studied. Recently, dynamic characteristics of TMW material have been recognised and understood using different models. Detailed work always focuses on the properties of the material itself. No analytical work can be found in relation to the application of these components in a realistic TMD, especially work to predict the performance of these devices.

1.3 Aims and objectives

The aims of this work are to: a) investigate the feasibility of employing nonlinear materials to a passive, adjustable TMD that affect broad frequency range; b) develop techniques that are suitable for analysing and optimising such devices. To achieve these aims, several objectives were set,

- The feasibility of suppressing multi-mode, multi-direction vibration needs to be investigated for the proposed adjustable device with a viscoelastic circular O-ring or the TMW particles. The significance of using these devices on a typical continuous structure needs to be examined.

- The modelling, both analytical and numerical, of the TMD using O-rings needs to be established in relation to the variation of geometry, material properties and working modes, especially focusing on the nonlinear stiffness and damping behaviour. Following this, a suitable model of the TMD on a typical engineering structure needs to be developed based on both configurational and material considerations.

- Stiffness and damping behaviour of the temperature-insensitive TMW particles needs to be investigated, especially for the consistency of the different collections of particles with similar physical configurations, and then predictions of the resonance frequencies and damping for this TMW TMD should be carried out.

- On achievement of the previous objectives, a TMD design criteria using complex power should be proposed to extend parametric optimisation for a nonlinear multiple mode vibration suppression device.

1.4 Thesis layout

This thesis conduct a generic study of nonlinear, passive TMDs, including experiments and modelling, both analytical and numerical. The thesis is divided into six chapters and six appendices. A brief summary of each chapter is provided below.

Chapter 2, the literature review, introduces the classic TMD including the design criteria. was carried out in Chapter 2. Following this, up-to-date TMD devices intended to provide a wider tuning frequencies range are considered. Possible limitations of these devices are also discussed. Then the dynamic properties of the possible nonlinear elements are investigated along with existing models of the nonlinear elements selected for the proposed TMDs. The possible reasons for errors deriving from these models are also discussed. Finally, comparisons are made with different parametric design criteria and the limitations of each method are identified.

Chapter 3 introduces a proposed adjustable TMD using elastomeric O-rings. It then explains the experiments conducted with different excitation frequencies, static and dynamic strains to identify the hysteresis behaviour of the O-rings. Next, it describes the establishment and validation of the analytical and Finite Element models for this TMD. Finally, the performance of the TMD incorporating an elastomeric O-ring on a hollow beam structure is considered. The accuracy of the beam model incorporating this TMD is also established and validated based on the experimental results.

Chapter 4 considers the effectiveness of a TMD incorporating TMW particles by measuring the latter's characteristics, especially the repeatability of the individual and bundle of particles restricted by a cavity. This chapter then discusses the microstructure properties of the damping mechanism of TMW particle damper using various experiments with different displacement amplitude and particle configurations. Finally, it explains the establishment of an equivalent viscoelastic model with semi-empirical modifications to predict the stiffness of these particles, and the estimation of the damping using a low wave speed medium assumption.

Chapter 5 discusses the novel design of an algorithm for the TMD over a wide frequency range based on the Differential Evolution (DE), numerical search method. It describes the comparisons made between different optimisation targets, such as minimum peak resonance and minimum kinetic energy over selected frequencies. The chapter then introduces the use of complex power to select the optimal parameters of the TMD incorporating the nonlinear elements. The physical meaning of this novel performance indicator is discussed in detail, as well as verifications of the proposed routes for both linear and nonlinear TMD carried out through applying different mass of the TMD to the system.

Chapter 6 discusses the novel contribution of this study and makes suggestions for further work.

Chapter 2

Literature survey

2.1 Introduction

A Tuned Mass Damper (TMD) is an effective device for suppressing structural vibration. One of the main issues with this device is its narrow working range. To broaden the working frequency range, many types of nonlinear TMDs, incorporating either a combination of mechanical structures or smart materials, have been developed. In this section, several typical devices aimed at suppressing vibrations over a wide frequency range are discussed. Comparisons of different types of TMD are summarised and then recommendations are made of appropriate nonlinear material for an adjustable TMD. Based on this choice of nonlinear material, the dynamic characteristics and corresponding models are reviewed. The last section discusses the common design optimisation strategies for TMDs.

2.2 Introduction of TMDs aimed at multi-mode vibration suppression

2.2.1 Multiple TMDs

One of the easiest ways to address the narrow-band nature of a TMD is to use several devices at once to suppress the vibration at various target frequencies.

Kwon [16] applied multiple TMDs to control bridge flutter and the result showed that the critical wind speed was increased by 57%. This provides evidence of potential to apply multiple TMD to suppress vibration over a wider frequency range. To this point, very few practical such devices have been invented that address multi-mode, multi-directional structural vibration issues, especially for mechanical structures. One of the most critical underlying reasons is the high additional weight. The additional weight on the host structure may promote unwanted vibration for other modes.

2.2.2 TMDs using mechanical stiffness/inertia altering elements

One alternative and very popular type of device that has been developed is the stiffness adjustable TMD. Nagarajaiah [1] designed a semi-active and independently variable stiffness TMD - see Figure 2.1.

The stiffness of the TMD was modulated by the angle of the spring connections the equivalent stiffness being inversely proportional to $\sin 2\theta$. Similar devices were discussed by Farshi [17], Alexander [18] and Deshpande [19]. The common framework for this kind of stiffness adjustable TMD is to use geometry boundary conditions and the connection of a spring to gain a higher stiffness range.

However, the disadvantage of these structures is that most of these types of devices are still designed to address only one mode of vibration. The frequency uncertainty over which they can be adjusted is only about 15%. Furthermore, these

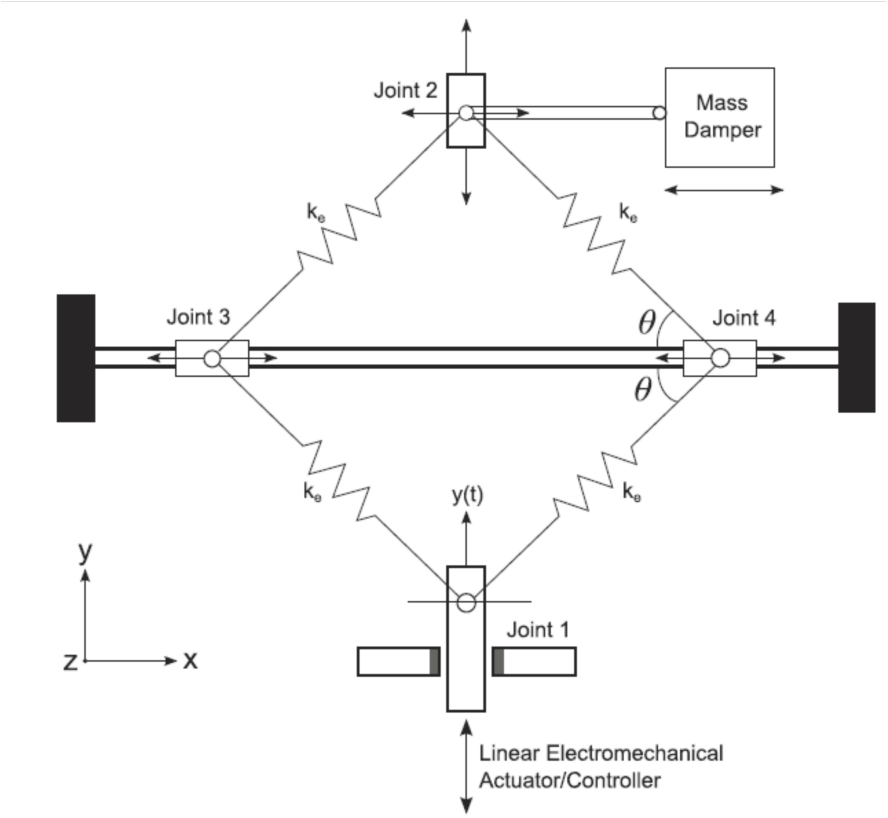

Figure 2.1: Variable stiffness TMD [1]

dampers add large amounts of weight to the main structure, which is undesirable particularly if the application involves rotating environments.

Acar [2] provided an alternative approach for achieving a variable stiffness TMD - see Figure 2.2. In this design, the tension of a string is introduced to adjust the stiffness of the damper. It is interesting to note that a second mode of string could also be involved in the structure and would appear as a working mode for the damper.

The working frequency of this kind of TMD can be doubled by using limited string end displacement. The other advantages are that it is light-weight and low volume, which makes it easy to apply in real engineering applications. However, one of the serious issues with this type of TMD is its low working frequency due to the low equivalent stiffness of the string. Besides, no damping components have

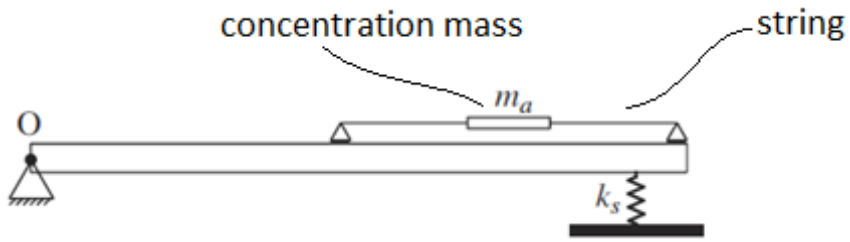

Figure 2.2: Variable stiffness TMD using tension of string [2]

been involved in this kind of TMD device, and therefore its performance would be further restricted by the two additional high peaks near its original resonance.

The other type of TMD using frequency altering mechanics is the variable inertia TMD. A number of research studies have focused on TMDs whose effective mass can be changed [3, 20]. Change to the inertia in these devices is usually achieved by altering the rotational inertia of a moving part. An example is presented in Figure 2.3. Here the TMD involves pendulum-like structures connected to the host through fixed stiffness elements. The moment of inertia of each pendulum can be altered by moving the position of the mass and therefore the overall effective mass can be adjusted. Previous research has shown [3] that this type of device can improve the working frequency range by 34% although to achieve a higher working frequency range, the arms would have to be lengthened – making the design potentially less practical.

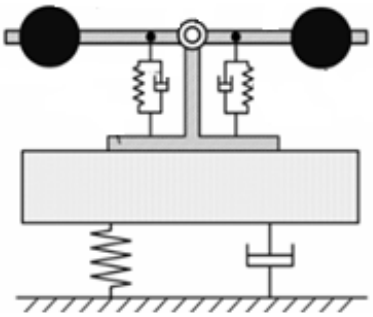

Figure 2.3: Variable inertia TMD [3]

To conclude, incorporating mechanical resonance altering mechanics into the

design of the TMD has the advantages of simple and reliable implementation. However, most of these devices only have a relatively small frequency altering range due to the requirement for linearity of the elastic elements. Also, the high additional mass, that is introduced in these types of device, limits their further application on a mechanical structure.

2.2.3 TMD using smart material

As mentioned in the previous section, one of the main issues for mechanical adjustment of the TMD is the high additional weight introduced. To avoid this disadvantage, novel nonlinear stiffness materials can be used in this type of TMD. In this section, several typical examples of these devices are introduced and discussed.

One of the most long-standing and commonly-used smart materials is Piezoelectric ceramic, normally used in the form of tiles or patches. Piezoelectric materials couple mechanical and electrical behaviour. One relatively common research activity in recent decades has been to attach a piezoelectric element to a vibrating system and also connect it electrically to a resistance-inductance-capacitance circuit. Correct tuning of the electrical components results in an oscillator that provides the same effect as a physical TMD. Despite extensive research interest, this concept has not seen significant practical success as overall performance is limited by the capacity of the piezoelectric element and its sensitivity to small changes in capacitance (e.g. from temperature changes). In some variants, the resistor is replaced by an energy harvester to store the generated charge. An example of one such configuration is shown in Figure 2.4.

The strain energy is dissipated using the deformation of the PZT cantilever beam and then converted into electrical power. These electrical voltages are then stored in the inductor - like energy storage element. The most attractive property of this structure is its self-adaptive properties without any energy input, which extends its usage for an adaptive TMD. However, this device is only designed for a narrow frequency range. It can only address the vibration of one selected

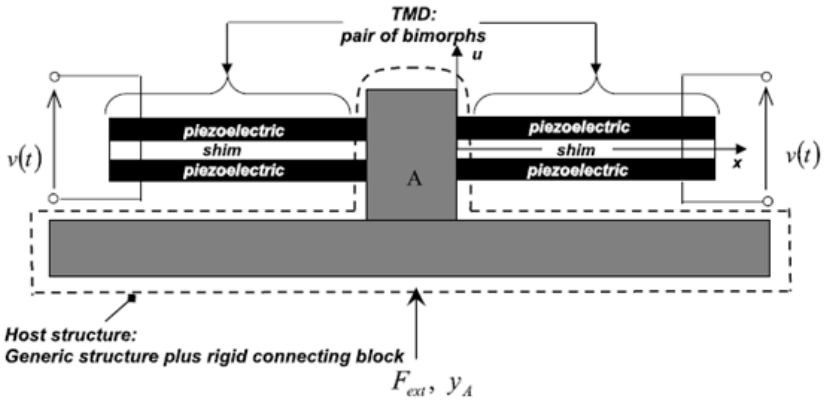

Figure 2.4: TMD with energy harvester [4]

mode, while other modes of the mechanical system, that are far away from the given mode, cannot be suppressed. Also, the voltage output level is normally low. Therefore, coupling of PZT actuators to the mechanical system is not easy to activate.

To overcome the low efficiency of the PZT actuators in a TMD, the magnetic effect of electric current was introduced. The magnetic effect itself, although extremely nonlinear, can be used to link the vibration of a host structure with a secondary oscillator. A permanent magnet moving near a conductor with coils can generate electrical eddy currents. Shunt circuits were then connect to this conductor. As a result, the energy dissipation for this type of the TMD can be enhanced, compared with the PZT patches [21]. However, one of the critical issues for this configuration is its narrow working frequency. To sort out this problem, a magnetic TMD can be devised – see Figure 2.5

In this device, the effect of the eddy currents, generated by the stationary magnetic fields, is utilised to adjust damping to the oscillator [5]. The frequency adjustment of this device was achieved by the length of the cantilever structure in this TMD. Another way to improve the energy dissipation is to use an external electric controller to adjust the equivalent stiffness and damping property of the eddy current damper, which would enlarge the working frequency range of this device. Nevertheless, as this highly nonlinear element is hard to model, this is not

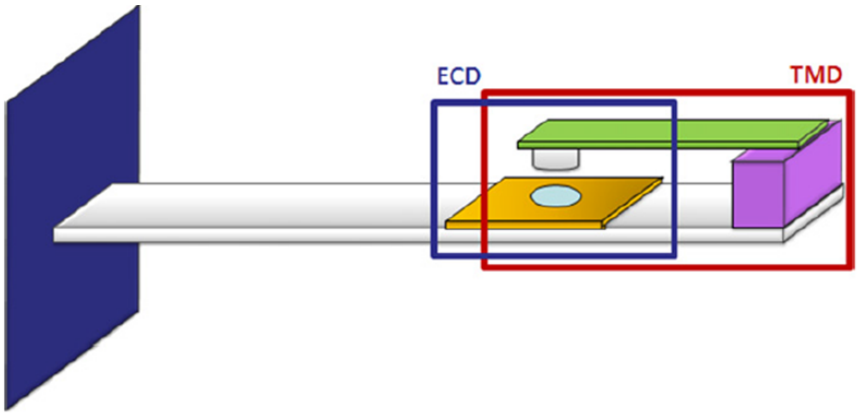

Figure 2.5: Magnetic tuned-mass-damper [5]

a convenient way to design a nonlinear TMD.

Recently, Mann and Sims [6] invented a new kind of energy harvester incorporating the electromagnetic effect. The schematic diagram of this system is shown in Figure 2.6. The magnetic levitation can be fitted by a third order polynomial function, to form a typical Duffing oscillator, which is the simplest nonlinear system. An interesting part of this study is that this system absorbs energy for a wider range of frequency.

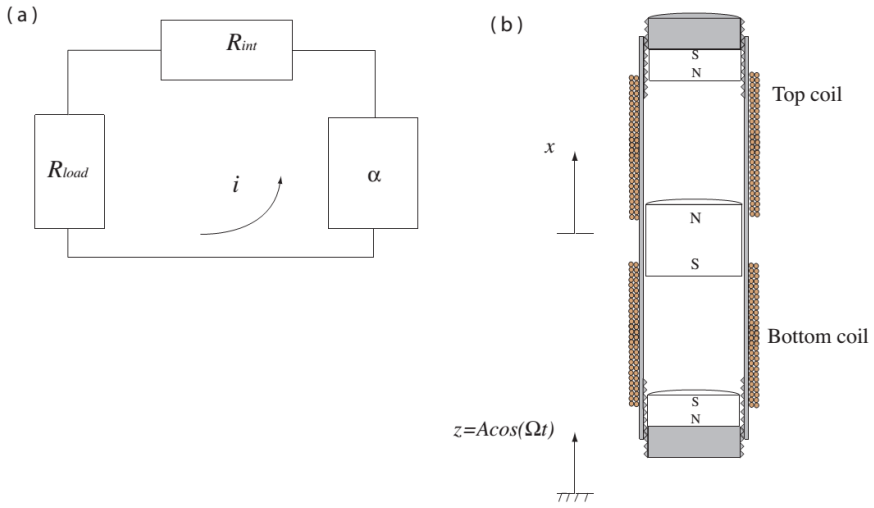

Figure 2.6: Magnetic tuned-mass-damper [6]

Neild [22] continued studying this device and found that the nonlinearity of the system would not affect the power output. But, it could shift the system resonant response without movement of mass and stiffness, which was shown to improve the output voltage. Currently, this device acts as low voltage supplier. When this is designed as a vibration absorber, the structure should achieve a balance between mistuning and suppression of the dominant frequency. Although its potential use as a damper for a flexible structure is still to be identified, this device offers many attractive properties, especially the simplest nonlinear behaviour.

In addition to these mechanical-electrical energy converters, other nonlinear damping material can also be used in developing adjustable TMDs. Figure 2.7 shows a typical embodiment of a TMD that uses Shape Memory Alloy (SMA) [7]. In this example, the temperature is the variable used to control the nonlinear damping force in SMA.

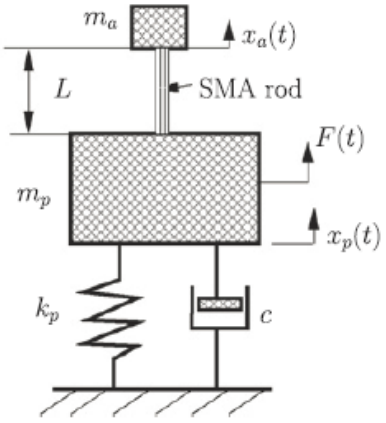

Figure 2.7: SMA based TMD [7]

All of these studies focused on theoretical modelling and validation. The barrier to this application, even in a prototype scale, is the temperature control strategy. The response of temperature is slow and the cooling problem with the SMA is hard to solve. Besides, the working temperature range for shape memory effect on SMA is limited to about 125 ^{o}C, which greatly restricts its application in structures such as gas turbine components.

Another recent innovation is Tangled Metal Wire material. This material is a type of porous material formed by compressing helical wires together in a mould. An air film damper embedded with these materials [8] is shown in Figure 2.8. The detailed adaptive feedback loop is shown in Figure 2.9. Eventually, the rotor

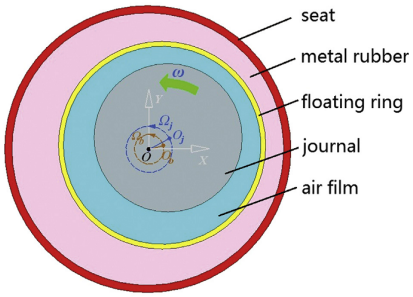

Figure 2.8: Air film damper [8]

imbalance is suppressed to a very low level. Tangled metal wire itself has mass and a certain level of stiffness, and, therefore can be considered as the additional degree of freedom system attached into the vibrating rotor. The stress on the TMW material and the volume of the air film might be changed to produce the nonlinear restoring and dissipating force in semi-active control. However, the dynamic properties of TMW block are highly nonlinear. The current literature has not even produced a statistical model, which prevents further development on applying these materials to a TMD.

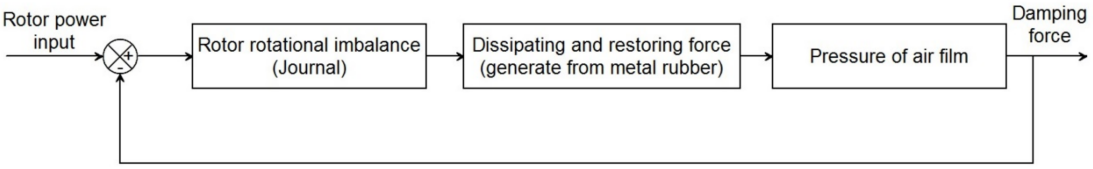

Figure 2.9: Adaptive feedback loop

2.2.4 Summary

To conclude, the effectiveness of all the devices developed in the literature has been illustrated, while the main challenge has always been the high complexity of modelling these smart materials. Additionally, heavy additional weight may restrict further applications of these devices, especially for mechanical structures. To make this frequency-adjustable device simpler, some nonlinear materials, with simple stiffness-altering mechanics are introduced in the next section.

2.3 Dynamic characteristics of selected nonlinear elastic and damping elements

In this section, two different nonlinear elastic and damping elements, elastomeric O-rings and TMW particles, are introduced. Since the elasticity of elastomers has been developed for many years, this section focuses on discussion of analytical models for polymeric material. However, as the TMW particles are a recently developed material, there is limited literature that demonstrates the properties of these particles. Hence, most of this section of the review is related to the genetic properties of the TMW material, although the one analytical model for TMW particles is discussed as well.

2.3.1 Elastomeric O-rings

Elastomeric material has been used in vibration suppression for many years. The material combines the advantages of predictable modulus and relatively high damping. Although the typical elastomeric cube is too stiff to form a TMD for mechanical structures, the O-ring has been introduced to overcome this issue. The O-ring can provide a lower stiffness due to the relatively small ring diameter. The geometry nonlinearity of the circular O-rings brings in the feature of static compression-dependent stiffening, and therefore the altering resonance frequency of the TMD.

One of the most commonly used analytical models of elasticity for polymer was established by Treloar [23]. The change in thermodynamic energy, entropy, has a certain relation to the change in chain vector length or molecular dimensions. Assuming that the end-to-end distance for the assembly of the chain follows the Gaussian distribution for a polymer, by knowing the number of chain per unit volume and the mean square end-to-end distance for the assembly of the chain, the entropy produced by the macroscale strain can be obtained. Using the conservation of the entropy and work done by the deformation, the stress-strain relationship and hence the stiffness for any loading conditions can be derived. However, several assumptions, as listed below, resulted in unwanted errors for this analytical model.

- The volume of the solid remains unchanged when applying the deformation
- The maximum extensibility of the molecular chain is not considered in this model. As a result, the Gaussian distribution of distances between the assembly and the neighbouring chain no longer exists.
- The intra-molecular internal energy, widely known as Van der Waal's forces, was not considered in this model.

Nevertheless, this analytical model still accounts for most of the geometric nonlinearity, especially when compressing the elastomer.

Payne [24] introduced the shape factors to account for the geometric variation, especially the expansions of the cross-sections of the O-rings in the radial direction, of the polymer during the compression of the O-ring. The work presented empirical expressions of the shape factors for different cross-sections including annular rings, cube and cylinder. Additionally, the expression of the compression-stiffness relationship in shear direction was also demonstrated. The limitation of this work derives from the assumption of the isotropic elastic model, as the strain-dependent modulus is not included in this model.

To explain the material nonlinearity of the elastomers, some high-order hyperelastic models, including those of Mooney-Rivlin [25–27], Yeoh [28], Gent [29–31]

and Boyce [32], were introduced. Most of these models have demonstrated their effectiveness for predicting uniaxial stress for a selected strain, especially when subject to high stretch of the polymer. However, obtaining these fitted parameters in such models generally requires a great number of experimental calibrations. For the deformation subject to low-to-moderate extension or compression, the rearrangement of the crosslinking is not vital to the strain-dependent stiffness of the polymer [33]. It is not necessary to employ these high-order models to predict the stress-strain relationships, and hence the low-order hyperelastic model is selected in this work.

Lindley [34] carried out experimental investigations of the elasticity of rubbery O-rings, and then established an analytical model of the O-rings [35]. The essence of this model is that the load-carrying element of a O-ring is a rectangular-sectioned ring, whose cross-section is formed by the deformed thickness and contact length – see the rectangle surrounded by ABCD in Figure 2.10.

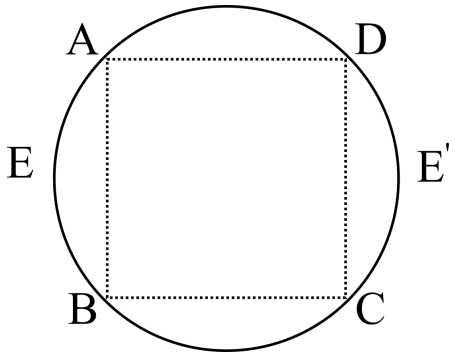

Figure 2.10: Cross-section of the O-ring representing the load-carrying area

With a high compression, the crosslinks in the molecular chains of the polymer are re-arranged, and therefore a the higher rate of stiffening can be observed. To compensate for this nonlinear stiffening, empirical polynomial terms were used in this model. The limitation of this analytical model is that the expansion of the nominal diameter of the O-ring in the radial direction is not included in this model. Also, the deformation of the O-rings, especially for the curved edge in the cross-sections – see the area surrounded by AEB and CE'D in Figure 2.10, causes some degree of softening in this model.

2.3.2 TMW particles

Tangled metal wire, also called metal mesh or metal rubber, is a type of porous material formed by compressing helical wires together in a mould. The damping mechanism for this material is dominated by hysteresis through dry friction generated by the contact between neighbouring springs [36]. Some loss also occurs from plastic deformation of the separated springs due to the squeezing and torsion of the wires [37]. Since the microstructure of TMW material is somewhat similar, albeit on a much larger scale, to that of a polymer, rubber-like modulus and damping properties are obtained. Compared with rubber, TMW has superb properties on fatigue and corrosion resistance. Additionally, its performance is relatively insensitive to temperature.

Generally, the energy dissipating performance of TMW material is closely related to its microstructure. As uniform alignment and patterns of internal coils do not exist in TMW material, the properties are somewhat variable [38]. The behaviour of the TMW material is also highly nonlinear under static and dynamic strain. When the static compression is low, the dynamic characteristic of TMW material is dominated by the compression of free coils inside the TMW material. At this stage, the stiffness is highly linear, while it is very difficult to observe this stage in the load-deflection curve. When the static compression increases, sliding between neighbouring coils occurs. At this stage, dry friction is the leading damping mechanism, which improves the energy dissipation of the TMW material. The equivalent loss factor decreases if the external load exceeds the critical value. Under these circumstances, the spring is pressed out between 2 coils and more contact points are developed in the TMW material [37, 39, 40]. In this situation, the TMW material can support more load with less deformation and the relative sliding between coils ceases.

The TMW particle is a recent innovation. Generally, the dynamic characteristics of these particles have similar properties to those of the typical TMW material. However, the variations in the properties of these particles are expected to be much larger because the stiffness of these particles is much lower. The microstructure of

each individual particle, which is determined in the fabrication process, occupies a more important role on the elastic and damping behaviours [41]. Additionally, performance degradation of metal rubber is still to be investigated.

The only analytical model presented in the literature was a quasi-static version, based on estimations of the elastic behaviour in the microstructure [13]. In this model, the microstrip between the neighbouring intraconnection points in the TMW particles is assumed to be a helical spring. Using the classic helical spring design criteria, the expressions for the radial and axial stiffness of the micro-strips were obtained. Three different contact arrangements between neighbouring microstrips – no contact, sticking and slipping – were identified for the neighbouring microstrips. Considering the frictional status in different contact arrangements, the expression of effective stiffness, related to orientation angle of applied force and stiffness of helical wire, was determined. The contributions of each arrangement was then defined for individual TMW particles. It is worth noting that the importance of each contact arrangement was represented using percentage weighting factor, and these factors were identified from experimental fitting. By combining the percentage contribution of contact arrangement and the corresponding stiffness expressions for local metal strips, the overall stiffness was obtained. This model does provide a good estimation of quasi-static stiffness, while the damping is overestimated. More importantly, the repeatability of these tests was not checked in their paper [13]. TMW particles are very sensitive to applied strain. In the process of modelling, the percentage contribution of the contact status needs to be calibrated experimentally. After this procedure, it is likely that these TMW particles will have stiffened, which will therefore lead to additional unwanted errors.

2.4 Optimal design criteria for a nonlinear TMD

Another important topic in relation to designing a TMD is design optimisation. Performance of a classic TMD is sensitive to

- the mass ratio between the damper and the host system

- the ratio of natural frequencies between the damper and the host system and
- the damping in the host structure.

If the host structure has no damping, it has been shown [42, 43] that optimum performance is obtained when,

$$\frac{\omega_{n,\text{TMD}}}{\omega_{n,\text{host}}} = \frac{1}{1+\mu} \text{ and } \zeta = \sqrt{\frac{3\mu}{8(1+\mu)^3}} \tag{2.1}$$

where $\omega_{n,\text{TMD}}$ and $\omega_{n,\text{host}}$ are the fundamental frequency of the TMD and the host structure respectively, μ is the mass ratio of the TMD and host structure. ζ is the optimal damping ratio. Under these conditions, the maximum dynamic magnification is,

$$\frac{X}{X_{\text{static}}} = \sqrt{1+\frac{2}{\mu}} \tag{2.2}$$

X_{static} is the static deformation of the secondary mass. Much of the theoretical optimisation of multi-mode dampers and semi-active systems is still based on the original scheme, while several researchers [44–50] have worked on parametric studies of multiple TMDs on a single DOF host system and noted the following points:

- The optimal damping ratio should be obtained by a numerical route rather than the classical way in the presence of inherent structure damping.
- The individual optimal damping ratios for multiple TMD are much lower than for single TMD designs.
- The number of TMDs does not affect tuning frequency and the overall performance.
- The optimal frequency spacing, average damping ratio and tuning frequency ratio can greatly improve the performance of multiple TMD systems.

Owing to the nature of the vibration suppression using a TMD - a balance between energy transfer from the primary system and energy dissipation from the TMD, several other design indicators were used. Krenk [51] proposed introduced the criterion that the optimal stiffness ratio of the TMD should still be similar to that obtained by classic method, while the optimal damping should be obtained using minimisation of the relative displacement for the TMD. The essence of this criterion is to find the damping ratio, where the two peaks in the frequency response start merging into one. Miller [52] and Yamaguchi [53] demonstrated the use of a stability law to design a kind of TMD. The aim of this criterion is to make the transient response of the host structure decay as fast as possible. By selecting the proper natural frequency and damping of the TMD, the poles of the overall 2DOF system were pushed to the left-most part of the phase plane.

Although these algorithms gave some suggestions on extending the classic design criteria to address the situation of multiple TMDs, they cannot deal with the case of designing a TMD incorporating nonlinear elements or designing a TMD for a nonlinear host structure.

One of the most direct approaches is to minimise the mean squared displacement over the selected frequency range. The expressions for the optimal frequency ratio and damping, when subject to this optimisation are given by Iwata [54] and Warburton [55]. Warburton also demonstrated the design formula for the TMD using minimisation of kinetic energy over selected frequencies [55]. More recently, Zilletti [56] introduced the criteria that the power dissipation of the TMD needs to be maximum for the given frequency range. Their work demonstrated that the maximisation of power dissipation is equivalent to minimisation of the kinetic energy. Nevertheless, no work as yet still exists that has applied these design criteria to a nonlinear TMD device.

2.5 Summary

These sections reviewed the state-of-the-art TMDs, targeting the vibration suppresion over a broad frequency range. Although most of these devices brought useful

levels of energy dissipation, a light-weight, easy to produce frequency-altering device is still to be developed. One common approach is to incorporate te smart structures. The properties of two typical smart components, elastomeric rings and TMW particles, was discussed. Elastomeric rings had well-developed design formulas for the stiffness and damping in tensile-compressive direction. The lack of knowledge on the stiffness model in the shear and tilting directions may be an obstacle to developing an adjustable TMD. On the other hand, there is very limited literature reporting on TMW particles, especially for the static compression dependent stiffness and damping, and the repeatability of different collections of particles with similar physical properties. An analytical model that can represent the nonlinear stiffness and damping needs to be established, especially in the case where these particles are subjected to low dynamic strains. Although a design for optimisation of the host structure with a linear TMD has been in existence for a long time, it is almost impossible to extend this method to optimise a nonlinear TMD. Although some energy-based optimisation strategies have been discussed, validations on a selected nonlinear TMD still needed to be carried out.

Chapter 3

Adjustable Tuned Mass Damper using Elastomeric O-rings

3.1 Introduction

In the previous chapter, the reasons why a TMD is suitable for the vibration suppression for mechanical structures are stated. One of the most significant limitations for classic TMDs is their narrow working frequency range. One way to extend the effective frequency range of a TMD is to make it adjustable.

This chapter reports work that was carried out to investigate an adjustable TMD incorporating elastomeric O-rings. The elastomeric O-ring was selected as it offers important advantages over other nonlinear elements. These main reasons are listed below.

- Elastomeric O-rings have the benefit of nonlinear stiffness. A minor adjustment to the static compression dramatically changes the stiffness and hence the resonance frequencies of the TMD. The capability of adjustable tuning frequency range of this TMD is enhanced.
- Since the O-rings exhibit strain-related nonlinear stiffness, the mechanical structures that can provide resonance adjustment are relatively simple.

- The damping provided by an elastomeric O-ring is relatively uniform even when subject to significant deformation as the main loss mechanism is linear viscoelasticity of the polymer. For given mass ratio of TMD and main system, this allows a simple parameter designs for the TMD that can target more than one mode of a continuous structure.

3.2 Viscoelasticity of elastomers

This section briefly summarises the mechanical characteristics of elastomers. A brief explanation of the linear viscoelasticity of polymers is given to provide the theoretical background for the subsequent analysis. Further reading for this topic can be found in Drozdov's book [57].

A conventional elastomer is made from long chain molecules, which comprise repeating backbone connecting carbon atoms [58]. The backbone of a conventional elastomer molecule is a long chain of carbon atoms. This chain can be linear or branched. Attached to this chain are repeating units comprising hydrogen and atoms of other elements. Significant entropy reduction occurs only when the stretch of elastomer is very large - the chains align to give a more ordered structure. The large-scale rearrangement of atoms occupies the leading roles, meanwhile, the length and angle of these long chains distort for these elastomers. As a result, the molecular chains move to locations with greater internal energy. The elasticity of an elastomer is achieved as these rearrangements of molecules is reversible, while the damping is caused by the internal friction between these molecular chains.

3.2.1 Linear viscoelasticity - Boltzmann superposition principle

An elastomer operating in its rubbery zone displays behaviour that is almost linear elastic - namely that the stress is proportional to the applied strain. For this linear viscoelastic material, Boltzmann's superposition principle [59] can give the

relationship between the stress at any time t and strain at any previous instantaneous time τ,

$$\sigma(t) = \int_{-\infty}^{t} E(t-\tau)\frac{d\varepsilon}{d\tau}d\tau \tag{3.1}$$

where $E(t-\tau)$ is the relaxation modulus at previous time $t-\tau$ for each individual strain. Equation 3.1 indicates that the response of the elastomer is dependent on that at any previous time and the modulus of elasticity varies with not only time but the previous strain history at given temperature.

Viscoelastic properties of a material are often estimated using steady-state, harmonic loading. The Fourier transform is applied to obtain the modulus at given frequencies. The frequency spectrum of Equation 3.1 is given by,

$$\sigma(\omega) = \int_{-\infty}^{+\infty}\left[\int_{-\infty}^{+\infty} E(t-\tau)\, i\omega\varepsilon(t)\, d\tau\right] e^{-i\omega t}dt \tag{3.2}$$

where ω is angular frequency and i is $\sqrt{-1}$. Applying convolution theory, Equation 3.2 can be expressed as,

$$\begin{aligned}\sigma(\omega) &= i\omega\int_{-\infty}^{+\infty} E(t)\, e^{-i\omega t}dt\,\varepsilon(\omega)\\ &= E^{*}(\omega)\,\varepsilon(\omega)\end{aligned} \tag{3.3}$$

where $E^{*}(\omega)$ is the complex modulus. The complex modulus is often represented as,

$$E^{*}(\omega) = E^{'}(\omega)\,(1+i\eta), \quad \eta = \frac{E^{''}}{E^{'}} \tag{3.4}$$

where $E^{''}$ and $E^{'}$ is loss and storage modulus respectively. η is defined as loss factor.

3.2.2 Frequency-temperature equivalence

An interesting, and very useful property of an elastomer is the frequency-temperature equivalence. For some polymers, the high capability of energy dissipation occurs in relatively high frequencies. These features obtained experimentally are often

not reliable due to limitations of the test equipment. The frequency-temperature equivalence provides an alternative way to measure the full range of properties of these polymers.

It is well known that temperature and frequency have a great influence on the modulus [11]. The elasticity of polymer is controlled by the rearrangement of molecule chains. The rate change of the molecular configurations is estimated based on Arrhenius's observation [60–62],

$$\text{rate} \propto \exp\left(\frac{-E^{\dagger}}{RT}\right) \tag{3.5}$$

where $E^{\dagger}$ is the activation energy for the process, R is the universal gas constant, T is the surrounding temperature. It can be seen from Equation 3.5 that the molecular mobility increases with surrounding temperature. Consequently, this polymer softens and exhibits rubbery behaviour - a relatively low modulus and moderate energy loss. Conversely, when the temperature decreases, the movement of molecular chains is frozen and only elastic bond stretching is possible. As a result, the elastic modulus increases, and glassy status of the polymer is observed.

In the same way, the local reaction time of amorphous chain molecules can cause these changes of the molecular configurations as well. At high frequencies, most of the molecular configurations remain unchanged as there exists insufficient time for these chains to react. Under this condition, the polymer resembles a rigid glassy solid. When subject to low frequency, the large scale of molecular deformation can be observed and thus the polymer is in a rubbery region.

Pioneering studies were performed by Leaderman [63] to confirm this equivalence experimentally. In order to obtain the modulus of the polymer at high frequencies, the shift procedure was applied using this equivalence, as shown in Figure 3.1.

It is worth noting that the axes of the frequency-modulus curve in the following analysis are in logarithmic scale. The effect of increasing temperature on the modulus curves is simply equivalent to shifting the viscoelastic curves to low

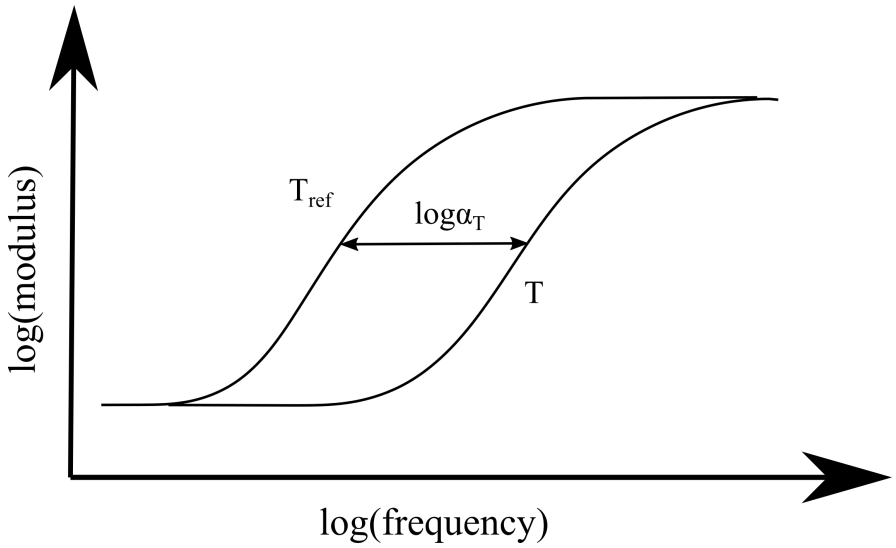

Figure 3.1: Temperature-frequency shift factor

frequencies without changing their gradient. To describe this multiplier quantitatively, a 'shift factor', $\alpha(T)$, is defined,

$$\log\left(\alpha(T)\right) = \log\left(E_{\omega(T)}\right) - \log\left(E_{\omega(T_{\text{ref}})}\right) \tag{3.6}$$

where T_{ref} refers to the reference temperature and $E_{\omega(T)}$ is the elastic modulus at the selected frequency ω and temperature T. An empirical equation for the frequency-temperature shift factor with temperature change has been developed by Williams, Landel and Ferry - so-called WLF function [64]. The details of this equation is given by,

$$\log \alpha_T = \frac{-C_1(T - T_{ref})}{C_2 + (T - T_{ref})} \tag{3.7}$$

where C_1 and C_2 are the empirical parameters whose values depend on the selection of material and the reference temperature. The WLF shift becomes less useful if the material exhibits several significant transitions or the presence of fillers distorts behaviour. One way to ascertain the likelihood of success when using a particular material dataset is to create a log-log plot of loss against storage modulus. If the data points describe an inverted 'U' shape, a shift function based on the WLF approach is likely to be successful [65].

The schematic diagram for constructing the master curve of an elastomer is then shown in Figure 3.2

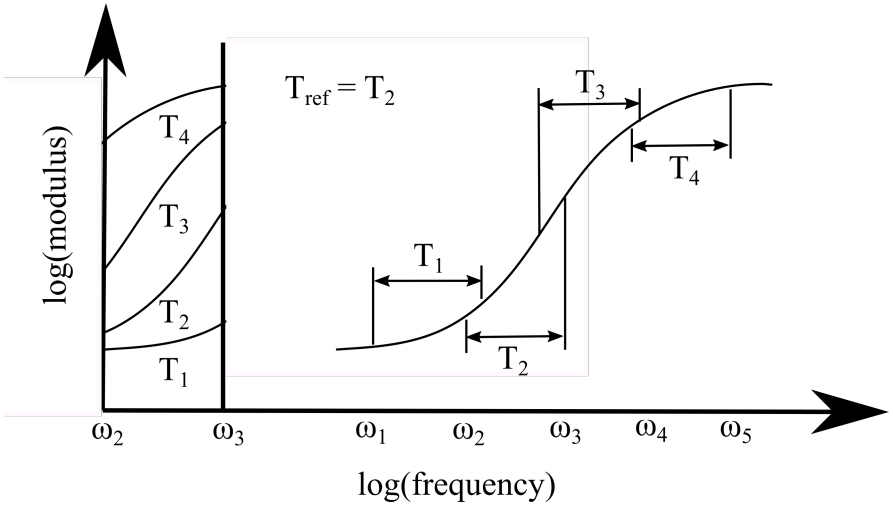

Figure 3.2: Construction of master curve using frequency-temperature superposition, Data collected at temperatures T_1 to T_4 in the frequency range of $10^{\omega_2} - 10^{\omega_3}$ Hz are superimposed on the T_2 curve by applying horizontal shifts to each isothermal curve

3.2.3 Mechanical models for linear viscoelastic solids

Several viscoelastic models, including Voigt, Maxwell, Zener and Maxwell-Wiechert have been developed to describe the mechanical behaviour of polymers, especially relaxation and energy loss. In this section, only the Zener and Wiechert models are discussed because these models are able to represent the stress relaxation and creep behaviour simultaneously. Simplified viscoelastic models can be represented using an elementary spring and dashpot element, as shown in Figure 3.3.

The elasticity of an elastomer K_1 is instantaneous bond deformation and entropic coiling and uncoiling of molecular chains, and therefore, can be simulated using a mechanical Hookean spring. One extra spring K_e is involved in this mechanical model as molecular chain change for the real polymer is limited by the

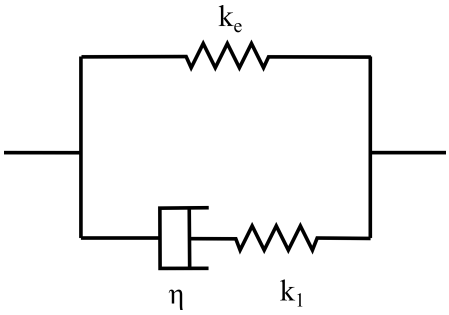

Figure 3.3: Zener (standard linear material) model

network of entanglements or other junction points. Since the deformation of a polymer in its microstructure involves a fluid-like reversible process, 'Newtonian dashpot' can represent this behaviour well.

It is widely accepted that the standard linear model can represent the modulus in the glassy and rubbery regions relatively well, while the abrupt change of modulus in the transition region is less well modelled. One of possible reasons is the variations of the shape and length of the molecular chains in an elastomer. Simpler and shorter molecular segments result in a faster relaxation. The Zener model is insufficient to predict the overall distribution of relaxation modulus in practice. Therefore, a Wiechert-Maxwell model is introduced, as illustrated in Figure 3.4.

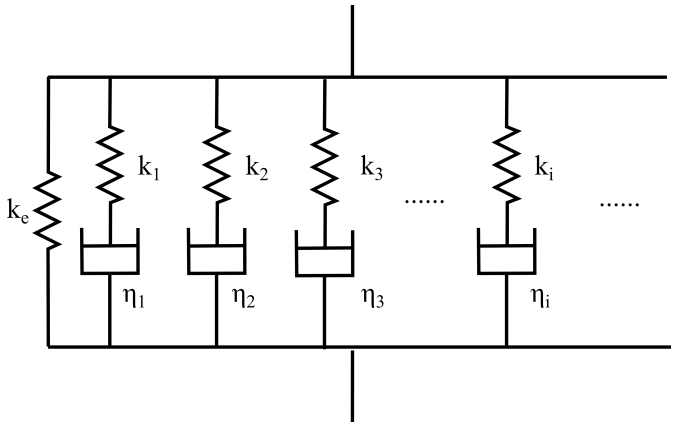

Figure 3.4: Wiechert-Maxwell model

The Wiechert model provides multiple spring-damper series elements that are

connected in parallel. Several authors [66–70] have shown that this model can represent creep and relaxation behaviour of a real polymer. From this model, the modulus history [71] can be given by,

$$E(t) = E_e + \sum_{n=1}^{N} E_n e^{-\frac{t}{\tau_n}} \tag{3.8}$$

where τ_n is time constant. This mathematical presentation of this equation is widely known as the Prony series. Although this model represents the frequency-dependent storage modulus well, some deviations can still be observed for the energy loss-frequency curve. One reason is that the fitting error of the loss factor is the combination of the errors in dissipated and storage modulus. Furthermore, the elastomer experiences a sharp rise of energy loss against the frequencies at given temperature in the glass transition status, and therefore, the fluctuations are more evident in this region. Nevertheless, the Prony series is still used to predict elastomer response of the numerical model of O-rings in the following work due to the fact that this series is the only model the commercial FE code allows for the frequency-dependent modulus for polymers.

3.2.4 Estimation of hysteresis using time history of elastomers

Damping from elastomers subject to steady state loading can be estimated from the phase shift between the excitation and response signal. In practice, some non-linearities may occur, for example the stiffening caused by complex geometry. In this case, a multiple-frequency response may arise from mono-sinusoidal excitation, and hence, it can become different to determine the phase shift of the system. The hysteresis loop is the other strategy, that is widely accepted, to estimate the energy dissipation and stiffness for the given material. The strain-dependent non-linear stiffness can be easily subtracted for the purpose of evaluating damping.

A typical hysteresis loop, as shown in Figure 3.5, indicates the relationship between force and displacement for any mechanical elements. Using the gradients

of the average reaction force over loading and unloading, the stiffness for structures subject to any selected cyclic loading can be estimated. In this work, the controlled strain energy is defined as twice the peak strain energy. The energy dissipation can then be represented as the ratio of dissipated and controlled strain energy over one cycle, known as energy loss factor. Note that inertia forces are considered small when subject to low-frequency excitation.

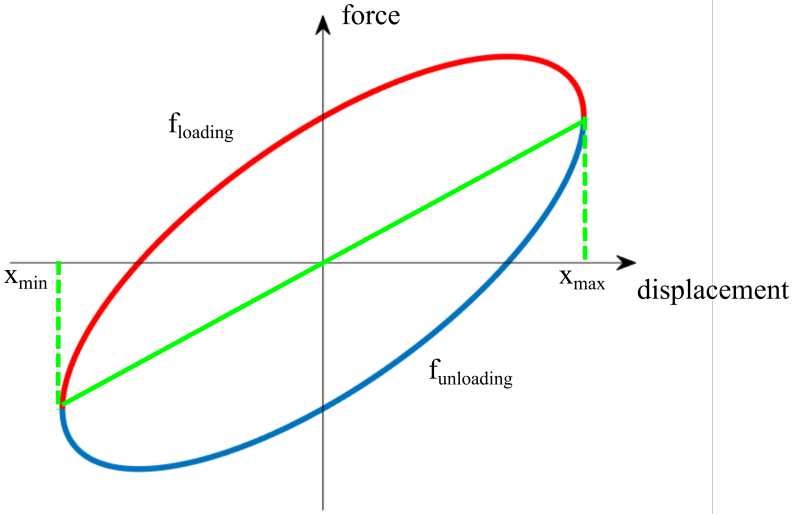

Figure 3.5: Typical hysteresis loop

Referring to Figure 3.5, the controlled strain energy per cycle, U, is given by

$$U = \int_{x_{\min}}^{x_{\max}} \frac{1}{2} |(f_{\text{loading}} + f_{\text{unloading}})| \, dx. \tag{3.9}$$

The dissipated energy per cycle, the area enclosed within the loop, can be expressed as,

$$W = \int_{x_{\min}}^{x_{\max}} (f_{\text{loading}} - f_{\text{unloading}}) \, dx. \tag{3.10}$$

The energy loss factor is therefore defined as,

$$\eta = \frac{W}{U\pi} \tag{3.11}$$

In practice, noise always accompanies signals collected experimentally. As the stiffness is estimated from the gradient of the average load-deflection behaviour, even low-level noise can significantly affect results, and hence, the accuracy of numerical interpretation of the midpoint stiffness. In order to smoothen these signals, zero-phase delay low-pass filters were applied to the force and displacement histories. Since the noise signal comprises unwanted high-frequency components, a low-pass filter can remove them effectively. In the following analysis, a 3rd order Butterworth filter was used due to its ease of design and common application to engineering signal processing.

For a viscous system, these filters do not cause serious problems due to its linear nature. When nonlinearity is presented, filters may affect the shape of the hysteresis loop. To demonstrate the importance of the design parameters of a Butterworth filter on the hysteresis, a typical frictional load-defection relationship, as shown in Figure 3.6, is used as an example. Figure 3.6 indicates the filter works

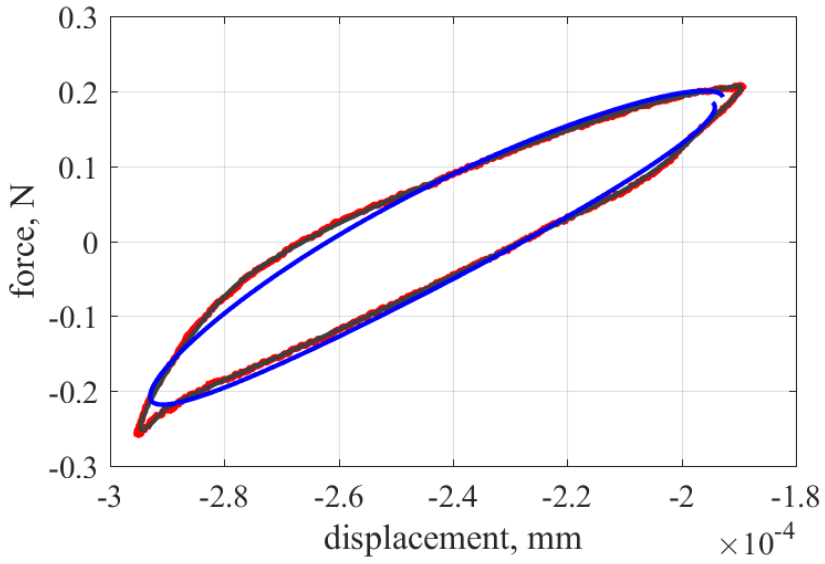

Figure 3.6: Effect of 3rd order Butterworth filter on a typical frictional system, (red line: unfiltered, black line: cutoff frequency: 50 Hz, blue line: cutoff frequency: 5 Hz)

well when the cutoff frequencies are carefully selected. The shape of hysteresis loop

tends to be an ellipse when the cut-off frequency of the filter is set too low because nonlinear components of the signals (observable as higher-order harmonics) are removed as well as the white noise. In this work, most of the dynamics tests have excitations of 2.5 Hz. So, the cutoff frequency of the third order Butterworth filter was chosen as 50 Hz.

An alternative method to remove the white noise is to fit cubic splines to the force-displacement curves. The advantage of this method was that spikes in the force plot, arising from local relaxation events could be smoothed. The filtered signal obtained using the 3rd order Butterworth low pass filter are compared with those produced using the spline smoothing for a typical hysteresis loop in Figure 3.7.

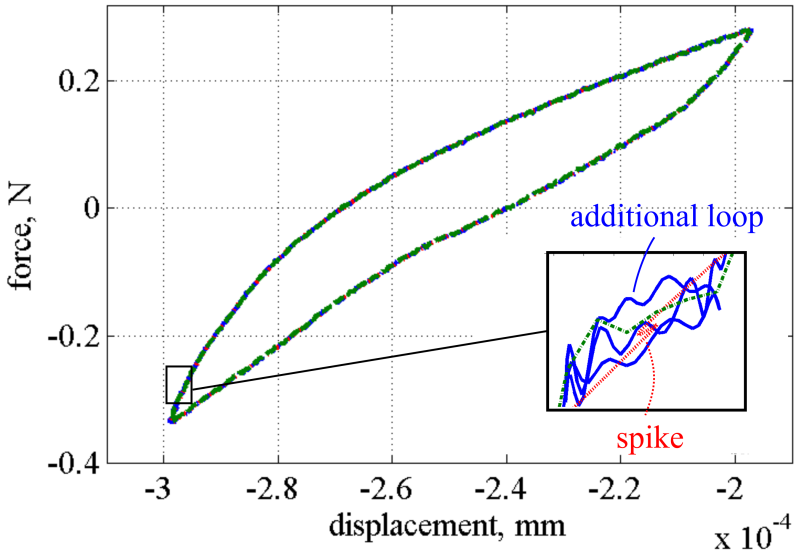

Figure 3.7: Comparison of two different types of filters (blue solid line: unfiltered, red dash line: Butterworth filter, green dash-dot line: spline fitting)

It can be seen that the Butterworth filter is more effective at suppressing high frequency noise while the spline fit smoothing deals with the local relaxation effects.

In the following work, a combination of both strategies was carried out. The average load-deflection curve was obtained using the spline fitting approach. Fol-

lowing this, the low-pass filter was applied to this curve to remove the further tiny oscillations for the sake of accurate estimate the midpoint stiffness.

3.3 Configuration and initial evaluation of TMD incorporating O-ring

Real TMDs rarely have one single vibration mode. This work starts with the premise that this characteristic provides an opportunity to generate damping over a broader frequency range. An initial numerical study was carried out to identify the principal modes of an O-ring TMD of the kind shown in Figure 3.8 and to estimate its sensitivity to axial compression.

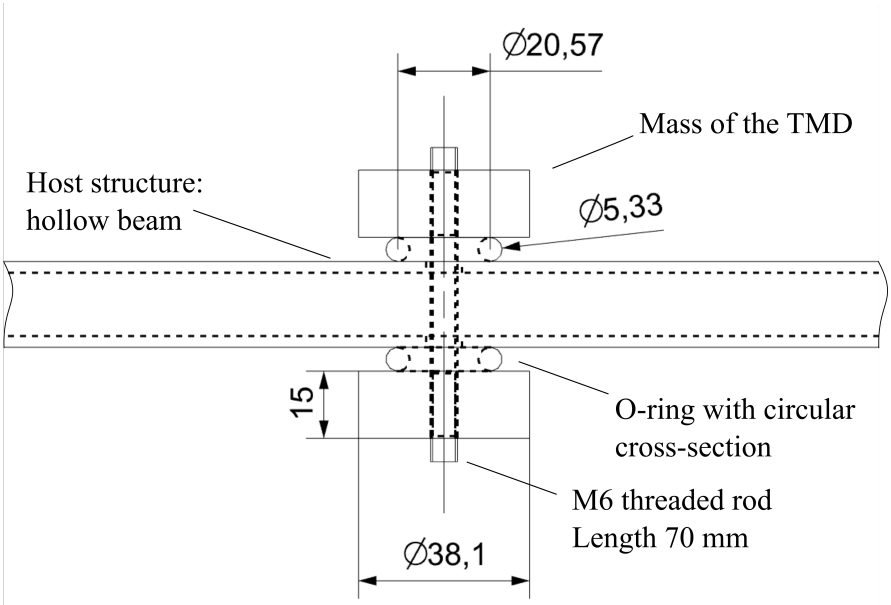

Figure 3.8: Adjustable TMD using elastomer O-ring

3.3.1 Detailed configuration

The configuration of the adjustable, O-ring based, TMD examined in this work is shown in Figure 3.8. This damper uses two identical circular discs and elastomeric

O-rings that are mechanically attached to host structures. Two threaded holes are made in the middle of these discs. These two halves of the TMD are clamped onto the host structure using a threaded rod that passes through the host structure without touching it. The static compression of the O-rings can be adjusted using the threaded rod resulting in a simple device that minimises interface friction. The critical dimensions of the damper are given in Table 3.1.

Variables	Value
Dimensions of each disc	ϕ 38.1 mm $\times$ 15 mm
Mass of each disc	152 g
Modulus of each disc	117 GPa
Mass of each O-ring	1.8 g
Type of each O-ring	BS312
Nominal modulus of each O-ring	9.3 MPa
Nominal Poisson's ratio of each O-ring	0.49
Dimensions of the threaded rod	M6 $\times$ 1
Length of the threaded rod	70 mm
Mass of the threaded rod	9 g
Modulus of the threaded rod	200 GPa

Table 3.1: Properties of this TMD

3.3.2 Numerical set-ups

An initial numerical study was conducted in order to identify the vibration modes typically occurring in such devices. The analysis first needed to obtain the deformed condition caused by the static pre-load, which in practice, is always required in order to hold the damper to the host structure. To minimise computational effort, the deformed shape for the O-ring cross-section was first obtained using a 2D finite strain analysis using a high density mesh. This deformed shape was then used to construct a 3D model from which natural frequencies and mode

shapes were calculated. In this model, the threaded rod was simplified to a cylinder for the sake of computational effort. This cylinder was bonded to the mass block to ensure the boundary condition between threaded rod and discs remain unchanged. Friction between the O-ring and discs was ignored for the modal analysis. Most of this FE model was made from solid 20-nodes quadratic hexahedron elements. Since one of the key design features for this kind of TMD is stiffness of the O-rings, a fine meshing strategy was required for the O-rings. The total amount of elements is 6190, in which case two-thirds are meshes of O-rings.

3.3.3 Working modes

Excluding the twisting motion, this device displays three types of vibration mode - extension, rocking and shear modes at given frequencies. Typical mode shapes of these three modes are shown in Figure 3.9. For modes with higher frequencies, the local resonance of the O-rings occupies the leading roles, which causes difficulty in estimating stiffness. In the devices proposed here, only first few modes which involve the rigid body motion of metal blocks are considered.

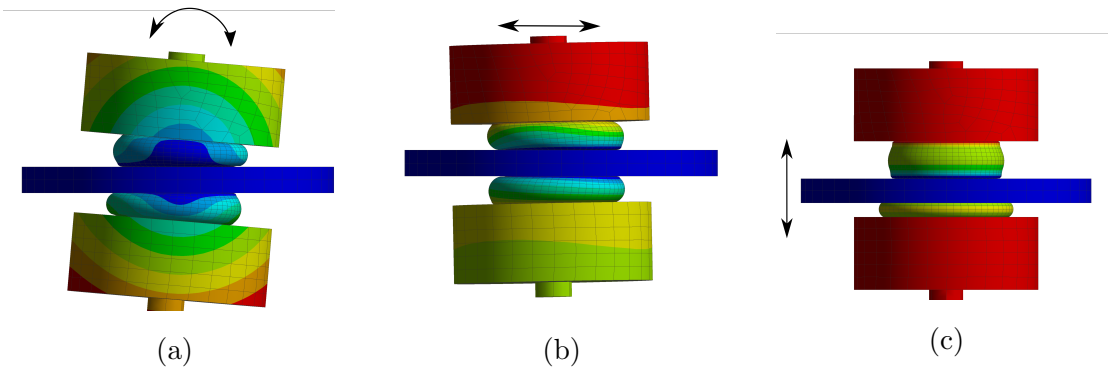

Figure 3.9: Working modes of the O-ring TMD (a) rocking mode (b) shear mode (c) extension mode.

Figure 3.9 also indicates that multi-direction vibration suppression can potentially be achieved as motion exists parallel and perpendicular to the damper axis. Even for a single static compression, two different modes, working in the same

direction, extends the working frequency range effectively. Since two working modes exists for this TMD, the strain energy of the host structure over the frequencies, that is restricted by two resonance frequencies of the TMD, can transfer to both vibration modes. The corresponding equivalent damping of this system is therefore significant for a wide frequency range.

3.3.4 Effect of static compression

When this system is subjected to pre-compression, the natural frequencies move to higher frequencies. To demonstrate this behaviour, a comparison between two different static compressions applied to the O-ring was carried out.

Static compression	Shear mode	Rocking mode	Compression mode
0.05 mm	121 Hz	113 Hz	274 Hz
2.1 mm	256 Hz	413 Hz	638 Hz
Frequency ratio $\omega_{2.1}/\omega_{0.05}$	2.12	3.66	2.33

Table 3.2: Comparison of resonance frequencies for different modes

It can be seen from Table 3.2 that the resonance frequencies of this damper increase considerably with static compression. The sensitivity of the stiffness to the geometric nonlinearity in different directions can be seen in the differences by which the natural frequencies increase. The higher sensitivity of the rocking mode to initial compression occurs because this deformation does not only increase the contact length at the cross-section, it also moves material further from the centreline of the damper increasing its resistance to transverse rotation. For other modes, position with regard to the damper centreline is not important. Therefore, a greater stiffening can be observed for rocking modes.

To conclude, the working frequencies of these devices are sensitive to pre-compressions showing that the O-ring condition is fundamentally important to this type of TMD.

3.4 Experimental evaluation of compressive stiffness and damping of O-rings

The significance of compressive behaviour of O-rings has been demonstrated in the previous section. Experimental studies of different loading conditions, including excitation frequencies, static compression and dynamic displacement amplitudes, are evaluated for stiffness and damping in this section.

3.4.1 Choice of elastomer

The damping level in a TMD is an important design criterion – simply increasing the damping level does not guarantee an improved damper. Different materials was first characterised in order to obtain a suitable level of damping.

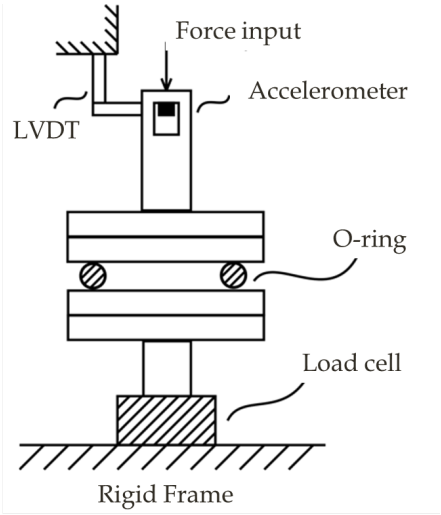

Figure 3.10: Dynamic Compressive Test Machine

Quasi-static axial compressive tests were carried out in order to obtain the dynamic stiffness and damping of circular O-rings. A Metravib VA2000 visco-analyser was used to measure the displacement response of the specimen when subject to harmonic excitation. A piezoelectric(PZT) load cell was used to detect

the force signal from the specimens. This load cell has a nominal force capability of 150 N and a resolution of 0.1 N. Meanwhile, this test machine is capable of measuring the frequency range between 0.001 to 200 Hz. When the excitation frequency is lower than 150 Hz, the displacements are identified using the linear variable differential transformer (LVDT) while the accelerometer took over this measurement in high frequency region. The maximum displacement measurement for this machine is 7 mm. Using a ceramic chamber, the testing temperature of the specimen can vary from -150 ^oC to 400 ^oC.

The load arrangements for these sets of tests are shown in Figure 3.10. The harmonic displacements, which are controlled using the hydraulic system, are generated on the top boundary surfaces. The O-ring was placed between the parallel plates of the fixture in ths machine.

Considering the geometry of O-rings used in these experiments, the fundamental natural frequency of O-ring itself is far higher than working frequency range of mechanical structures (approximately 50Hz to 1000Hz). A relative low excitation frequency, 2.5Hz, is used for these sets of experiments.

In order to demonstrate influence of material on dynamic characteristics of O-rings, hysteresis loops for four different materials for O-ring were obtained. A pre-compression of 0.3 mm was applied to each O-ring. Since the stiffness changes with initial cycles, the compressive displacement rather than force was chosen as the control indicator. In these experiments, the peak to peak dynamic displacement was selected as 0.05mm. The details for these O-rings are shown in Table 3.3.

Model	Material	Cross-sectional diameter	Inner diameter	Hardness
Poly 70	Polyurethane	3.53mm	17.04mm	70
BR 70	Butyl	3.53mm	17.04mm	70
ACM 70	Polyacrylate	3.53mm	17.04mm	70
NBR 70	Nitrile	3.53mm	17.04mm	70

Table 3.3: O-rings sample details

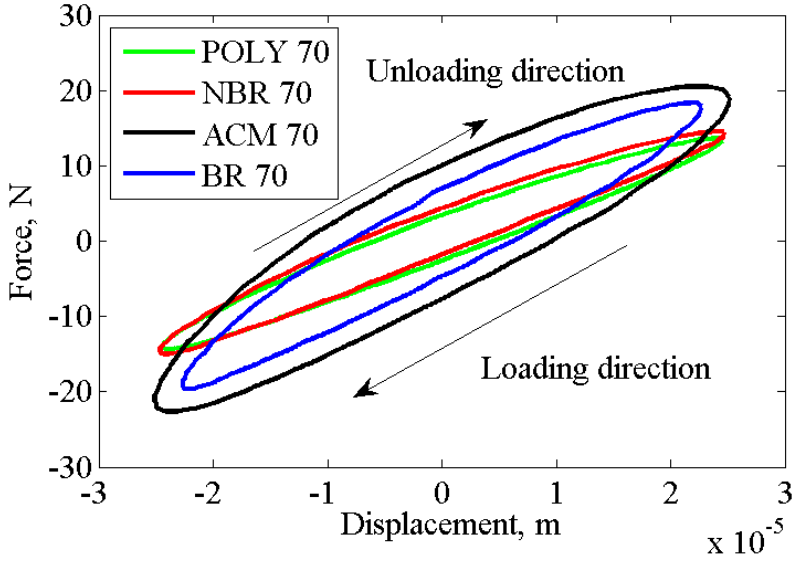

Figure 3.11: Typical hysteresis loops for O-rings with different material

It can be seen from Figure 3.11 that the loss factor varies from 0.15 to 0.5 with different rubbers. Also, it is interesting to note that obvious stiffening behaviour appears for Butyl O-ring. An initial thought of this phenomenon is that the deformed cross section of O-ring and the nature of nonlinear elasticity of polymer are the main resources for these stiffening effect. A further investigation will be demonstrated in Section 3.4.4.

The energy loss factor in room temperature, identified using hysteresis loops, is shown in Table 3.4.

	Polyurethane	Butyl	Polyacrylate	Nitrile
Energy loss factor	0.23	0.32	0.46	0.20

Table 3.4: Damping from O-rings with different material

Considering the role of O-ring in proposed TMD, a material with the linear behaviour near selected compression level is preferable. Meanwhile, the damping level required for a TMD is relatively low. Therefore, Nitrile O-ring is chosen as the damping element for TMD in the further investigation.

3.4.2 Modulus and energy loss of nitrile rubber

The characteristics of the nitrile rubber were identified using Metravib VA2000 viscoanalyser. The complex modulus is introduced to evaluate the elasticity and damping of this given polymer. Different loading and thermal conditions were applied to construct the viscoelastic master curves. Measurements were made over a wide range of temperatures at a number of different frequencies.

Prismatic test specimens were prepared from the original nitrile O-ring. This specimen was bonded to the boundary plates of the viscoanalyser. In order to obtain different thermal conditions, the samples were put in a ceramic chamber and the surface temperature was measured using a thermocouple. The test conditions are shown in Table 3.5.

Variable	Value
Specimen dimension (mm)	$8.06 \times 3.02 \times 2.96$
Excitation frequency (Hz)	1, 1.46, 2.13, 3.11, 4.53, 6.62, 9.65, 14.01, 20.56, 30
Temperature (°C)	-40, -35, -30, -25, -20, -15, -10, -5, 0, 5, 10, 15, 20, 25, 30, 35, 40, 45, 50, 55, 60, 65, 70, 75, 80
Stablisation time at each temperature (s)	120
Dynamic strain	0.001

Table 3.5: Properties of validation rigs

The tensile-compressive stiffness was obtained from the hysteresis loop at different loading conditions. The modulus of the nitrile elastomer was calculated using,

$$E = \frac{kL}{A(1+2s^2)} \tag{3.12}$$

where k is tensile-compressive stiffness, L is specimen length, A is cross-section area and s is shape factor. The shape factor [24] is an empirical parameter that accounts for deformatin perpendicular to the loading direction on the unrestrained

surfaces of the specimen. A simplified approach is to represent this constant using the ratio of contact area and load-free surface.

The wicket plot, as shown in Figure 3.12, was obtained to check whether this elastomer is thermorheologically simple, and hence the principle of superposition can be applied. It is interesting to note that one small curvature change occurs when the storage modulus is close to 20 MPa. One probable reason is that one additional glass transition occurs. The shifted curves shown in Figure 3.12 have a similar shape to a classic viscoelastic master curves, and therefore was used in the following analysis.

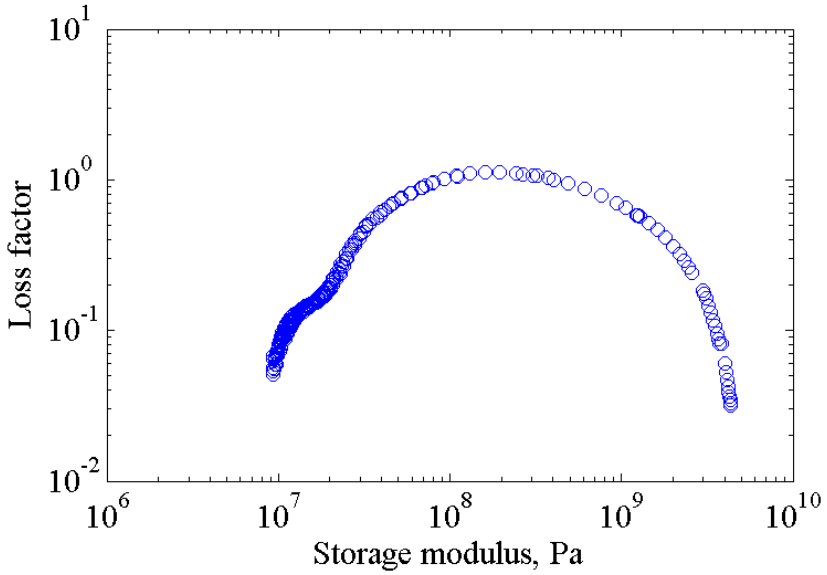

Figure 3.12: Wicket plot for shifted modulus and loss factor

Following this, the principle of superposition was applied to obtain a complete viscoelastic master curve of the polymer at room temperature. The shift factor, as shown in Figure 3.13, was obtained using the William-Landel-Ferry equation.

The individual shifted modulus in the viscoelastic master curve are then obtained and shown in Figure 3.14. Figure 3.14 also illustrates the thirty-order Prony series fitted curve for the complex modulus at different frequencies. The least square algorithm is applied and the cost function is selected as the root sum

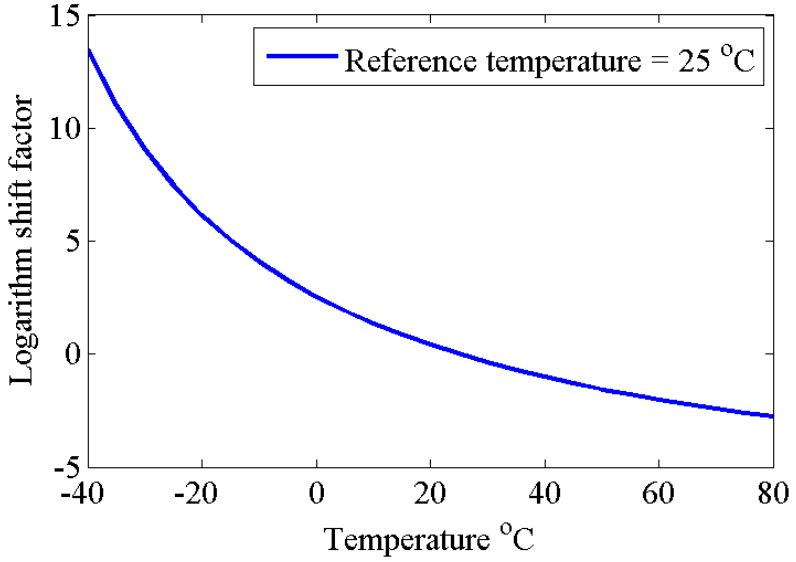

Figure 3.13: Temperature shift function versus temperature for the elastomer of the O-ring ($C_1 = 7.76 \quad C_2 = 112.60$)

squared of errors from the fitting curve for modulus. The coefficient of the best-fit curve are presented in Appendix A. It can be seen that the fit is of high quality - particularly for the storage modulus.

In summary, nitrile elastomer always shows rubbery behaviour at room temperature when applied excitations have a relatively low-frequency profile. In this region, the variation of energy dissipation can be negligible. Prony series provides a way to predict modulus in entire frequency ranges with reasonable accuracy.

3.4.3 Static compressive tests: O-rings

Deformation-dependent stiffness is an important feature of an elastomeric O-ring. The nonlinear stiffness forms the basis of developing an adjustable TMD – altering resonance frequencies. Preliminary static compressive tests were carried out to ascertain whether the O-rings used in this work have this nonlinear behaviour. The details on test set-up are shown in Figure 3.15.

The load was applied to O-rings using screws and nuts. The load cell and

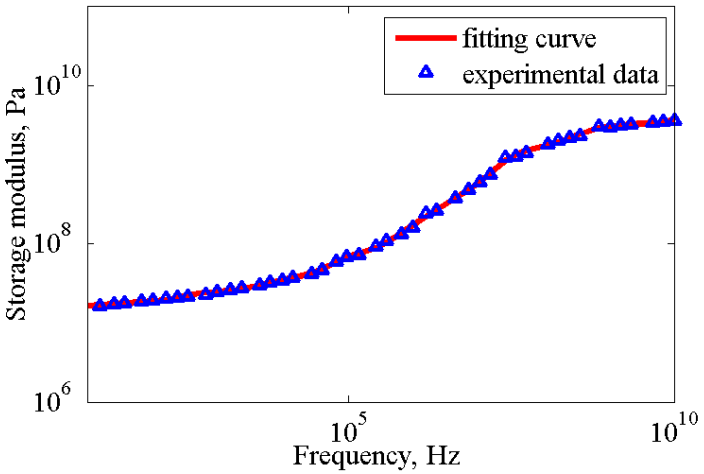

(a)

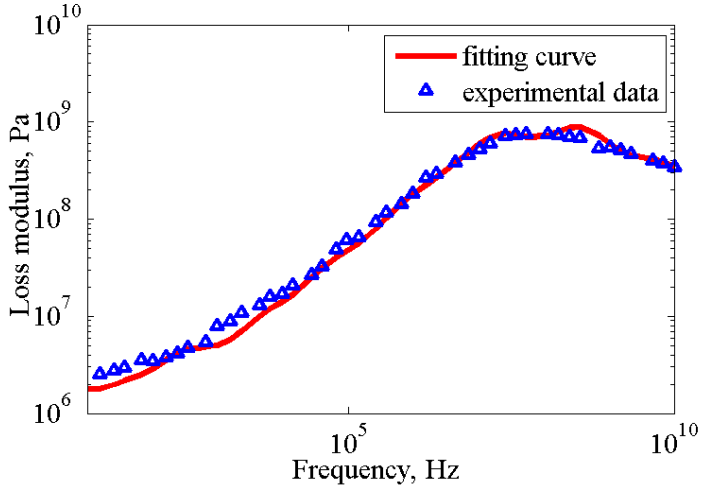

(b)

Figure 3.14: Complex modulus master curve for O-ring rubber showing fit to measured data (a) storage modulus (b) loss modulus

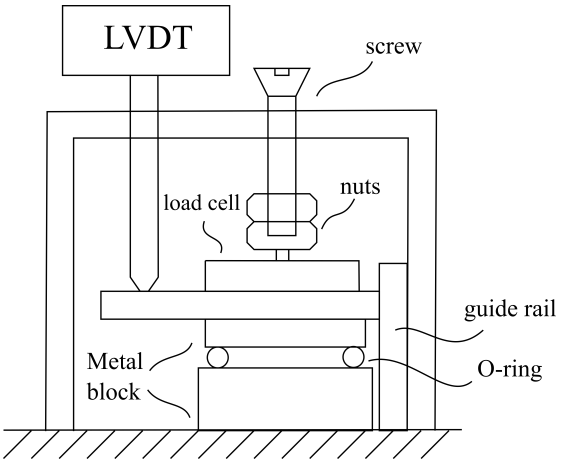

Figure 3.15: Static compressive test rig for elastomeric O-ring

LVDT were used to acquire the force and displacement, respectively. Three different O-rings, shown in Table 3.6, were used to demonstrate these relationships.

Specimen	Material	cross-sectional diameter	Inner diameter
BS318	Nitrile	5.33mm	24.77mm
BS209	Nitrile	3.53mm	17.04mm
BS312	Nitrile	5.33mm	15.24mm

Table 3.6: O-rings sample details

Since the nominal and cross-sectional diameters of these O-rings are different, the dimensionless stiffness was introduced. This dimensionless applied load is defined as

$$\epsilon = \frac{P}{DdE\pi} \tag{3.13}$$

where P is the applied load, D is the nominal diameter, d is the cross-sectional diameter, and E is the modulus of elasticity of elastomer.

The experimental results, shown in Figure 3.16, were compared with two analytical models - a plane strain model (described in Appendix B and Lindley's semi-empirical formula [34] for O-rings).

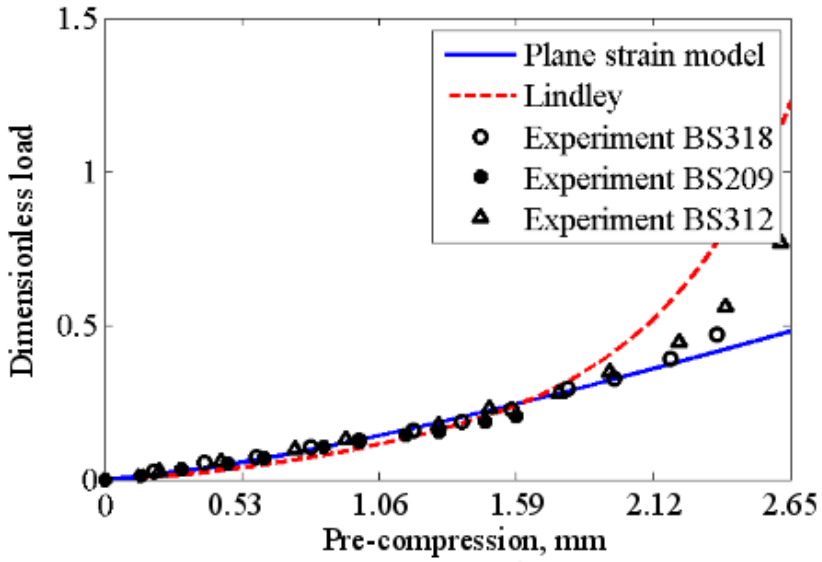

Figure 3.16: Dimensionless static load-deflection relationships for the selected circular O-rings

It can be seen that the O-rings show a strong hardening behaviour. The stiffness, which is proportional to the gradient of the curve, increases by up to three times the original value when the strain reaches 0.5. Difficulty in identifying the exact position for zero load lead to some uncertainty in the results. Also, there was a need for estimates of energy dissipation. Therefore, more accurate dynamic compressive tests were subsequently carried out.

3.4.4 Dynamic compressive tests: O-rings

Dynamic compressive tests using a uni-axial servo-hydraulic test machine were carried out to obtain O-ring load-deflection data in the axial direction. The MTS 858 system employed for this work comprised a self-contained hydraulic power unit, a load frame with a cross-head mounted actuator and a closed-loop controller. The system was operated in displacement-controlled mode using the signal measured by an eddy current sensor with a maximum range of 100 mm that tracked the motion of the upper grip. A 25 kN capacity load cell attached between

the lower grip and the load frame. In operation, the position of the upper grip was measured using the linear voltage differential transformer. The system also allowed testing to be carried out in a controlled temperature environment using a Thermcraft LB series oven that enclosed the specimen and grips.

Tests were carried out at three different excitation frequencies – 2.5 Hz, 10 Hz and 30 Hz – and nine different compression levels. The nitrile O-rings used in these experiments had a nominal diameter of 20.57 mm and a cross-sectional diameter of 5.33 mm. At each test condition, the O-ring was subjected to 50 cycles of displacement-controlled sinusoidal loading with a peak-to-peak amplitude of 0.5 mm. The hysteresis loop was obtained using the ensemble average of the force trace. From this, the stiffness and energy loss were found. A third order Butterworth low-pass filter with a cut-off frequency of 50 Hz was used to remove noise from experimental data. A typical displacement time history is shown in Figure 3.17

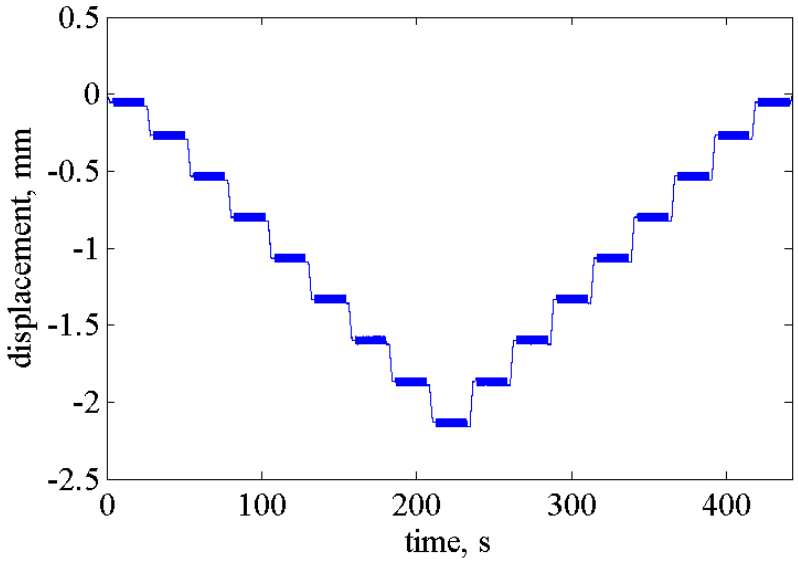

Figure 3.17: Displacement time history for dynamic tests

The typical force history at one test condition is shown in Figure 3.18. In this figure, slow relaxation of the polymer can be observed. Comparisons of the stiffness and damping obtained from the ensemble average and from the data where

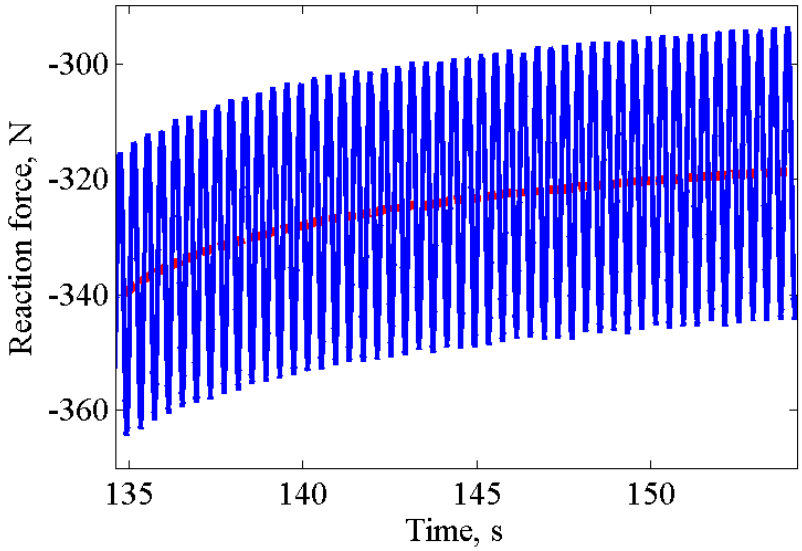

Figure 3.18: Typical force time history at selected static compression (blue solid line: force signal, red dash line: underlying stress relaxation)

stress relaxation effect was eliminated by subtracting the underlying relaxation curve.

The results are shown in Figure 3.19 where it can be seen that both strategies provide very similar results. Therefore, the ensemble average was therefore considered to be a suitable way to estimate stiffness and damping of the O-rings.

Slight different behaviour was noted between increasing and decreasing static loading. The effect of loading direction is shown in Figure 3.20 where it can be seen that the stiffness values are lower as the ring is unloaded than for identical compression levels as the compression was being increased. One likely reason for this observed behaviour is the Mullins' effect – the stress-strain response of the elastomeric polymer, especially for filled rubber, softens with the strain history. One possible explanation of this effect is the the filler (carbon black in nitrile rubber) is reorganised with deformation. Additionally, the breakdown of filler particles and the interface between these fillers and polymer matrices promote further softening. Further explanations can be found in the following literatures [72–78].

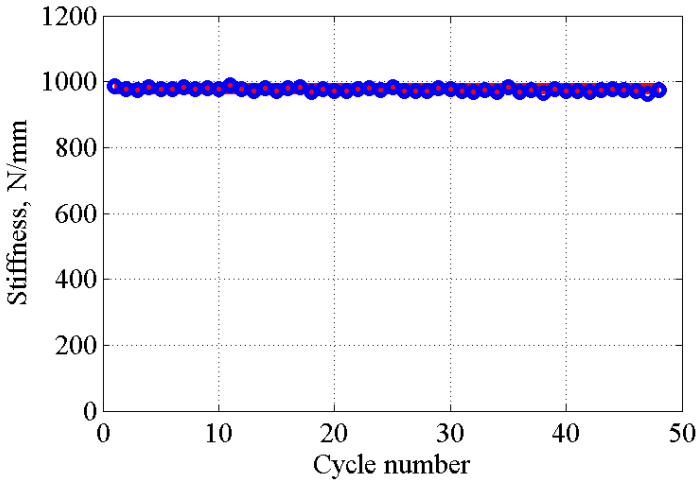

(a)

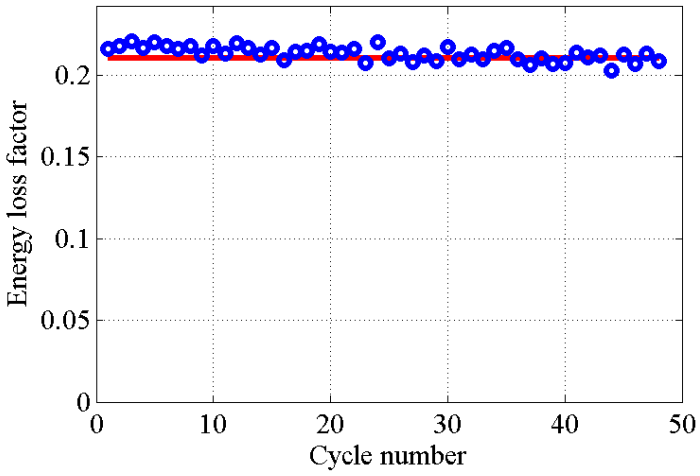

(b)

Figure 3.19: Effectiveness of the ensemble average (a) stiffness (b) damping (blue circle: removal relaxation; red dash line: ensemble average)

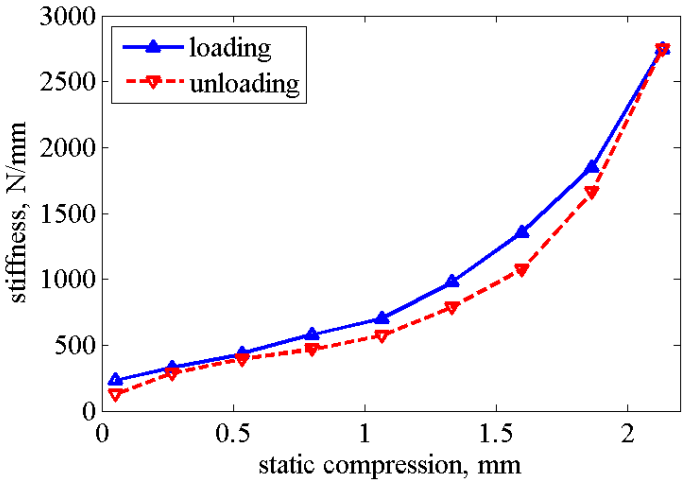

(a)

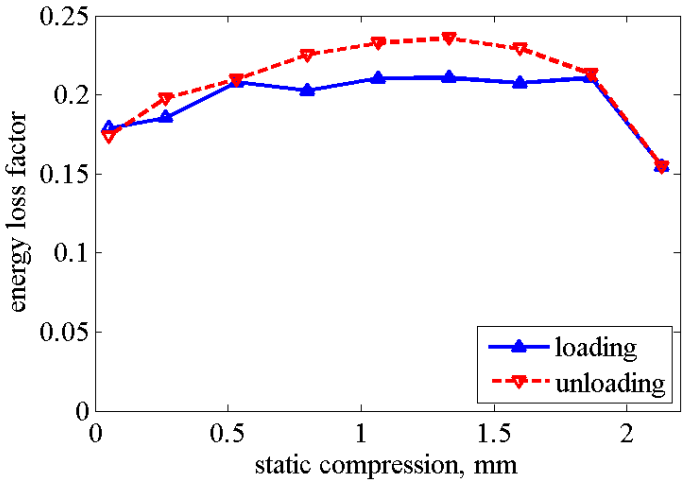

(b)

Figure 3.20: Effect of loading directions on (a) stiffness behaviour (b) damping behaviour for O-rings (dynamic displacement amplitude = 0.025 mm)

Figure 3.21 shows that the stiffness increases dramatically with axial compression while the loss factor remains almost unchanged. The primary factor affecting stiffness is the cross-section geometry which changes with the loading procedure of the O-ring. Bending and elastic buckling of molecular chains dominates the elasticity of a polymer in the low-strain region. At higher compressions, densification of molecule chains may also cause further stiffening, also referred to material nonlinearity. The slight increase in stiffness with excitation frequency can be attributed to viscoelasticity.

For the condition where the static compression was 0.85 mm and the excitation frequency was 2.5 Hz, the testing was carried out at different dynamic amplitudes. The dynamic amplitude-dependent stiffness are then presented in Figure 3.22.

It can be seen from Figure 3.23 and 3.22 that damping does not change significantly for different dynamic amplitudes. The stiffness, however, drops considerably as the dynamic amplitude increases. This phenomenon is thought to be an example of the Payne effect of rubber materials [79] in which the modulus of a reinforced elastomeric material reduces reversibly as the strain amplitude is increased, due to the re-organisation of weak physical bonds in the microstructure.

Figure 3.23 illustrates the typical hysteresis loops when subjected to different levels of dynamic excitations. The local stiffening with dynamic displacements can be observed due to the variations of the geometry, while the equivalent stiffness (refers to the instantaneous stiffness where dynamic displacement is zero) softens from which it can be interpreted that the Payne's softening is activated under significant dynamic amplitude.

Figure 3.24 shows the typical normalised hysteresis loops. At low amplitude, the hysteresis loop traces and ellipse - as would be expected from a linear viscoelastic material. At high dynamic amplitude, the shape of the loop reveals significant underlying nonlinearity - the source of which could be geometric effects, Payne's effect of interfacial friction between the O-ring and restricting plates. In practice,

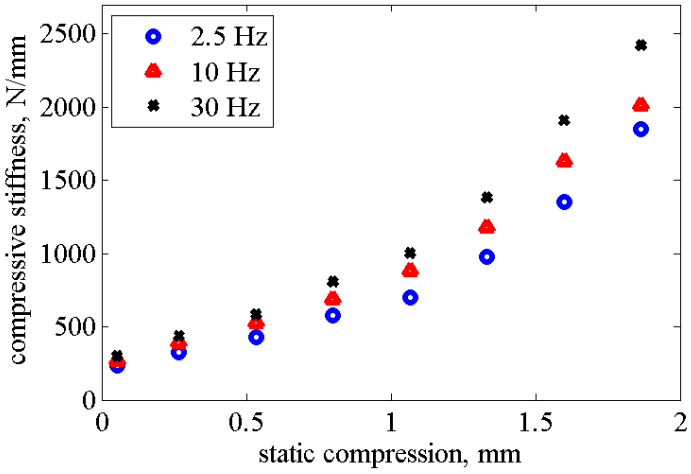

(a)

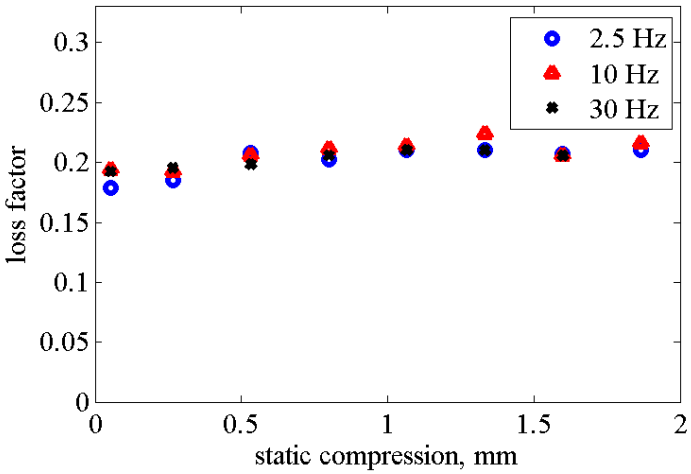

(b)

Figure 3.21: Effect of static compression and excitation frequencies on (a) stiffness (b) damping behaviour for cicular O-rings (dynamic displacement amplitude = 0.025 mm)

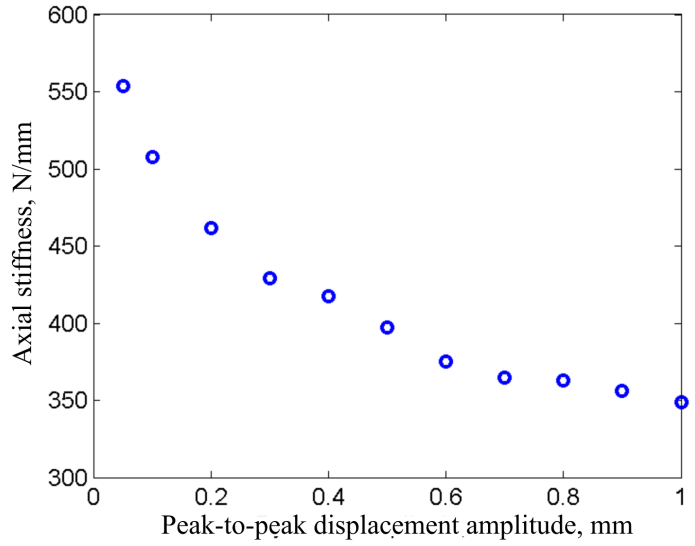

(a)

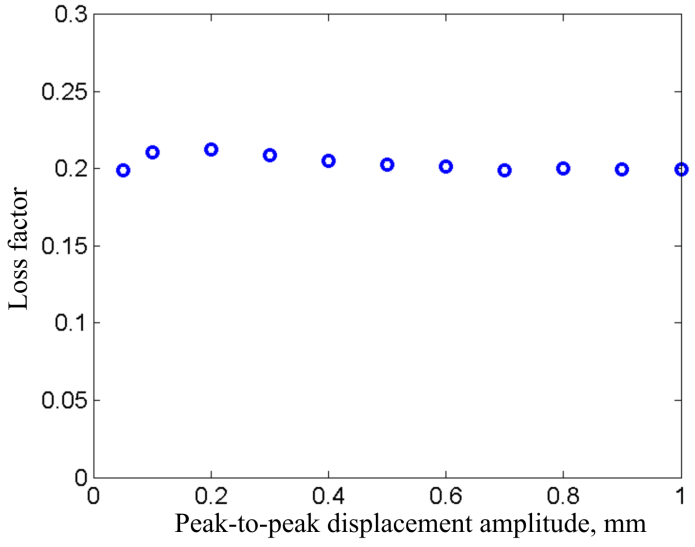

(b)

Figure 3.22: Effect of peak-to-peak dynamic displacement amplitudes on (a) axial stiffness (b) damping (static compression = 0.85 mm)

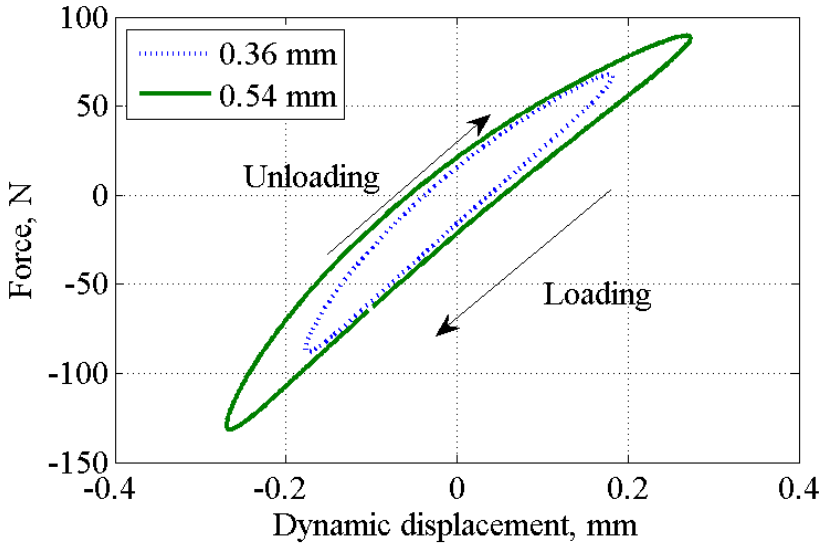

Figure 3.23: Typical hysteresis loops for the O-rings when subjected to different dynamic displacement amplitudes

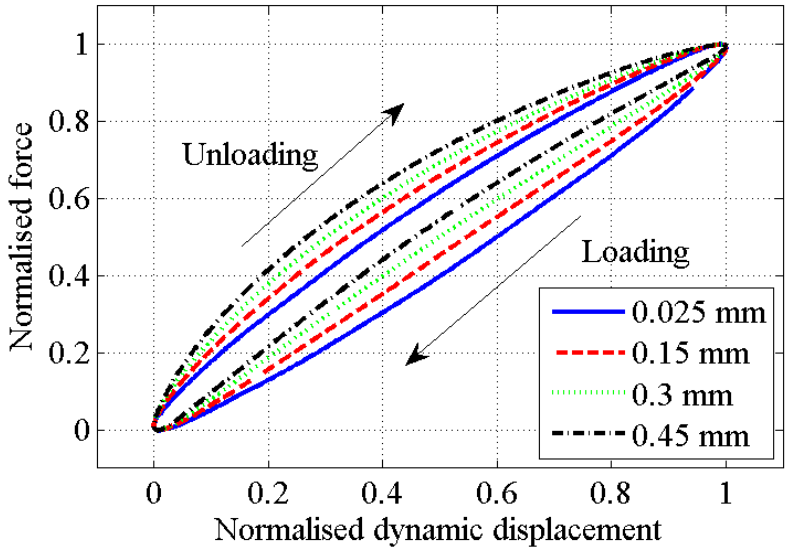

Figure 3.24: Normalised hysteresis loops for the O-rings when subjected to different dynamic displacement amplitude

the dynamic amplitude of the O-rings when incorporated in a mechanical application is usually small. As a result, the dynamic-displacement dependent stiffness

is not significant. Therefore, sensitivity of the stiffness to static compression is much more significant than that seen from dynamic loading.

3.4.5 Summary

In conclusion, the nitrile O-rings were chosen due to their damping being suitable for a typical TMD. An obvious strain-dependent stiffness can be observed, which provides a sound basis for designing an adjustable TMD. Also, the damping remains almost unchanged. The provides some spaces for widening the working frequency ranges of this TMD.

3.5 Analytic model of elastomeric O-rings

Experimental work, reported in the previous section, has shown that the stiffness of an elastomeric O-ring is very sensitive to the deformation present, but the damping is not. For the purpose of designing TMDs incorporating O-rings, analytical models were developed to simulate load-deflection behaviours more rapidly. To represent all the working modes of this type of TMD, stiffness and damping models in compressive, rotational and shear directions were established. However, to minimise the complexity, the following assumptions were made:

- The elastomer is assumed isotropic and homogeneous, displaying nonlinear elasticity.
- The mechanical model developed for the O-rings is deformation-dependent only. The effect of the excitation frequencies and the temperature is explained by the elastic modulus.
- The plain strain model is used, and therefore, no strain in the directions perpendicular to selected cross section is considered. A rectangular ring with deformed height and contact length (the area surrounded by ABCD in Figure 2.10) is used to represent the load-carrying of O-ring at given compression.

- The material is assumed incompressible. The Poisson's ratio is, therefore, 0.5.
- The damping from the O-rings is assumed to be linear viscous, when subject to a particular frequency.
- The shape of the free edges of the deformed cross-section can be represented using a parabolic function [80].
- Friction between the O-rings and restricting plates is ignored.

This section describes the development of the analytical models of the O-ring in tensile-compressive, shear and rocking directions.

3.5.1 Tensile-compressive behaviour

First, the analytical model in the tensile-compressive direction was developed, as this model forms the basis for those in other directions. A schematic diagram of this analytic model subject to tension-compressive motion is shown in Figure 3.25.

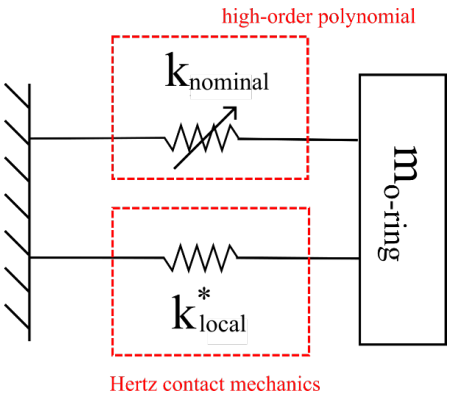

Figure 3.25: Analytic model for elastomeric O-ring in tension-compression

The analytical nonlinear stiffness model, comprising k_{local} and k_{nominal}, is then considered for this elastomeric O-ring. In this analytical model, k_{local} accounts for

the stiffening caused by deformation of the wire cross-section, while k_{nominal} accounts for radial expansion of the O-ring itself, especially when subjected to high static compressions. As the O-ring is axisymmetric, a plane strain model incorporating geometric nonlinearity through the cross-section is applied to establish the load-deflection relationship.

This phenomenon of local deformation can be represented by the Hertz contact method and, as shown by George [81]. The pressure distribution of O-ring in its axial direction follows elliptical function. Following Johnson's derivations [82], stress at any point inside the O-ring is given by

$$\sigma_x = \frac{P}{\pi}\left[\frac{1}{R} - \frac{2(l^2+2z^2)}{l^2(l^2+z^2)^{1/2}} + \frac{4z}{l^2}\right] \tag{3.14}$$

$$\sigma_z = \frac{P}{\pi}\left[\frac{1}{R} - \frac{2}{(l^2+z^2)^{1/2}} - \frac{2}{2R-z}\right] \tag{3.15}$$

where σ_x and σ_z are stress distribution in the radial and axial directions respectively. z is the distance from the loading surface of the O-ring cross section, P is the applied load and R is the cross-sectional radius. l is the contact half-length and is given by,

$$l = \sqrt{\frac{4PR(1-\nu^2)}{\pi E}} \tag{3.16}$$

in which ν is Poisson's ratio, E is the elastic modulus and is a function of temperature and excitation frequencies. Using the classic strain-stress relationship, the axial strain at any point is,

$$\epsilon_z = \frac{1-\nu^2}{E}\left[\sigma_z - \left(\frac{\nu}{1-\nu}\right)\sigma_x\right] \tag{3.17}$$

Following this, the axial deformation of the O-ring in the centre can be represented as,

$$\delta_z = 2\int_0^R \epsilon_z dz \tag{3.18}$$

The deformation of O-ring can be obtained by substituting Equations 3.14 and 3.16 into Equation 3.18,

$$\delta_z = \frac{2\,(1-\upsilon^2)}{E}\frac{P}{\pi}\left[\frac{1-2\nu}{1-\nu} - \frac{2\,(1-2\nu)}{1-\nu}A_1 + \frac{4\nu}{(1-\nu)\,l^2}A_2 - 2\ln 2 - A_3\right] \tag{3.19}$$

where A_1 refers to,

$$\ln\left(R+\sqrt{l^2+R^2}\right)-\ln\left(l\right) \tag{3.20}$$

A_2 is given by,

$$\frac{1}{2}R(l^2+R^2)^{0.5}-\frac{1}{2}l^2\ln\left[(l^2+R^2)^{0.5}+R\right]+\frac{1}{2}l^2\ln\left(l\right) \tag{3.21}$$

and A_3 is,

$$\frac{2\nu R^2}{l^2\left(1-\nu\right)} \tag{3.22}$$

The nonlinear stiffness from geometric variation with compression is given by

$$k_{\text{local}}=\frac{\partial P}{\partial \delta_z} \tag{3.23}$$

A detailed derivation can be found in Appendix B.

Since the contact length of the O-rings is dependent on the static compression, the analytical solution of Equation 3.19 is difficult to obtain. however, it can be obtained numerically, as shown in Equation 3.24

$$k_{\text{local}}(\delta_z)=\frac{\Delta P}{\Delta \delta_z}=\frac{P\left(\delta_{z,i}\right)-P\left(\delta_{z,i-1}\right)}{\delta_{z,i}-\delta_{z,i-1}} \tag{3.24}$$

Testing reported in the previous section shows that the O-ring stiffens considerably with compression level (refer to Figure 3.21). The developed model is not able to match this behaviour completely when the material modulus is assumed linear. To allow for the stiffening due to the expansion of the nominal diameter at large deformation level, an additional high order term – obtained using experimental data fitting method – can be included in this analytical model. Alternatively, Lindley [34] provided the expression of this polynomial term as given by,

$$k_{\text{nominal}}=300\pi DE\left(\frac{x}{d}\right)^5 \tag{3.25}$$

where k_{nominal} is the additional stiffness caused by the expansions of the nominal diameter, D is the nominal diameter of O-ring, E is the equivalent modulus of elastomer, x is the deflection and d is the cross-sectional diameter. This widely accepted expression was used in the following analysis.

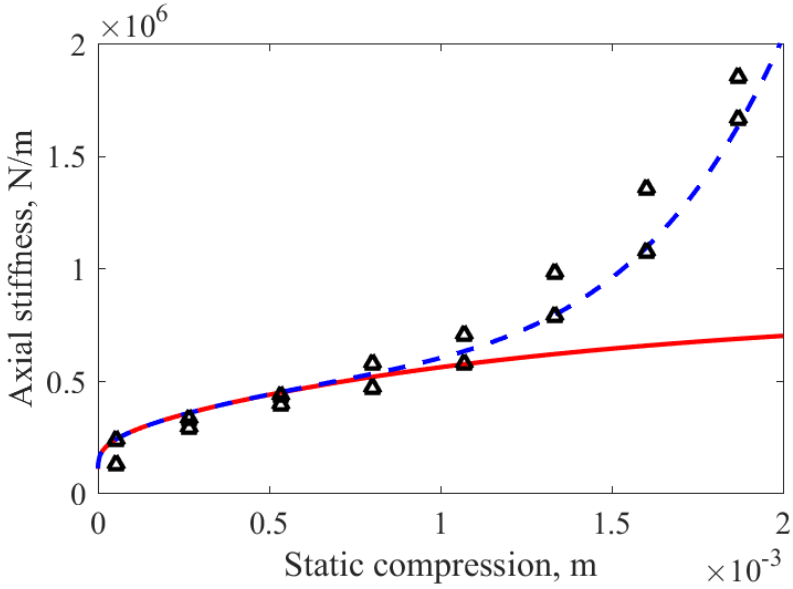

Figure 3.26: Comparisons of different analytical compressive stiffness models for O-ring. Red solid line refers to the modified Johnson's model (k_{local}). Blue dash line refers to developed model considering the expansion of the nominal diameter ($k_{\text{local}} + k_{\text{nominal}}$). Black triangles refer to experimental data

Figure 3.26 shows the comparison of analytical models and experimental results. Note that two experimental data points exist for one static compression level. The upper one is obtained from the gradient of the load-deflection curve during the loading operation while the lower one is obtained during unloading operations. Both models work well when the static compression is less than 15 %. When the pre-strain is higher than 15 %, the developed model with the high order term can reach acceptable accuracy.

Since the Hertz contact was applied to model the local deformation of the O-rings, it was assumed that the pressure is only applied throughout a limited ring-shape contact region. In this situation, the contact stress distribution is not massively influenced by the fluctuation of given loads and the resulting strain is small enough for the material to behave as linear elastic. The other assumption is that the interfacial friction is ignored. In the proposed TMD, the O-ring may withstand a high pre-strain so that the interfacial friction is no longer negligible

anymore. Therefore, the Hertz assumption may not hold, as has been demonstrated by many authors [82, 83]. At this point, it can be hypothesised that the local deformation does not have a significant effect on the O-ring stiffness. Preliminary evidence has been shown in Figure 3.26 and will be discussed further in Section 3.6

It can also be seen from Figure 3.26 that the axial stiffness is slightly different between analytical and experimental results. This small difference in the stiffness might come from the estimation errors for the elastic modulus of rubber. The samples used to obtain the modulus of rubber were tested in the circumferential direction due to the size of the O-ring. Since the synthetic rubber is not entirely homogeneous [84], the axial modulus of this elastomer might be different from the tangent modulus.

Energy dissipation for this TMD mainly comes from the material damping within the elastomer and hence, damping from interfacial friction can be ignored. The loss factor for the O-ring can be estimated using the ratio of dissipated and storage strain energy. Limited research has been carried out on the effect of high steady strain on the energy dissipation and particularly, the loss factor, of a polymer. In the analytical model, the strain energy associated with stiffening at high strain (represented here using a high-order polynomial) is not used when evaluating the damping arising from the O-ring. The other factor that has significant effect on the strain energy is the contact half-width subject to different compressions.

The nature of the viscoelasteic material – the damping is independent of strain – exists for the elastomeric O-rings, and therefore, the loss factor of this given elastomer can represent that of O-ring directly. The analytical damping model of the O-ring is presented in Figure 3.27.

Figure 3.27 shows that the damping indicated by the analytical model is close to the experimental results, especially when the pre-strain is moderate. One important feature is that the loss factor when subject to the increasing static loading is lower than that when subject to decreasing static loading. The energy dissipation is similar for both situations, while the stiffness, and hence, the strain energy

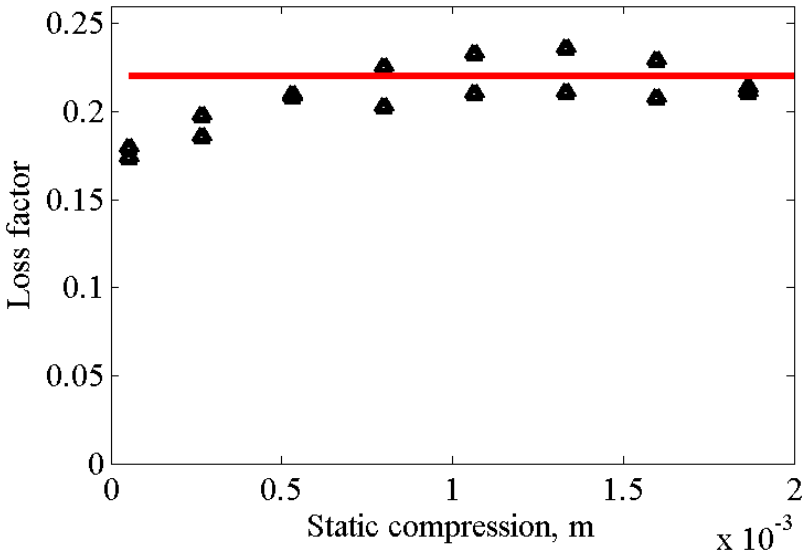

Figure 3.27: Analytical damping model for O-ring. Red solid line refers to developed model. Black triangle refers to experimental data

is much higher. At low static compressions, the analytical stiffness is slightly lower than the one identified from experiments. This small difference might come from the estimation errors for elastic modulus of rubber. The samples, which are used to obtain modulus of rubber, were tested in the circumferential direction due to the restriction on the size of the O-ring. When the static compression is high, the rate of increase of the stiffness in time becomes higher than that of the energy dissipation, the energy loss factor therefore drops slightly.

3.5.2 Rocking behaviour

The rocking mode, in which the damper rotates about an axis perpendicular to the central threaded rod, is a key feature for this type of TMD. The stiffness, under this kind of deformation, depends on the centre of rotation. Because of the symmetrical nature of the damper, this occurs at the midpoint of the threaded rod. A simplified sketch is illustrated in Figure 3.28.

Note that α is the rotational angle of this TMD and y refers to vertical de-

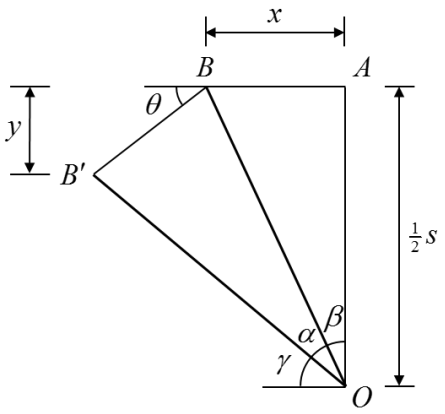

Figure 3.28: A schematic diagram of rocking mode. The O-ring has a radius of x and is centred around A. As the TMD rocks around an axis through O, the selected contact point moves from B to B'.

formation caused by this rocking motion. It is assumed that the length of the threaded rod is s and that the rotational axis goes through Point O while B is any selected point in the contact area of the deformed ring. Using the geometric relationship shown in Figure 3.28, the vertical displacement caused by rotational motion can be expressed as,

$$y = \frac{s}{2} - \overline{OB'} \sin\left(\frac{\pi}{2} - \alpha - \beta\right) \tag{3.26}$$

Since the $\overline{OB}$ is equal to $\overline{OB'}$, Equation 3.26 can be rearranged to

$$y = \frac{s}{2}(1 - \cos\alpha) + x \sin\alpha \tag{3.27}$$

When the vibrational amplitude is small, the high order terms in this expression are negligible. Therefore, the vertical deformation at selected point B is

$$y = x\alpha \tag{3.28}$$

The rotational stiffness of this TMD is then formulated using equivalent strain energy. The underlying assumptions for this analysis are as follows,

- The cross-section of the O-ring can be represented by an equivalent rectangular. This is a reasonable approximation if the O-ring is subject to significant axial pre-compression.

- As the dynamic amplitude is much less than the static compression, and therefore the compressive stiffness remains unchanged during vibration.
- The stiffness is uniform through the cross section of the O-ring as the nominal diameter is much larger than the cross-sectional diameter.

Important notation used in this analysis of the TMD rocking mode is shown in Figure 3.29.

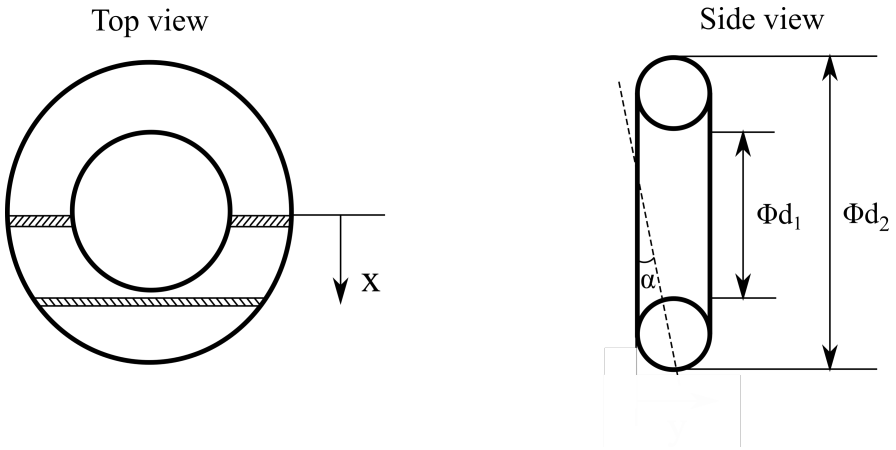

Figure 3.29: A schematic diagram of the rocking motion for the circular O-ring

The equivalence of strain energy between the rotational and translational coordinate can be given by,

$$\frac{1}{2}k_{\text{rot}}\alpha^2 = 2\int_0^{\frac{d_1}{2}} k_{\text{eq}}\left(2\sqrt{\left(\frac{d_2}{2}^2 - x^2\right)} - 2\sqrt{\left(\frac{d_1}{2}^2 - x^2\right)}\right)\frac{1}{2}y^2dx + 2\int_{\frac{d_1}{2}}^{\frac{d_2}{2}} 2k_{\text{eq}}\sqrt{\left(\frac{d_2}{2}^2 - x^2\right)}\frac{1}{2}y^2dx \tag{3.29}$$

in which k_{eq} is average compressive stiffness per cross-sections, d_2 is equivalent outer diameter of the O-ring, d_1 is equivalent inner diameter of the O-ring and x is the location along the cross section. Note that the relationship between rotational angle α and position x is defined in Equation 3.28. After rearrangement

of Equation 3.29, this equivalent rocking stiffness can be expressed by,

$$k_{\text{rot}} = \frac{\pi}{64} k_{\text{eq}} \left({d_2}^4 - {d_1}^4 \right) \tag{3.30}$$

The overall cross-sectional area of O-rings change with different static compressions. Using the geometric integration of cross-sections, the overall area, and thus, the average cross-sectional diameter can be estimated in the thickness direction, as shown in Equation 3.31. Details of derivations can be found in Appendix C.

$$d_0^{\text{eq}} = \frac{2l + 2d}{3} \tag{3.31}$$

in which l is the contact half-width; d is the cross-sectional diameter of the O-ring. The equivalent outer and inner diameter can be given by,

$$d_2 = d_n + d_0^{\text{eq}} \tag{3.32}$$

$$d_1 = d_n - d_0^{\text{eq}} \tag{3.33}$$

where d_n is the nominal diameter of O-ring. The average stiffness is then represented as

$$k_{\text{eq}} = \frac{\lambda k_{\text{c}}}{\frac{1}{4}\pi \left({d_2}^2 - {d_1}^2 \right)} \tag{3.34}$$

where k_{c} is the compressive stiffness of the cross-sections at given compression and λ is the shape factor that accounts for the effect of curved edges on the load-carrying capability. For an annulus geometry with large ratio of wire and nominal diameter, Payne [24] provides the expression for shape function,

$$\lambda = 1 + B \left(d_2 - d_1 \right)^2 / h^2 \tag{3.35}$$

where h is the thickness of O-ring and B is a shape coefficient, which is related to the shear modulus of elastomer.

Combining Equation 3.30 with 3.34, the rotational stiffness for the O-ring at selected static compression is represented as,

$$k_{\text{rot}} = \frac{1}{4\pi} \left({d_1}^2 + {d_2}^2 \right) \lambda k_c \tag{3.36}$$

For the analytic model developed here, some points need to be highlighted. The analytical rocking model is based on the analytical nonlinear stiffness model in tension-compression, which indicated that the O-rings were simulated using a rectangular ring with the same cross-sectional areas. The effect of the curved edges of the deformed cross-section is explained using the shape factor. Errors, especially those occurring when subject to rotational moment, are introduced because the movement of the centroid is not accounted for in the proposed model. In practice, the centroid of the cross-section shifts horizontally with static compression, thus stiffening the O-rings in the rotational direction. Also, the equation that estimates the contact length loses its effectiveness at high compressions, which stiffens the proposed analytical model. Comparisons with experimental results and numerical models were carried out and as reported in Section 3.6.2 to demonstrate the validity of the model.

3.5.3 Shear behaviour

For elastomer elements, it is usually assumed that bending is always accompanied with shear deformation [85]. Using Southwell's formula [85], the deflection-load relationship for an infinitesimal element of an elastomeric cylinder is given by,

$$P = \frac{\lambda G_{eq} A y}{h\left(1 + h^2/36k^2\right)} \tag{3.37}$$

where y is shear deformation, A is the cross-sectional area in the axial direction, k is the radius of gyration of the cross-section about the neutral axis of bending. h is height for this deformed O-ring cross-section. λ is the shape factor and G_{eq} is the equivalent shear modulus.

Since the elastomer experiences nonlinear stiffening under high strain, the shear modulus, that is used to estimate shear load, needs to be modified. Lindley's equation [34] for load-deflection of O-ring can be shown as follows,

$$P = 1.25\pi D\Big(\frac{x}{2R}\Big)^{1.5} E\left[1 + 40\left(\frac{x}{2R}\right)^{4.5}\right] \tag{3.38}$$

Since the geometry nonlinearity is mainly explained by the shape factors, the stiffening of the material can be estimated using the equivalent nonlinear stiffness scale, $1 + 40\left(\frac{x}{d}\right)^{4.5}$. The equivalent shear modulus is represented as

$$G_{eq} = \left[1 + 40\left(\frac{x}{d}\right)^{4.5}\right] G \tag{3.39}$$

where G is shear modulus of elastomer.

The notation of geometric parameters for the following derivation is illustrated in Figure 3.30.

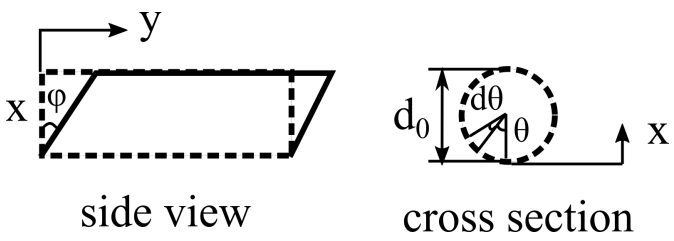

Figure 3.30: A schematic diagram of shear deformation where dash line is original shape and solid line is deformed structure

The shear load over the cross section can be represented as

$$\int dP = 2\int \frac{2\frac{h}{2}\lambda G_{eq}\sin\left(\theta + d\theta\right) d_0\varphi x}{x\left(1 + \frac{\left(\frac{d}{2} - \frac{d}{2}\cos(\theta + d\theta)\right)^2}{36k^2}\right)} - 2\int \frac{2\frac{h}{2}\lambda G_{eq}\sin\theta d_0\varphi x}{x\left(1 + \frac{\left(\frac{d}{2} - \frac{d}{2}\cos\theta\right)^2}{36k^2}\right)} \tag{3.40}$$

in which d_0 is nominal diameter of O-ring. Since dp and $d\theta$ are infinitely small, high order terms are eliminated. Thus, the shear stiffness can be expressed as,

$$k_s = 2\lambda G_{eq}\varepsilon\pi d_0 \int_0^{\frac{\pi}{2}} \frac{\left(\frac{10}{9} + \frac{1}{9}\cos\theta^2 - \frac{2}{9}\cos\theta\right)\cos\theta - \frac{2}{9}(1 - \cos\theta)\sin^2\theta}{\left(\frac{10}{9} + \frac{1}{9}\cos^2\theta - \frac{2}{9}\cos\theta\right)^2} d\theta \tag{3.41}$$

where ε is the strain of the O-ring.

3.5.4 Experimental validation

This section reports work done where a validation rig was used to evaluate the effectiveness of the analytic models established in previous sections. One of the

most important requirements of the rig was that the moving parts needed to have similar rigid body motion behaviour to that of the proposed TMD. The details of the experimental apparatus are shown in Figure 3.31

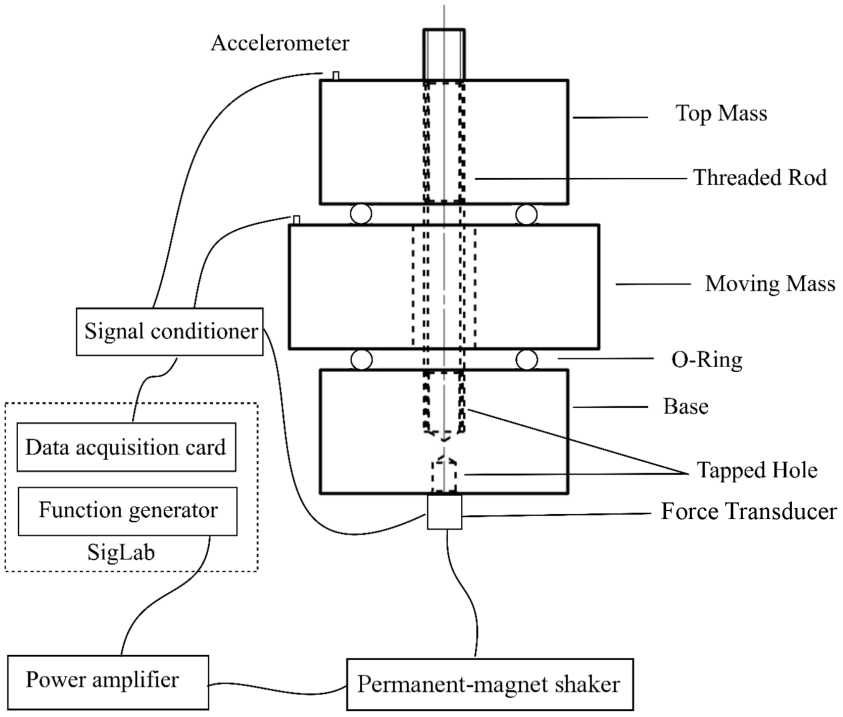

Figure 3.31: Sketch of test-rig for validation of stiffness in different modes

This validation rig used two fixed masses that were mechanically attached to a threaded rod. A central moving mass was placed between these two fixed discs. Two O-rings were located between the moving and fixed masses. The selected static compressions were accomplished by a rotating threaded rod. Slip gauges were used to ensure the accuracy of the pre-strain of the O-rings. Note that the two O-rings were assumed identical - thus achieving similar static compression. The properties of this validation rig are shown in Table 3.7.

Excitation from a random source, limited by an analogue filter to the range 50 to 1000 Hz, was applied by mounting this device on a shaker capable of 489 N peak sine force via a piezoelectric force transducer. Two miniature accelerometers

were mounted on the top and moving discs to measure the relative displacement of fixed and moving mass. For each test, a total collection time was 3.2 s at a sampling rate of 2560 Hz was selected. The ensemble average of frequency spectra over 20 cycles was used to remove noise. Three different pre-strains for the O-rings were chosen and the results, presented as transmissibility between the fixed and moving mass, are shown in Figure 3.32.

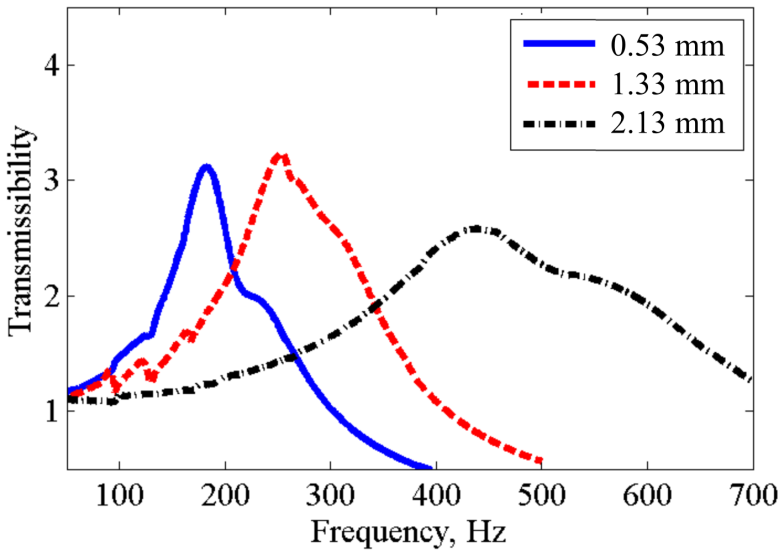

Figure 3.32: Transmissibility of moving and fixed mass subject to different pre-compressions of the O-rings

It can be seen from Figure 3.32 that at least two resonances exist for all static

Variable	Value
Mass of the top disc	54.63 g
Mass of the base disc	193.75 g
Mass of the moving disc	441.52 g
Dimensions of the moving disc	⌀50 mm × 30 mm
Type of O-ring	Nitrile BS312

Table 3.7: Properties of validation rigs

Staic Compression, mm	Coherence		
	Mean	Maximum	Minimun
0.53	0.9995	0.9999	0.9932
1.33	0.9997	0.9999	0.9988
2.13	0.9996	0.9999	0.9979

Table 3.8: Coherences for transmissibility curve subjected to different static compressions of the O-rings

compressions under 700 Hz. As the pre-strain applied to the O-ring increases, the resonances shift to higher frequencies. It is interesting to note that only two strong peaks, representing the tension-compression and rocking modes, occur for each frequency response. To examine the nonlinearity generated from the coupling of the rocking and tensile-compressive motion, a summary of the coherences for these transmissibility curves is listed in Table 3.8.

Table 3.8 indicates uniform coherences, and hence no significant coupling can be observed for both the modes. The discrete SDOF isolation models, as shown in Figure 3.33, were used to simulate this validation rig. The O-rings can be modelled as standard complex stiffness. The base excitation captured by the accelerometer on the top mass is transferred to the rigid moving mass.

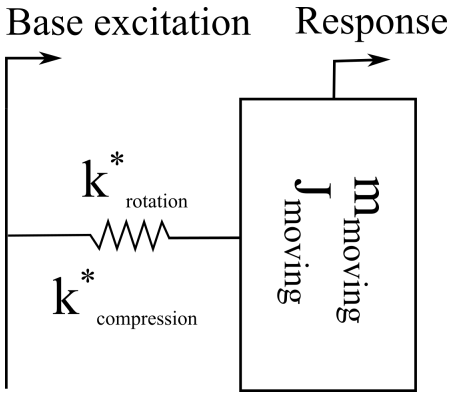

Figure 3.33: Analytic model for validation test rigs incorporating elastomeric O-rings

When the damping is relatively small, the damping ratio of viscoelastic material can be given by [86]

$$\zeta = \frac{\eta}{2} \tag{3.42}$$

where η is energy loss factor of the O-ring. Since the modulus of the elastomer is frequency-dependent, an amendment to the modulus was required. According to the polymeric master curve shown in Figure 3.14, multipliers of 1.4 and 1.64 were applied to the elastic modulus of nitrile rubber for a pre-strain of 0.1 and 0.4, respectively. Increasing prestrain increases geometric stiffness – hence a higher frequency for the resonance and therefore an increased modulus. Detailed parameters of the model are shown in Table 3.9.

Variable	Value
Mass Moment of Inertia of the moving disc	$1.02 \times 10^{-4} m^4$
Compressive stiffness (10%)	500 N/mm
Rotational stiffness (10%)	62.2 Nm/rad
Modal damping ratio for compressive mode (10%)	0.15
Modal damping ratio for rocking mode (10%)	0.09
Compressive stiffness (40%)	2900 N/mm
Rotational stiffness (40%)	344 Nm/rad
Modal damping ratio for compressive mode (40%)	0.14
Modal damping ratio for rocking mode (40%)	0.11

Table 3.9: Analytic parameters of validation rigs

Comparisons of the theoretical prediction and experimental results are shown in Figure 3.34. It can be seen that the measured experimental behaviour compares well with theoretical predictions for compression behaviour, especially near resonances. It can be seen that the peak for the rocking mode is higher than that for the compression mode. This is because the accelerometer was placed near the edge of the moving mass, accentuating the rocking motion. For rocking modes, the resonance frequencies identified from experiments are slightly higher than that from analytical model. One possible reason is misalignment of the O-rings during

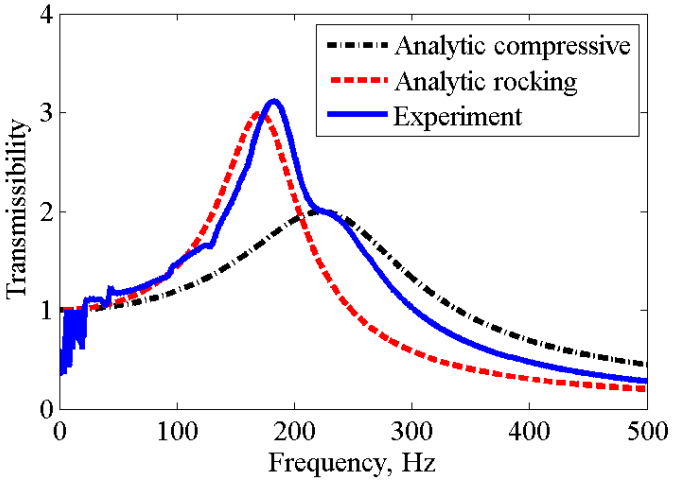

(a)

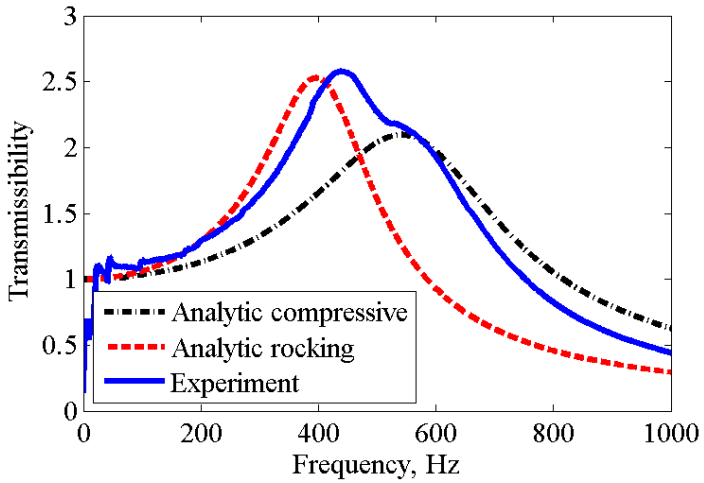

(b)

Figure 3.34: Analytic models for O-ring (a) 10% compression (b) 40% compression

assembly. These eccentricities, e, can stiffen the TMD. The rotational stiffness considering these eccentricities is given by,

$$k_{\text{rot}} = \left[\frac{\pi}{64}\left({d_2}^4 - {d_1}^4\right) + \frac{\pi e^2}{8}\left(d_2^2 - d_1^2\right)\right] k_{\text{eq}} \tag{3.43}$$

The detailed derivations for misaligning assembly of the TMD are shown in Appendix C. An other reason causing this unwanted softening for the analytical model may be the mis-estimation of the shape factor as the formula of the shape factor is not calibrated using the nitrile rubber.

3.5.5 Summary

In this section, the analytical models for the elastomeric O-rings were established. These models predict the performance of the O-rings, especially in the axial direction. Also, the stiffness of the O-rings over certain pre-strains can be estimated well.

3.6 Finite element modeling of TMD incorporating O-rings

Work presented in the previous section suggests that the analytical model works well for an O-ring with circular cross section. A limitation of this modelling strategy is that it involves the development of complicated expressions for the stiffness in the compressive and rocking directions, while this approach is feasible for O-rings with simple cross-sections, more complicated O-rings with a unique geometry such as X-shape requires a different approach. This section describes an approach using the commercial Finite Element (FE) code Ansys. The effects of various parameters, for example, the mesh density, hyperelastic material models and interfacial frictional coefficient, were investigated to ensure the accuracy. Once developed successfully, this numerical model was used to validate the analytical model of shear stiffness of the O-ring as it is hard to obtain these properties experimentally.

3.6.1 Compressive behaviour

An axisymmetric half cross-sectional model was developed to estimate the compressive stiffness and damping of the O-rings. The boundary conditions and loads do not vary in the evaluation of the charactersitics of the O-ring itself. The restricting plate is constrained with a uniform loading applied on the middle surface of the O-ring. The mesh and boundary conditions can be seen in Figure 3.35.

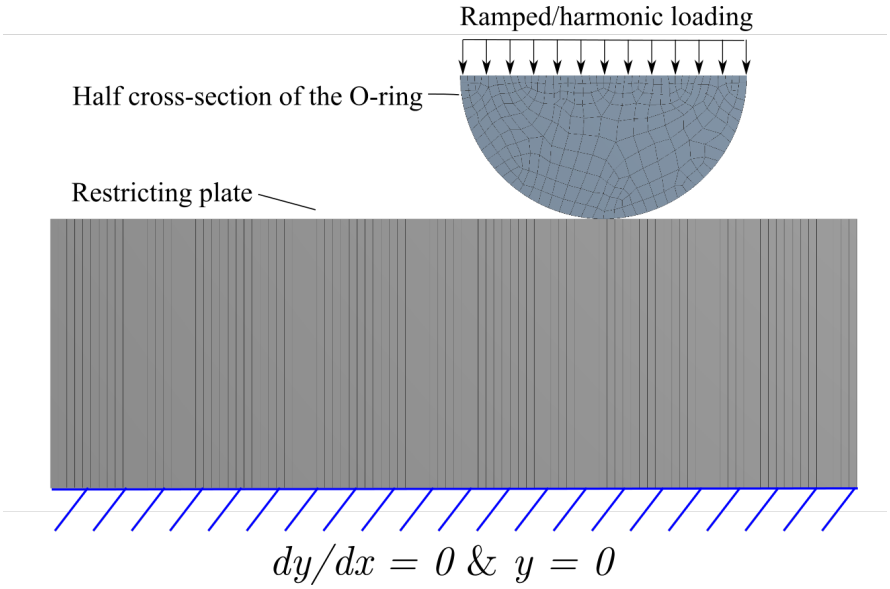

Figure 3.35: Typical meshed axisymmetric half cross-sectional model

The details of the material and geometric properties of the numerical models are listed in Table 3.10

3.6.1.1 Finite strain analysis for the circular O-rings

In this section, the feasibility of the proposed 2D axisymmetric numerical model was evaluated first. Following this, the effect of controllable parameters, for example the Poisson's ratio and interfacial frictional coefficient, was identified.

Since frequency-dependent compressive stiffness of O-rings are explained by the elastic modulus of the material, finite strain analysis (also called static compressive simulations) was used to evaluate the stiffness. The controlled ramped

displacements with 400 substeps for an effective strain of O-rings of 0.6 were applied on the half cross-section in a piecewise manner to promote the convergency and increase the accuracy of stiffness estimations.

3.6.1.1.1 Mesh convergence study

Mesh density has a significant influence on the simulation result, especially for stress distribution. In order to choose a suitable mesh density, different element numbers were assigned to the O-rings and the total reaction force on the O-ring was considered as an indicator to check the numerical convergence of this FE model. Since the stiffness of the restricting plate is far higher than that of the O-rings, the effect of the plate on the overall stress distribution of the O-ring is negligible. In this work, the total element number in the rigid support was always set to 100. The effect of mesh density is shown in Figure 3.36.

It can be seen that the mesh density has a negligible effect on the reaction force for three selected strain levels. Close examinations of the difference of the reaction force for different static compressions are performed using the relative error defined in Equation 3.44. Note that the highest mesh density is assumed to provide accurate results for all the compressions of interest.

$$\delta_{\text{reaction}} = \frac{F_{2050} - F_{\text{coarse}}}{F_{2050}} \tag{3.44}$$

Variable	Value
Nominal radius of O-ring	10.285 mm
Cross-sectional diameter of O-ring	5.33 mm
Elastic modulus for the elastomer	9.3 MPa
Poisson's Ratio for the elastomer	0.499
Dimensions of the restricting base	⌀30 mm × 5 mm
Material of the restricting base	standard stainless steel
Frictional coefficient between the O-rings and base	0.8

Table 3.10: Properties of numerical model

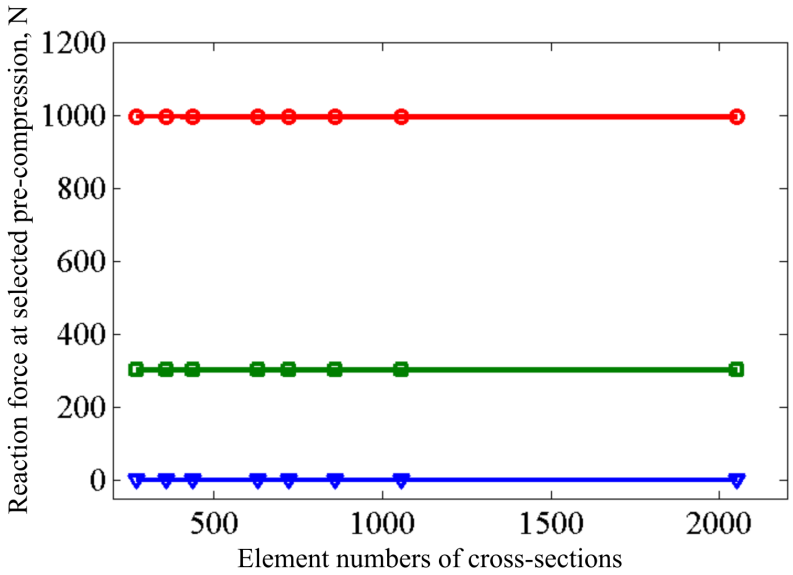

Figure 3.36: Effect of mesh density (blue triangle, green rectangular and red circle refer to reaction force subject to a static compression of 0.8×10^{-3} mm, 0.8 mm, and 1.6 mm respectively)

where F_{2050} is the reaction force in the condition in which the amount of elements for cross section is 2050. A plot of error against static compression for different meshes for the same O-rings is shown in Figure 3.37

To obtain a suitable mesh at the cross-sections, a threshold of 1% was set up. It can be seen from Figure 3.37 that the relative error meets the requirements for all mesh densities when static compression is higher than 0.08 mm. When subject to low compression, the elastic behaviour of the O-ring is dominated by the interfacial contact mechanics. The local mesh near contact regions occupies a significant role in estimating load-deflection relation. Under such circumstance, the reaction force is more sensitive to the mesh density. The proposed working range of the O-ring in this type of TMD does not target very low strain as these low levels are hard to achieve using normal mechanical adjustment. Therefore, a mesh density of 100 elements in the cross sections was sufficient in the following work.

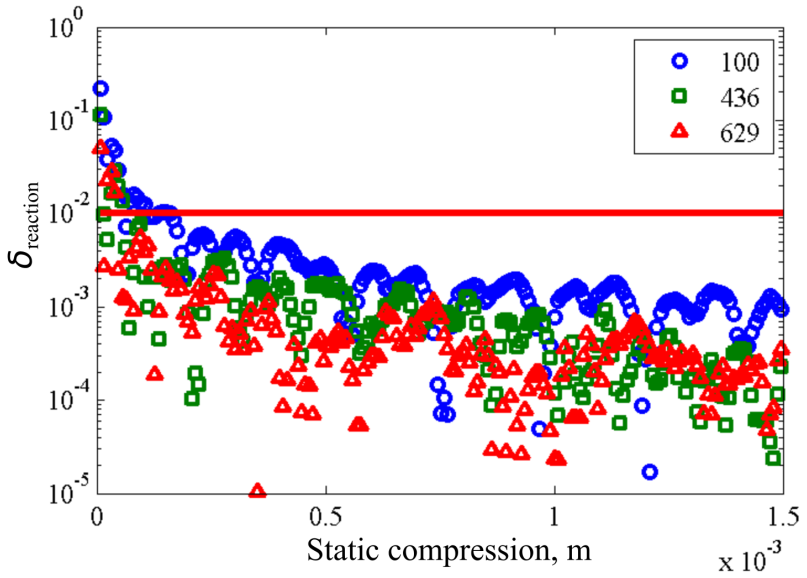

Figure 3.37: Errors of the reaction force for various mesh densities (red line refers to 1% error band)

3.6.1.1.2 Selection of the material model

Since the elastomer is a hyperelastic solid, a proper material model was vital to the accuracy of the numerical model. The Neo-Hookean model, based on the statistical energy potential approach, was introduced to represent the high compression for this incompressible solid. The advantage of the Neo-Hookean model is its simplicity. Additionally, all the coefficients have physical meanings for this material model. It is widely accepted that the Neo-Hookean model can estimate the biaxial state of stress up to 100% for selected filled polymers. However, some authors [87,88] also reported that the Neo-Hookean model is not able to deal with the stress subject to a tensile strain that is higher than 30% because of breakage of the intramolecular reaction force, whereas it can represent the compressive load-deflection accurately up to a strain of 100%. [89] Hill demonstrated similar results while also indicating that this first-order energy model loses its effectiveness in the situation of a high width-to-thickness ratio [90].

The strain energy potential for the Neo-Hookean material can be represented

as,

$$W = \frac{\mu}{2}(\overline{I_1} - 3) + \frac{K}{2}(J-1)^2 \tag{3.45}$$

where μ is the initial shear modulus, K is the bulk modulus, $\overline{I_1}$ is the first deviatoric strain invariant and J is the determinant of the elastic deformation gradient. Note that $\overline{I_1}$ and J depends on geometry and are determined by the shape function of the elements. Two features, as shown in the following list, can be observed from Equation 3.45.

- The material model is based on strain density function, and therefore, can explain the geometric nonlinear behaviours subject to high compressive strain.
- Only the μ and K is required for defining the numerical material model.

Comparison of the reaction force between the standard linear isotropic ($\overline{F}_{\text{Isotropic}}$) and Neo-Hookean model ($\overline{F}_{\text{Neo-Hookean}}$) is demonstrated in Figure 3.38.

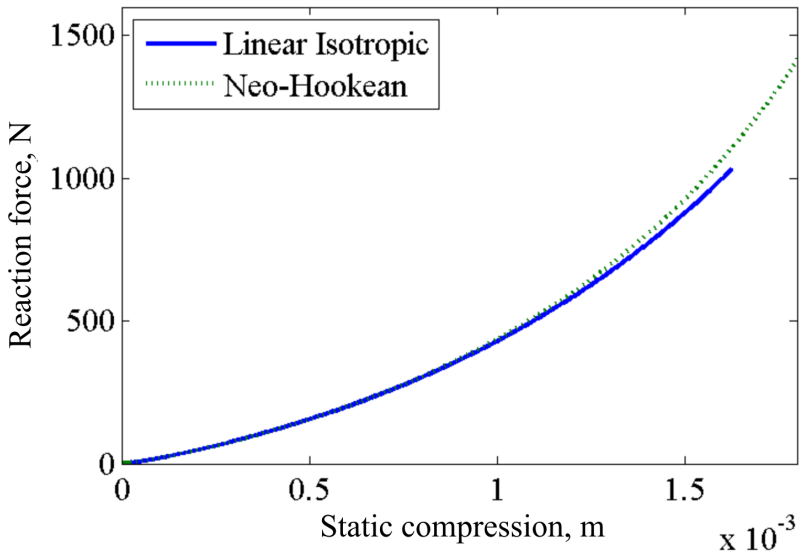

Figure 3.38: Comparison of reaction force against deflection for two different material models

The finite strain analysis halts for the linear isotropic model when subjected to a static compression higher than approximately 1.6 mm as the distortion of the geometry is observed, as shown in 3.39.

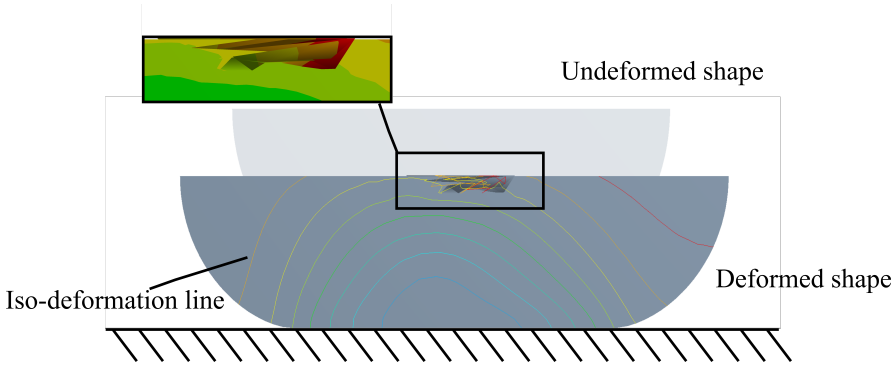

Figure 3.39: Typical numerical geometric distortion when using isotropic material model

The other interesting phenomenon is that the linear elastic model predicts a lower reaction force than the Neo-hookean model at higher strain. To demonstrate this difference clearly, a relative reaction force difference, as shown in Equation 3.46, was applied and results are demonstrated in Figure 3.40.

$$\delta_{\text{material}} = \frac{\overline{F}_{\text{Neo-Hookean}} - \overline{F}_{\text{Isotropic}}}{\overline{F}_{\text{Neo-Hookean}}} \tag{3.46}$$

Figure 3.40 shows that softening for the Neo-Hookean model can be observed at the low-strain region, while a substantial hardening is exhibited when the model is subject to high strain. The difference at low strain may come from the overestimation of the deformed cross-sections for the isotropic models, while the difference between both reaction forces is lower than 1%. With the increase of strain, the volumetric deformation of these hyperelastic material makes a greater contribution on the load-carrying of the cross-sections. The isotropic model does not account for this bulk deformation, and therefore, the unexpected softening appears for the isotropic model. One of the other important reasons why the Neo-Hookean model is selected in the following analysis is that the isotropic model is not able to

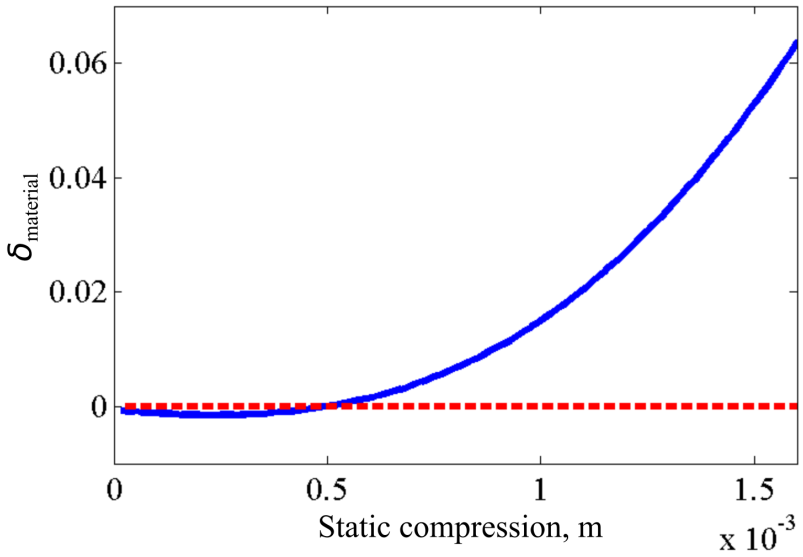

Figure 3.40: Reaction force difference between two models subject to various static compressions (red line refers to no differences)

represent load-deflection relationships at high strain due to geometric distortion in the numerical model.

To evaluate the elastic behaviour at large stretch from the numerical model, other hyperelastic models, for example, the Mooney-Rivlin or Ogden model, can be used. However, the material coefficients in these models need to be calibrated using massive amounts of experiments. Also, most of these coefficients do not have physical meanings. In the following work, the Neo-Hookean model is applied due to its capability in simulating high static compressions.

3.6.1.1.3 Sensitivity analysis - Poisson's ratio

Poisson's ratio of the O-rings may have a great influence on the load-deflections. A Poisson ratio of 0.5 is assumed for a common incompressible material and causes a bulk modulus to be mathematically impossible. In reality, this material constant may degrade to 0.49 due to the additives in the polymers. Several authors [91–93] have demonstrated that the Poisson's ratio, obtained from experiments, is close to a value of 0.49 for real polymers. A sensitivity analysis was carried out to

investigate the effect of Poisson's ratio using the numerical model. It is assumed that the coefficient of friction between the elastomer and stainless steel is 0.8.

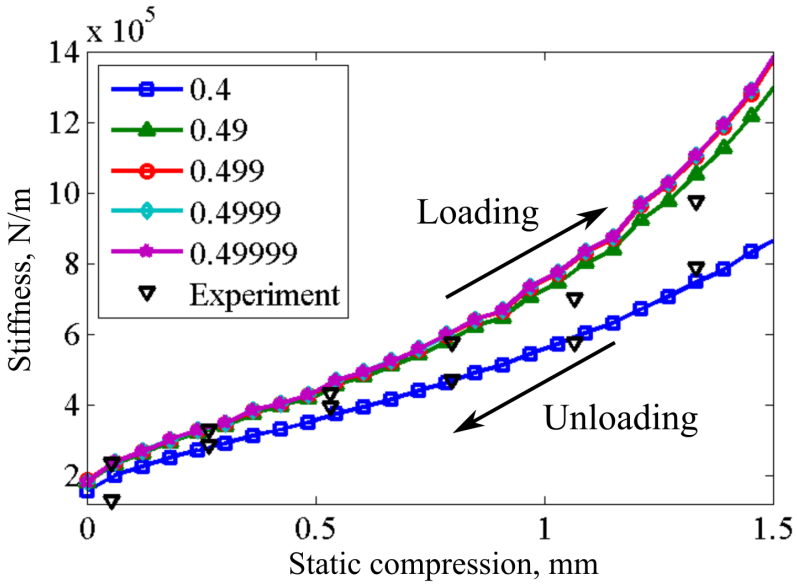

Figure 3.41: Stiffness-deflection curves subject to different Poisson's ratio

Figure 3.41 shows that the stiffness curves tend to converge when the Poisson's ratio exceeds 0.499. However, a much more accurate stiffness-deflection relationship can be achieved using a numerical model with a Poisson's ratio of 0.49 when subject to compressing the O-rings. This observation agrees with the concluding remarks from other papers [94, 95]. In summary, the Poisson's ratio of the numerical model needs to be carefully chosen for elastomers. In the following analysis, the Poisson's ratio is set to 0.49.

3.6.1.1.4 Sensitivity analysis - interfacial friction

The frictional coefficient between rigid plates and the O-rings may affect the prediction of the elasticity as well. Ten different frictional coefficients that may result in either free sliding or sticking of the O-rings were used. Contact status, including nominal diameters and contact length in the cross-sections, were detected. Typical stress and strain distributions can be seen in Figure 3.42.

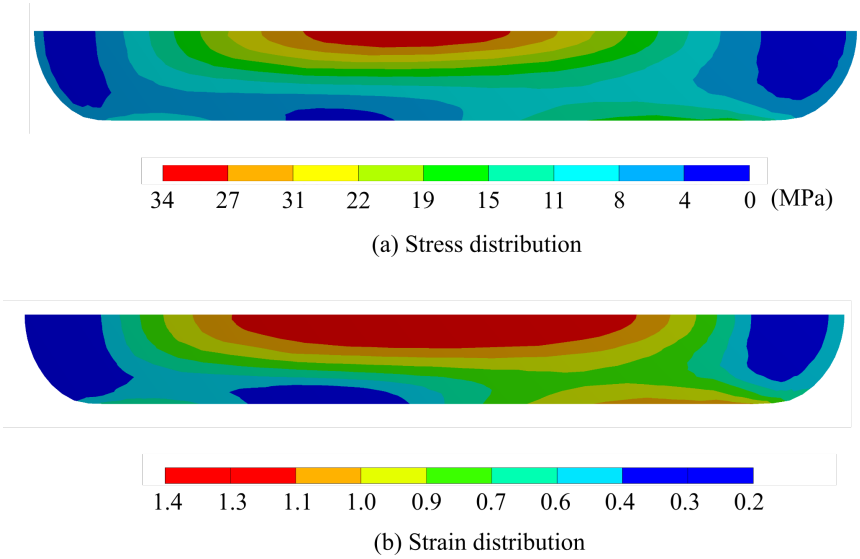

Figure 3.42: Stress/strain distributions of the O-ring when subjected to selected pre-compressions. Note that the Poisson's ratio of the elastomer is 0.49; interfacial frictional coefficient is 0.8; The static compression of O-ring is 3.2 mm

Both the stress and strain distribution were not symmetric due to both the cross-sectional local expansions and expansions of the nominal diameter. Typical examples for the deformed shape of the O-ring when subjected to two different static compressions are shown in Figure 3.43.

A normalised nominal diameter and contact length against frictional coefficients are shown in Figure 3.44.

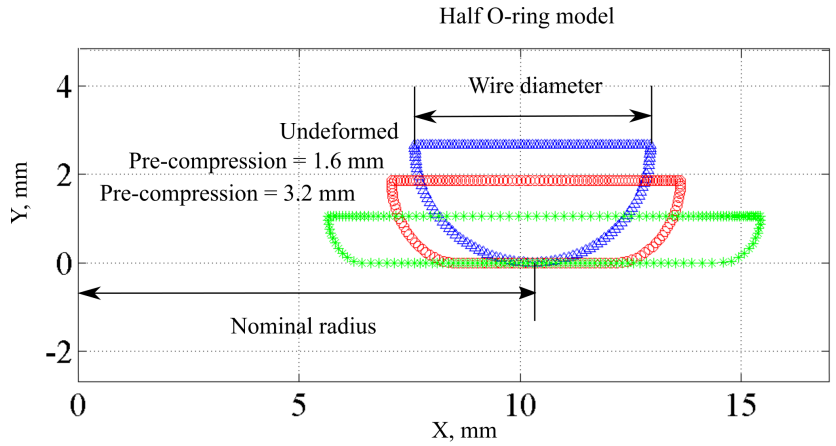

Figure 3.43: Deformed shape of an O-ring when subjected to selected pre-compressions. Note that the Poisson's ratio of the elastomer is 0.49; interfacial frictional coefficient is 0.8

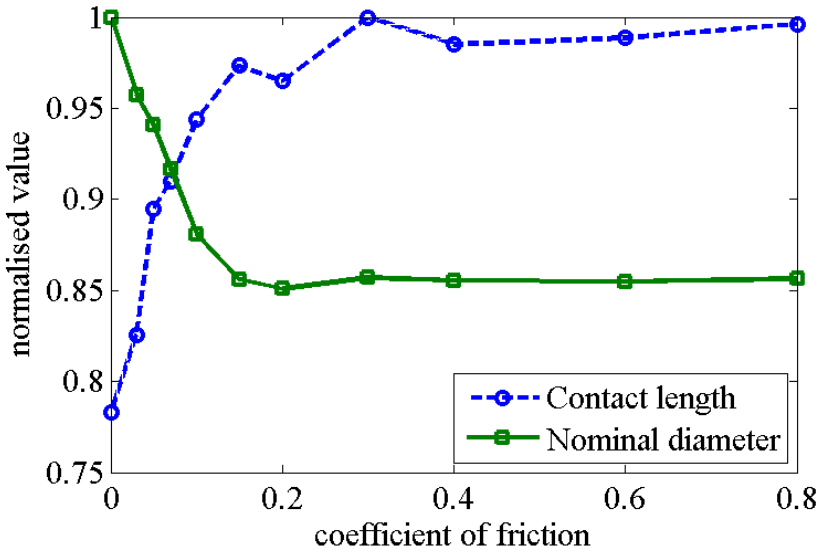

Figure 3.44: Contact status of O-rings subject to different coefficient of friction

It can be seen that the contact length increases with interfacial friction. The nominal diameter, however, follows the opposite trend. When the O-ring moves easily between the loading plates, the expansion of the O-ring in the radial direction can be observed. The effect of the free expansion is eliminated when the

coefficient of friction exceeds 0.2. In this situation, the sticking between loading plates and O-ring dominate the contact behaviour, and then an equal nominal diameter can be obtained. The relationships for these ten different interfacial frictions are shown in Figure 3.45

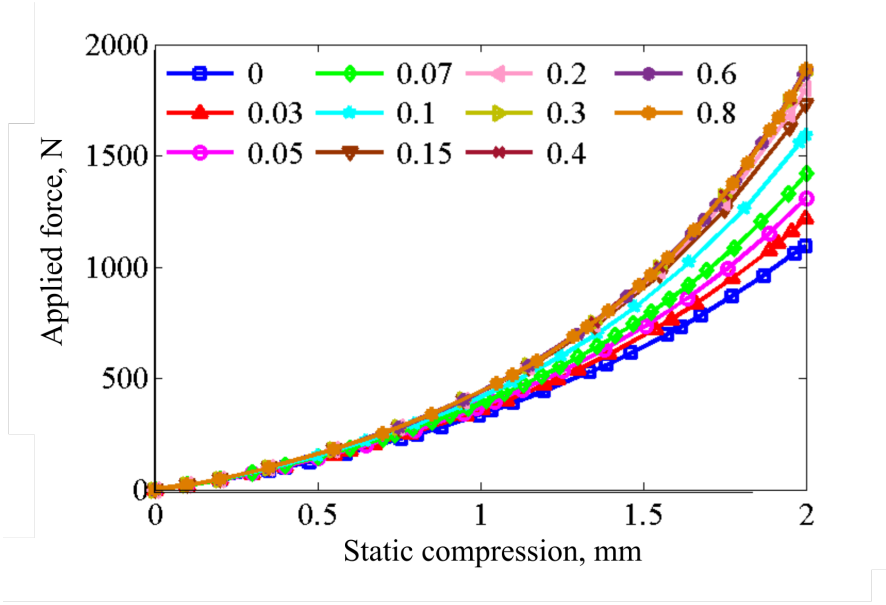

Figure 3.45: Load-deflection relationships subject to different coefficients of friction

Figure 3.45 indicates that the stiffness increases significantly with the interfacial friction when the O-rings slide over the loading procedures. The differences can be negligible when these elements start sticking on the loading plates. The stiffness of the O-ring is usually affected by the nominal diameter and elasticity of the elastomers. With a low coefficient of friction, the effect of applying an equivalent biaxial stress on the O-rings is contradictory to that of increase of nominal diameter on the stiffness of the O-rings. At the same static compressions, the reduction of the pre-stress, due to the increase of the nominal diameter, is apparent with low friction, and, therefore softens the O-rings.

3.6.1.1.5 Validation of the Finite Element model

Validation of the developed numerical model is shown in Figure 3.46. Since only the reaction force on the O-ring was obtained, the nonlinear stiffness with compression can be obtained numerically,

$$k_{\text{compression}} = \frac{\Delta P}{\Delta \delta_z} \tag{3.47}$$

where P is reaction force on the O-ring, and δ_z is static deformation of the O-ring.

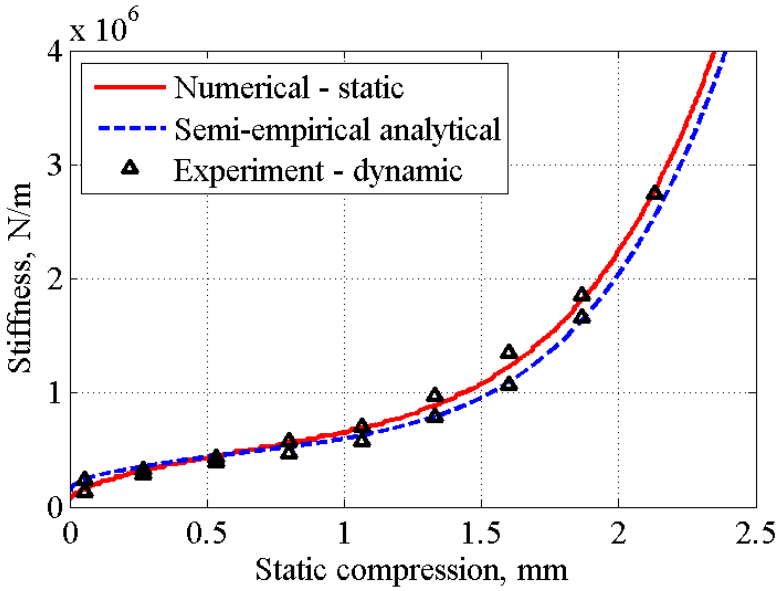

Figure 3.46: Comparison of nonlinear stiffness subject to semi-empirical analytical model, numerical model and experimental results

Note that the experimental results of the O-ring is obtained using quasi-static loadings with a frequency of 2.5 Hz. For each static compression, there exist two different stiffness value. They refer to the stiffness obtained in the loading and unloading process, respectively. Meanwhile, the static finite strain analysis was used to obtain the numerical stiffness. It can be seen from Figure 3.46 that the axial stiffness from the numerical model is similar to both the one from analytical model and experimental results.

3.6.1.2 Forced vibration simulation - circular O-ring

Forced-vibration simulations were used to evaluate the stiffness and damping at selected static compressions. The same loading history is followed as that for the static compressive simulations with the addition of a second loadstep with a harmonic displacement. A typical displacement history for the dynamic loading is shown in Figure 3.47

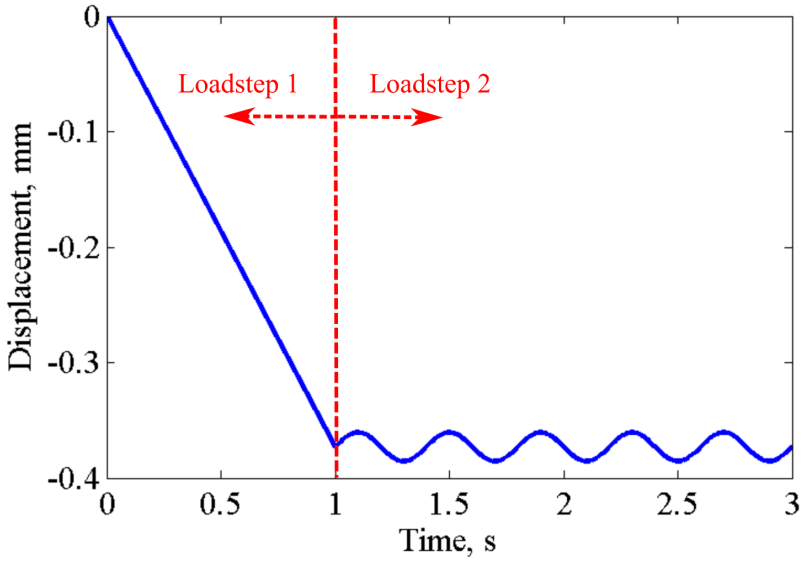

Figure 3.47: Typical loading history for the forced vibration simulations

The hysteresis loop, and then stiffness and energy dissipation of the O-ring was estimated using this dynamic transient analysis in the commercial FE code. Comparisons of energy dissipation between the FE models and experimental results for circular O-rings were then carried out. The result is presented in Figure 3.48.

It can be seen from Figure 3.48 that the dissipated energy is almost the same for the FE model and the experimental results, while the stiffness from the numerical model is slightly lower than the experimental values. Nevertheless, this tiny offset of stiffness is still negligible when calculating the resonance frequency of a TMD

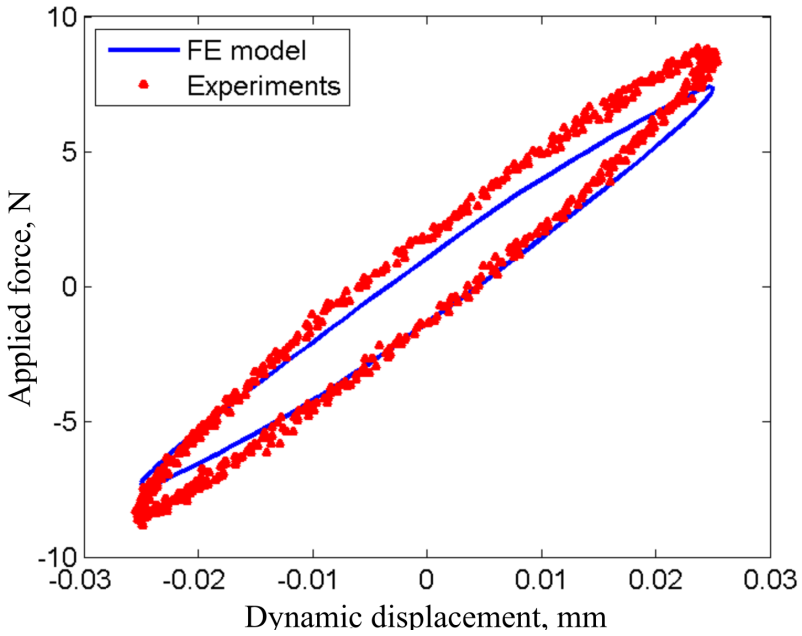

Figure 3.48: Comparison of hysteresis curves obtained from analytical and numerical models.(pre-strain of cross section = 0.14)

using O-rings. To conclude, this finite element model is still acceptable to predict the performance of the O-ring when subject to dynamic excitations.

3.6.1.3 Validation of the O-rings with irregular cross-section: finite strain analysis

As mentioned at the beginning of this section, the numerical model was developed to simulate O-rings with an irregularly shaped cross-section. In the following analysis, validation of the effectiveness of this numerical model was carried out using a nitrile O-ring with X-shape cross-section.

When the interfacial friction was ignored, the damping of the O-ring is proportional to the loss factor of the nitrile rubber directly, and therefore is not evaluated here. The finite strain analysis was introduced to predict the stiffness of this O-ring.

The nominal diameter of this O-ring is 19 mm. The geometry of the cross-section is shown in Figure 3.49.

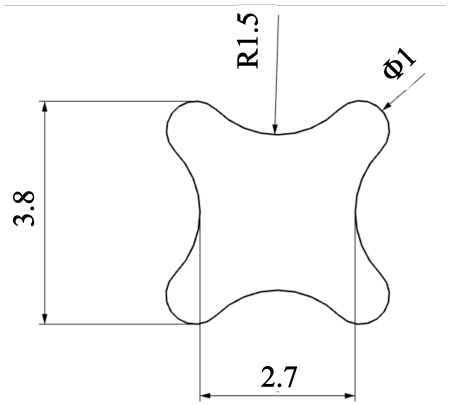

Figure 3.49: A schematic diagram of cross-sections of X-ring (Unit:mm)

The shear modulus of the nitrile rubber was set to 3.1 MPa and the Poisson's ratio was assumed to be 0.499. The model of this O-ring was generated using commercial FE code, Ansys. The half cross-sectional axisymmetric model of this O-ring was modelled with 6822 quadratic triangle elements. A coefficient of friction of 0.8 was assigned to the contact between restricting plate and O-ring. In the following analysis, only the static load-deflection relation was evaluated.

In order to estimate the nonlinear stiffness, noise caused by the errors in estimating contact stress needed to be removed in this model. A cubic spline interpolation with 20 knots was used to fit the load-deflection curve. Comparison of applied load against static compression between the fitting curve and experimental results is shown in Figure 3.50. It can be seen that the interpolation curves fit well with the experimental data.

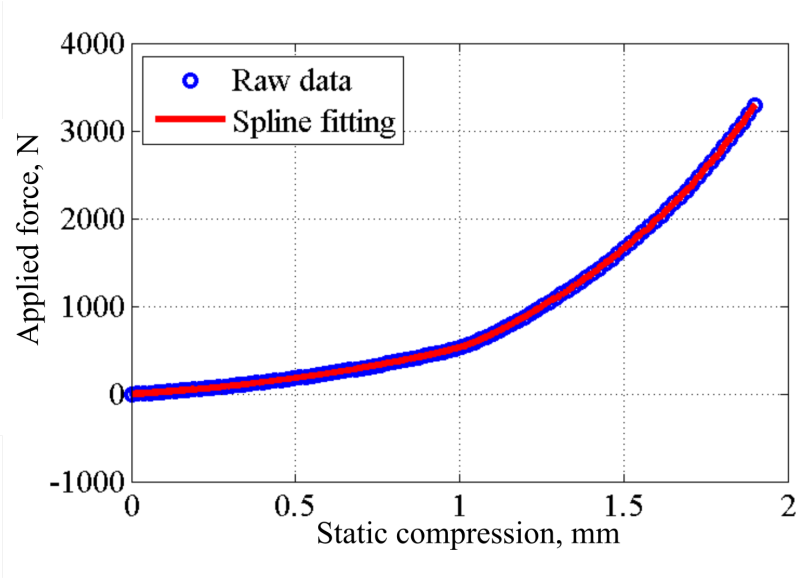

Figure 3.50: Applied load against deformation for nitrile X-ring

The deformation-stiffness curve was then obtained and is shown in Figure 3.51.

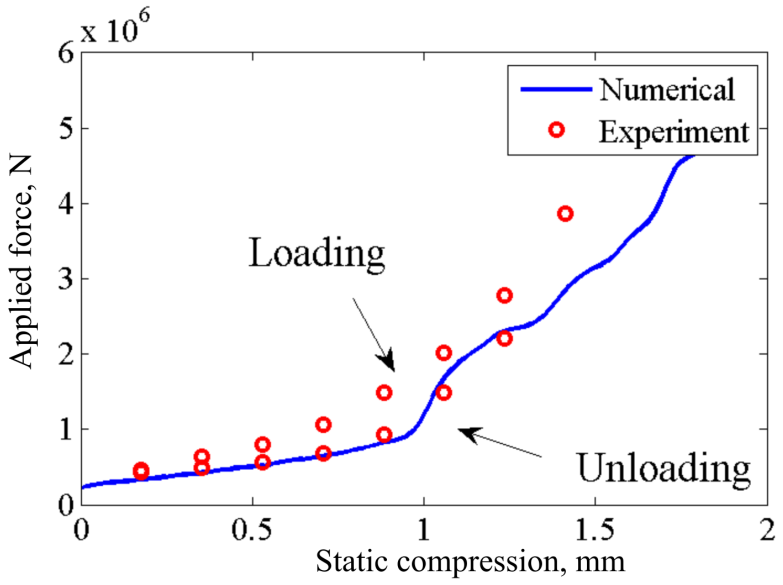

Figure 3.51: Stiffness against deformation for nitrile X-ring

Note that the experimental stiffness was obtained using the quasi-static com-

pressive tests with an excitation frequency of 2.5 Hz, and hence is close to the one obtained using static compressive loading. Figure 3.51 indicates that the stiffness estimated from the numerical model fits that observed experimentally for the unloading procedures. Several reasons for these uncertainties are listed below:

- The geometry of the X-rings is not accurately represented, especially for the convex regions in the cross-section.
- The interfacial frictional force is not consistent for the X-ring with strain at loading and unloading procedures. Frictional force occupies an important role in the nonlinear stiffness.

Nevertheless, this finite element model can still predict the performance of the X-ring with reasonable accuracy.

3.6.1.4 Summary

In this section, a 2D numerical model was developed to estimate the stiffness and damping of the O-ring in compressive direction. With careful choice of the frictional coefficient and material compressibility, this model can predict these properties well and with reasonable computational effort. Also, it has capability of the model to simulate the O-ring with an irregular cross-section has been demonstrated with reasonable accuracy.

3.6.2 Rocking and shear behaviour

An innovative approach using isotropic linear material assumption is introduced to estimate the shear and rotational stiffness - see Figure 3.52. The basic idea of this approach is to estimate the resonance frequencies for a given mass - deformed O-ring system, and therefore, the shear and rocking stiffness.

A 3D model, as shown in Figure 3.53 was developed as the rocking behaviour can not be evaluated using an axisymmetric model. The resonance frequencies,

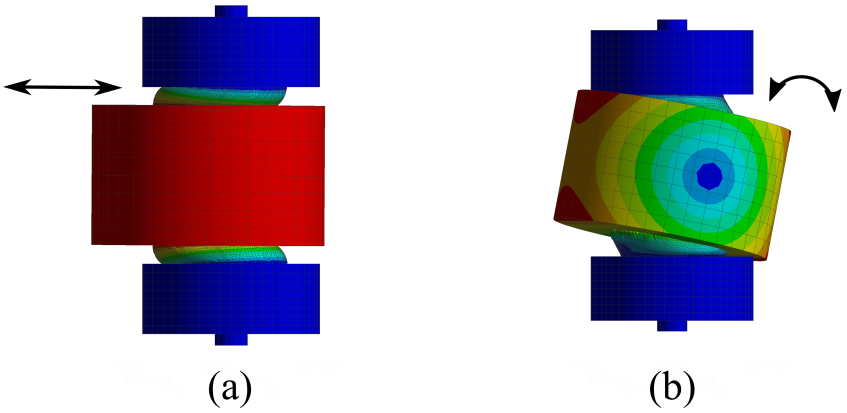

Figure 3.52: The models used to estimate (a) shear and (b) rocking stiffness of the O-ring when subject to a given static compression

followed by the stiffness, in the tensile-compressive, rocking and shear directions were then evaluated using finite element modal analysis. Since the pre-stress modal analysis in commercial FE code, Ansys, does not account for the geometric variation at a given static compression, the deformed cross-sectional shape of the O-ring was obtained from the 2D axisymmetric finite strain analysis, and then the numerical model of the 3D deformed O-ring was constructed accordingly.

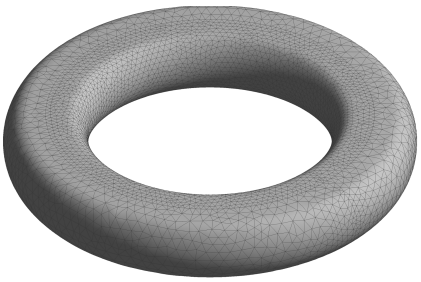

Figure 3.53: Typical 3D deformed O-ring model (static compression = 1.33 mm)

The isotropic linear material was then assigned to this O-ring because the commercial Finite Element code does not support hyperelastic models for the modal analysis. As mentioned previously, the O-ring, whose elasticity is modelled with the linear isotropic material model, may under-estimate the elastic behaviour, especially when subject to high static compression - see Figure 3.54. To compensate

this unwanted softening, the static compression-dependent elastic modulus, that was calibrated using the compressive stiffness obtained from the 2D axisymmetric numerical model, was assigned to this linear model. The interfacial contact between O-rings and fixed discs are assumed to be bonded in this model. The mechanical properties of the rig to represent this approach are exactly the same as those shown in Table 3.3.

Validations of the 3D models of O-rings were carried out using the 2D axisymmetric model. A finite strain analysis was conducted to examine the difference between the 2D and 3D models using applied load against static compression. The numerical configurations of the 2D and 3D models were almost the same. The elastic properties and geometry of the O-rings were exactly same as those described in the previous section. This 3D model was built using 20-node quadratic hexahedronal elements. 2444 elements were used for the elastomeric O-ring and 864 elements were assigned to the restricting plate.

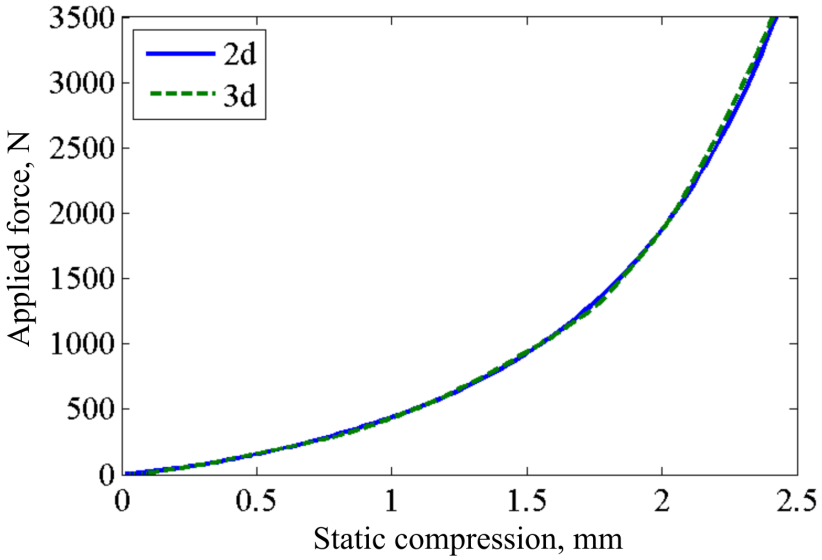

Figure 3.54: Load-deflection relationships for 2D and 3D numerical models

Figure 3.54 indicates very little difference exists between these two models. Such difference may derive from numerical errors, especially for difference in contact pressure in the contact region because the shear components of the contact

stress is neglected in a 2D axisymmetric model. Nevertheless, it can still be concluded that the 3D model can estimate the elasticity of the O-ring accurately.

The expressions of equivalent elastic modulus used in the following simulation was then derived. When subject to small dynamic oscillations, the O-rings can be modelled as a linear spring and dash-dot damping (viscoelastic) element. In this situation, the linear isotropic material model with equivalent modulus and Poisson's ratio can represent this hyperelastic material. For the Poisson's ratio, a choice of 0.499 was used in the following analysis. Since the load-deflection relationship for O-ring is nonlinear, an equivalent elastic modulus, which can account for material nonlinearity, is applied to this method. Lindley [35] suggests a load-deflection relation of O-rings to account for the geometric nonlinearity, as shown in Equation 3.48.

$$P_{\text{geo}} = 1.25\pi E d D^{-0.5}\delta^{1.5} \tag{3.48}$$

where d is the nominal diameter, D is the cross-sectional diameter, δ is the deformation of the O-ring and E is the initial elastic modulus of the O-ring.

Referring to the numerical model in compressive direction, a sharp raise of the stiffness can be observed with the static compression. One possible way is to use the equivalent modulus,

$$E_{\text{eq}} = \frac{P_{\text{compression}}}{1.25\pi d D^{-0.5}\delta^{1.5}} \tag{3.49}$$

in which $P_{\text{compression}}$ is the reaction force obtained from the numerical model developed in the previous section. Using Equation 3.49, the stiffening of the elastomer can be modelled with a strain-dependent modulus. Alternatively, Lindley also developed empirical equations that account for nonlinearity of the material, as shown in Equation 3.25. The strain-dependent scale factor of the equivalent modulus was then represented as $1 + 40\left(\frac{\delta}{d}\right)^{4.5}$.

Comparisons of compressive and rotational stiffness between 2D axisymmetric models and the resonance models were carried out to validate the effectiveness of estimation of elasticity. The resonance frequencies at four different static compressions were obtained and then the tensile-compressive stiffness was derived

using,

$$k_{\text{compression}} = \frac{(2\pi\omega_n^c)^2 \; m_{\text{moving}}}{2} \tag{3.50}$$

where ω_n^c is the resonance frequency in Hz and m_{moving} is the mass of the moving metal disc. Comparisons of tensile-compressive stiffness are shown in Figure 3.55.

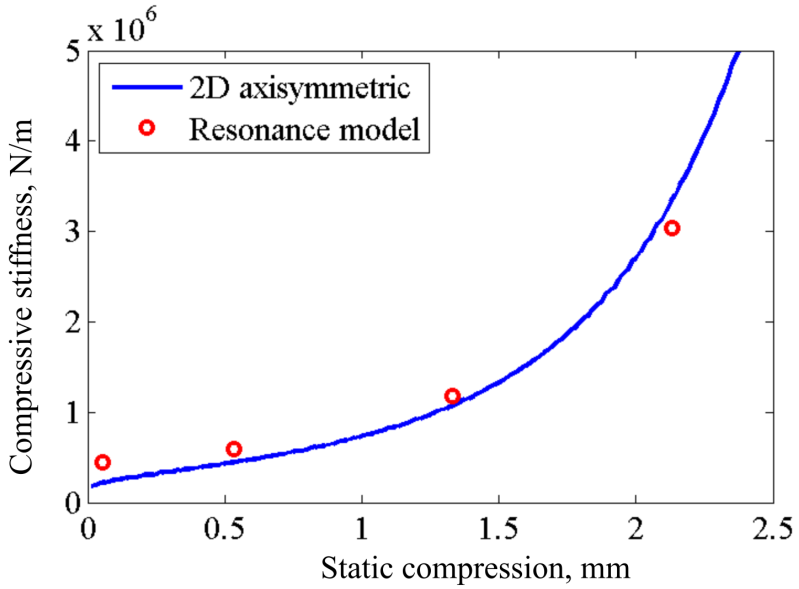

Figure 3.55: Comparisons of tensile-compressive stiffness at given strains of the O-rings between 2D and resonance model

It can be seen from Figure 3.55 that the proposed resonance models work well, especially at high static compression. For initial deformation, the stiffness of the proposed model is slightly higher due to the node distribution of both numerical models. Nevertheless, this proposed resonance model can predict the compressive-tensile elasticity for the purpose of designing TMDs.

Since this type of TMD has an additional working mode, the rocking mode, to suppress the vibration, the validation of the tilting stiffness around its central horizontal axis was then carried out. The results are shown in Figure 3.56. Note that the tilting stiffness can be calculated using,

$$k_{\text{tilting}} = \frac{(2\pi\omega_n^t)^2 \; J_{\text{moving}}}{2} \tag{3.51}$$

where ω_n^t is the rocking resonance frequency of this system, J_{moving} is the mass moment of inertia for the moving mass and can be given by,

$$J_{\text{moving}} = \frac{m_{\text{moving}}}{12}\left(3r_m^2 + h_m^2\right) \tag{3.52}$$

in which r_m is the radius of the moving mass and h_m is the thickness of this moving disc.

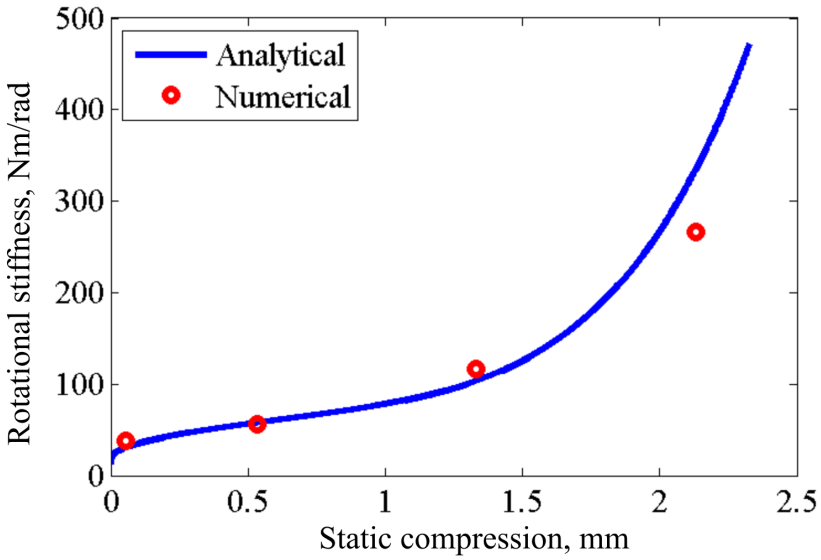

Figure 3.56: Comparisons of rocking stiffness at given strains of the O-rings between analytical and numerical model

Figure 3.56 indicates that stiffness estimated using this numerical model is slightly higher than that from the analytical model at low static compression. As mentioned in Section 3.5.2, the side expansion in the cross-section of the deformed O-ring is ignored in the analytical model. The load-carrying capability in the tensile-compressive direction is dominated by the equivalent rectangular cross-section. The rocking stiffness, however, has a more significant stiffening due to the additional resistance to the normal force caused by the side expansion. Meanwhile, the numerical model, unlike the analytical model, includes the side expansion in the geometry of the deformed cross-sections, when subject to low strain. As a result, softening in the rotational direction can be observed with the analytical

model, compared with the numerical estimation. At high strain, it is believed that the identical modulus of the O-ring is underestimated. Therefore, a lower rate of stiffening can be observed.

Hence this numerical resonance model was used to validate the analytical shear stiffness of the O-rings with different static compressions. The expression used to estimate the shear stiffness of the O-ring is,

$$k_{\text{shear}} = \frac{(2\pi\omega_n^s)^2 \; m_{\text{moving}}}{2} \tag{3.53}$$

where ω_n^s is the resonance frequency in Hz for shear mode. The results are shown in Figure 3.57

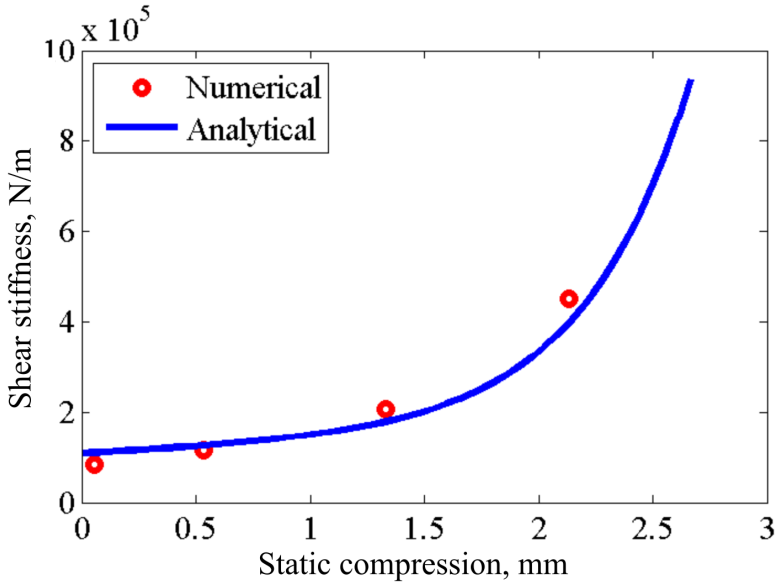

Figure 3.57: Comparison of shear stiffness at given strain of O-rings between analytical and numerical model

It can be seen from Figure 3.57 that almost no difference exists between the two models. The conclusion can therefore be drawn that the numerical model can predict the performance of O-rings well.

3.6.3 Summary

A 2D axisymmetric model was developed to predict accurately the compressive stiffness of O-rings with various cross-sectional shapes. Following completion of this task, a novel resonance model, established using the equivalent modulus and deformed geometries of the cross-sections, was developed to estimate natural frequencies of three different modes, in the compressive-tensile, shear and rotational directions. It can be concluded that this numerical model is able to estimate stiffness of the O-rings.

3.7 Response of the box section beam with this TMD

Results from Section 3.3.3 suggest that this type of TMD can work over a wide range of frequencies. In this section, the performance of this adjustable TMD was examined when it was applied to a rubber-ended hollow beam. The acceleration frequency response function was obtained to validate whether this type of TMD could alter the target modes of the host structure. The analytical model was then established to provide an efficient way to design this type of TMD.

3.7.1 Test procedures

The test set-up is presented in Figure 3.58. The adjustable TMD was attached to an aluminium hollow structure mounted on low-loss rubber supports at the end of the beam. The rubber blocks isolated the vibration from the ground and stand and provided a repeatable boundary condition. The overall length of the hollow beam is 500 mm. In order to avoid the nodes for target modes, a sinusoidal loading was applied to a position 115 mm away from one end of the beam and the accelerometer was attached 385 mm from the same end. Two displacement laser probes were placed on both sides of the beam to measure the pre-strain

on the O-rings. Because O-rings exhibit high nonlinear stiffness, identical static deformations were required for the O-rings on both sides. The bending of the hollow beam, caused by the rubber supports, introduces errors for pre-strain. To avoid this unwanted effect, the rubber supports were temporarily replaced by metal block when static compressions were applied to the O-rings. A filtered random excitation, whose frequencies ranged from 40Hz to 2000Hz, was used to drive the beam. The accelerometer was then attached to this beam to measure the performance of this TMD over the given frequencies.

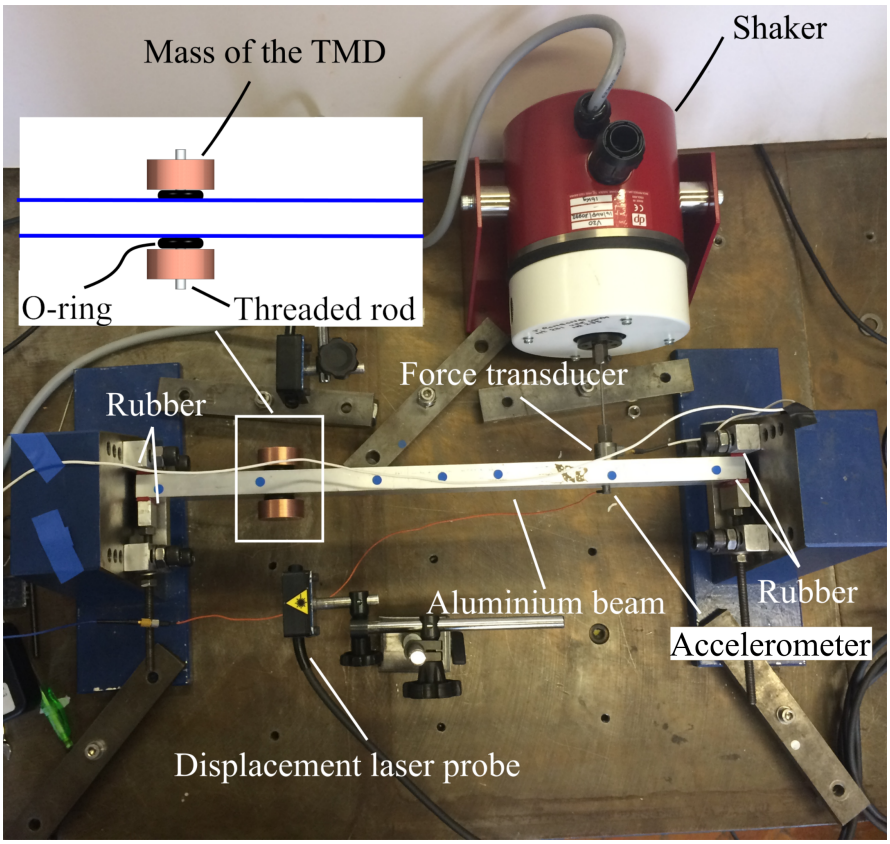

Figure 3.58: Test-rig for the rubber-end hollow beam

The detailed mechanical properties of the host structure are listed in Table 3.11

Experiments were carried out to ascertain whether the host mechanical structure would be suitable to investigate the performance of the TMD. When the

TMD was attached to the beam, the effective mass and mode shape of the beam changed. The accelerance frequency response function, as shown in Figure 3.59, was used to identify the frequencies shift caused by the updated mode shapes. Note that no O-rings were inserted in the TMD in these sets of experiments.

Figure 3.59 indicates that only two linear bending modes exist in the frequency ranges of 100 to 1000 Hz. As expected, the natural frequencies of these bending modes drop when the additional masses are attached. This is because of the increase of the kinetic energy on the host structure. Also, the peak magnitudes of the resonances for both configurations of the beam are almost identical.

To evaluate the effect of nonlinearity from the configurations of the rubber-ended boundary conditions, different dynamic acceleration amplitudes were applied to this beam structure. The extra discs from the TMD promote the deformation of the beam at its ends, and hence the stiffness of isolation rubber. So, plain mass blocks without elastomeric O-rings in the TMD were also attached to the beams in these tests.

It can be seen from Figure 3.60 that little nonlinearity was identified from the host structure. Damping increases slightly with amplitude because more friction between the beam and low-loss rubber arises, especially for the 2^{nd} mode. Compared with energy dissipation from the TMD, the damping from isolation rubber can be ignored. To conclude, the design of the current primary structure

Variable	Value
Young's modulus of the hollow beam	69 GPa
Mass of the hollow beam	290 g
Dimension of the hollow beam	500 mm × 38.1 mm × 19.1 mm
Wall thickness of the hollow beam	2.5 mm
Modulus of the isolation rubber	8.3 MPa
Dimension of the isolation rubber	19.1 mm × 10 mm × 3 mm
Loss factor from the isolation rubber	0.08 - 0.1

Table 3.11: Mechanical properties of host structure

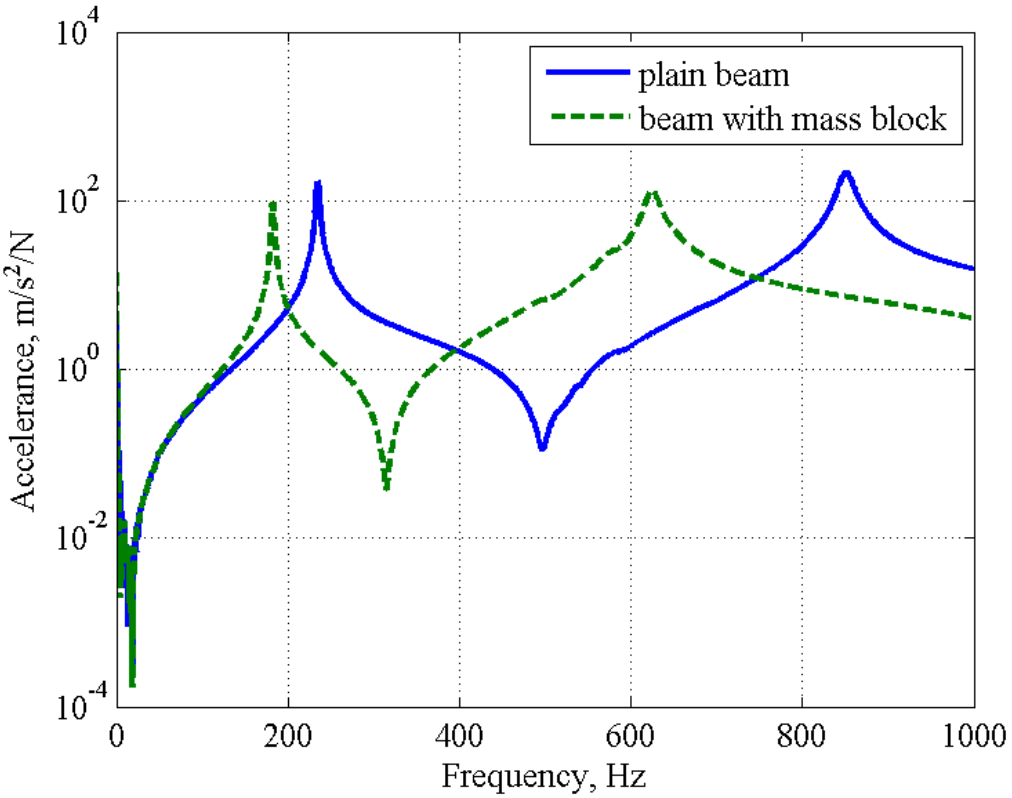

Figure 3.59: Comparisons of the frequency responses between plain beam and beam with mass of the TMD

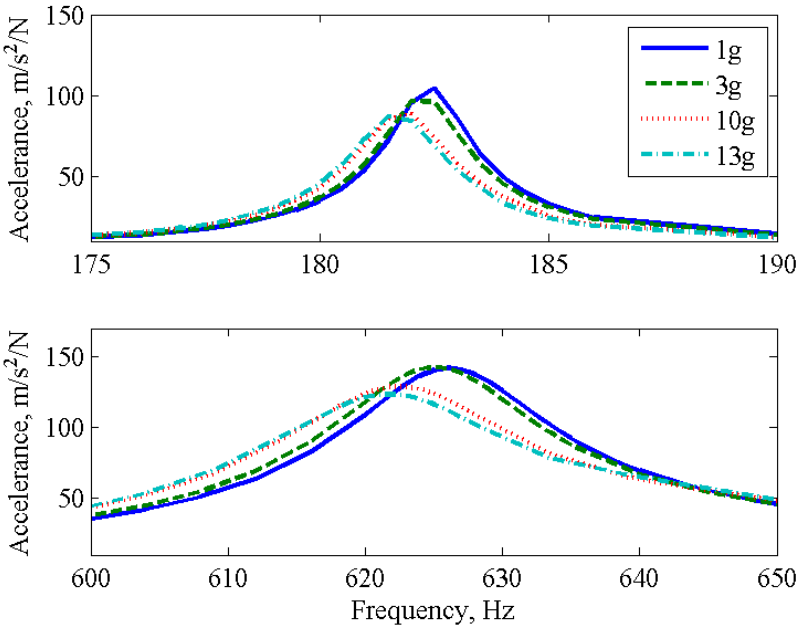

Figure 3.60: Effect of end rubber subject to different magnitudes of excitation

compromises two good linear bending resonances and limits the amplitude-dependent nonlinearity.

3.7.2 Choice of the static compressions

The proposed TMD has two working modes in the selected frequency ranges of the host structure. In practice, the design parameters of the O-ring TMD can be optimised using both the tension-compression and rocking modes. When employing suitable design parameters of the TMD, this TMD can achieve the best performance of vibration suppression over wide frequency ranges. In this preliminary analysis however, only the motion of the TMD in compression-extension were selected as the targeted working modes.

For the host structure, the first two resonance frequencies are approximately 182 and 625 Hz, respectively. If the host structure has little damping, it has been shown [42] that the optimal performance can be obtained when the resonance

frequency of the TMD is close to that of the host structure. The effective mass of the beam is an important design parameter, which affects the natural frequencies of the host structure, and therefore, the optimal TMDs. However, this effective mass is highly influenced by the configurations of the TMD. As a result, the iterating procedure need to be introduced to obtain the optimal TMD.

In this preliminary study, the optimal frequency of the TMD for tensile-compressive mode is assumed to be the natural frequency of the host structure at targeted mode. So, the optimal stiffness of each O-ring is given by,

$$k_{\text{opt}} = m_{\text{TMD}}(\omega_{n,\text{beam}})^2 \tag{3.54}$$

where m_{TMD} is the mass of the TMD, a value which is normally defined according to the mass of the host structure, the desired maximum damping and other design constraints. In this example, the two copper discs and threaded rod have a mass of approximately 320g. Substituting the mass of this TMD into Equation 3.54, the optimal stiffness values for each O-ring were 214.5 Nmm^{-1} and 2175 Nmm^{-1} for 1$^{\text{st}}$ and 2$^{\text{nd}}$ mode, respectively. Referring to Figure 3.26, the static pre-strains, 6% and 40% of the O-ring cross-section, were chosen accordingly. Meanwhile, the performance of this TMD with a static pre-strain of 15% of O-ring cross-section was investigated to demonstrate the effectiveness of this TMD at the frequencies other than the targeted ones.

3.7.3 Performance of TMD at selected static compressions

The performance of TMD was then evaluated using the rubber-ended beam. For three different working conditions of the TMD, the accelerances of the host structure when subjected to random excitations are shown in Figure 3.61.

Figure 3.61 demonstrates high energy dissipations at low static compressions regardless of the frequency, and meanwhile relative flat peaks can be observed under these working conditions. Compared with harmonic excitations, the wide broadband excitation activates unexpected large displacements at certain working

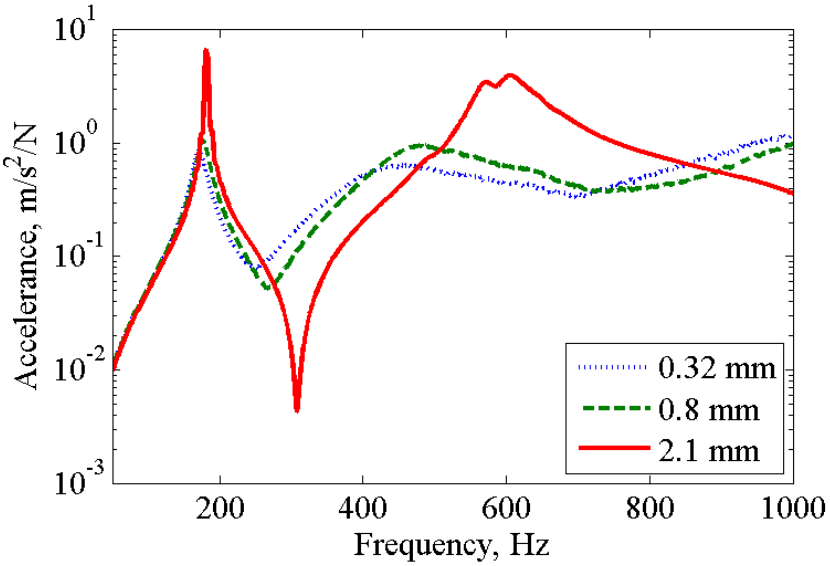

Figure 3.61: Performance of O-ring TMD with various static compressions when subjected to random excitations

frequencies of the TMD. These relative large displacements may promote the sliding between the O-ring and the host structure, and therefore the nonlinear stiffness and damping in this beam-TMD system. Figure 3.62 shows the corresponding coherences of the inertance to identify the participation of the nonlinearity, where it can be seen that the coherence approaches to unity with the increase of the static compressions.

At low static compressions, the set-ups of the O-ring and the mass of the TMD is loosen. Significant sliding preserves in the interface between the TMD and host structure, and lead to a low coherences under broadband random excitation. These nonlinearities disappear when the static compressions increase due to these relative motions dismisses. To evaluate the performance of the TMD at resonances, controlled stepped sinusoidal accelerations of 9.8ms^{-2} was used to investigate the performance precise at selected frequency ranges.

Figure 3.63 and 3.64 show the acceleration frequency responses for the host structure with the TMD subjected to different working conditions. The lateral vibrations around 185 Hz were suppressed by approximately 1000% when the

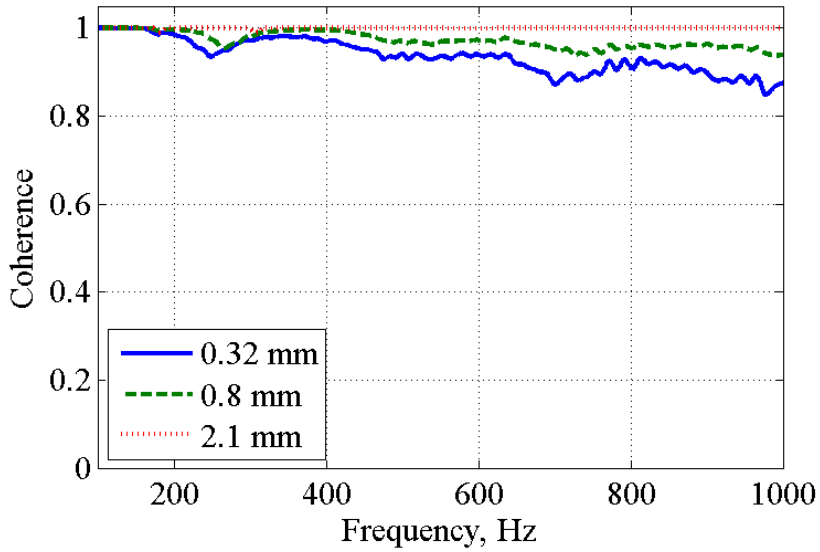

Figure 3.62: Coherence of the beam when subjected to random excitation

O-ring was subjected to static deformation of 6%. With the increase of static compression, this damper lost its effectiveness for the first mode. Meanwhile, the vibration at 600 Hz was suppressed by 750% when the pre-strain was set to 40%.

The other significant findings in Figure 3.64 is the unexpected frequency shift, especially for the 2nd mode. In the current design, the mass of the TMD is about the same as the host structure. This TMD has a great influence on the mode shape of the host structure. Additionally, the damping also affects the interaction, and hence the involvement of the TMD mass on the host structure. The Finite Element modal analysis was introduced to predict these mode shapes, and the corresponding effective mass (calculated from the mode shapes) are shown in Table 3.12. Note that the effect of the damping on the mode shapes can not be evaluated in this numerical analysis.

Table 3.12 indicates a relative uniform effective mass for the 1st mode while a steep fall for the 2nd mode. Compared with experimental results, the natural frequency of the 2nd mode at a static compression of 6% was under-estimated in this numerical analysis. Since the TMD was attached on the anti-nodes of the 2nd bending mode, the significant additional mass participates on the host structure.

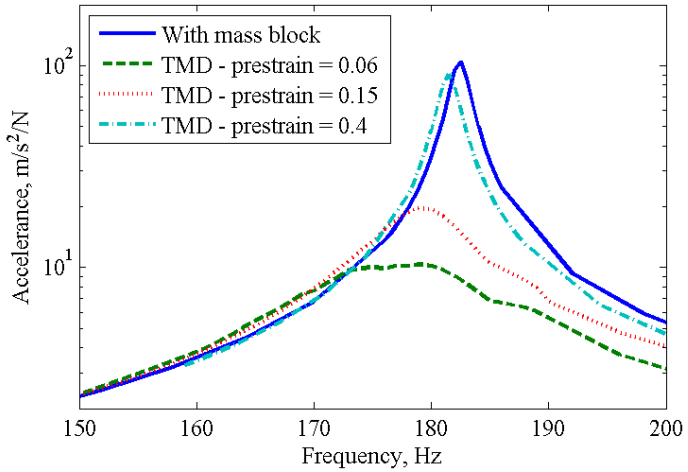

(a)

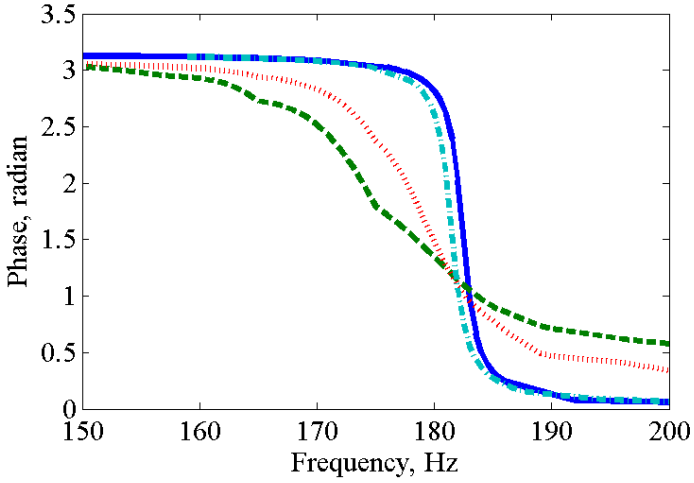

(b)

Figure 3.63: Performance of O-ring TMD with various static compressions for 1st mode (a) magnitude (b) phase

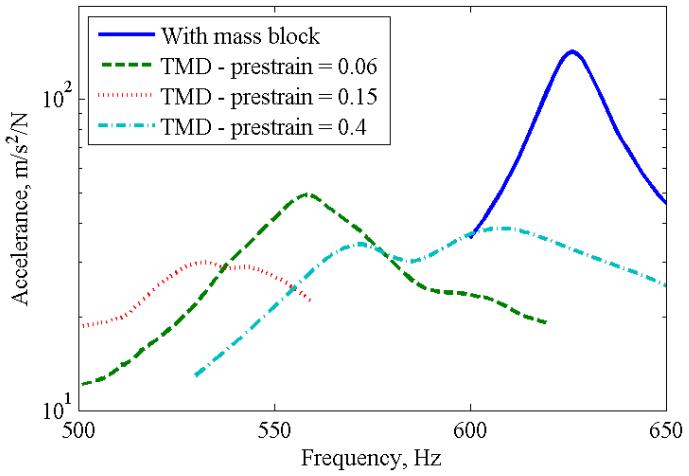

(a)

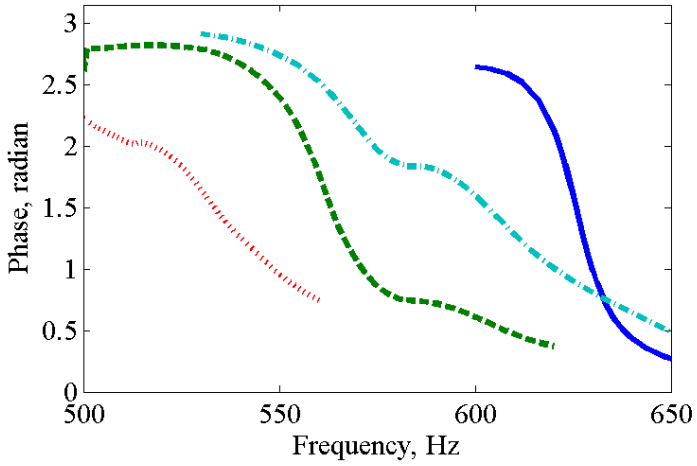

(b)

Figure 3.64: Performance of O-ring TMD with various static compressions for 2nd mode (a) magnitude (b) phase

Mode	Modal property	Static compression, %		
		6	15	40
1st	Effective mass, g	164	164	164
	Natural frequency, Hz	167	171	173
2nd	Effective mass, g	102	95	72
	Natural frequency, Hz	506	525	563

Table 3.12: Modal properties of the beam with the TMDs at different working conditions

Also, the interficial friction has a great effect on this additional effective mass. As a result, the involvement of the mass and inertia of the TMD on the hollow beam is difficult to predict.

Another interesting phenomenon that can be observed in Figure 3.63 is that both of the resonance peaks from 100 to 1000Hz can be suppressed where O-rings in this device have a static compression of 25%. One possible explanation is that both rocking and extension-compression modes were participating in the energy transfer and dissipation between the host structure and the TMD. In order to validate this conjecture, two accelerometers were placed at different locations on the moving discs. Note that the accelerometers placed in the centre, was called 'Accelerometer 1', while the other one placed 15 mm away from the centre was called 'Accelerometer 2'. The static pre-strain of the O-rings was set to 0.15. The acceleration time histories in both positions are shown in Figure 3.65.

No significant difference in response in the two selected positions can be observed under the condition of an excitation frequency targeting the second mode of the beam. When the TMD rotates along the width direction of the host structure, a significant magnitude drop can be observed at the position close to the centre of the moving disc. Therefore, this TMD only moves up and down when excited at these frequencies. Additionally, the apparent nonlinear response was captured under the condition of low-frequency excitation. The magnitudes of the higher order spectral components are presented in Table 3.13.

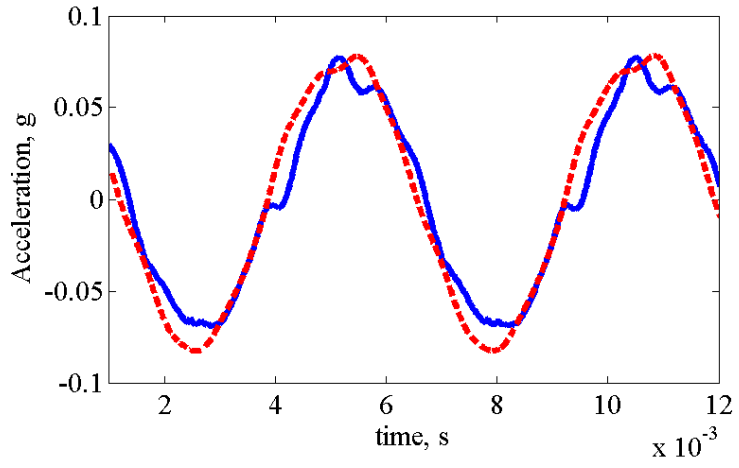

(a)

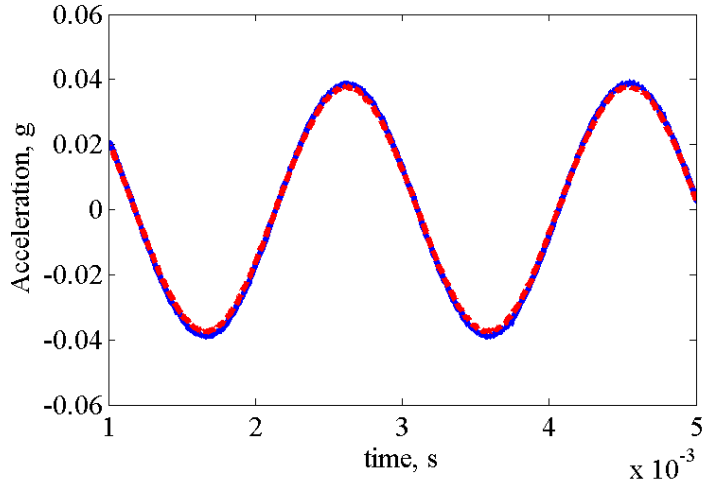

(b)

Figure 3.65: Acceleration response of this TMD with pre-strain of 0.25 in two different positions (a) 166 Hz (b) 513 Hz, Note that red dash line refers to response from accelerometer 1, blue solid line refers to response from accelerometer 2

Frequency, Hz	170	340	510	680	850
Acceleration, ms^{-2}	68.6	1.96	2.94	1.96	3.92

Table 3.13: Acceleration spectrum on the moving mass (excitation frequency is 170 Hz)

The nonlinearity identified can be explained by the nonlinear stiffness of the TMD. Additionally, the relative flat peak shape in Figure 3.65 indicates that interfacial friction may be involved in the energy transfer between host structure and the TMD. The presence of friction may also explain why the resonance frequency of the 2^{nd} mode is reduces as the strain is increased from 6% to 15% in Figure 3.64(b).

3.7.4 Mixed analytical/numerical model of hollow beam with TMD

The analytical model was then developed for the purpose of rapid design of this type of TMD for a given engineering structure. Previous sections indicate that only three rigid body vibration modes work for this type of TMD. To minimise the complexity, the following restricting assumptions were applied to the proposed model,

- The friction between the O-rings and metals is negligible. The O-rings are assumed to bond on the mass block of the TMD and the primary structure.
- The dynamic strain of the O-ring is far less than the static compression, and therefore, the extensional and rotational modes of the TMD are linear.
- The shear mode of this TMD is not considered in this work.

The expressions of kinetic and strain energy are derived from the rigid body motion of the mass component of this TMD - comprising the proof mass and threaded rod. The tensile-compressive movement, shear motion and rotational

angle were selected as the generalised coordinates. The Equation of Motion was then obtained using Lagrange equations. The displacement time histories for a selected excitation were simulated numerically to examine whether the nonlinear cross-coupling between the structures and the TMD could be ignored. Finally, comparisons between the analytical models and experimental results were carried out to validate the effectiveness of this model.

3.7.4.1 Generalised coordinates

Figure 3.66 shows the deformations considered in this analysis and the nomenclature used. Note that the motion of the host structure is not represented in this figure.

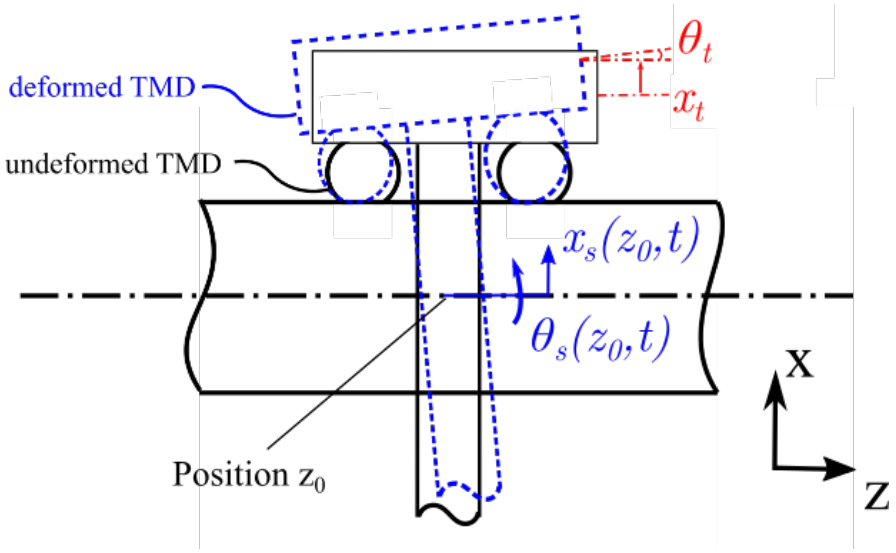

Figure 3.66: Deformation of main structure with TMD

The displacement of the mass block in the extensive-compressive and rotational direction is defined as x_t and θ_t respectively. The generialised coordinates can be then established,

$$x_s(z,t) = \phi(z)w_s(t) \tag{3.55}$$

$$x_t(z,t) = X_{t_0}w_t(t) \tag{3.56}$$

$$\theta_t(z,t) = \theta_{t_0}w_t(t) \tag{3.57}$$

where $\phi(z)$ is the generalised coordinate for the host structure, $w_s(t)$ and $w_t(t)$ are the principal coordinates for the host structure and TMD respectively, X_{t_0} and θ_{t_0} are the constant.

One more constrained function, linking the rotational and translational motions of the host structure, is applied to simplify the Equation of motion. The rotational angle of the host structure is defined as,

$$\theta_s(z,t) = \frac{\partial x_s(z,t)}{\partial z} = \frac{d\phi(z)}{dz} w_s(t) \tag{3.58}$$

By combining the Equations 3.55 and 3.58, the relationship between x_s and θ_s is established and defined as,

$$\theta_s(z,t) = \frac{d\phi(z)}{dz} \frac{x_s(z,t)}{\phi(z)} \tag{3.59}$$

3.7.4.2 Expressions of kinetic and strain energy

The kinetic energy of the beam is,

$$T_{\text{beam}} = \frac{1}{2} \int_0^l \frac{m}{l} \left[\frac{\partial x_s(z,t)}{\partial t} \right]^2 dz = \frac{1}{2} \frac{m}{l} \dot{w}_s^2(t) \int_0^l \phi^2(z) dz \tag{3.60}$$

where l is the length of the hollow beam. To simplify the expressions, the equivalent mass $m_{z_0}^{\text{eq}}$ of the host structure at selected position z_0 is introduced. The kinetic energy of the beam can be defined as,

$$T_{\text{beam}} = \frac{1}{2} m_{z_0}^{\text{eq}} x_s^2(z_0,t) = \frac{1}{2} m_{z_0}^{\text{eq}} \phi^2(z_0) \dot{w_t}^2(t) \tag{3.61}$$

Substituting Equation 3.60 into 3.61, this equivalent mass for given mode can be given by,

$$m_{z_0}^{\text{eq}} = \frac{m}{l} \frac{\int_0^l \phi^2(z) dz}{\phi^2(z_0)} \tag{3.62}$$

The kinetic energy of this beam-TMD system is therefore given by,

$$T = \frac{1}{2} m_t \left[\left(\dot{\theta}_t L \sin\theta_t + \dot{x}_t \right)^2 + \left(\dot{\theta}_t L \cos\theta_t \right)^2 \right] + \frac{1}{2} J_t \dot{\theta}_t^2 + \frac{1}{2} m_{z_0}^{\text{eq}} \dot{x}_s^2(z_0,t) \tag{3.63}$$

where L is the distance from the middle surface of the cross-section of the hollow beam to that of the mass block, the overdot symbol represents the time derivative $\frac{\partial}{\partial t}$. J_t is the mass moment of inertia of the mass block in side view, which is given by,

$$J_t = \frac{m_t}{6}(3r_t^2 + h_t^2) \tag{3.64}$$

where r_t is the radius of the upper constraint circular plate and h_t is the distance between the centreline of the hollow beam and the circular disc.

The strain energy of the beam can be defined as,

$$U_{\text{beam}} = \frac{1}{2}\int_0^l \frac{EI}{l}\left[\frac{\partial^2 x_s(z,t)}{\partial z^2}\right]^2 dz = \frac{1}{2}\frac{EI}{l}w_s^2(t)\int_0^l \left[\frac{d^2\phi(z)}{dz^2}\right]^2 dz \tag{3.65}$$

where E is the elastic modulus of the beam, and I is mass moment of inertia. To simplify the expression, the equivalent stiffness $k_{z_0}^{\text{eq}}$ was introduced at the position z_0. The strain energy of the beam can be also represented as,

$$U_{\text{beam}} = \frac{1}{2}k_{z_0}^{\text{eq}}x_s^2(z_0,t) = \frac{1}{2}k_{z_0}^{\text{eq}}\phi^2(z_0)w_s^2(t) \tag{3.66}$$

Combined Equation 3.65 and 3.66, the equivalent stiffness of the beam can be obtained,

$$k_{z_0}^{\text{eq}} = \frac{EI}{l}\frac{\int_0^l \left[\frac{d^2\phi(z)}{dz^2}\right]^2 dz}{\phi^2(z_0)} \tag{3.67}$$

The strain energy of the O-rings is in the form,

$$\begin{aligned} U = \frac{1}{2}k_{z_0}^{\text{eq}}x_s^2(z_0,t) + \frac{1}{2}k_t\left(x_t - x_s(z_0,t)\right)^2 + \frac{1}{2}k_{\text{rot}}\left(\theta_t - \theta_s(z_0,t)\right)^2 \\ +mgL\left(1-\cos\theta_t\right) \end{aligned} \tag{3.68}$$

where k_{rot} is the rotational stiffness of the O-ring, θ_s is the rotational angle of the host structure at the selected location. Note that the rotational angle of the TMD is normally small due to the relative high resonance frequencies of the host structure. Therefore, the gravity term, $mgL(1-\cos\theta_t)$, can be ignored.

It is worth noting that these equivalent mass and stiffness at selected position for the given modes can be obtained using experimental Nyquist circle fitting technique from the displacement frequency responses for the host structure.

3.7.4.3 Mode shape of host structure using numerical model

To link the rotational and translational motion of the beam, the mode shape vectors of the beam at different resonances are of importance. As described in Section 3.6, it has been shown that the behaviour of O-rings in the compressive, shear and rotational directions can be modelled using a numerical model with deformed cross-sections and equivalent elastic modulus. When the TMD was attached to the rubber-ended beam, this numerical model could still be applied to obtain the mode shape vectors subject to different initial compressions of the TMD.

Figure 3.67 indicates the mode shape of the beam obtained from the numerical model. This figure indicates that the vibration shape of the beam is sensitive to the working conditions of the TMD. When this TMD works at its resonance, the portion of mass devoted to the host structure is reduced. The peak of amplitude-normalised mode shapes decreases and is moved towards the location of the nodes. Since this TMD is placed on the anti-node locations of the 2$^{\text{nd}}$ bending mode, with the mode shape of the host structure is more sensitive to different conditions of the TMD. Therefore, fewer variations can be observed for the 1$^{\text{st}}$ mode on the different initial compression. The 2$^{\text{nd}}$ bending mode, however, is profoundly affected by the conditions of the TMD.

3.7.4.4 Lagrange equations

Once the mode shapes of the hollow beam with TMD obtained, the Lagrange equations was used to describe the motion of this system. Lagrange equation [96] states that,

$$\frac{d}{dt}\left(\frac{\partial\left(U-T\right)}{\partial\dot{q}_i}\right)-\frac{\partial\left(U-T\right)}{\partial q_i}=\frac{\partial\left(\delta W\right)}{\partial q_i} \tag{3.69}$$

where δW is the work done by external driving force, the q_i is the generalised coordinates. Substituting Equation 3.63, 3.68 and 3.58 into Equation 3.69, three coupled equations of motion can be obtained and are represented in matrix form

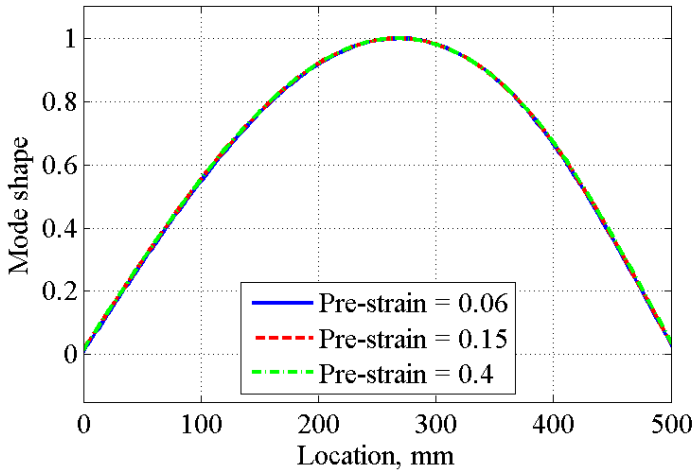

(a)

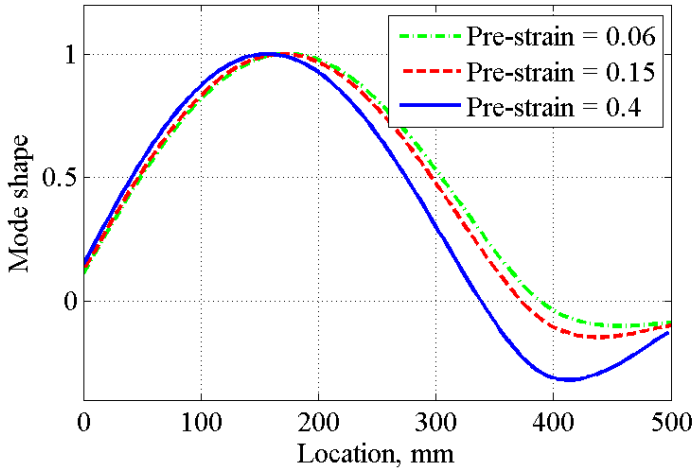

(b)

Figure 3.67: Normalised mode shape of rubber-ended hollow beam subject to three different initial conditions of the TMD (a) 1st mode (b) 2nd mode

as,

$$\begin{bmatrix} m_{z_0}^{\text{eq}} & & \\ & m_t & \\ & & J_t \end{bmatrix} \begin{bmatrix} \ddot{x}_s(z_0) \\ \ddot{x}_t \\ \ddot{\theta}_t \end{bmatrix} + \begin{bmatrix} & & \\ & m_t\ddot{\theta}_t L & \\ & & \end{bmatrix} \begin{bmatrix} \dot{x}_s(z_0) \\ \dot{x}_t \\ \dot{\theta}_t \end{bmatrix} + \begin{bmatrix} k_{z_0}^{\text{eq}} + k_t + k_{\text{rot}}\left(\frac{1}{\phi}\frac{d\phi}{dz}\right)^2 & -k_t & -\frac{d\phi}{dz}\frac{1}{\phi}k_{\text{rot}} \\ -k_t & k_t & m_t\ddot{\theta}_t L \\ -\frac{d\phi}{dz}\frac{1}{\phi}k_{\text{rot}} + \theta_T L k_t & -\theta_t L k_t & k_{\text{rot}} \end{bmatrix} \begin{bmatrix} x_s(z_0) \\ x_t \\ \theta_t \end{bmatrix} = 0 \quad (3.70)$$

3.7.4.5 Effect of cross-coupling of rotational and translational motions

Equation 3.70 indicates that the existence of the self-coupling terms, $m_t L\dot{\theta_t}^2$ and cross-coupling terms, $m_t L\ddot{\theta}_t\theta_t$, $Lk_t\theta_t x_s$, $-Lk_t\theta_t x_t$. For direct frequency response analysis, it is almost impossible to introduce these nonlinear terms into the Equation of Motion. In the proposed structure, it was assumed that the effect of these terms can be neglected when subject to small oscillations. To evaluate this hypothesis, the displacement history of this hollow beam was obtained using numerical strategy. For the sake of feasibility to simulate this system, a state-space presentation of Equation 3.70 is derived first. The generalised coordinates of this state-space form of Equation 1.64 are defined as,

$$\begin{bmatrix} y_1 \\ y_2 \\ y_3 \\ y_4 \\ y_5 \\ y_6 \end{bmatrix} = \begin{bmatrix} x_s(z_0) \\ \dot{x}_s(z_0) \\ x_t \\ \dot{x}_t \\ \theta_t \\ \dot{\theta}_t \end{bmatrix} \quad (3.71)$$

Substituting Equation 3.71 into Equation 3.70, a state-space representation

was then formed,

$$\begin{bmatrix} \dot{y}_1 \\ \dot{y}_2 \\ \dot{y}_3 \\ \dot{y}_4 \\ \dot{y}_5 \\ \dot{y}_6 \end{bmatrix} = \begin{bmatrix} 0 & 1 & 0 & 0 & 0 & 0 \\ A & 0 & \frac{k_t}{m_{z_0}^{\text{eq}}} & 0 & \frac{1}{m_{z_0}^{\text{eq}}\phi}\frac{d\phi}{dz}k_{\text{rot}} & 0 \\ 0 & 0 & 0 & 1 & 0 & 0 \\ \frac{k_t}{m_t} & 0 & -\frac{k_t}{m_t} & 0 & C & -y_6 L \\ 0 & 0 & 0 & 0 & 1 & 0 \\ B & 0 & \frac{1}{J_t}Lk_t y_5 & 0 & -\frac{1}{J_t}k_{\text{rot}} & 0 \end{bmatrix} \begin{bmatrix} y_1 \\ y_2 \\ y_3 \\ y_4 \\ y_5 \\ y_6 \end{bmatrix} + F \tag{3.72}$$

in which A is defined as,

$$A = -\frac{1}{m_{z_0}^{\text{eq}}}\left[k_{z_0}^{\text{eq}} + k_t + k_{\text{rot}}\left(\frac{1}{\phi}\frac{d\phi}{dz}\right)^2\right] \tag{3.73}$$

B is represented as,

$$B = \frac{1}{J_t}\frac{1}{\phi}\frac{d\phi}{dx}k_{\text{rot}} - \frac{1}{J_t}Lk_t y_5 \tag{3.74}$$

C is given by,

$$C = -\frac{m_t L\dot{y}_6}{m_t} \tag{3.75}$$

In the expression of C, the term, $\dot{y}_6$, can be substituted by a function of y_1, y_3 and y_5, which is defined by the last row of Equation 3.72. F is the excitation force vector,

$$F = \begin{bmatrix} 0 & f\sin(\omega t) & 0 & 0 & 0 & 0 \end{bmatrix}^T \tag{3.76}$$

Once the state space presentation of this Equation of Motion was established, the fourth order Runge-Kutta method [97] was introduced to evaluate the roles of these nonlinear terms. Using the Taylor expansions, the displacement of selected components could be estimated using its own response in the previous time. A detailed introduction of this numerical strategy can be found in [98]. The numerical configuration is shown in Table 3.14,

Figures 3.68, 3.69 and 3.70 show the comparisons of displacement amplitudes of the host structure against excitation frequencies for different configurations of

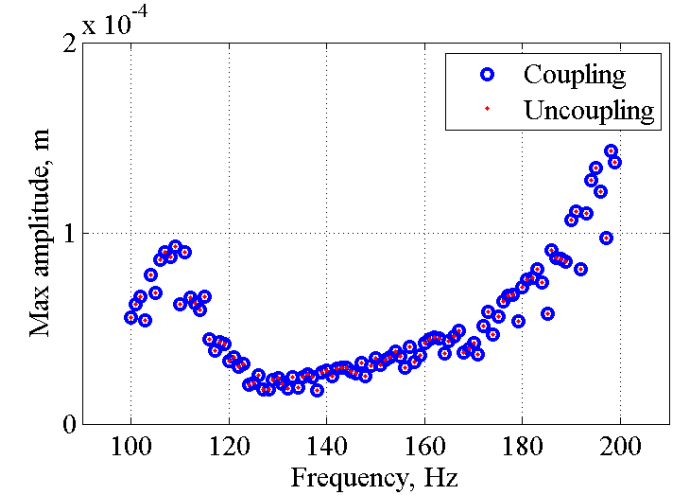

(a)

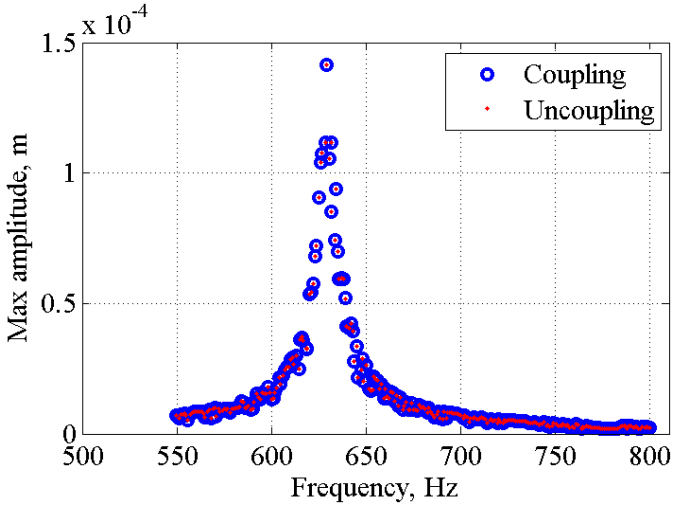

(b)

Figure 3.68: Frequency response of host structure with the TMD of 1% static compression (a) 1st mode (b) 2nd mode

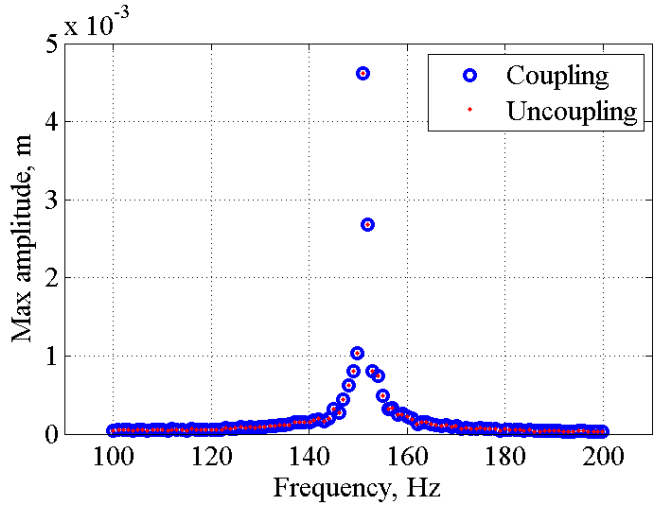

(a)

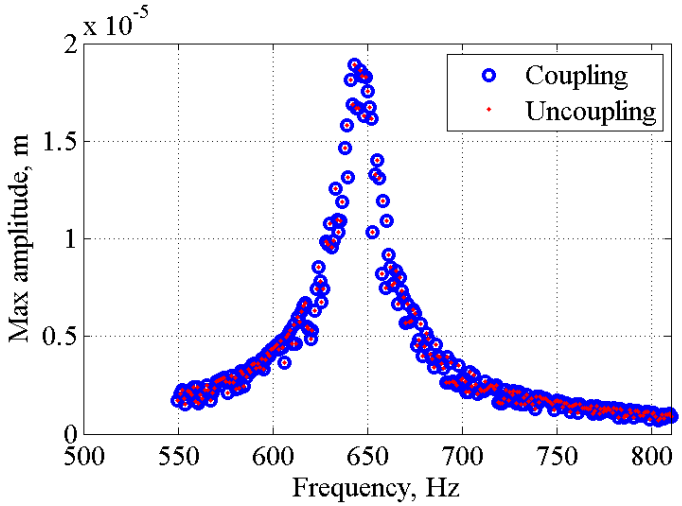

(b)

Figure 3.69: Frequency response of host structure with the TMD of 25% static compression (a) 1st mode (b) 2nd mode

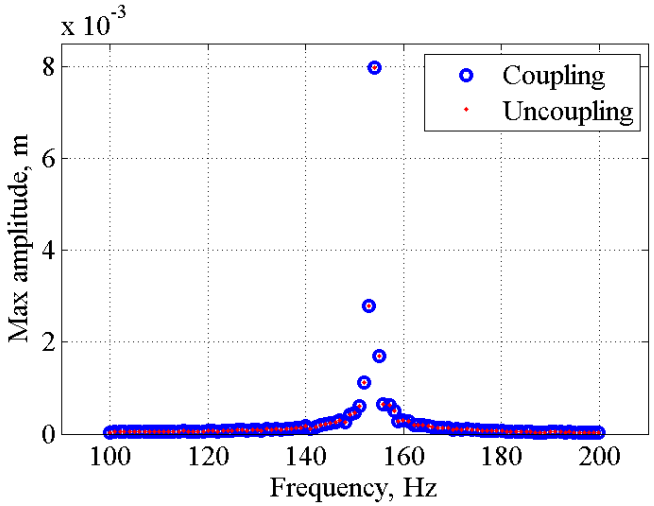

(a)

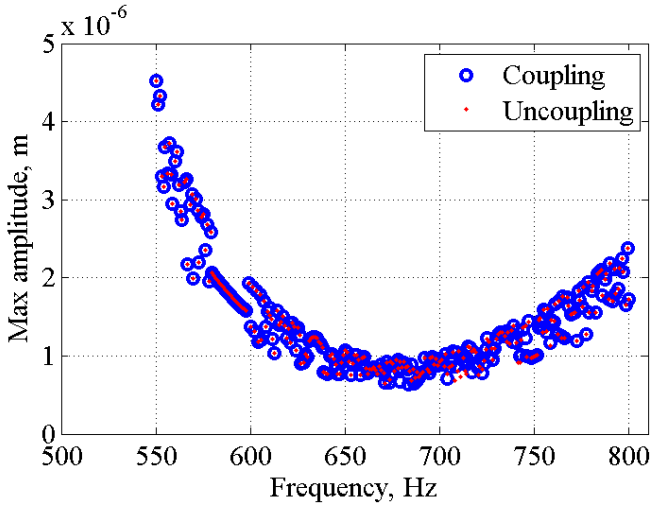

(b)

Figure 3.70: Frequency response of host structure with the TMD of 40% static compression (a) 1st mode (b) 2nd mode

Variable	Value
Time interval	50 s
Initial conditions	$y_i(0) = 0$ where i is integer and $i \in [1, 6]$
Excitation frequencies	100 – 200 Hz and 500 – 800 Hz
Relative tolerance	1e-7

Table 3.14: Numerical configurations

TMD. Note that the frequency ranges chosen in these figures are near to the first two resonances of the host structure.

Figures 3.68, 3.69 and 3.70 demonstrate that almost no difference exists in the frequency response between the models with and without coupling terms. In the following analysis, all of the coupling terms are ignored when establishing the receptance frequency response function of the host structure with TMD in different working frequencies.

3.7.4.6 Validation of the analytical/numerical models

The validation of the analytical models of the beam incorporating TMDs was then carried out. Two different set-ups of this type of TMD, with static compressions of 6% and 40% respectively, were used to identify the effectiveness of both linear and rotational motions.

Details of the parameters used in the analytical model are shown in Table 3.15. Since damping is not involved in estimating the mode shape of the TMD, some uncertainties may arise in this analysis. Also, the damping of the O-ring defined in rotational direction is slightly lower than that obtained in the high dynamic-strain analysis. The possible reason is the interfacial contact between the O-ring and the proof mass of this TMD. This phenomenon can also be observed in the resonance numerical model, as shown in Table 3.9.

The displacement receptance, obtained from the direct frequency response analysis, was then compared with the experimental results. These receptances are shown in Figure 3.71.

Variables	Value
Mass normalised mode shape at the position of excitation (1st mode)	0.5315
Mass normalised mode shape at the position where TMD is attached (1st mode)	0.7286
Mass of the TMD	320 g
Mass Moment of inertia of the TMD (prestrain = 6%)	7.4×10^{-5} kgm^2
Stiffness of the O-ring (prestrain = 6%)	4.29×10^{5} Nm^{-1}
Damping ratio of the O-ring in rotational direction (prestrain = 6%)	0.14
Rotational stiffness of the O-ring (prestrain = 6%)	73.42 Nmrad^{-1}
Damping ratio of the O-ring in tensile-compressive direction (prestrain = 6%)	0.21
Equivalent mass of the hollow beam for the 1st mode	0.5315 kg
Equivalent stiffness of the hollow beam for the 1st mode	1.15×10^{6} Nm^{-1}
Equivalent damping ratio of the hollow beam for the 1st mode	0.005
Mass normalised mode shape at the position of excitation (2nd mode)	1.9906
Mass normalised mode shape at the position where TMD is attached (2nd mode)	0.5380
Stiffness of the O-ring (prestrain = 40%)	4.35×10^{6} Nm^{-1}
Rotational stiffness of the O-ring (prestrain = 40%)	449.07 Nmrad^{-1}
Damping ratio of the O-ring in rotational direction (prestrain = 40%)	0.1
Damping ratio of the O-ring in tensile-compressive direction (prestrain = 40%)	0.06
Equivalent mass of the hollow beam for the 2nd mode	250 g
Equivalent stiffness of the hollow beam for the 2nd mode	7.15×10^{6} Nm^{-1}
Equivalent damping of the hollow beam for the 2nd mode	0.009
Mass Moment of inertia of the TMD (prestrain = 40%)	6.77×10^{-5} kgm^2

Table 3.15: Key parameters of the hollow beam and TMD

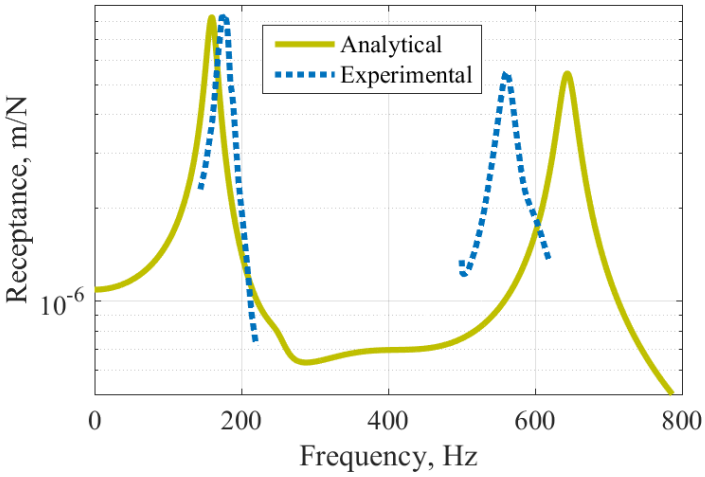

(a)

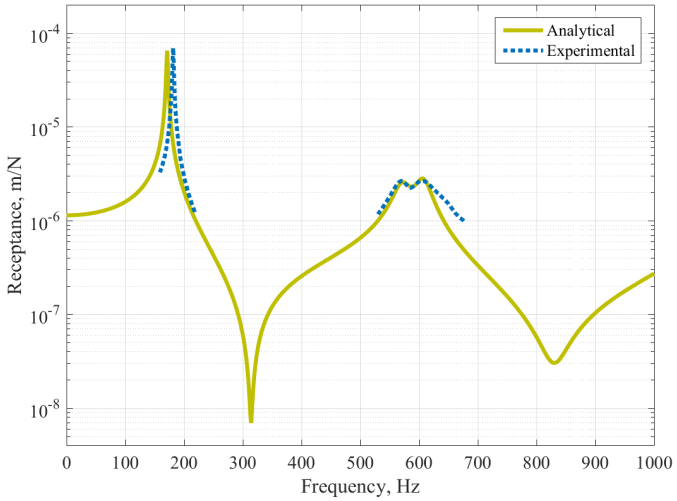

(b)

Figure 3.71: Comparisons of the receptance of the beam (a) a static compression of 6% (b) a static compression of 40%

Figure 3.71 indicates that the proposed analytical model works well generally for targeted modes. Close examination suggested that this numerical model over-estimates the resonance of the 2nd mode of this beam. One possible reason is the absence of nonlinear element in this analytic model. To evaluate the type of the

nonlinearity, random forces with three different root-mean-squared magnitudes were used to drive the beam.

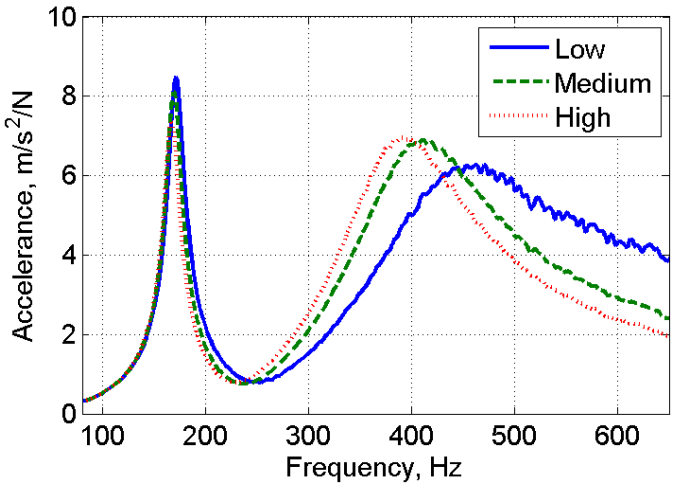

(a)

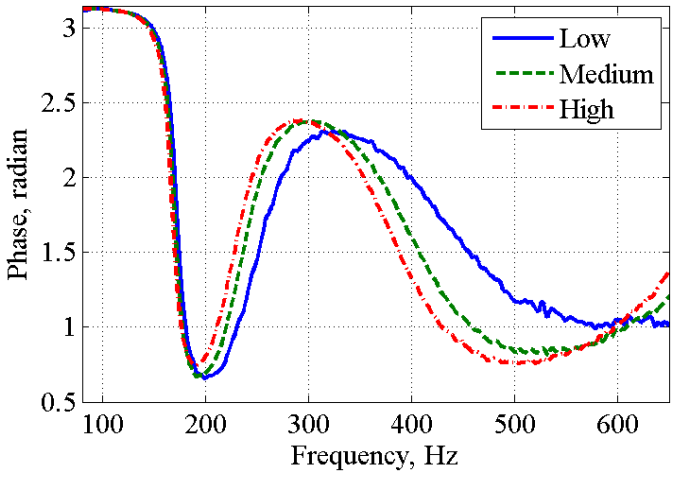

(b)

Figure 3.72: Comparisons of the accelerances of the beam when subjected to different excitation levels (a) Magnitude (b) Phase (static compression of the O-ring = 0.32 mm)

Figure 3.72 demonstrates the displacement-dependent nonlinearity for the 2nd mode. With the increase of the dynamic excitations, the resonance frequencies of

this mode drops significantly. However, the relative displacements at the position where the TMD was attached were not uniform over the selected frequency ranges due to the involvement of the low resonance components. Thus, controlled stepped harmonic excitations were used for 2nd mode.

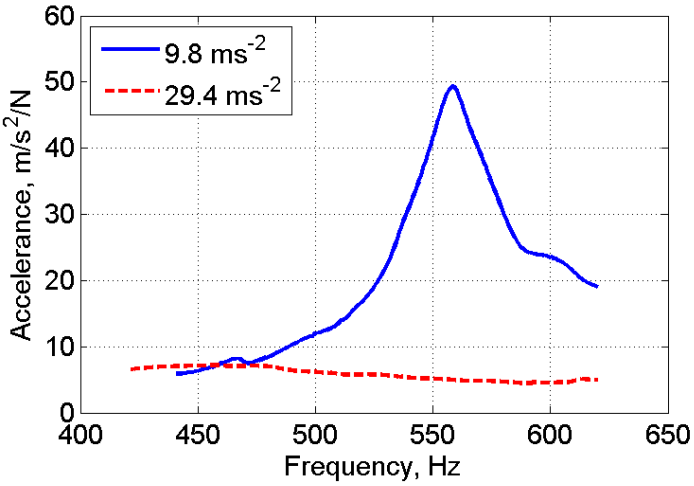

(a)

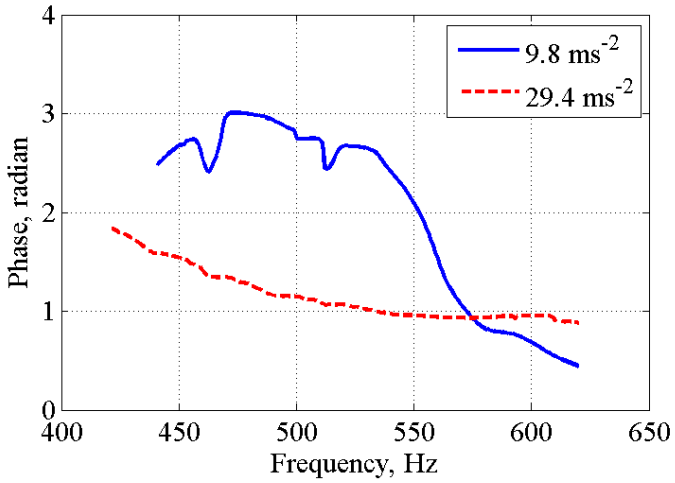

(b)

Figure 3.73: Comparisons of the accelerances of the beam for 2nd mode when subjected to different dynamic amplitudes (a) Magnitude (b) Phase (static compression of the O-ring = 0.32 mm)

It can be seen from Figure 3.73 that both resonance peak and natural frequency for the 2nd mode reduces with increase of excitation levels. Besides, a relative flat peak can be observed when the acceleration at selected point is approximately 29.4 ms^{-2}. It can be interpret the existence of the frictional damping. Also, the softening for the first mode can be observed due to the underestimation of the modulus of the material. Nevertheless, the analytical model can still predict the resonance peak with reasonable accuracy.

3.7.5 Summary

In this section, the performance of the proposed TMD on a hollow beam was evaluated and predicted using a mixed analytical and finite element model. The experiments showed that this damper could suppress the selected vibration modes with different static compressions. Additionally, the proposed models could represent the practical performance of this damper with reasonable accuracy.

3.8 Conclusion

In this chapter, the adjustable TMD incorporating the elastomeric O-rings, produced from commonly used materials, was shown to extend the classic TMD to a multi-mode, multi-directional energy dissipation device. This device aims for vibration suppression of the mechanical structure over a wider frequency range. This TMD was attached on a typical engineering structure - rubber-ended beam, and is able to tune the targeted vibration at selected compressions.

The stiffness and damping of the elastomeric O-rings when subject to different elastomers, static compressions, dynamic amplitudes and excitation frequencies were investigated. It has been shown that the damping of this component is relatively uniform, while the stiffness, however, is strongly affected by the static compression. Since the static compression has a greater influence on the elasticity of the O-ring than dynamic displacements, only static compression-dependent stiffness was investigated and modelled in this study.

A modification to the modelling of the load-deflection relationship for the elastomeric O-rings in the tensile-compressive direction was introduced, which improves the accuracy, especially when subject to low static compression. By introducing the shape factor of the O-ring, reasonable accurate analytical expression for the stiffness in the shear and tilting directions, when subject to a given static pre-compression, have been developed.

A novel experimental rig was developed to obtain the shear and rocking stiffness of the O-ring at a certain static pre-compression, using the resonance frequencies of the rigid body modes, and, hence the difficulty in obtaining proper interfacial boundary conditions between the O-rings and restricting plates was avoided. Excellent agreement of the shear and rocking stiffness between the analytical model and experimental results was achieved.

Numerical models of this adjustable TMD were developed using the finite element modal approach. This numerical model was shown to be able to estimate the stiffness of the O-rings. Furthermore, this numerical model is able to deal with O-rings with an irregular cross-sectional shape, for example X-shape cross-section.

Modelling of this adjustable TMD on a low loss polymer isolated beam was developed with reasonable accuracy, especially for the modes that the TMD was targeting. It has been shown that the cross-coupling between the two working modes of the TMD can be neglected, when subject to low amplitude vibration.

Although this TMD has been shown effective for adjustable tuning, some limitations are still to be resolved. The details of these restrictions and their potential solutions are listed below,

- The cross-sectional diameter of the O-rings used in the current device is too small, so that the mechanical adjustment of the static compression is inaccurate. When assembling this TMD, the misalignments of the O-rings can be observed. Under these conditions, the additional working modes of the TMD may interact with the host structure.

- For the analytical stiffness model of the O-ring in tension-compression, the influence of nominal diameter expansions of the O-rings is explained using

a high-order experimental fitting term. The fitting coefficients are not the same for the different contact conditions, and therefore may have a great influence on the prediction of the stiffness using the proposed semi-empirical model. Meanwhile, slight difference for this model damping model exists, especially when static compression of the O-ring is not in a moderate level.

- In the current study, this optimal frequency is assumed to be equal to the resonance frequency of the host structure with mass of the TMD. The estimation of effective mass of the beam is inaccurate, which leads to the inaccurate design of the TMD. Since the mode shape of the host structure is affected by the configurations of the proposed TMD (including natural frequency and damping), the optimal tuning frequency of this device need to be chosen using iterative process.

- Two working modes of this TMD exist in a given direction. Under some conditions, both two modes works for multiple modes of the host structure, and the design criteria including optimal resonance frequencies and damping of the TMD is not fully developed in the current study.

- The existence of the interface frictions between the proposed TMD and host engineering structures made the tuning capability of this devices improved, especially when subjected to random excitations. However, the influence of these frictions are difficult to predict in the developed analytical/numerical model, especially under the random excitations.

Although this polymeric TMD can work well in the room temperature, its performance will degrade at an extreme high temperature. One alternative is to use a kind of material that can both work with high temperature and have the adjustable stiffness and uniform damping. In the next chapter, one innovative material, Tangled Metal Wire particles, was used as the elastic components of this type of TMD.

Chapter 4

Adjustable Tuned Mass Damper using Tangled Metal Wire Particles

4.1 Introduction

The previous chapter demonstrated the effectiveness of a novel Tuned Mass Damper (TMD) incorporating elastomeric O-rings in suppressing the multiple-mode vibration of a typical flexible structure. One limiting factor for this device is that elastomers have a limited range with regard to temperature. Few TMDs have been proposed for vibration suppression at high temperatures. This chapter reports the investigation of a novel concept TMD using a recent innovation – Tangled Metal Wire (TMW) particles.

TMW, also called metal rubber or metal mesh, is a porous material formed by compressing helical wires together in a mould. Several studies [12, 14] reported that the TMW devices display strain-dependent nonlinear stiffness and provide damping of a similar level to that of a typical elastomer. The microstructure involves many, closely spaced, wire-to-wire contacts. The stiffness is affected by the typical length of the wire segments between contacts, while the damping arises

from dry friction generated at the contact points [36]. Some loss also occurs from plastic deformation within the wires and at contact points [13]. Most investigations of TMW involve cylinerical blocks where the stiffness and damping change only slightly with repeatedly applied loads. However, because TMW blocks have a relatively high stiffness, the corresponding mass of an optimal TMD would need to be high: the mass required to set the TMD natural frequency close to that of a typical mechanical sturcutre would approach the mass of the structure itself making the system inefficient. The alternative use of this TMW material is in particle form. TMW particles have a lower stiffness than the TMW blocks. Meanwhile, quasi-static experiments for TMW particles [13] have shown that a medium energy loss is achieved over a wide frequency and temperature range. Therefore, TMW particles have shown their potential to work as an elastic and damping medium for this adjustable TMD.

This chapter focuses on the evaluation of the TMD using TMW particles. The damping mechanism in terms of microstructure properties was investigated for single particles. The mechanical similarity of different particles has also been evaluated. The nominal properties of a collection of TMW particles were then investigated. These particles and restricting mass were then assembled as a novel Tuned Mass damper and the adjustable stiffness and damping of this device was investigated. This TMD was finally attached to the low-loss hollow beam used in Chapter 3 to demonstrate the effectiveness of this device.

4.2 Experimental investigations of individual TMW particles

The tangled metal wire particles, constructed from stainless steel, are shown in Figure 4.1. The properties of individual particles vary as they are fabricated manually. Typically, the TWM particles comprise metal wire formed into a sphere-like structure with diameter of 4 to 5 mm.

In the experiments reported here, the wire diameter used for the TMW is

Figure 4.1: Tangled wire metal granular material

0.12 mm. The average individual mass of these particles is 0.06 g and the mean diameter of the particles is 4.65 mm.

4.2.1 Dynamic compressive tests

Dynamic tests were carried out on different TMW particles using the Metravib Viscoanalyser machine, as shown in Figure 3.10. A pre-compression of 0.3 mm was applied to the TMW particles and the excitation frequency was 2.5 Hz. Since the stiffness of the TMW particle changes with loading history, dynamic strain rather than force was chosen as the control indicator. In this work, the peak-to-peak dynamic displacement was set to 0.1 mm. Fifty different TMW particles

were used in this work to identify the variation of energy loss and elasticity of individual particles.

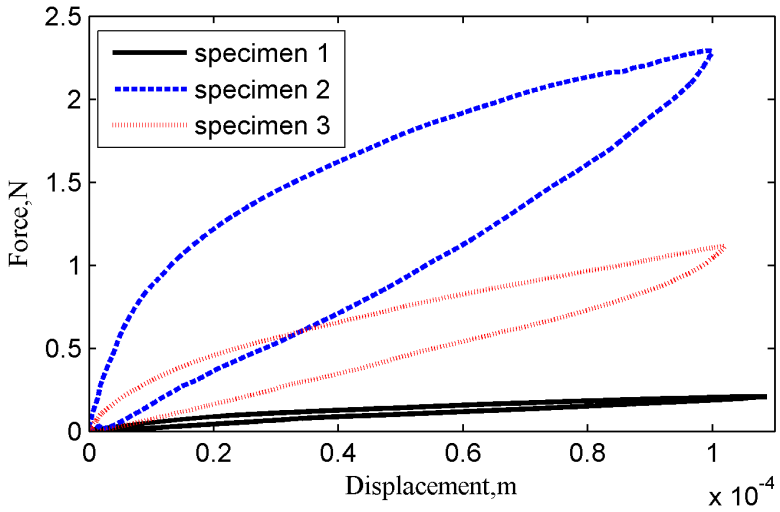

Figure 4.2: Typical hysteresis loops for three different TMW particles

The typical hysteresis loops for three different TMW specimens are shown in Figure 4.2 where it can be seen that the energy dissipation and average stiffness vary significantly for different particles. Generally, the TMW particles display high energy dissipation levels regardless of the variation of individual particles. A detailed picture of the variation of these characteristics with different particles is presented in Figure 4.3.

Close examination of Figure 4.3 reveals that energy loss for the single particle has no obvious correlation to stiffness. To illustrate the effect of the microstructure on energy dissipation, the relationship between stiffness and dissipated energy is shown in Figure 4.4.

With increase of the stiffness, the dissipated energy has an upward trend generally. One probable reason for this variation of stiffness in TMW particles is the geometry uncertainties of particles in the manufacturing stage. High stiffness of the TMW particle can be achieved when high local shape change, caused by plastic deformation, and friction between internal wires in this particle occurs.

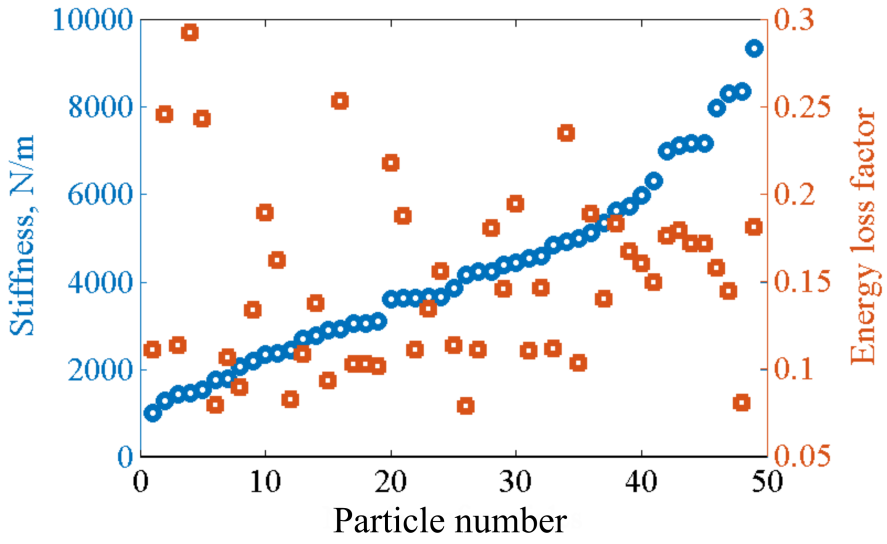

Figure 4.3: Stiffness and damping for fifty different TMW particles (blue circle refers to stiffness and red square refers to energy loss factor)

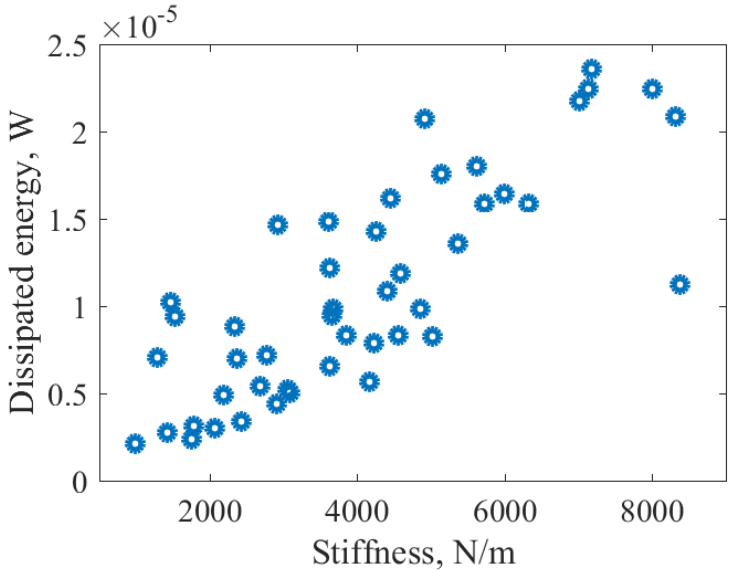

Figure 4.4: Relationship between stiffness and dissipated energy for single partiles

The dissipated energy for a stiff particle is generally higher than in the case of a more flexible particle while the overall strain energy of one particle is much more

sensitive to the stiffness of the particles. As a result, there is considerable scatter in the loss factor for different samples.

At given stiffness, the energy dissipation is still not uniform for different particles due to the inconsistent and changeable nature of the microstructure of the TMW particles. When calculating the density of the TMW particles, these particles were assumed to be perfect spheres. The diameter of these particles was taken as the average derived from three different measurements. The relationship between the density of the particles and the stiffness is shown in Figure 4.5

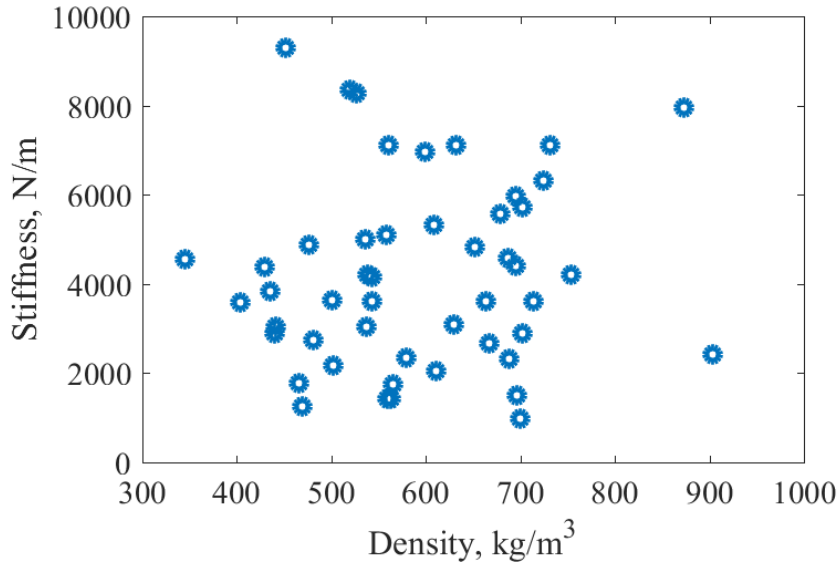

Figure 4.5: Relationship between the stiffness and equivalent density for single partiles

Figure 4.5 indicates that despite the particles being of similar stiffness, there is still some variation in the number of internal contacts. Therefore, the stiffness and damping of this kind of particles is almost impossible to predict using its geometric properties.

Since the dynamic characteristics are greatly influenced by the micro-structure, the effect of cyclic loading on a single particle was investigated using dynamic compressive tests.

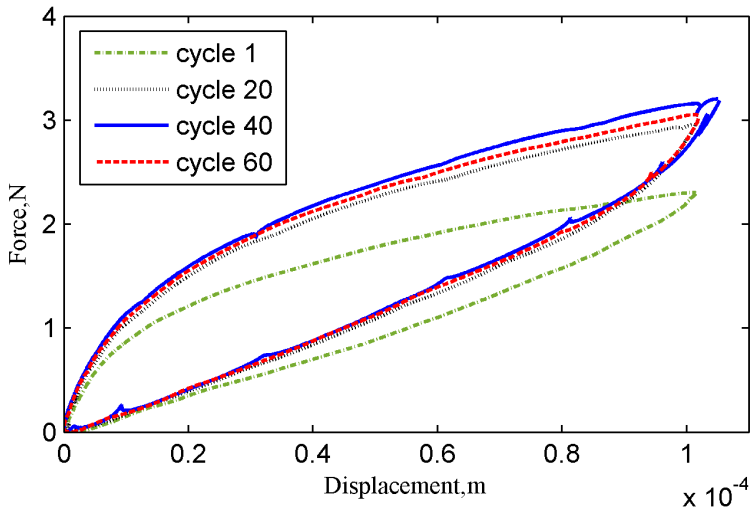

Figure 4.6: Typical hysteresis loop of one particle under cyclic loading

Figure 4.6 demonstrates that the stiffness and damping of this TMW particle changed slightly with the number of loading cycles undergone. The probable explanation is as follows. Initially, most of the wires were not interacting with each other during each loading cycle, wires came into and then out of contact. The structure altered somewhat during repeated cycling such that some inelastic deformation took place in the wires and some contacts became 'frozen' in place. After a number of cycles, these processes stabilised, and, therefore, the dynamic properties (e.g. loss factor, dynamic stiffness) tended to reach equilibrium. The stiffness and damping of this particle against a long excitation history can be seen in Figure 4.7.

It can be seen in Figure 4.7 that the stiffness and damping of the particle studied reached a steady state after approximately 500 cycles. It is interesting to note that this trend did not hold as the test continued. Instead, a number of jumps to different 'steady-state' conditions can be seen. One possible reason is that the particle rotated due to the friction between the restricting plates and itself. In this situation, the load distributions between wires inside this particle would change resulting in a different configuration. Since the stiffness increases at a higher rate than the damping, the energy loss factor drops correspondingly.

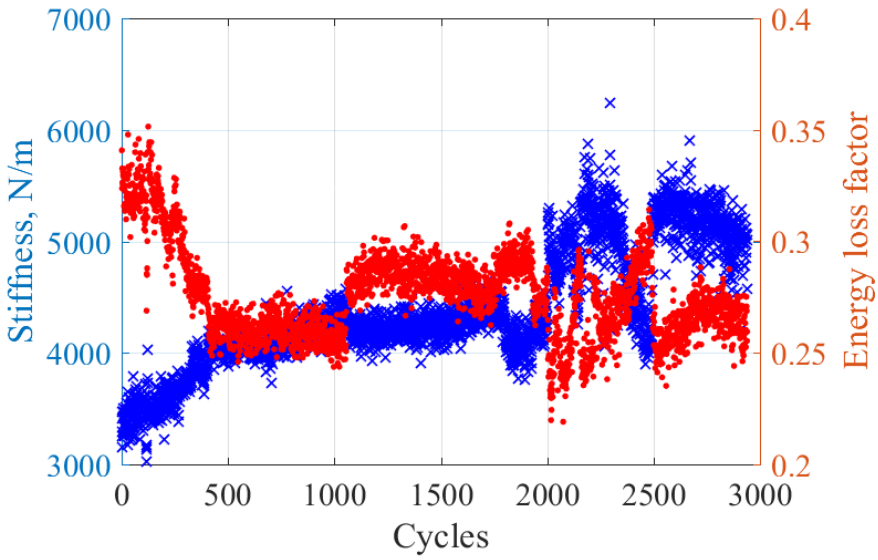

Figure 4.7: Effect of load cycle on dynamic properties of a TMW particle

The sensitivity of the single particles to the static compression was then investigated and the results are shown in Figure 4.8.

Generally, the stiffness and damping increase significantly with static compression, especially in the region of low static compressions. With increasing the static compression, a higher number of internal contact points lead to a rapid rise in the stiffness. An increase of the friction results in a higher energy dissipation, while the overall strain energy increases as well. Minor variations can be found for energy loss factor when the static compression is higher than 25% of its original height.

Overall, it can be concluded that TWM particles, although friction dominated, might be treated as a kind of hysteretic medium with nominal loss factor is no less than 20%. Since the TMW particles experiences relatively low compressions at elevated frequencies in practical damping devices, investigation of energy dissipation of TWM particles under these conditions was thought to be important. Since the strain caused by the impact from a given height is small, drop-rebound tests were carried out to identify damping from individual particles subject to low strain.

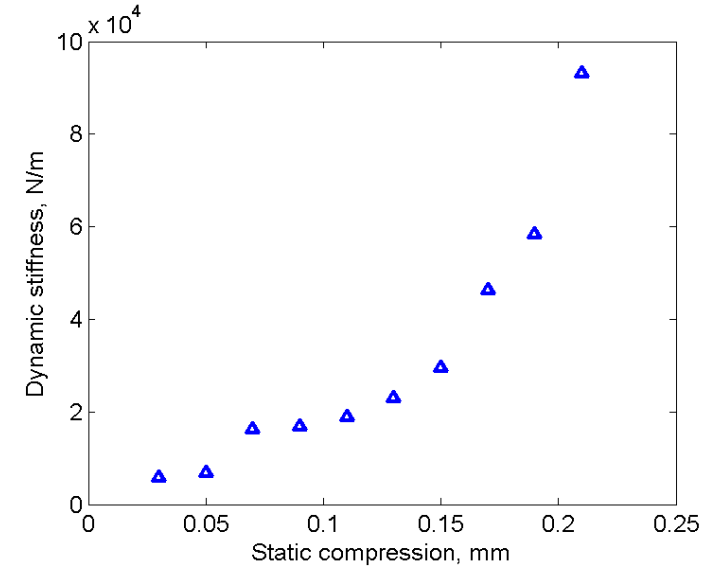

(a)

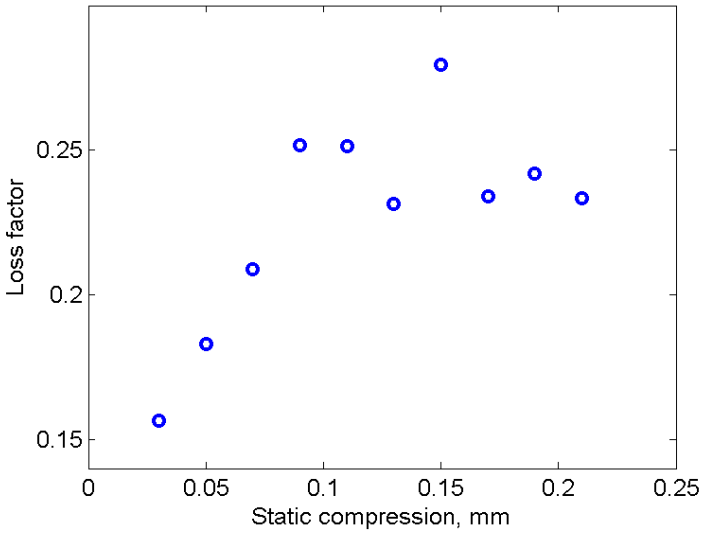

(b)

Figure 4.8: Effect of the static compression on single TMW particle (a) Stiffness (b) Damping

4.2.2 Drop-rebound tests

4.2.2.1 Methodology

In this section, a brief introduction to the estimation of the damping associated with individual particles using the drop-rebound test is provided. Detailed derivatives can be found in Nagurka's work. [99]. Assuming that the individual particle is a SDOF mass-spring-viscous damping system, during the whole drop-rebound procedure, the aerodynamic effect is negligible as the maximum velocity of the particle is low. A schematic presentation of one full cycle is shown in Figure 4.9.

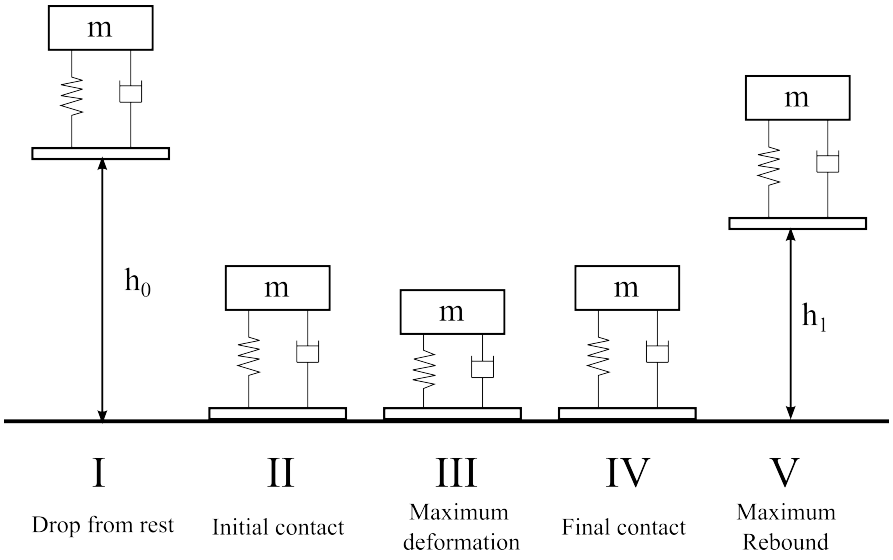

Figure 4.9: Schematic figure of a particle showing impact at the first bounce

Note that h_0 refers to the initial height on release of the particles and h_1 is the first rebound height. The displacement history of the first few bounces is shown in Figure 4.10

When the particle contacts the ground initially, as shown in stage II to IV of Figure 4.9, the full cycle of deformation-restitution can be observed. In this stage, the Equation of Motion of a particle can be described as,

$$m_p\ddot{x} + k_p x + c_p\dot{x} = -m_p g \tag{4.1}$$

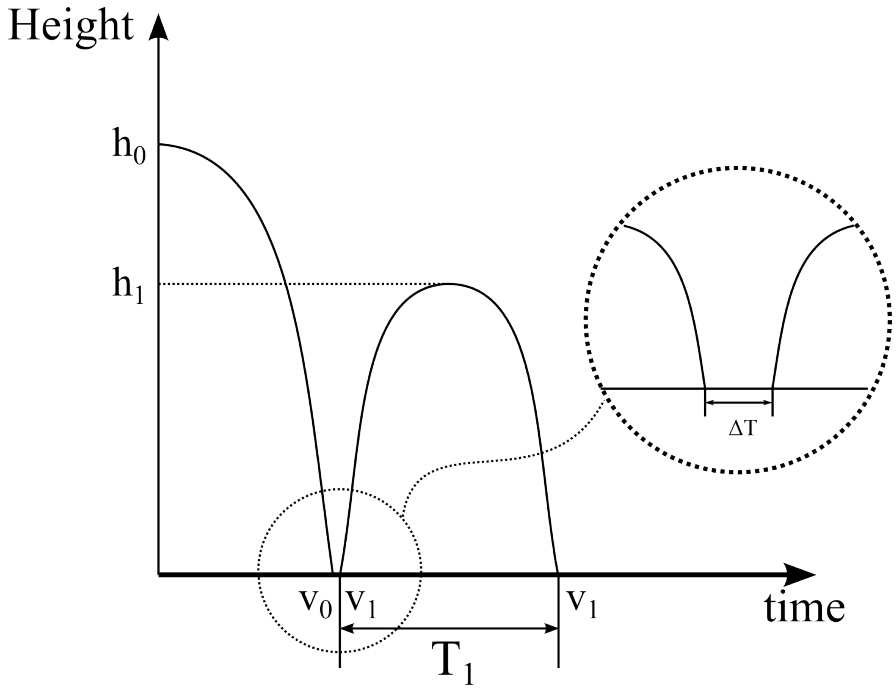

Figure 4.10: Bounce history showing displacement and time

where m_p is the mass of the individual particle, k_p is the average stiffness and c_p is equivalent damping coefficient. Once the particle touches the ground, the initial displacement and velocity are $x(0) = 0$ and $\dot{x}(0) = -v_0$, respectively. By solving Equation 4.1, the displacement of the particle can be given by,

$$x(t) = \exp(-\frac{c_p}{2m_p}t)\left[\frac{c_p g - 2k_p v_0}{2k_p\omega_d}\sin\omega_d t + \frac{m_p g}{k_p}\cos\omega_d t\right] - \frac{m_p g}{k_p} \tag{4.2}$$

where ω_d is the damped natural frequency. After re-arrangement, this displacement is,

$$\begin{aligned} x(t) = &-\frac{v_0}{\omega_d}\exp\left(-\frac{c_p}{2m_p}t\right)\sin\omega_d t \\ &-\frac{m_p g}{k_p}\left[1 - \exp\left(-\frac{c_p}{2m_p}t\right)\left(\cos\omega_d t + \frac{c_p}{2m_p\omega_d}\sin\omega_d t\right)\right] \end{aligned} \tag{4.3}$$

In the work done here, the fundamental resonant frequency of a single particle is greater than 1000 Hz. [13] The initial velocity of one particle is smaller than 3

m/s. It is easily shown through the following relations,

$$\left|\frac{m_p g}{k_p}\right| \ll \left|\frac{v_0}{\omega_d}\right| \tag{4.4}$$

Using Equation 4.4, the displacement during the contact can be simplified into,

$$x(t) = -\frac{v_0}{\omega_d} \exp\left(-\frac{c_p}{2m_p} t\right) \sin \omega_d t \tag{4.5}$$

It was assumed that the local deflection of the TMW particles is negligible with initial height. This behaviour can be represented analytically,

$$x(\Delta t) = 0 \tag{4.6}$$

where Δt is the contact time of the particle and is illustrated in Figure 4.10. Mathematically, the contact time can be obtained by substituting Equation 4.6 into 4.5.

$$\Delta t = \frac{\pi}{\omega_d} \tag{4.7}$$

Substituting Equation 4.7 into Equation 4.5, the initial post-impact velocity at the first bounce is then represented as,

$$\dot{x}_1 = \dot{x}(\Delta t) = \dot{x}_0 \exp\left(-\frac{c_p \Delta t}{2m_p}\right) \tag{4.8}$$

The coefficient of restitution is defined as,

$$\varepsilon_p = \frac{\dot{x}_1}{\dot{x}_0} \tag{4.9}$$

Combining Equation 4.8 and 4.9, the damping coefficient can be given by,

$$c_p = -\frac{2m_p \omega_d \ln \varepsilon_p}{\pi} \tag{4.10}$$

Using the definition of the damped natural frequency, Equation 4.10 and 4.6, the stiffness, k_p, can be represented as,

$$k_p = m_p \left(\frac{\pi}{\Delta t}\right)^2 \left[1 + \left(\frac{\ln \varepsilon}{\pi}\right)^2\right] \tag{4.11}$$

The equivalent damping ratio is then obtained using,

$$\begin{aligned}\zeta_p &= \frac{c_p}{2\sqrt{k_p m_p}} \\ &= \frac{-\ln \varepsilon_p}{\pi}\left[1+\left(\frac{\ln \varepsilon_p}{\pi}\right)^2\right]^{-1/2}\end{aligned} \tag{4.12}$$

Since the TMW particle has an irregular shape, the stiffness in different directions can vary. When this type of particle hits the metal table, the reaction force is not perpendicular to the table surface. This leads to some particle rotation in the rebound, and hence some potential energy converted into rotational energy. To consider this rotational kinetic energy, the coefficient of restitution was modified. The approaches used by Stronger [100, 101] give,

$$\varepsilon_p = \sqrt{\frac{\text{Kinetic energy before collision}}{\text{Kinetic energy after collision}}} = \sqrt{\frac{{}^1\!/\!_2 m_p {v_0}^2}{{}^1\!/\!_2 J_p \dot{\theta}^2 + {}^1\!/\!_2 m_p \left({v_1}^2/2\right)}} \tag{4.13}$$

where ε_p refers to the energetic coefficient of restitution. Using energy conservation before collision, the kinetic energy can be represented as,

$${}^1\!/\!_2 m_p {v_0}^2 = m_p g h_0 \tag{4.14}$$

At the highest rebound point, the linear velocity of the particle is eliminated. Since the rotation of the particle is caused by the irregular contact surface, it is reasonable to assume that the rotation of the particle before collision is negligible. Using the definition of the velocity, the restitution time can obtained using,

$$v_1 = \frac{g T_1}{2} \tag{4.15}$$

Substituting Equations 4.15 and 4.14 into Equation 4.13, the coefficient of restitution can be represented as,

$$\varepsilon_p = \sqrt{\frac{{}^1\!/\!_2 m_p g h_0}{{}^1\!/\!_2 J_p \dot{\theta}^2 + {}^1\!/\!_2 m_p \left({}^{gT_1}\!/\!_2\right)}} \tag{4.16}$$

where J_p is the mass moment of inertia of particles. If the TMW particles are assumed to be a solid sphere, the rotational inertia is then given by,

$$J_p = \frac{2}{5} m_p r_p^2 \tag{4.17}$$

in which r_p is the equivalent radius of the particle. Combining Equation 4.12, 4.16 and 4.17, the damping of the individual particles can be estimated when the physical properties, initial height, rotation speed and first rebound duration of this particle are known.

4.2.2.2 Experiment Investigations

The drop test, whose test rig is shown in Figure 4.11, aims to identify the energy loss of TMW particles when they impact a rigid wall.

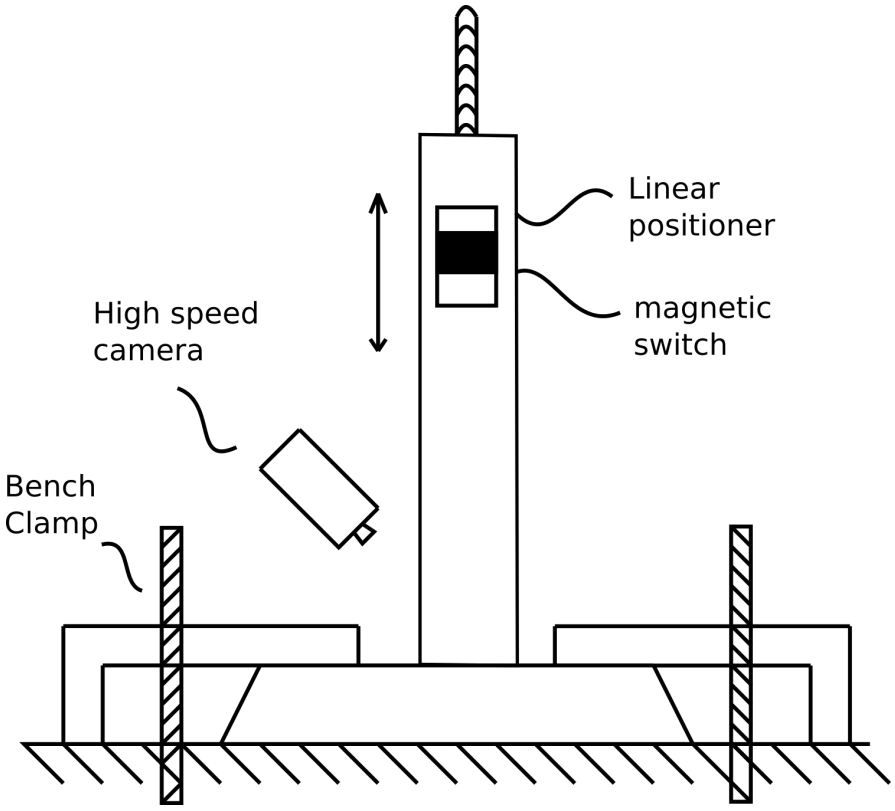

Figure 4.11: Drop test rig using high speed camera and magnetic switch

Energetic coefficient of restitution (defined in Equation 4.13) was used as an indicator because the nominal loss factor of the particle is directly linked to it. To hold the TMW particle at a specific height, a magnetic switch was used. Once the particles were placed on the switch, the linear positioner was adjusted to suitable height to gain accurate initial height, and hence collision velocity. A high speed camera was placed in front of the linear positioner to capture the trace of the TMW particle. The video was captured at 1400 fps in a 512 x 512 resolution area. One floor light was used to minimise the presence of shadows and provide enough light for the image capturing. For each drop height, experiments were carried out 3 times to ascertain repeatability. The rebound time is calculated using,

$$T_1 = f\Delta \tag{4.18}$$

where f is the sampling frequency of the camera, and Δ is the number of frames counted from the start to the peak of rebound. The particle rotation speed is estimated using the count of the cycle numbers during the first bounce. Since the shape of a TMW particle is irregular, one unique position can be observed to track the rotation at the end of micro-helical wires in a TMW particle.

A typical high speed image is shown in Figure 4.12.

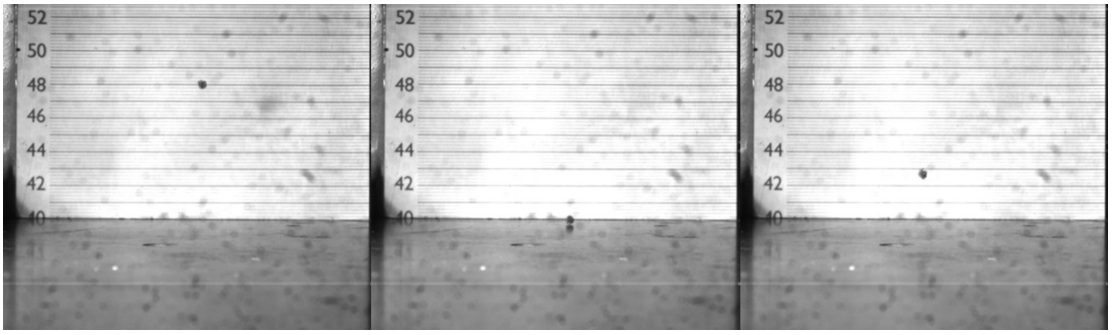

Figure 4.12: Typical image of high speed camera (left: frame 242 middle: frame 293 right: frame 363)

Since the TMW particle has an irregular shape, the first bounce height was not necessarily the same for repeated tests. As a result, the stiffness in different

directions is somewhat non-uniform, and the rotation of the particle is activated during the rebound. In order to identify the significance of the rotations of the particles, comparisons of the linear and rotational kinetic energy during the rebound is shown in Table 4.1. These kinetic energy can be estimated using Equation 4.13. The detailed experimental results are shown in Appendix E.

Collision velocity, m/s	2	1.8	1.6	1.4	1.2	1	0.8
Rotational speed, rad/s	41.84	24.71	51.9	40.57	41.87	79.38	46.27
Rotational kinetic energy, W	0.01	0.01	0.01	0.01	0.01	0.02	0.01
Translational kinetic energy, W	1.97	1.80	1.12	1.01	0.58	0.10	0.22

Table 4.1: Comparisons of the rotational and translational kinetic energy

Note that the average values of three measurements were used in this table. It can be seen that the rotation becomes more significant when subjected to high collision velocity. Therefore, Equation 4.16 was used to calculate the coefficient of the restitution, and therefore the energy loss factor.

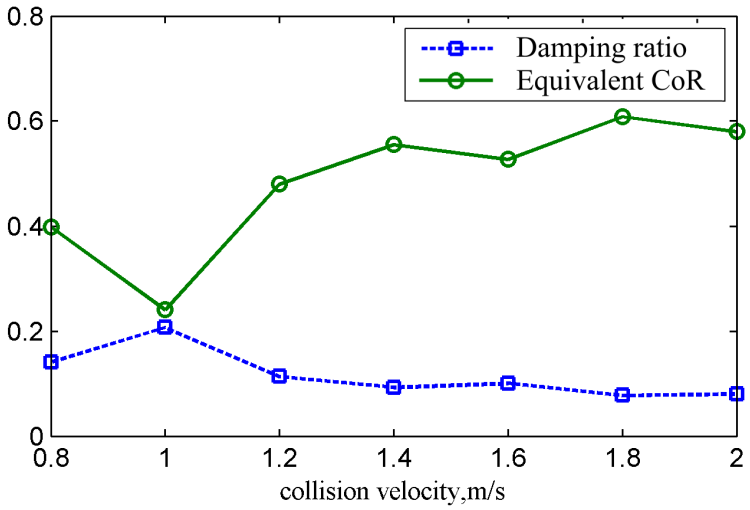

Figure 4.13: Loss factor and Coefficient of Restitution against collision velocity

The loss factor and coefficient of restitution against initial collision velocity are shown in Figure 4.13 where it can be concluded that the average loss factor

for this particle is approximately 0.15, which is somewhat lower than the value of 0.2 obtained from Visco-analyser. This is understandable as the dynamic strain for the drop test is much lower than that in the Visco-analyser. The number of contacts in the TMW particles is far fewer when the dynamic strain is low.

In practice, TMW particles are usually not exposed to high dynamic strain, and thus, the reasonably good damping capability for this type of particle under low strain has expanded the applications of these particles. Typical applications can include the low wave-speed medium or the elastic components for a Tuned Mass Damper.

4.3 Nominal properties of a collection of TMW particles

The previous section has shown that the stiffness and damping of a single particle is somewhat difficult to predict because of the poor repeatability coming from fabrication. It was expected that a collection of particles could average out these uncertainties. In this section, the nominal properties of a collection of TMW particles are investigated.

4.3.1 TMW particles subject to high dynamic strain

Dynamic compressive testing is a direct approach to investigate the stiffness and damping subject to different loading conditions. The Viscoanalyser, whose loading configurations are shown in Figure 3.10, was used to obtain the hysteresis of these sets of particles. In order to hold a collection of particles, a hollow cylindrical cavity with an inner diameter of 38 mm was designed and attached to the lower restricting plate of the machine. Considering the inner diameter of the cavity and the arrangement of the particles, each layer has approximately 34 particles. In these investigations, the excitation frequency was 2.5 Hz based on the limitations of the machine.

4.3.1.1 One layer of TMW particles

Initially, the repeatability of one layer of the TMW particles was investigated. This section reports experiments aiming to evaluate the extent to which collections of TMW particles reduce the level of uncertainty. Figure 4.14 shows the variation of the stiffness and damping for three different sets of particles. The mass of each set of specimens is shown in these figures. The average number of particles is approximately 34 and these particles only fill one layer of this cavity. In use, the dynamic strain for the TMW particles was expected to be low, and therefore static and dynamic displacements of 0.3 and 0.05 mm respectively were chosen.

It can be seen from Figure 4.14 that the stiffness and damping for the same collection of particles does not vary with time. However, no obvious correlation appears to exist between the dynamic characteristics and different samples. One explanation is the relatively small number of particles. Additionally, controllability of the static compression was difficult to achieve as TMW particles are sensitive to static compression. Even a tiny deformation results in a sharp stiffening. Therefore, experiments were repeated using three layers of particles.

4.3.1.2 Three layers of TMW particles

In this section, variations caused by the different three layer samples of TMW particles were investigated first. Note that the selected static compression of the three layer particles was 0.5 mm. The peak-to-peak dynamic amplitude of excitation was 0.05mm and the excitation frequency was 2.5 Hz. The results are shown in Figure 4.15.

Figure 4.15 indicates that more consistent values of stiffness can be obtained when a number of TMW particles is present. However, the collection of particles was still not enough to average out the uncertainty completely. In practice, the TMW particles are much more suitable to work as high loss fillers when being applied to engineering structures, as this kind of energy dissipation device is not particularly sensitive to the stiffness variations. The other possible application of these particles is the adjustable TMD.

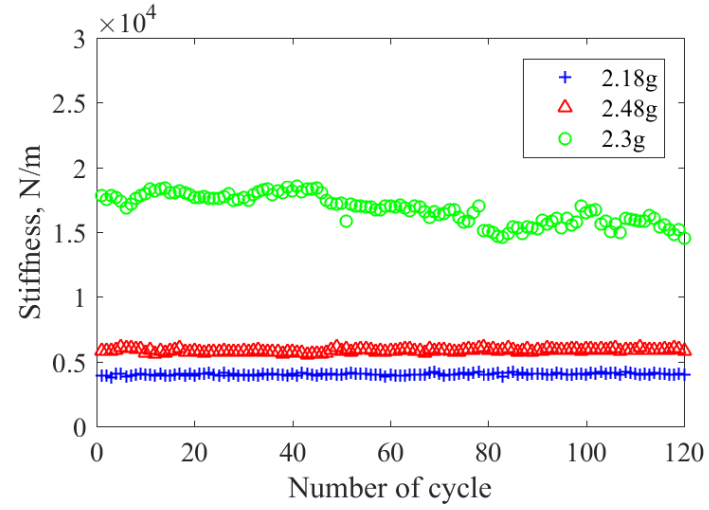

(a)

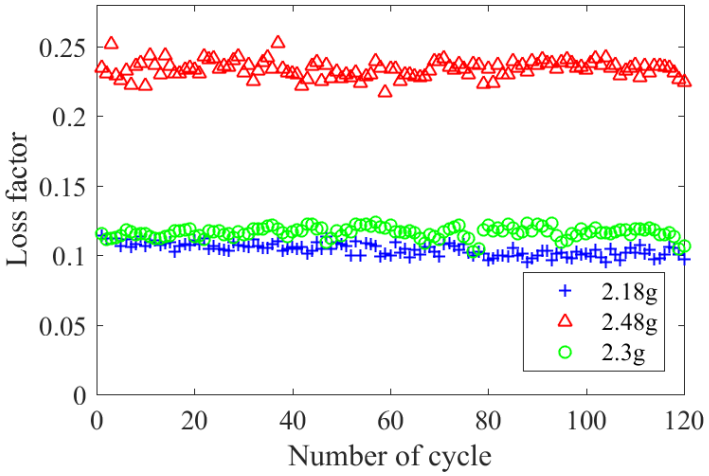

(b)

Figure 4.14: Repeatability of one layer of TMW particles (a) stiffness (b) damping (Note that the mass is used as an indicator to demonstrate different sets of samples.)

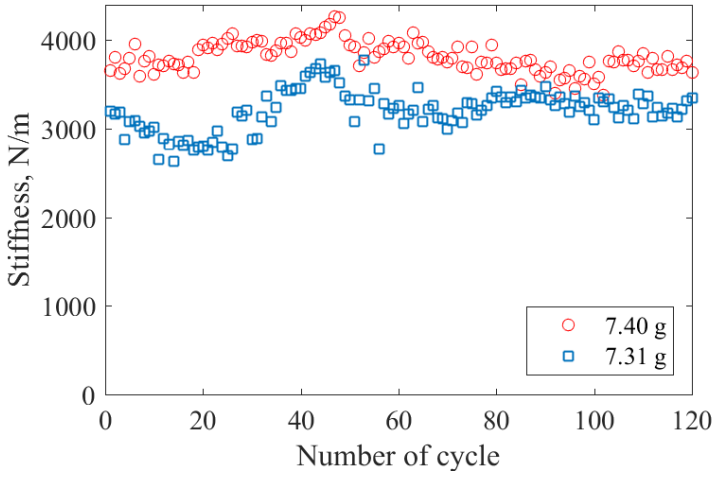

(a)

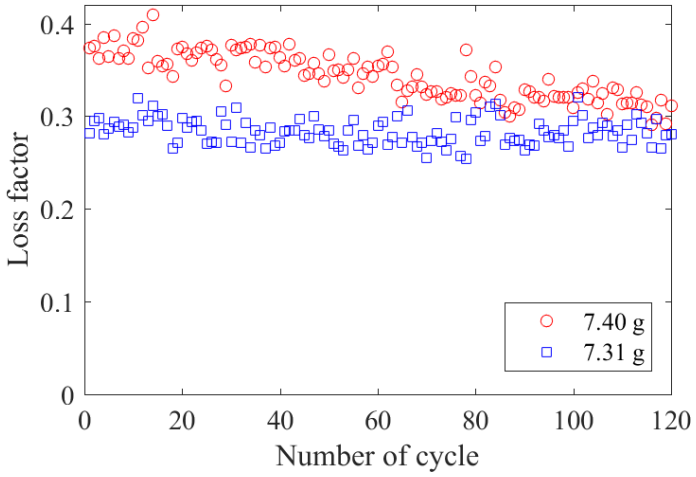

(b)

Figure 4.15: Repeatability of three layers of TMW particles (a) stiffness (b) damping (Note that the mass is used as an indicator to represent different sets of samples.)

To investigate its feasibility to assemble this type of TMD, the effect of the static compression was then evaluated. Three layers of the TMW particles were chosen in this instance, as this would provide sufficient height allowing accurate adjustments to be made to the static compression. Six different static compressions - 0.5 mm, 0.9 mm, 1.3 mm, 1.7 mm, 2.1 mm and 2.5 mm - were used. To access the shape of hysteresis loop, the reaction force was normalised by dividing the maximum compressive force in each case. The force-normalised hysteresis loops used to evaluate the damping mechanism from different densities of the same collection of particles, is shown in Figure 4.16.

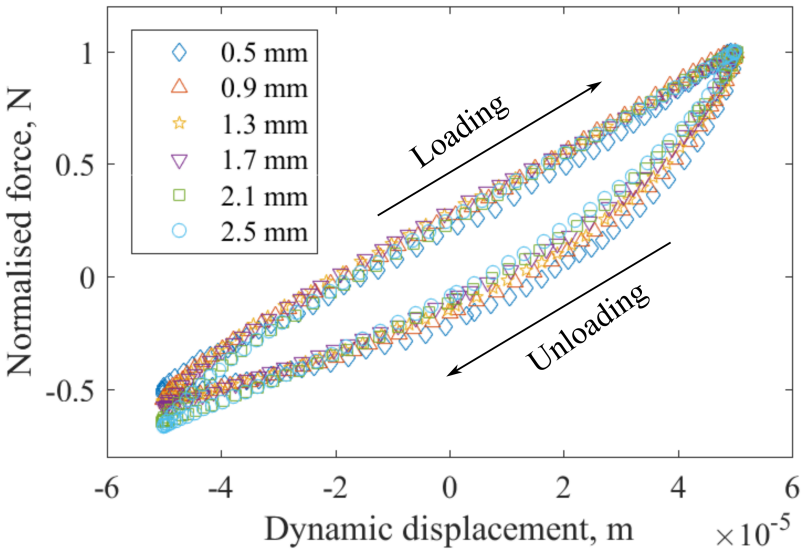

Figure 4.16: Normalised hysteresis loop for three layers of TMW particles

It can be seen from Figure 4.16 that the shape of the hysteresis loop remains the same, although the static compression is different. The softening during unloading can be observed clearly to low static compression as the particles fill the cavity relatively loosely. More friction and less stored strain energy can be obtained, and therefore a high energy loss factor can be observed in these situations. The variations in the stiffness and damping subject to different static compressions is shown in Figure 4.17.

Figure 4.17 indicates that the stiffness of this collection of particles can increase

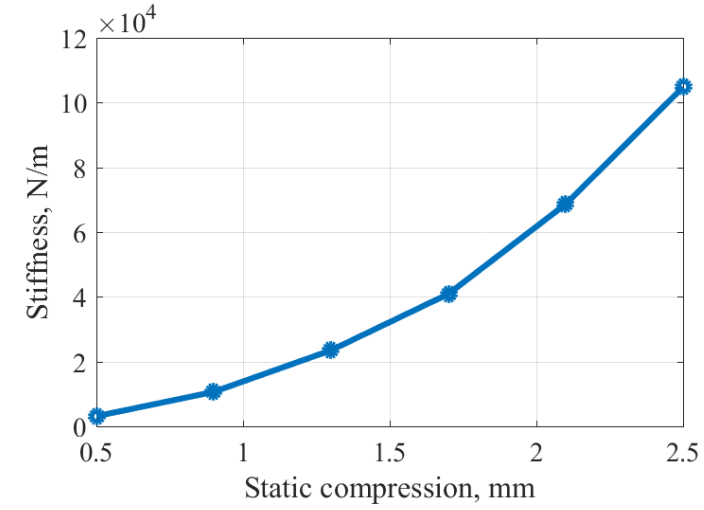

(a)

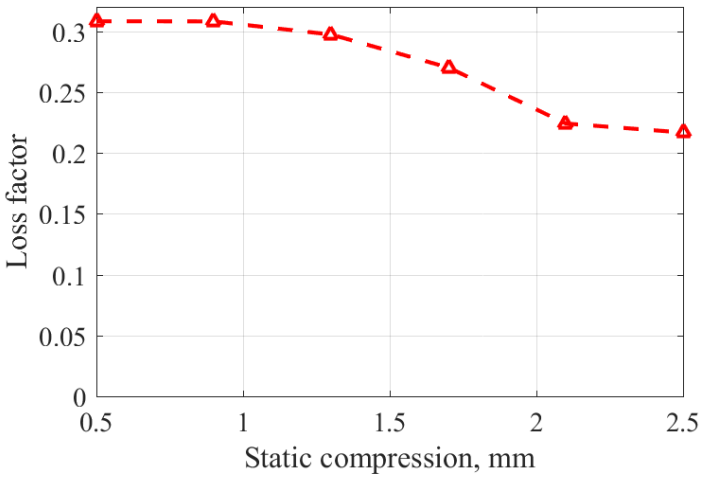

(b)

Figure 4.17: Nonlinear stiffness and damping of three layers of TMW particles subject to different static compressions (a) stiffness (b) damping

up to 30 times when the pre-strain rises from 3 % to 16 %. The energy loss factor drops from 0.3 to 0.2 due to the resulting rise in stored energy. Nevertheless, the damping of these particles is still in the working range of an adjustable TMD.

4.3.2 TMW particles subject to low strain

Since the dynamic displacement of the proof mass for a TMD used in a mechanical structure is generally low, the performance of the TMW particles, when subjected to low strains, was investigated using the concept of particle damper.

4.3.2.1 TMW particle damper

A particle damper was introduced to evaluate the performance of these TMW particles subject to very low excitations. A typical example of this type of particle damper is shown in Figure 4.18. A Perspex cylinder cavity was used to contain the TMW particles. The transparent material allowed movement between particles to be seen when the structure was shaken. A threaded cap was used to control the static pressure on the particles.

Figure 4.18: Typical tangled wire metal particle damper

The details on the cavity of the TMW particle damper are shown in Table 4.2.

The damping performance for TMW particles used in this configuration was evaluated by measuring the power dissipated when subjected to sinusoidal vibrations. The particle damper was directly screwed onto a force transducer and then

mounted on an electrodynamic exciter. One 10 mV/g sensitivity piezoelectric accelerometer was bonded on the top of the lid of the particle damper to measure the acceleration response. The power flow method was used to estimate the dissipated energy, and hence the loss factor of this damper. A detailed illustration of this power-flow method is shown in Appendix **??**. For a SDOF system, the complex power [102] can be represented as,

$$P(\omega) = \frac{1}{2}\left[X^2 c\omega^2 + jX^2\omega\left(-m\omega^2 + k\right)\right] \tag{4.19}$$

where j is the $\sqrt{-1}$, the other symbols follow their common meanings. Generally, the loss factor is defined as

$$\eta = \frac{D}{2\omega W} \tag{4.20}$$

in which D is the energy dissipation per cycle and W is energy stored in that cycle. In the form of complex power, the loss factor can also be given by

$$\eta = \frac{\text{Real}\left[P(\omega)\right]}{\text{Imag}\left[P(\omega)\right]} \tag{4.21}$$

From Equation 4.19, it can be seen that the real and imaginary power representation for the system loss factor can be estimated only if excitation frequency is not close to system natural frequency. For this Perspex cylinder cavity, the fundamental natural frequency in axial direction is higher than 2000Hz. Meanwhile,

Variables	Value
Mass of cavity	105.24 g
Maximum height	110 mm
Minimum height	76 mm
Outer diameter	38 mm
Inner diameter	32 mm
Effective length	20 mm

Table 4.2: Test-rig information of TMW particle damper

the armature resonance of the shaker is higher than 6000Hz, and therefore, this structure can be assumed to be a SDOF system. The proposed complex power flow method can be used to estimate system energy loss.

Results for different excitation levels and frequencies are presented in Figure 4.19

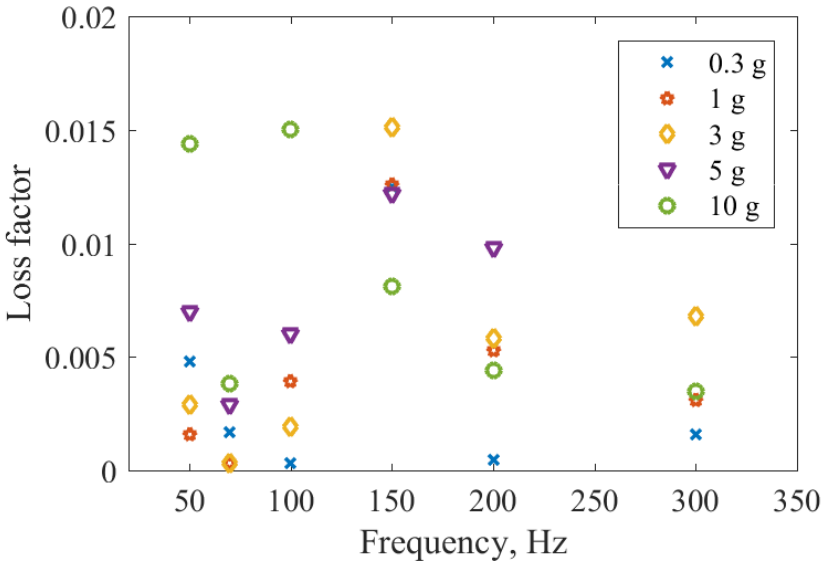

Figure 4.19: Loss factor of a TMW particle damper

From Figure 4.19, it can be seen that no remarkable energy loss was identified for this damper. During testing, it was observed that the particles rotated around the axis of the cylinder parallel to the excitation directions at certain frequencies, which indicates the particles were activated. However, the energy loss is still low compared with that seen during the hysteresis loop and drop-rebound tests of individual particles. One probable reason is that mass ratio between particles and cavity is really low. In this work, only 5g of TMW particles was filled into the cavity. The inertia of particles was not high enough to create deformations between particles, hence, dissipate energy. Nevertheless, it can be observed that an slightly enhancement of energy dissipation occurs at 150 Hz. One possible explanation is that local resonances within the collections of these particles are activated. A further investigation is reported in Section 4.5.2.

Results from the Visco-analyser suggested that TMW particles have the capability of high energy loss as a low wave speed medium. In this section, a comparison study on one stiff box beam with different particle damper, filled with TMW and hard plastic particles, was carried out. Additionally, the energy loss of a box beam with TMW particles filling was also investigated.

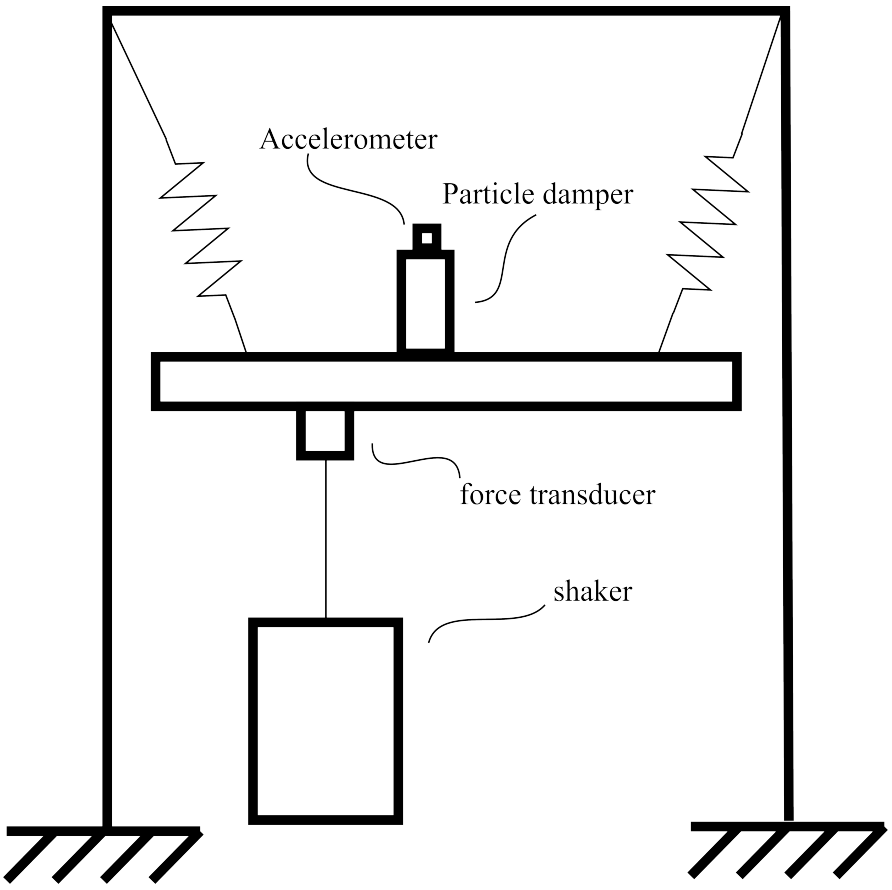

Figure 4.20: Sketch of test-rig: hollow beam with TMW particles

The sketch of test rig is shown in Figure 4.20. An aluminium beam with 1m length was suspended by light springs and Nylon line. An electrodynamic exciter was attached to provide a periodic input and placed 400mm from one end of the beam. The accelerometer was attached to the particle damper was placed on the middle of the beam. The critical dimensions for this aluminium beam are shown in Table 4.3.

A random excitation of up to 1000Hz was used to identify the resonance and the resulting inertance for the hollow beams under empty and filled conditions. Two types of filler were considered: TMW and hard polyurethane spheres. Results are shown in Figure 4.21.

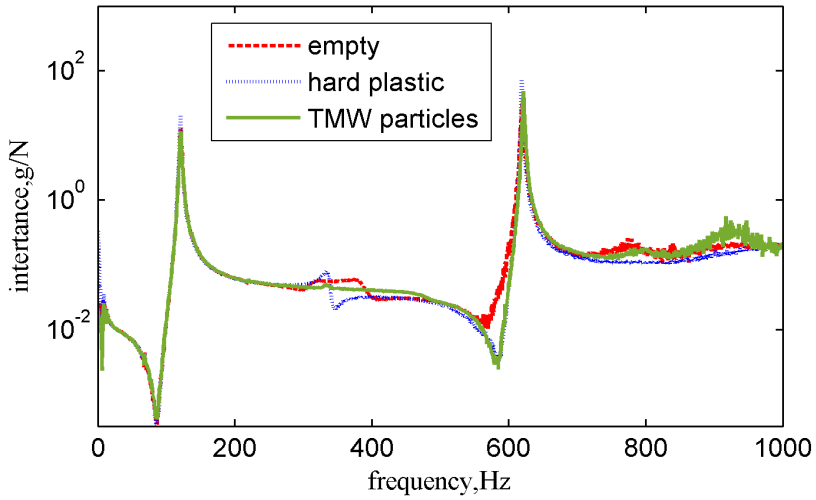

Figure 4.21: Frequency response of box section beam subjected to random vibration

From Figure 4.21, it can be seen that two obvious resonances exist for this hollow beam and addition of fillings has little effect on the natural frequencies. Close examination of Figure 4.21 reveals two additional features. At approximately 400 Hz, small peaks exist for empty cavity and hard polyurethane cases. This is likely

Variables	Value
Length	1000 mm
Width	38.1 mm
Depth	19.1 mm
Wall thickness	2.1 mm
Mass	0.714 kg

Table 4.3: Properties of box section beam

to be the second mode - particularly because the response point coincides with the node. The additional mass of the particle damper slightly shifts the mode shape. Therefore, a tiny peak occurs near 500Hz. The other feature is that double peaks occur at the third mode of this beam (near 630 Hz). This is probably caused by the local mode of the particle damper. In the work presented here, only the first mode was used to identify the damping of the system.

Since the dynamic displacement for random excitation is uncontrollable over selected frequency range, a stepped sine test was introduced. The natural frequency and damping ratios for the first mode were obtained using Nyquist circle fit approach. The result is shown in Figure 4.22.

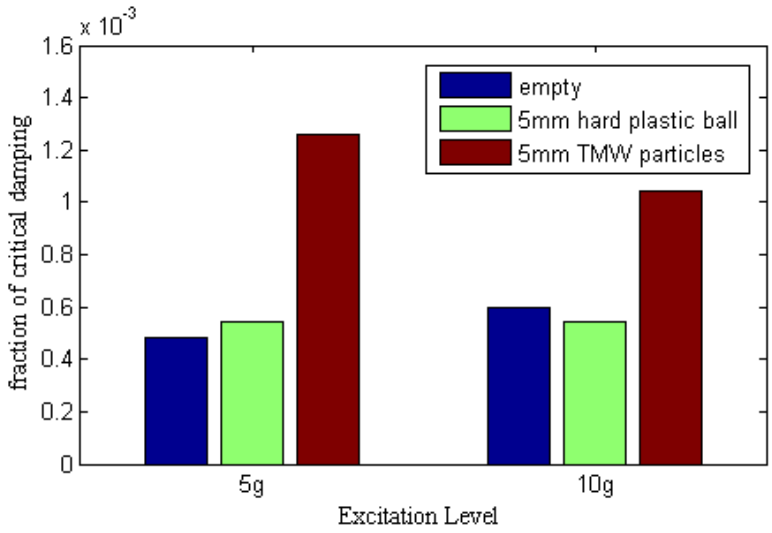

Figure 4.22: Comparison of loss factor of particle dampers with different fillings

Figure 4.22 indicates that TMW particles were somewhat more effective than the hard polyurethane spheres when they were filled into the particle damper cavity. When the structure was excited, rotation and sliding between particles could be observed. However, the damping level was still very low. The mass ratio of particles to the structure was only 0.95%, which limited the energy dissipation of the TMW particle damper.

4.3.2.2 TMW filler

A different way to damp vibrations in structures using lossy particles is to use them to fill hollow cavities. If internal resonances within the granular medium can be excited, significant energy dissipation can occur. The performance of TMW particles in this type of application was investigated using the same box-section beam as before but filling it with particles rather than attaching a separate damper. Tap testing, using an instrumented force hammer was carried out. The box beam was freely suspended on a rigid frame, as shown in Figure 4.23. An accelerometer was placed on the middle point of the beam. Other relevant information about the test rig is summarised in Table 4.4.

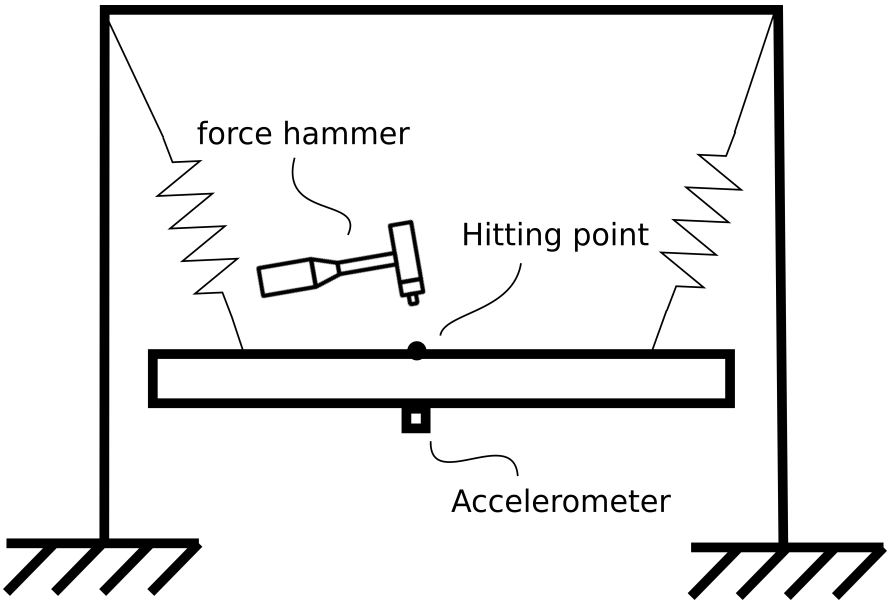

Figure 4.23: Test set-up for box beam

Three different configurations – empty beam, half-filled beam and full-filled beam – were tested and the weight of these beams was 83.04g, 95.75g and 101.65g respectively. The resulting acceleration response can be seen in Figure 4.24.

When the particles were fully filled into the structure, acceleration response decreased considerably. The fraction of damping for this configuration is identified using half power method and the damping ratio is approx. 5.9%.

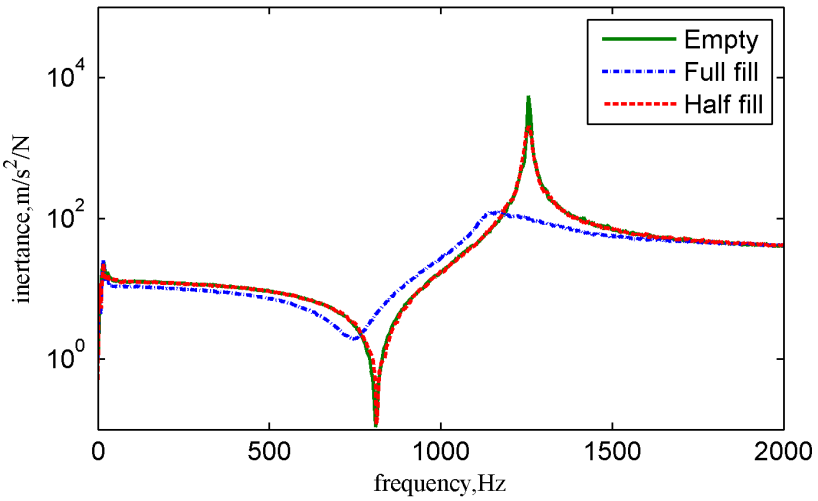

Figure 4.24: Acceleration frequency responses for box beam

This collection of the TMW particles can be assumed as a linear elastic medium. Typical values of stiffness and density for TMW particles suggest that bulk wave speeds within a cavity filled with them are below 40 ms^{-1} [13]. For the box-beam used, the lowest frequency standing wave in the thickness direction for a full fill beam would therefore be expected at approximately 1000 Hz. As the first flexural resonance of the box-beam is slightly higher than this value, the

Variables	Value
Length	260 mm
Width	25 mm
Depth	12.5 mm
Wall thickness	1.6 mm
Mass	0.083 kg
Young's modulus of the aluminium beam	70 GPa
Density of the aluminium beam	2700 kgm^{-3}
Poisson's ratio of the aluminium beam	0.3

Table 4.4: Properties of box section beam

presence of standing waves within the granular medium would be expected.

One of the key parameters for estimation of these standing waves is the equivalent elastic modulus. Since the interaction between the filler and hollow box beam is complicated to determine, a Finite Element modal analysis with optimisation procedures was introduced [103]. In this modal analysis, the filled beam is modelled as a composite comprising the steel shell and a equivalent linear elastic medium. In order to estimate this equivalent elastic modulus, the first resonant frequency of the filled beam was used - 1163 Hz in this case. The optimal equivalent modulus of this TMW block are obtained when the difference of these simulated and experimental natural frequencies achieves its minima. Overall, the detailed properties of TMW particles are listed in Table 4.5.

Variables	Values
Elastic moduli	389 kPa
Density	376.56 kgm^{-3}
Wave speed	31.42 ms^{-1}
Resonance frequency for 1^{st} wave mode	1010 Hz

Table 4.5: Summary of the properties of TMW fillers

The low wave speed approach only focuses on the direction perpendicular to the excitation. Additionally, the rotational motion may also improve the damping. The finite element modal analysis was introduced to identify the local resonances near the structural fundamental resonant frequency. Since the first resonance of the filled beam identified from experiments was approximately 1163 Hz, only the mode shapes around this frequency are illustrated. The deformed shapes of this collection of the TMW particles are presented in Figure 4.25.

It can be seen from Figure 4.25 that the internal resonances occur near the selected structural fundamental frequencies. Combining with the hysteresis properties of TMW particles, it is understandable that these particles cause high energy loss from the structure. Interestingly, the performance of TMW particles drops

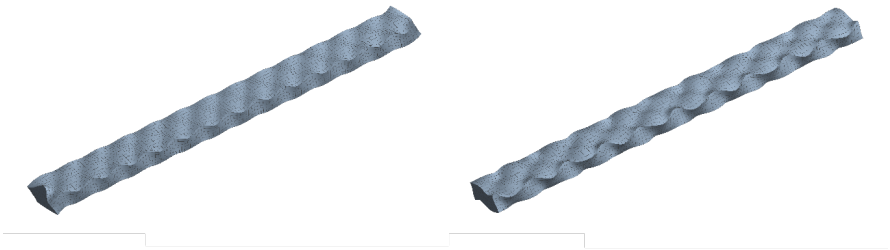

(a) 1162 Hz (b) 1169 Hz

Figure 4.25: Section views of deformations within the granular medium at different frequencies

dramatically when this hollow structure is filled only half-full. Under these conditions, standing waves in the thickness direction would only be expected above 2000 Hz, and hence the first flexural resonance of the beam would not activate the wave modes. Since the excitation also results in rigid body motions, the particles in the partial fill configuration, are not constrained to move with the hollow beam. Thus, the resonance of the filled beam does not shift. Also, the inertia of TMW particles is not high enough to generate static deformations as the force excited by the instrumented hammer is low. The dry friction between particles and inside particles is not well developed, and therefore the energy loss for this structure is low.

4.4 Tuned Mass Damper using TMW particles - experimental investigations

The previous section indicated that TMW particles can achieve reasonable damping only when 1) internal resonances of the TMW particles are activated 2) significant strain is applied to this collection of particles. To achieve these conditions, a mass was placed between two collections of particles to increase the dynamic strain that they experiences.

This tuned mass damper consists of an acrylic casing, a metal proof mass, a securing ring and a screwed hollow cap. Transparent acrylic material was used

to allow observation of the motion of the individual particles and the proof mass. The cap was designed to alter the distance between the lower restricting surface and the top of the cavity. Also, a hollow structure was used for the cap of this damper so that the overall weight of the damper would be reasonably low, and therefore, the fundamental frequency of the empty cavity would be lower than 1000 Hz. Drawings of the container are shown in Figure 4.26.

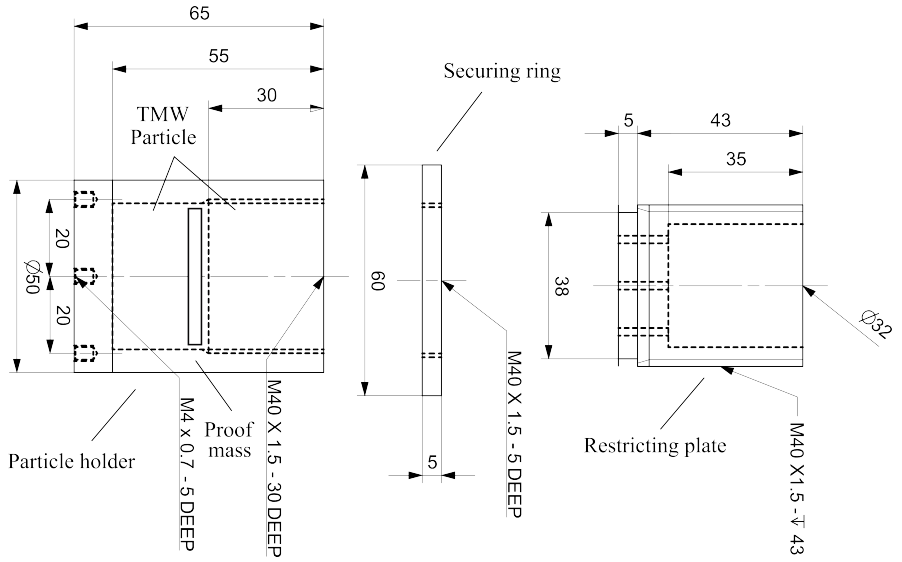

Figure 4.26: Schematics of the TMW Tuned mass damper (unit: mm)

4.4.1 Test configurations

Transmissibility between the proof mass and excitation was used to study the performance of this type of TMD. A steel disc, 30 mm in diameter and 2.5 mm in thickness, was used as the mass. A 6 mm diameter hole was drilled through the centre of the disc and it weighted 20.49 gram. A 10 mV/g miniature accelerometer was attached to the mass, the weight of the accelerometer needed to be added to the mass of this TMD. Thus, the overall weight of mass element in this TMD was set as 22 g. Three layers of the particles were put in each side of the proof mass. The original height of these particles was approximately 15 mm. The overall weight of these particles was approximately 12.32 g. The damper was mounted

directly onto the platform of a permanent magnet shaker with 480N peak sine force capacity. A second accelerometer was attached to the shaker table. The detailed test configuration is shown in Figure 4.27.

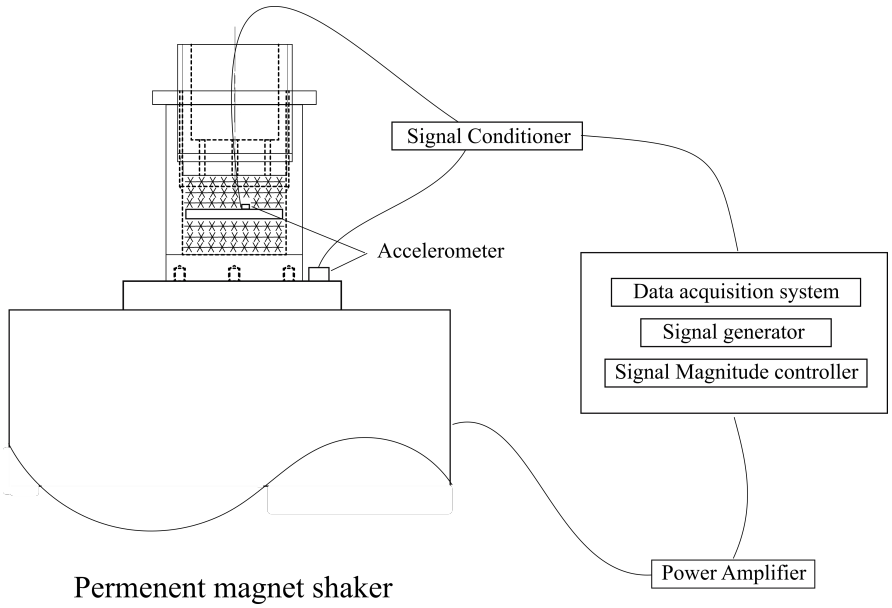

Figure 4.27: Schematics of test set-ups for TMW TMD

The repeatability of this TMD for different configurations was explored using magnitude-controlled stepped sinusoidal signals. The base acceleration was used to control the excitation level and the control tolerance was selected as 3% of the targets. A tracking filter of 50 Hz was used to remove the background noise of the signal. The average of ten responses was used to ensure the repeatability of the tests. Initial tests were conducted to show the repeatability of the dynamic performance of this TMD. One typical frequency response is shown in Figure 4.28. The full results of the repeatability tests can be found in Appendix F.

It can be easily concluded from Figure 4.28 that the performance of a given TMW TMD tends to be stable after several repeat tests. Also, it is interesting to note that a relatively flat peak can be observed in the transmissibility curves due to the internal friction between the contacts of the individual particles. Besides, several fluctuations can be observed even in the frequency range away from

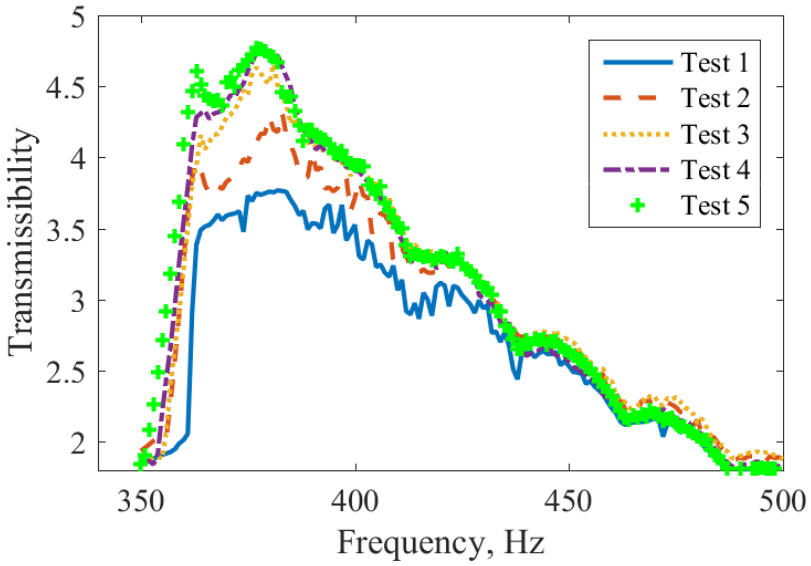

Figure 4.28: Typical transmissibility curves for selected configurations of TMW TMD subject to different loading history (static compression of particles is 0.45 mm)

the main resonance. The internal resonances may increase the damping capability of this system, and therefore promote the vibration mitigation across a wide frequency range.

The other important conclusion that can be drawn from Figure 4.28 is that the performance for a given TWM particle based TMD tends to achieve uniformity after several test runs. This result differs from the repeatability obtained from the single particles. The difference found between individual particles was obscured by using a collection of particles. It is emphasised that this conclusion can only be valid for the TMD with a given collection of particles. For collections of particles with similar geometric properties, the dynamic stiffness and damping may still show some difference.

Although several peaks exist for this response, the mean damping can still be obtained using linear system assumption. The average fraction of critical damping is estimated using the Nyquist circular fit. A typical example is shown in Figure 4.29.

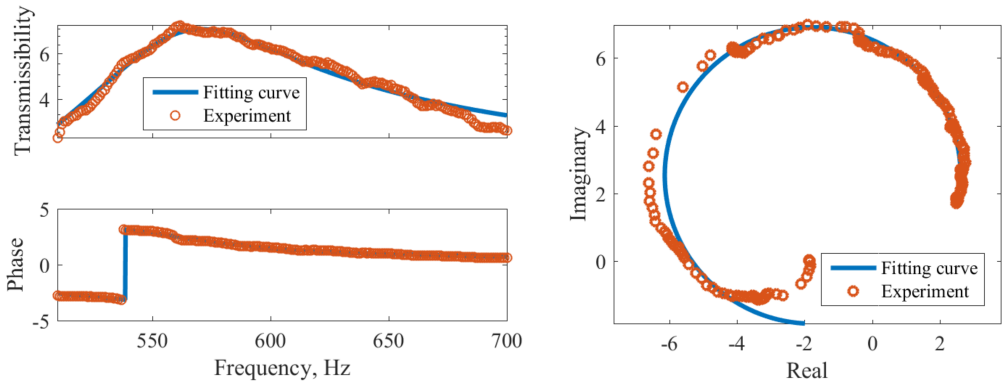

Figure 4.29: Fit to experimental data

It can be seen from Figure 4.29 that only one main resonance exists at selected compressions. In terms of designing the TMD, having one resonance at given compressions makes the design of this type of TMD easier. Also, several fluctuations can be observed in the Nyquist circle because several local resonances exist for this damper over the given frequency ranges. As a result, errors can be observed in the peak height of the transmissibility curve. Nevertheless, these errors are still relatively smaller than the peak response, and therefore, the Nyquist circle fit routine is still eligible to estimate the working resonances of this TMD with reasonable accuracy.

The effectiveness of this TMW TMD is shown in Table 4.6.

Item	Fraction of critical damping
Without mass	0.0075
With mass	0.2035

Table 4.6: Effect of the TMW TMD

With a tiny proof mass, the capability of energy dissipation of the TMW particles improves significantly. Also, this level of damping is in the useful range for designing a TMD.

4.4.2 Static compression-dependent stiffness and damping

To investigate the potential of designing an adjustable TMD, the strain-dependent nonlinear stiffness of this TMD was investigated. Preliminary investigations using random excitations were carried out and the transmissibilities of this damper were chosen to show the nonlinear stiffness. Close examination using stepped sinusoidal signals at selected accelerations was then conducted to gain the precise trend of stiffness and damping with static compressions.

It is worth noting that the static compression of the TMW particles refers to the strain of the collection of particles in one side of the proof mass. The overall static deformation of the particles in this damper is two times the value shown in this section. Random excitation with a frequency range between 10Hz and 1000Hz was used in this preliminary study. An analogue high pass filter with a cut-off frequency of 10Hz was connected to the function generator as the effect of the rigid body motion of the proof mass strongly affected the deformation of the particles, and therefore the resonance of this TMD. The transmissibility curves with different effective damper heights are shown in Figure 4.30

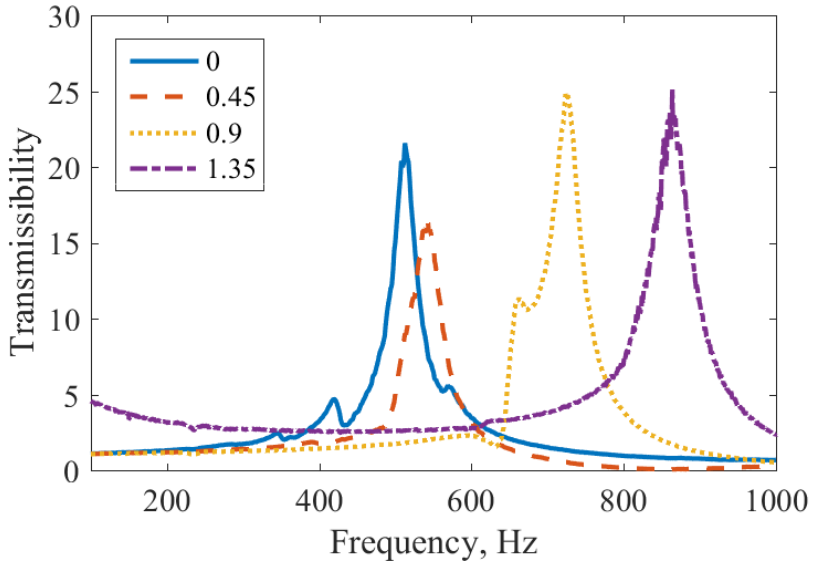

Figure 4.30: Effect of static compressions: experimental results

Figure 4.30 shows that the resonance frequencies of this damper increase with the static compressions. Some minor peaks can be observed near the main resonances of this transimissibility curve as extension-compression and rocking modes exist for this damper. Since the accelerometer was attached near the centre of the proof mass, the resonance peak of the rocking mode is lower than that of the extension-compression one. When the static compression of the particles approaches to zero, the resonance frequency and hence the stiffness is very close to the one with a static compression of 0.45 mm. Since the shape of each particle is irregular, some difficulties exist in determining the initial compression of this damper. Meanwhile, the stiffness of the TMW particles is very sensitive to their pre-strains. Therefore, stiffening of these particles can be observed in the experiments. Also, the impact between neighbouring particles can be observed during the experiments when the static compression is low. The low frequency components of the excitation signals may activate undesired internal resonances, and therefore, additional resonances appear in estimation of the resonance of this system.

To remove the effect of these unwanted errors, stepped sinusoidal signals were used to investigate the capability of the stiffness and damping adjustment for this damper. The controlled base acceleration was selected as 3g in these sets of experiments. Results from stepped sinusoidal excitation are shown in Figure 4.31

Figure 4.31 indicates that several peaks occur for these transmissibilities. The Nyquist circle fitting can only provide an average damping in these cases. Some errors, especially in estimating damping, are still introduced from these curves. The relationship between the dynamic characteristics and static compressions is shown in Figure 4.32. To ensure resonances were at around 500Hz from random excitations at the conditions where the TMW particles have no static compression, the selected frequency range of the stepped sinusoidal excitation signals was from 100 to 600 Hz.

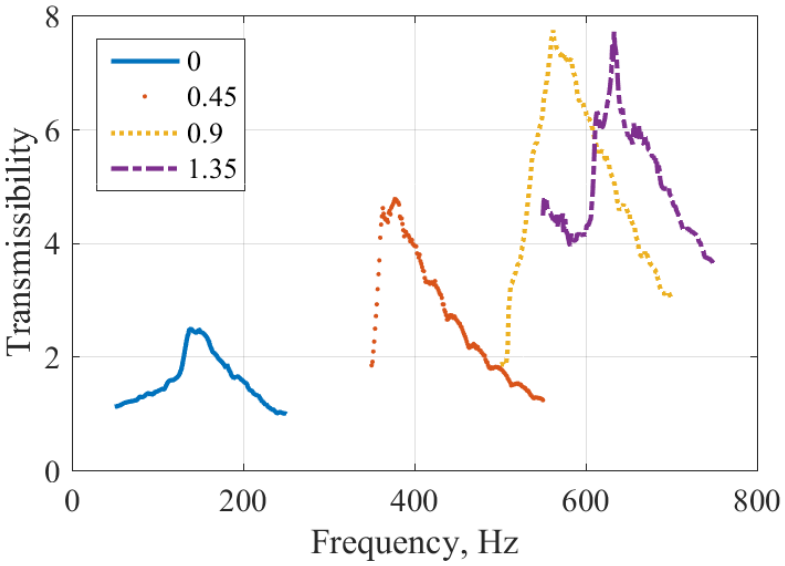

Figure 4.31: Effect of static compressions: close examination

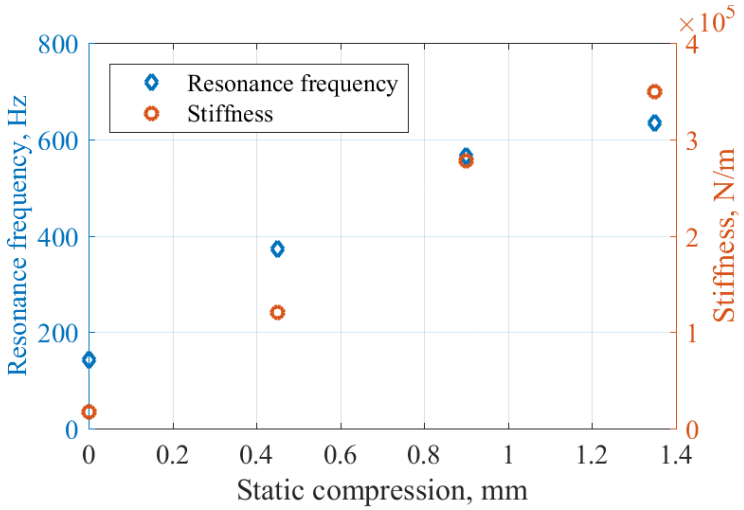

(a)

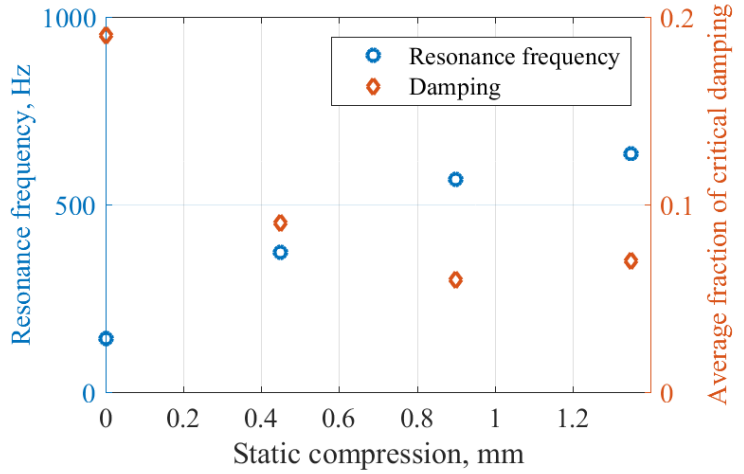

(b)

Figure 4.32: Static compression-dependent dynamic characteristics (a) stiffness

It can be seen from Figure 4.32 that the resonance frequencies of this damper at low compression are much lower than those obtained for random excitation. The damping is near a level of 0.07 except at very low static compression where it is much higher. It should be noted that the resonance occurred near 150 Hz for this condition - a frequency already associated with high damping in earlier tests (see Figure 4.19) It is reasonable to interpret that some local resonances, also called wave modes in some papers [103–105], are activated, and high strains of the particles are achieved. Nevertheless, these TMW particles can still provide the capability of alternative stiffness adjustment and similar damping with elastomeric O-rings, and therefore are suitable for the design of an adjustable TMD.

4.4.3 Effect of dynamic amplitude

Since the TMW particles are sensitive to imposed displacement, the effect of dynamic amplitude on the TMW TMD was investigated. A static compression of 0.45 mm was applied to these particles in these experiments. A stepped sinusoidal waveform with a controlled base acceleration of 3g was used. Results are presented in Figure 4.33.

With increase of the dynamic amplitude, the resonance peak shifts towards the low frequency. In the same way as heating softens an elastomer, softening of the TMW particles may be caused by re-organisation of the internal micro-structure. The positions of the contact points may change to a position of lower strain energy, and therefore softening can be observed with the dynamic strain.

The resonances and damping of this TMD with different dynamic amplitudes are shown in Figure 4.34.

Figure 4.34 indicates that the damping of this TMD tends to be uniform when the dynamic amplitude is higher than 6 μm. At very low dynamic amplitudes, some of the interwire friction may not be activated. As a result, the energy dissipation is slightly lower.

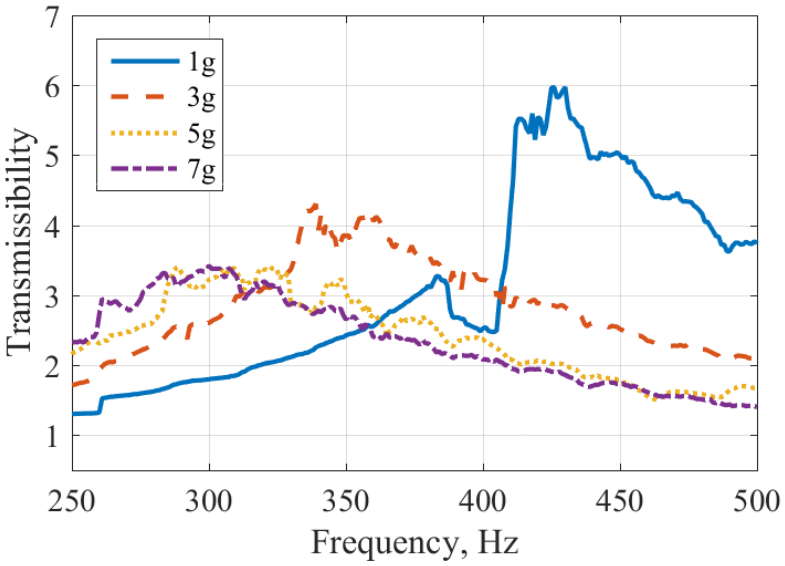

Figure 4.33: Effect of dynamic amplitudes subject to different dynamic strains

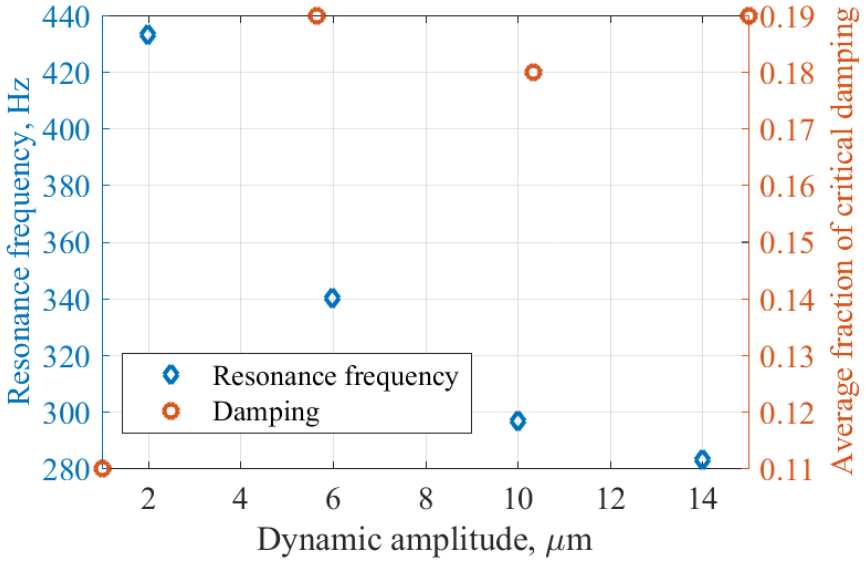

Figure 4.34: Dynamic characteristics of this damper subject to different dynamic amplitudes

4.4.4 Effect of loading direction

The other important factor, that may affect the consistent behaviour of this TMD is the the direction, where the TMW particles were compressed - denote as 'loading' direction. Effects of the loading direction were investigated. Results of fundamental frequencies of this damper and the energy dissipation are demonstrated in Figure 4.35.

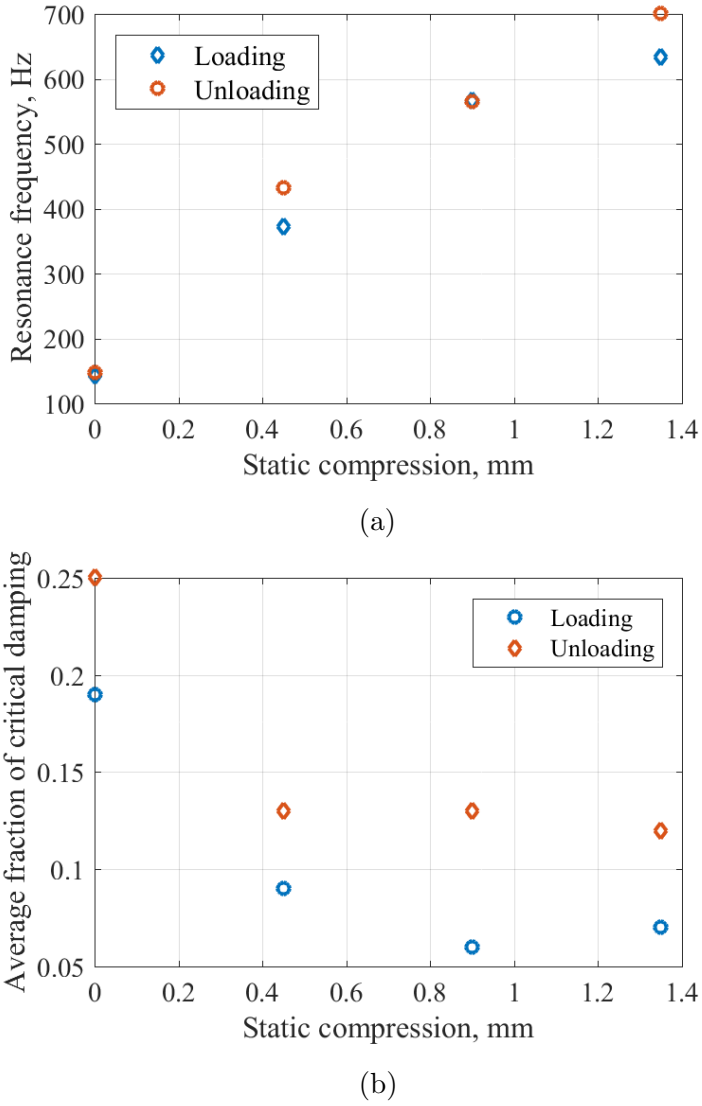

Figure 4.35: Effect of loading direction on the dynamic characteristics of the TMW TMD (a) stiffness (b) damping

The resonance frequency of this device is relatively consistent with regard to the loading direction. The damping, when unloading however, is around twice that when loading. When the particles are compressed to a certain level, re-orientation of the particles occurs and more interwire contacts may be generated than with the original configurations. As a result, a higher capability of energy

dissipation can be obtained. In terms of designing a TMD, the relative uniformity of the resonance frequencies is a benefit as this device is much more sensitive to the stiffness. Pre-conditioning of this type of TMW TMDs is required to ensure the properties of this damper become uniform.

4.5 Modelling of TMW TMD using wave speed medium approach

It has been indicated in the previous section that the TMW particles produce variations in stiffness and damping even when using a significant number of particles. A suitable approach needs to be developed to evaluate the properties of this type of TMD. This section introduces a useful procedure for designing a TMD using TMW particles.

4.5.1 Evaluate the nonlinear stiffness subject to static compressions

For a typical adjustable TMD, the nonlinearity of the stiffness, and therefore, the resonance frequency of this TMD is of great importance. As shown in previous sections, the properties of a collection of TMW particles can, as a first estimate, be represented by a hysteretic damping material such as polymer. Therefore, a classic Neo-Hookean material model was applied to simulate the strain-dependent stiffness. Using this Neo-Hookean hyperelastic material model, the relationship between load and deflection can be expressed as,

$$\frac{F}{A} = \frac{E}{2\left(1+\nu\right)}\left[\frac{1}{\left(1-{}^{u}/_{h}\right)^{2}} - \left(1-{}^{u}/_{h}\right)\right] \tag{4.22}$$

where F is the applied load, A is the inner cross-sectional area of the cavity, E is the equivalent elastic modulus of the stacks of TMW particles, ν is the Poisson's

ratio of the TMW particles, u is the static compression, h is the initial height of TMW particles. The stiffness, denoted as k_a, is then obtained using,

$$k_a = \frac{dF}{du} = \frac{EA}{2h\,(1+\nu)}\left[1 + 2\left(1 - \frac{u}{h}\right)^{-3}\right] \tag{4.23}$$

Although these TMW particles can be considered analogous to polymer, the modulus of the material is not constant. The number of interaction points between neighbouring wires is far less than the number of molecular chains in a typical polymer. As a result, the strain-dependent nonlinear stiffness is much easier to observe. Referring to Figure 4.32, the increase of the stiffness is linear at low strain as the microstructure of this material is loosely configured. With the increase of static compression, some contacts in these particles begin locking up. Meanwhile, permanent plastic deformation and yielding of local metal wires occurs. Therefore, the incremental rate of stiffness slows down. To compensate for the mentioned difference, an empirical scale function was applied and then the modified stiffness could be represented as,

$$k_b = k_a\left[1 + c\log_{10}\left(1 - {}^{u}/_{h}\right)\right] \tag{4.24}$$

where c is the fitting parameter. For the work presented here, the key parameters of this device are listed in Table 4.7

Variables	Value
Cross-sectional area A	1.1×10^{-3} m^2
Initial height h	0.015 m
Poisson's ratio ν	0
Equivalent modulus E	0.13 MPa
Scale factor c	-231.5

Table 4.7: Key parameters of TMW particle damper

Note that the scale factor c and equivalent modulus of this collection of particles E were obtained using the fit of the stiffness-deflection curves shown in Figure 4.32. Comparison between the analytical and experimental models is shown in Figure 4.36.

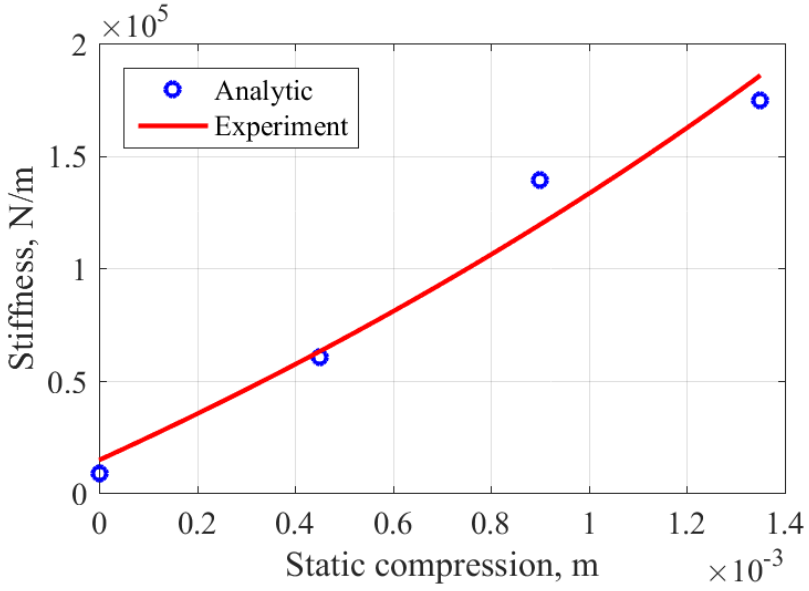

Figure 4.36: Comparison between analytic model and experimental results

It can be seen from Figure 4.36 that the proposed model can represent the nonlinear behaviour of strain-dependent stiffness well. Once this relation is set up, the master curve of nonlinear stiffness for this type of TMD can be formed provided that the stiffness of this type of TMD is calibrated without any static strain on the TMW particles. The advantage of the proposed route in estimating stiffness is that no permanent re-location and deformation of the local wire occurs in the process of calibration.

4.5.2 Evaluate the damping subject to static compressions

Damping of TMW particles is sensitive to static compression. Because of the low dynamic strain applied on these particles, elastic components are considered as a equivalent hysteretic polymer. The relative displacement of the proof mass in this TMD needed to be evaluated when subject to a base excitation of 3g. The effective root-mean-square dynamic displacement amplitudes of the proof mass in this TMD are shown in Table 4.8

Table 4.8 indicates that the dynamic strain is relatively small when static

Static compression	0 mm	0.45 mm	0.9 mm	1.35 mm
Dynamic amplitude	0.15 mm	0.023 mm	0.016 mm	0.014 mm

Table 4.8: Relative dynamic displacement of proof mass in this TMD (base excitation = 3 g)

compressions are higher than 0.03. Therefore, the assumption that the collections of TMW particles can be considered as a hysteretic solid can be applied in most of the working cases of this TMD.

As shown in Section 4.3.2.2, a collection of TMW particle can be regarded as low wave speed medium. The local resonance of the particles may promote the energy dissipation of the devices. This frequency-dependent damping applies to the TMW TMD as well, and typical deformed shapes of this equivalent solid at selected static compression are presented in Figure 4.37.

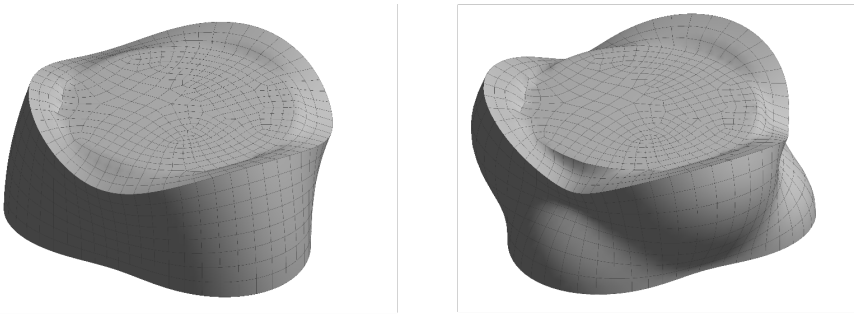

Figure 4.37: Section views of deformations within the TMW particles at different frequencies (no static compression)

It can be seen from Figure 4.37 that both bending, torsion and twisting can be observed in the practical local resonance. Rongong developed a direct frequency response approach to estimate the frequency-dependent damping using classic Finite Element procedure, while it is not convenient to extract the vibration mode at various static compressions. This was because the equivalent modulus of the TMW particles is sensitive to the static compressions. Instead,

the simple two-dimensional approach developed originally for thick viscoelastic layers can be applied in this case.

Regarding the hysteretic medium, modes in the direction perpendicular to the motion may occur when subject to rigid body motions. In the TMW TMD, the direction of the wave propagation for this TMW particles is illustrated in Figure 4.38.

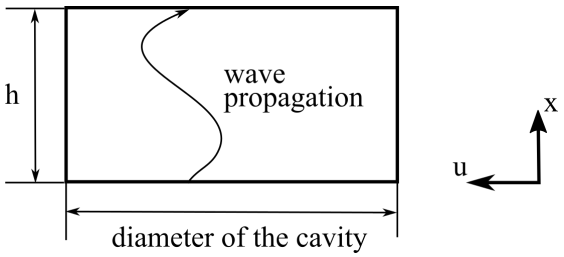

Figure 4.38: Schematics of the wave propagation inside a collection of the TMW particles

Darabi [103] provides a routine to obtain the damping of these polymers within a tube from 0 to 1000 Hz. Mathematically, this phenomenon can be given by,

$$\frac{d^2u}{dx^2} + k^2u = 0 \tag{4.25}$$

where x is the position and u is the displacement perpendicular to the motion. Ungar and Kerwin [105] provide the standing wave numbers for a hysteretic solid in transverse direction subject to excitation,

$$k = k^{'} + jk^{''} = \omega \left(\frac{\rho\,(1+\nu)\,(1-2\nu)}{E(1-\nu)} \right)^{\frac{1}{2}} \tag{4.26}$$

Although the TMW particles were enclosed between the cavity and the proof mass, the boundary conditions were not identical to those described in previous work. The transverse motion of the proof mass was strictly prevented, and therefore these particles on the edge of the proof mass could only move in the direction of the motion of the standing wave. For these TMW particles, with given wave speed, the maximum amplitude of the internal resonance occurs at the position

between the $\frac{\pi}{2k}$ and $\frac{\pi}{k}$ in the thickness direction. Mathematically, this position can be represented using $\frac{\pi}{\lambda_p k}$ where λ is in a range between 1 and 2. This assumes that the localised mode shape of these equivalent hysteretic blocks can still be represented using,

$$u = u_0 \frac{\cos\left(\frac{k}{2}\lambda_p x - \frac{k}{2}\lambda_p h\right)}{\cos\left(\frac{k}{2}\lambda_p h\right)} \tag{4.27}$$

where u_0 is the motion of the block of TWM particles, h is the height of the TMW block. Note that λ_p is a scale factor to evaluate the effect of free motion in excitation direction. Using the standard mode shape function for lateral vibration of beam with different boundary conditions, this λ_p can be interpreted. In this analysis, λ_p is selected as 1.5 with reasonable accuracy as the restriction of these particles is close to a fixed-fixed clamping arrangement. The average energy dissipation per radian is then represented as,

$$D = u_0^2 \left(\frac{\rho\omega^2 h}{4} \frac{\eta}{\sqrt{1+\eta^2}} \frac{\frac{\sinh\left(k''\lambda_p h\right)}{k''\lambda_p h} - \frac{\sin\left(k'\lambda_p h\right)}{k'\lambda_p h}}{\cos^2\left(\frac{k'\lambda_p h}{2}\right) + \sinh^2\left(\frac{k''\lambda_p h}{2}\right)} \right) \tag{4.28}$$

Similarly, the peak kinetic energy in the stacks of particles is given by,

$$T = u_0^2 \left(\frac{\rho\omega^2 h}{4} \frac{\eta}{\sqrt{1+\eta^2}} \frac{\frac{\sinh\left(k''\lambda_p h\right)}{k''\lambda_p h} + \frac{\sin\left(k'\lambda_p h\right)}{k'\lambda_p h}}{\cos^2\left(\frac{k'\lambda_p h}{2}\right) + \sinh^2\left(\frac{k''\lambda_p h}{2}\right)} \right) \tag{4.29}$$

The kinetic energy of unit surface area of the inner bottom surface is defined as,

$$T_b = \frac{1}{2} m\omega^2 u_0^2 \tag{4.30}$$

Compared with Darabi's work [103], an apparent difference with the proposed TMD is that the fundamental natural frequency of the cavity is higher than the working frequency range of the TMD. Only single vibration shape has the influence of energy dissipation. When the identified damping is small, the damping ratio of this system is half of the system loss factor and can be represented as,

$$\zeta = \frac{\eta}{2} = \frac{1}{2} \frac{\text{energy dissipated per radian}}{\text{peak strain energy}} \approx \frac{DA}{2(TA + T_b)} \tag{4.31}$$

In this case, strain-dependent damping is vital to the design of this adjustable TMD. From Table 4.8, it can be seen that the dynamic amplitude is almost the same when the static compression is higher than 0.45 mm. To keep the analysis simple, it was assumed that the effect of dynamic amplitude is not accounted for in the following analysis. The strain-dependent equivalent modulus of elasticity, $E(u)'$, can be obtained using the transformation of Equation 4.23 and 4.24. Damping from a collection of particles can be estimated using polynominal fit of relationship between the static compression-damping curves. In the current set-up of the TMD, this experimental compression-damping curve is shown in Figure 4.17. Mathematically, the strain-dependent damping for these three layers of TMW particles can be given by,

$$\eta(u_s) = -10.67\left(\frac{u_s}{h}\right)^2 + 1.056\left(\frac{u_s}{h}\right) + 0.2861 \tag{4.32}$$

where u_s is the static compression on the TMW particles. Comparison between the experiment and analytical fitting curve is shown in Figure 4.39.

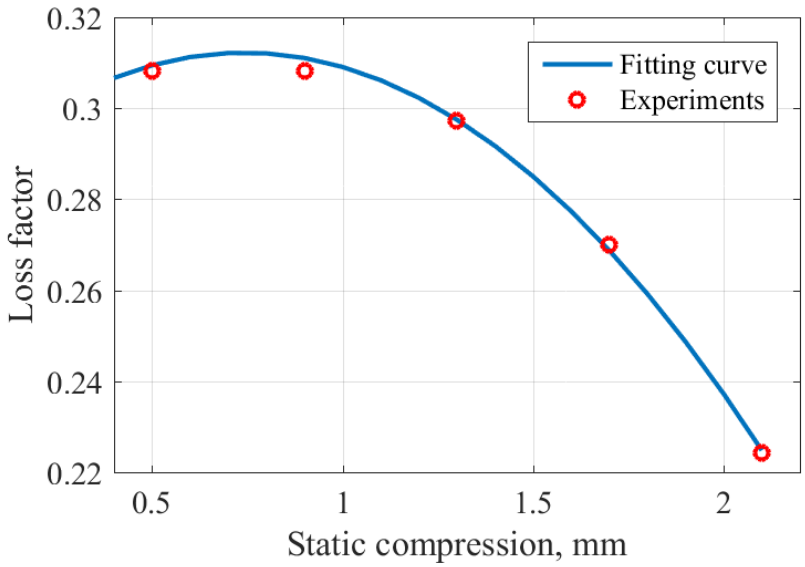

Figure 4.39: Comparisons of damping between fitting curve and experimental results subject to static compressions

The complex modulus of the TMW particles is then represented as,

$$E^*(u_s) = E(u_s)^{'}\left(1 + j\eta(u_s)\right) \tag{4.33}$$

Once the nonlinear complex modulus has been obtained, the damping at given frequencies of interest can be obtained. The tensile-compressive resonance frequencies of this TMD are defined as,

$$f_{\text{tmd}}(u_s) = \frac{\sqrt{\frac{2k_b(u_s)}{m_{\text{tmd}}}}}{2\pi} \tag{4.34}$$

Figure 4.40 demonstrates the master curve of damping for a selected collection of TMW particles. When the static compression applied on these particles

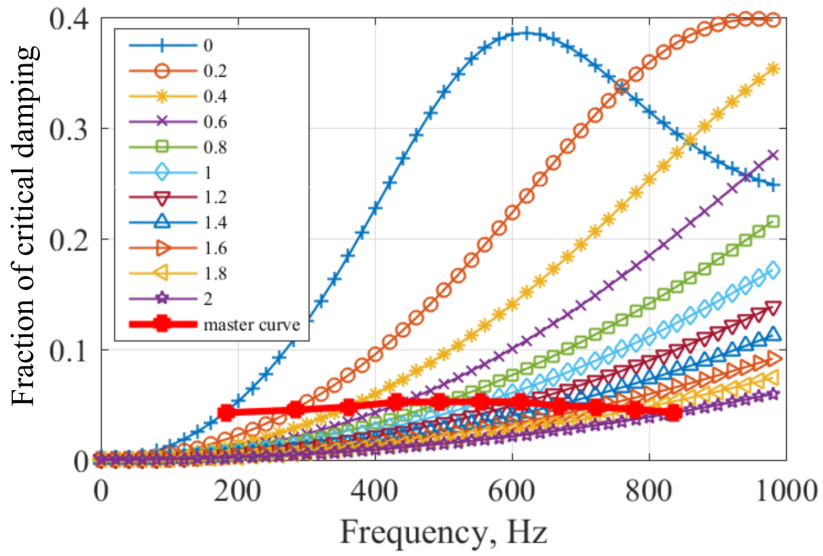

Figure 4.40: Master curve of the damping of TMW particles subject to different static compressions

increases, both stiffness and damping of the TMD shift - see Equation 4.32 and 4.24. At a certain level of the static compression, Equation 4.31 provides the frequency-dependent damping behaviour. A master curve - see Figure 4.40, was then constructed to represent the frequency-dependent damping at various static

Static compression of the TMD, mm	0	0.8	1.6	2.4	3.2
Elastic modulus, MPa	0.13	0.48	0.84	1.2	1.6
Density, kgm^{-3}	362	372	382	393	405
Wave number	18.95	35.92	46.89	55.26	62.85
Resonance frequency, Hz	581	1161	1541	1921	2181

Table 4.9: Summary of the properties of TMW particles and corresponding resonances of the hysteretic solid model

compressions. For a given static compression, the natural frequency of the TMD can be obtained using Equation 4.34. Once obtained, the mapping between the loss factor and natural frequency in the master curve was carried out to find out the energy loss factor, $\eta\left(f_{\mathrm{tmd}}(u_s), u_s\right)$, at these static compressions. A summary of the equivalent modulus, density, wave speed and fundamental natural frequencies at selected compressions are listed in Table 4.9

Comparison between the analytical damping and experimental results is shown in Figure 4.41.

Figure 4.41 indicates that the proposed model underestimates the ability of energy dissipation of these TMW particles. One possible reason for this phenomenon is the variation of the dynamic strains for different dynamic amplitudes. As shown in Figure 4.34, the loss factor increases massively with the dynamic amplitudes. Since this portion of damping is ignored in the proposed model, the under-estimation of this TMD is apparent, especially when resonance frequency is low.

4.5.3 Limitations of the proposed model

In the previous section, a semi-empirical model was developed to estimate the damping and stiffness of a collection of TMW particles subject to very low relative motion. The underlying assumption of this model is that the dynamic strain has a limited effect on the performance. To evaluate the performance of dynamic

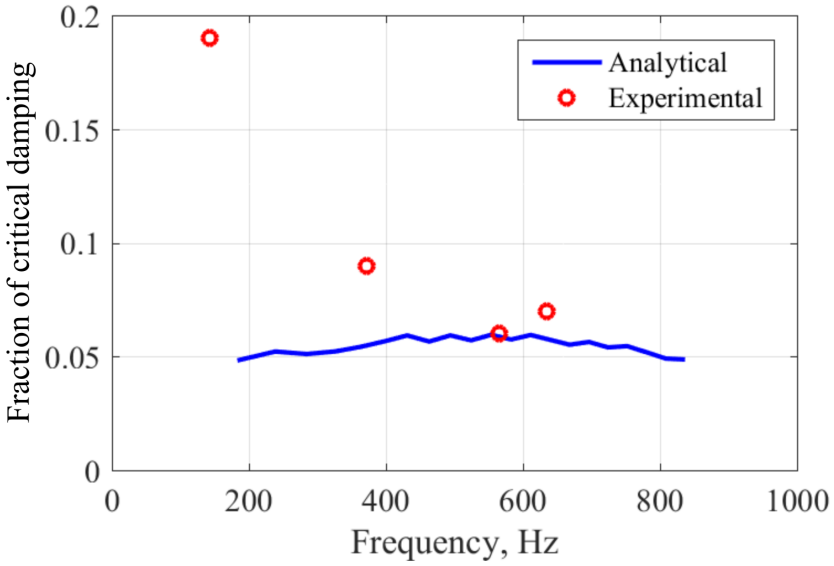

Figure 4.41: Comparison of damping between analytical model and experimental results subject to different static compressions

strain, comparison of the stiffness was carried out and the results are shown in Figure 4.42.

As has been demonstrated in Figure 4.42, massive differences in stiffness can be observed for these particles when subject to different dynamic strain. High dynamic strain promotes interwire friction, and therefore softens the overall system and increases the capability of the energy dissipation massively. In terms of establishing an analytical model, it is vital to figure out a reliable relationships between the dynamic strain and stiffness. Once this relationship is established, an independent three dimension mapping routine can be developed for the proposed model to increase the accuracy of the prediction.

The other uncertainty for the developed model is the equivalent elastic modulus of the stack of TMW particles. The modulus in the current routine is obtained using the curve fitting from the modified Neo-Hookean solid model. The stiffness of the collection of particles was calibrated using a resonance rig with relative low dynamic strain. A main challenge is to achieve the accuracy of the stiffness-modulus model. To ensure the completeness of the proposed model, extra

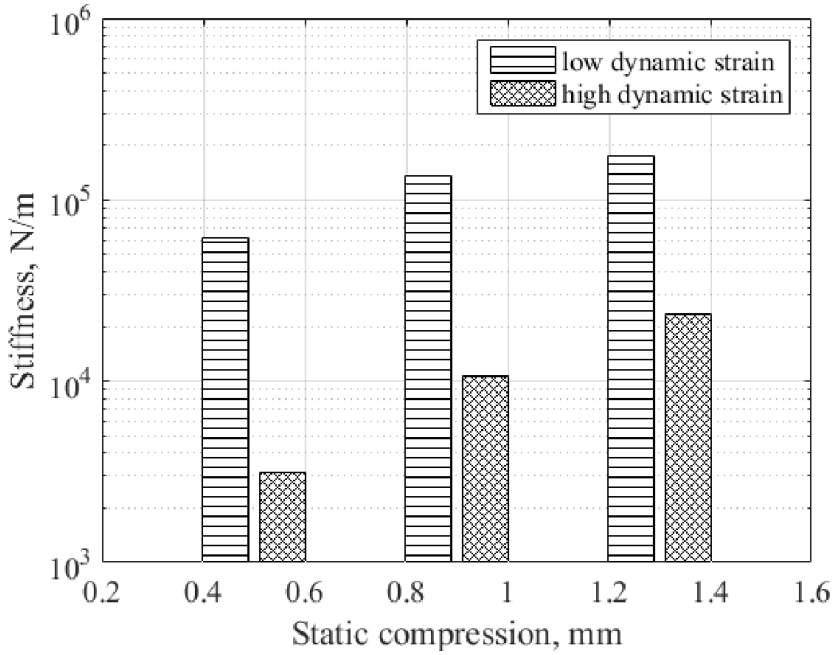

Figure 4.42: Comparison of stiffness for TMW particles subject to different dynamic strain

experiments need to be carried out. In addition to the proposed model, two other strategies can be applied to obtain this effect modulus.

One classical way is to characterise these collections of particles using a dynamic compressive test machine. The stiffness and damping can be identified using a time-domain hysteresis loop. Since the TMW particles have no Poisson's effect, the elastic modulus of this collection of particles can be represented as,

$$E = \frac{kl}{A} \tag{4.35}$$

where k is the stiffness identified from the hysteresis loop, l and A are the thickness and the cross-sectional area of this elastic medium, respectively.

The other way to predict the modulus is to consider this stack of particles as randomly packed high-loss elastic spheres. Walton [106] derived the expressions of equivalent elastic modulus. The Young's modulus is given by,

$$E = \frac{1-2\nu}{2}\left(\frac{3E_v^2\phi^2N^2p}{\pi^2(1-\nu^2)}\right)^{\frac{1}{3}} \tag{4.36}$$

where E_v is the elastic modulus of individual TMW particles, ϕ is the packing ratio, N is the average number of contact points per particle and p is the confining pressure of these particles.

A series of dynamic compressive tests on the individual TMW particles was carried out to identify the stiffness and damping of the particles. Following Lindley's work [35], the elastic modulus of a smooth sphere can be estimated using,

$$E_v = \frac{1.5k}{x^{0.5} D^{0.5}} \tag{4.37}$$

where x is the applied displacement and D is the nominal diameter of the sphere. A face-centred cubic (FCC) arrangement was selected because significant gaps exist in the outer surface of these particles. As a result, a high packing factor and coordinate number are achieved.

The gravity of this low wave speed medium causes the variation of the pressure alongside the thickness, and therefore, the confining pressure can be obtained using,

$$p = \rho_v g h \tag{4.38}$$

where ρ_v and h are the effective density and the thickness of the medium, respectively. Rongong [107] has indicated that this equivalent fluid can achieve reasonable accuracy, only when the depth of the medium is small. The detailed parameters used to define these TMW particles are listed in Table 4.10.

Parameters	Symbol	Value
Packing ratio	ϕ	0.74
Coordination number	N	12
Gravity, ms^{-}2	g	9.81
Density of TMW blocks, kgm^{-}3	ρ_v	509.29
Poisson's ratio	ν	0

Table 4.10: Relative dynamic displacement of proof mass in this TMD (base excitation = 3 g)

Strategy	Experimental source	Dynamic strain	Elastic modulus
A	Three layers of TMW particles	low	1.35 MPa
B	Three layers of TMW particles	high	0.13 MPa
C	Individual TMW spheres	high	1.97 MPa

Table 4.11: Comparison of equivalent elastic modulus of TMW medium using different strategies

Comparison of the equivalent modulus obtained using these three different models is listed in Table 4.11.

It can be seen from Table 4.11 that direct modelling of these particles as a hysteretic block achieves the lowest modulus. One probable reason is the uncertainty from different samples. Since the overall number of particles is not enough to squeeze out the uncertainty from the manufacturing of the particles, this noise is difficult to remove entirely. Also, the dynamic strain applied to the particles is much higher than with the TMD. More interwire frictions may be observed in the cyclic procedures. As a result, estimating the stiffness using this route may cause underestimation compared to the practical device.

In contrast to the procedure of modelling equivalent elastic solids, the modulus identified from a model using individual TMW particles exhibited the highest value among these models. In this model, the ensemble average of 50 particles was used to remove the variation of the properties of the TMW particles from the manufacturing process. However, the TMW particles were assumed to be smooth in the current model. The filling fraction and contacts between neighbouring particles were under-estimated. Low frictional force was identified in this model. Therefore, the modulus of these particles is well over-estimated.

Comparison of frequency-dependent damping among these three routes is shown in Figure 4.43.

It can be seen from Figure 4.43 that the damping of this TMD is strongly affected by the choice of modelling strategy. Hence, it is important that a suitable strategy is chosen.

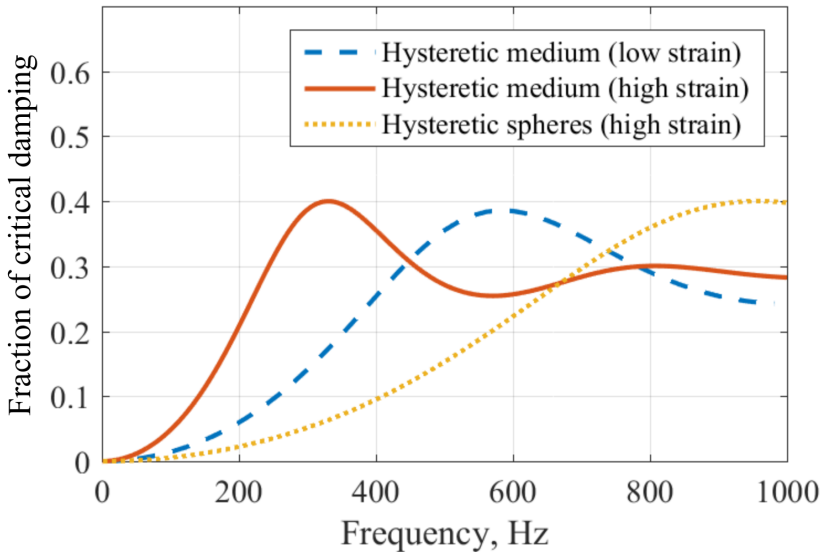

Figure 4.43: Comparison of frequency-dependent damping obtained using three different strategies

4.5.4 Summary and further work

In this section, an innovative routine was developed to predict the strain-dependent stiffness and damping of this TMD. A brief summary is provided below.

- The stiffness and damping for a given TMW TMD without static compression need to be calibrated first. Using the developed stiffness model of layers of these TMW particles - see Equation 4.23 and 4.24, the performance of this device in various static compression conditions can be obtained.
- Damping of these layers of TMW particles was measured using a dynamic compressive test machine. The static strain-dependent loss factor could then be estimated using the empirical model developed.
- Using the hysteretic medium approach, the localised mode shape in the transverse direction to the motion of the damper was calculated and then the energy dissipation of the overall system could be predicted, provided that the effect of wave motions was taken into account.

- Once the master curve of the stiffness and damping of TMW TMD was developed, the full working conditions of this damper were mapped.

Some further recommendations on the developed model are identified below.

- The effects of the static compressions need to be tested using extra samples of the TMW particles. Verification of the developed model for static strain-dependent stiffness needs to be carried out.
- The effect of the dynamic strain needs to be evaluated and modelled numerically in this developed model. It has been shown that the dynamic strain has a great effect on both the resonance peak and width of this TMD.
- As indicated in Figure 4.35 , the stiffness and damping changes for different loading directions were slight. Permanent plastic deformations and sliding may occur when strain is applied to the TMW particles. A model needs to be developed to evaluate this effect of loading history.

4.6 Response of the box beam with TMW TMD

This adjustable TMD, whose calibration was reported in the previous sections, was attached to a box-section beam. The host structure was identical to that used in the Chapter 3. Using this beam, the effectiveness of this TMD on multiple vibration modes was evaluated. The performance of this TMD was then compared with a TMD incorporating an elastomeric O-ring.

The test configurations of the beam TMD are shown in Figure 3.58 and Table 3.11. The sensor and data acquisition system was the same as those used to evaluate the performance of the TMD incorporating O-rings. This adjustable TMD was attached in the same location as the TMD with O-rings. A random excitation with a frequency range from 0 to 1000 Hz was used to obtain the accelerance of the system. The results are shown in Figure 4.44.

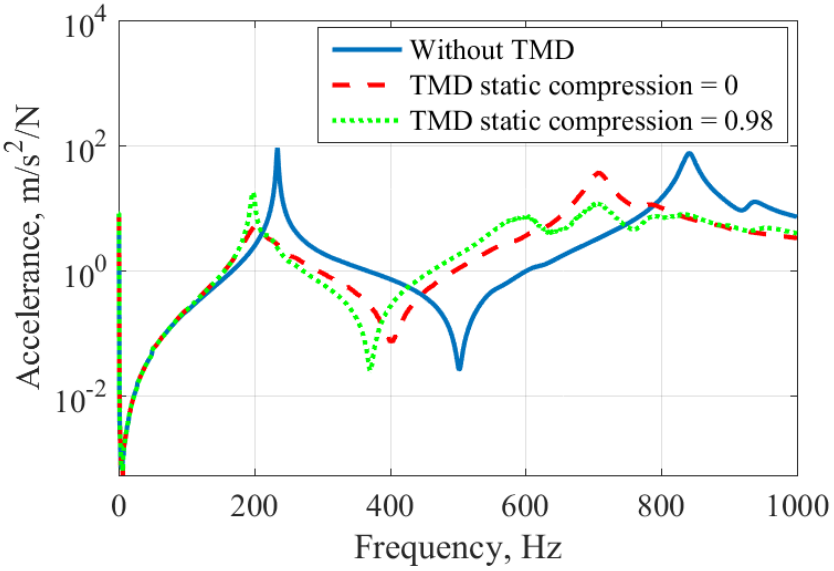

Figure 4.44: Effect of the adjustable TMD using TMW particles subject to different static compressions

It can be seen that this adjustable TMD can target a selected resonance of the beam. The TMW damper is more sensitive to static strain then the O-ring damper, allowing a greater range to be addressed. However, because the TMW layers are also thicker than the O-rings, set values are easier to achieve in practice. One possible problem when using a random excitation source is that the performance may affect by the low frequency components of the excitation. Large dynamic displacement may be activated, and therefore a higher frictional damping can be observed. To remove this undesirable behaviour, a controlled-amplitude stepped sinusoidal signal was used and comparisons of the performance of TMW particles and O-rings were carried out. The accelerance FRFs of the beam are shown in Figure 4.45.

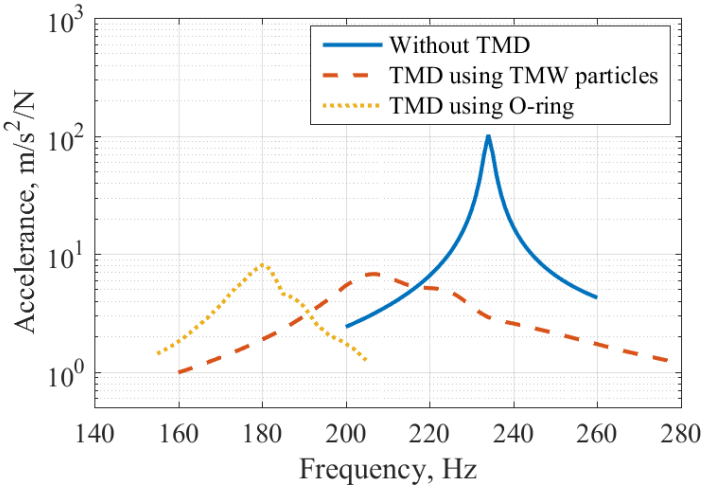

(a)

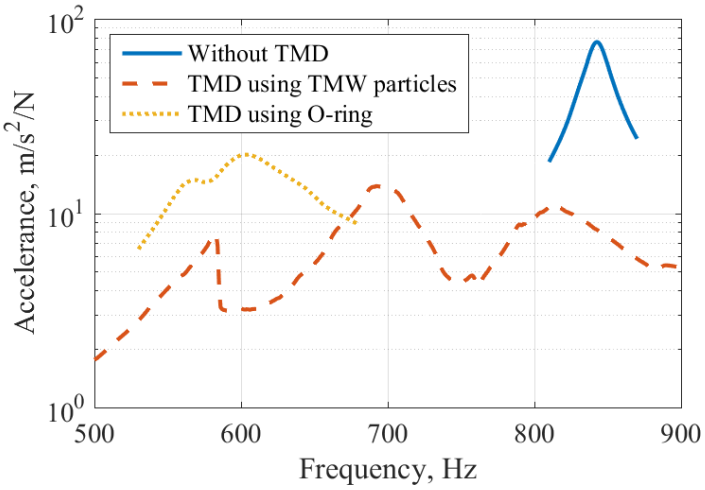

(b)

Figure 4.45: Effect of adjustable TMD on the rubber-ended beam (a) 1st mode (b) 2st mode

Figure 4.45 indicates that the performance of this adjustable TMD was identical when subjected to both random and stepped sinusoidal excitation source. Also, it can be seen that the performance of this TMD is similar to that of the TMD with elastomeric O-rings. As mentioned in the beginning of this chapter, this TMD with TMW particles can maintain its effectiveness at high tempera-

tures. Also, the overall weight of this TMD is much smaller than that of a TMD incorporating O-rings. Details are listed in Table 4.12.

	O-rings	TMW particles
Mass of the TMD	320g	78g

Table 4.12: Mass of the TMD

It is also important to note that most of the mass of the TMW TMD is associated with the cavity, while in the O-ring TMD the effective mass is in the proof mass. Eventually therefore, the weight of the TMW TMD can be reduced further.

4.7 Conclusion

This chapter describes a preliminary study of a TMD using Tangled Metal Wire particles. For extreme high temperature mechanical applications, this TMW TMD provides a relatively consistent performance under selected working conditions. The adjustable tuning of this device can be achieved using the static and dynamic strain-dependent stiffness of these particles. A useful level of damping also preserves for this TMW TMD, especially when this damper was attached on a host structure. Compared with classic polymeric TMD, this damper is much lighter. As a result, this damper has a less influence on the modal properties of the host structure.

When characterising single TMW particles, drop-rebound tests were introduced to estimate the damping from the TMW particles at tiny strain. A configuration of the particle damper was then used to demonstrate the energy dissipation for a collection of particles. All of these tests indicated that damping from these particles at low strain is lower than that at high dynamic displacement. The individual TMW particles provide significant damping when relative strain on the particles is large. The controlled adjustable stiffness can be achieved regardless of static and dynamic strain.

Since the stiffness and damping is very sensitive the internal configurations of the individual particles and loading histories, the characteristics of a collection of TMW particles were carried out. Results from experimental investigations for the collections of particles showed some levels of randomisation for the stiffness and damping, when subject to different dynamic displacements and static compressions. The static compression-dependent stiffness could still be seen for a given collection of particles, and, the variation of the damping was observed as well. Repeatability of the properties cannot be achieved for both the individual and the collection of particles. Thus, each TMD needs to be calibrated before application to a practical structure.

A semi-empirical model of the TMD with TMW particles has been developed successfully, especially in the case where the dynamic strain is high. The equivalence of the TMW particles and hyperelastic material was assumed, and hence the Neo-Hookean model was introduced to predict the static compression-dependent stiffness with a correction factor. The approach to damping, however, is based on the assumption of internal resonances of the low-wave speed damping medium. The proposed model has shown great accuracy for the stiffness, while it only worked for the damping at high static compressions.

Overall, the proposed TMD can target multiple modes on a continuous structure. It has also demonstrated that this damper has a higher temperature capability and lower weight than the TMD using O-rings.

Although some investigations on the properties of the TMW particles and TMD were carried out, a great number of limitations are still to be resolved. Some of the principal issues and potential solutions are listed below,

- Large variations of the individual TMW particles can be observed. One of the main reasons for these variations comes from the manufacturing process. A more controlled fabrication procedure need to be developed to ensure more consistent micro-structures. When the TMW particles are characterised, uncertainties of determining the initial compression lead to great errors because these properties are sensitive to the strain.

- In the drop-rebound tests, the rotational energy occupies an important role in calculating equivalent coefficient of restitution, and therefore damping. In the current tests, the rotational speed of the particle is estimated roughly. A better method need to develop to evaluate the performance of the particles.

- Since there only exists a limited number of the particles with similar geometric properties, more repeatability tests are required for each configuration of the TMW particles. Therefore, the repeatability of the TMW particles can not be concluded in this study.

- In the semi-empirical model, uncertainties of the analytical expressions for the stiffness exists due to the lack of experimental data. When calibrating the TMW TMD, more experiments need to be carried out at different static compressions. The other important features of the TMW particles are dynamic-strain dependent stiffness and damping. These properties need to be included in the analytical model to ensure the accurate prediction of this damper.

The feasibility of the TMW TMD has been demonstrated in this chapter. The significant damping can be observed for this adjustable damper when it attached on the host structure. A preliminary analytical model was given for the purpose of the design these dampers. Considering this type of adjustable TMD, the controlled nonlinear stiffness is very important. The next chapter focuses on development of the design criterion for a TMD incorporating some nonlinear elements.

Chapter 5

Optimal design criteria for TMDs

5.1 Introduction

Previous chapters have demonstrated that an adjustable TMD can achieve excellent multi-mode vibration suppression of a typical engineering structure. A critical topic in using TMDs is the optimisation of the dynamic parameters of the secondary oscillator. Generally, the classical design criteria for a TMD with, only one working mode, are based on the fact that two invariant points always exist on the frequency response function of the host structure with respect to different TMD damping ratios, as shown in Figure 5.1.

The applicability of the classical design criteria vanishes when: 1) several working modes of the TMD are able to suppress the structural vibration simultaneously; 2) strain-dependent nonlinear stiffness and damping elements are incorporated in the TMDs; 3) the damping of the host structure is high. In this section, several different strategies, including numerical investigations and innovative energy transfer concept, are applied to improve the performance of the TMDs for a wide range of working frequencies. The potential of applying these methods to a nonlinear TMD is also investigated.

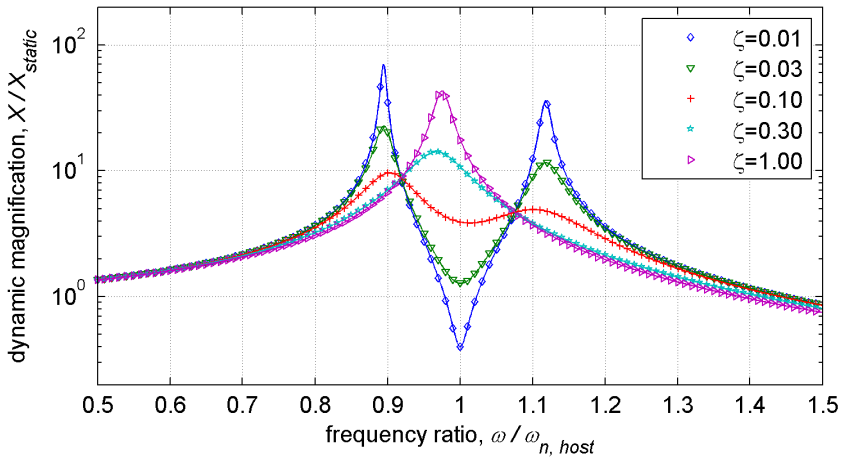

Figure 5.1: TMD performance for various damping ratios when $\omega_{\mathrm{n,tmd}}/\omega_{\mathrm{n,host}}$ and the mass ratio $\mu = 0.5$

5.2 Parametric optimisation of the TMD using the Differential Evolution algorithm

To overcome the limitations of the classic TMD, a numerical search method, Differential Evolution (DE), was applied to identify the optimal stiffness and damping of the TMD in a realistic engineering scenario. The basic idea of this method is to determine the minimum value of the selected evaluation function efficiently using an iteration procedure.

5.2.1 The Differential Evolution algorithm

This section introduces the numerical search algorithm used in this part of the study. The optimisation of a linear TMD is used as an example to describe how this numerical mapping method works. A schematic diagram showing the use of differential evolution to design a TMD is shown in Figure 5.2.

To explain the DE algorithm, certain concepts need to be defined using the proposed SDOF-single TMD (SDOF-STMD) example, as shown in Figure 1.1. Details of these definitions are listed below:

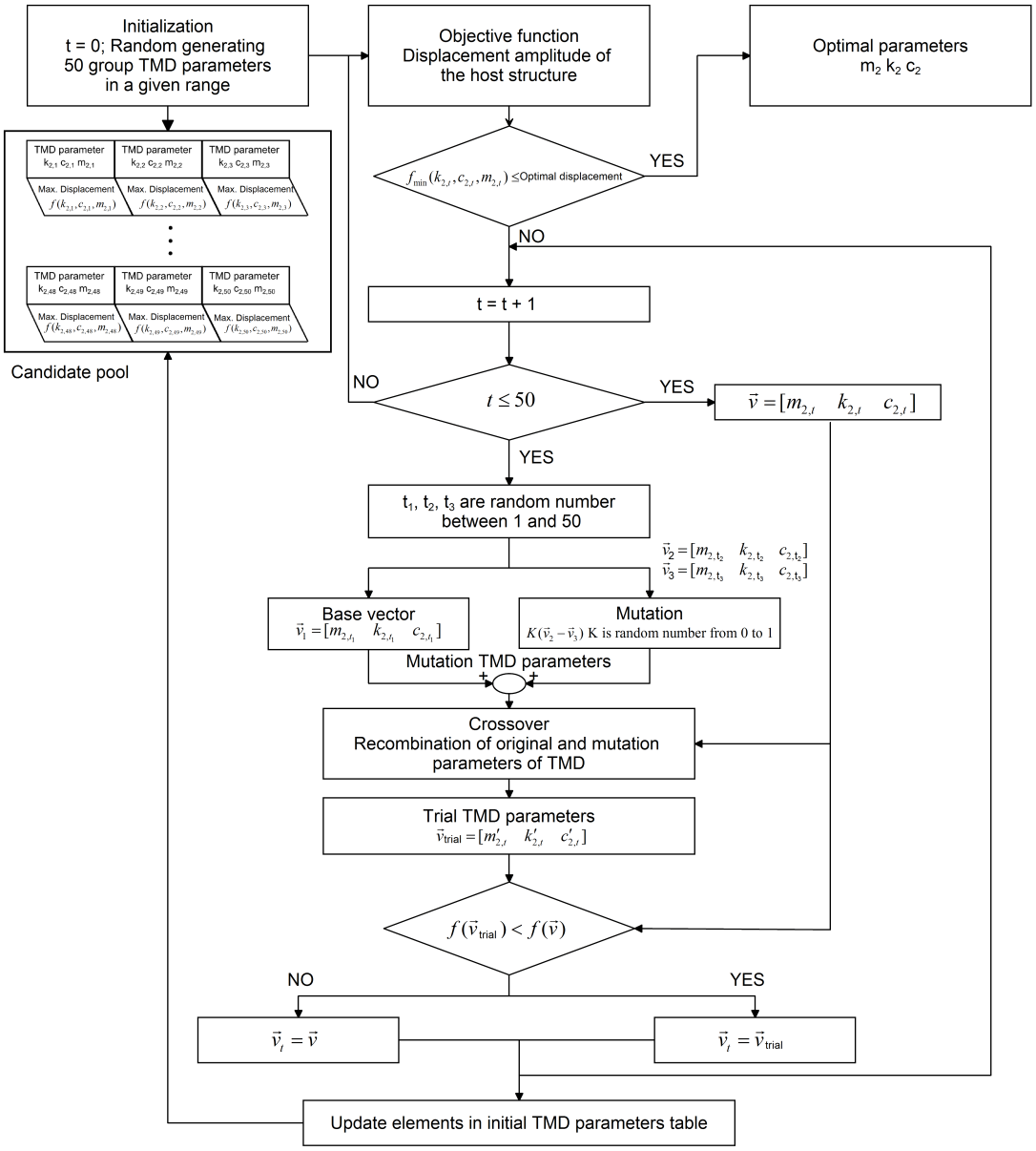

Figure 5.2: Differential Evaluation algorithm for optimisation of TMD

- Candidates – vectors of the parameters that are required to design a TMD.
- Candidate pools – a group of candidates (50 Initial candidates).

- N^{th} generation – the parameter vectors in the N^{th} candidate pool need to be evaluated.
- Objective function – the minimum value for this function needs to be found. In the flow chart, the peak displacement amplitude of the host structure is the selected objective function.
- Targeted candidate solution – selected sets of the design parameters of the TMD that need to be updated in a given generation.
- Trial candidate solution – the candidates that need to be evaluated in the given generation. This candidate solution also provides new initial components of the pools in the next generation.

The design candidate comprises mass (m), spring stiffness (k) and damping ratio (c) for the secondary oscillator. Proper restricting ranges can be applied to these candidates to increase the searching speed in this simulation. Initially, the code generates a trial pool of 50 candidate solutions with equal probability. This initial pool works as the first generation in the whole procedure. A certain targeted candidate is selected in this initial generation. The performance of the TMD designed using this candidate is evaluated using the objective function. A series recombination process was then performed to develop a new candidate in the next generation when the response of the host structure is higher than the desired level.

In a DE algorithm, the core strategies for speeding up the calculation are the parameter updating technologies using recombination processes - mutation, crossover and selection. Mutation in terms of the DE algorithm means that some elements of a particular candidate (i.e. stiffness, mass or damping ratio) are replaced by a linear combination of the other candidates and a random multiplier in the same generation. Mathematically, the mutated candidate can be represented as,

$$\bar{v}_m = K\left(\bar{v}_2 - \bar{v}_3\right) \tag{5.1}$$

where $\bar{v}_2$ and $\bar{v}_3$ is the candidate other than the one evaluated in a given generation, K is any random number that is between 0 and 1.

Following this process, cross-over of the mutated and the targeted candidate, as shown in Figure 5.3, is introduced to produce the selected trial candidate.

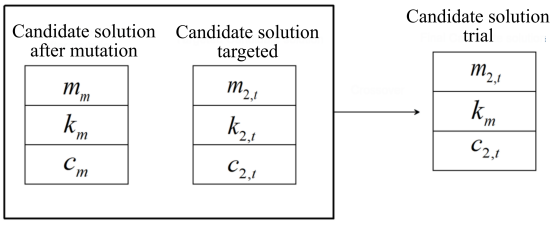

Figure 5.3: Typical cross-over procedures for a TMD in the DE algorithm

Eventually, comparisons of the objective function result using the trial and the original candidate are carried out and the best candidate is selected as the final candidate. Considering the TMD design criteria, possible options for the objective function include,

- peak displacement amplitude of the host structure
- sum of peak kinetic energy of the host structure over the frequency range of interest
- sum of the peak dynamic stress of the host structure for selected vibration modes

When a selected candidate does not meet the targeted levels of vibration mitigation, this candidate passes into the components of the initial pool for the next generation. The whole procedure is repeated until a TMD with better performance is produced. This procedure is halted once the structure with TMDs reaches the desirable vibration level.

In practice, the optimal response of the host structure is sometimes unknown. In this case, the algorithm can not determine when to finish the automatic calculations. One possible solution is to set a certain number of iterations. In the

analysis described below, the targeted result from the objective function with the optimal candidate was always set to zero – a value that is impossible to achieve. The optimisation procedure was paused when the set number for the generation was achieved. The alternative design requirement – the identical last 10 sets of optimal candidates – was configured. The DE code continued running until this new set requirement was achieved.

5.2.2 Verification of the DE algorithm

In this section of the work, optimisation of the TMD using the DE algorithm was introduced for the purpose of designing a nonlinear and multi-mode TMD, noting that the multi-mode TMD refers to a device that utilises more than one vibration mode to target a structural vibration over a wide frequency band. The SDOF-TMD system was used to verify the effectiveness of the DE algorithm in designing TMDs. The classic and widely accepted TMD design criteria [108] were used as the optimum reference. As in the classic optimisation routine, the objective function chosen was the highest displacement response of the main structure. Comparisons of the optimal TMD gained using classic strategy and the DE algorithm are shown in Figure 5.4.

Figure 5.4 shows that the optimal parameters gained from DE are very close to those obtained using the classic method for both optimal frequencies and damping. Therefore, it can be summarised that the DE algorithm is appropriate for optimising TMDs.

5.2.3 Single TMD targeting multi-mode vibrations

Since engineering structures are usually excited over a broad frequency range, the performance of a TMD on multiple mode vibration was considered worth investigating. The dynamic parameters of the host structure were identified experimentally using a curved pipe. The geometry of this pipe are shown in Figure 5.5.

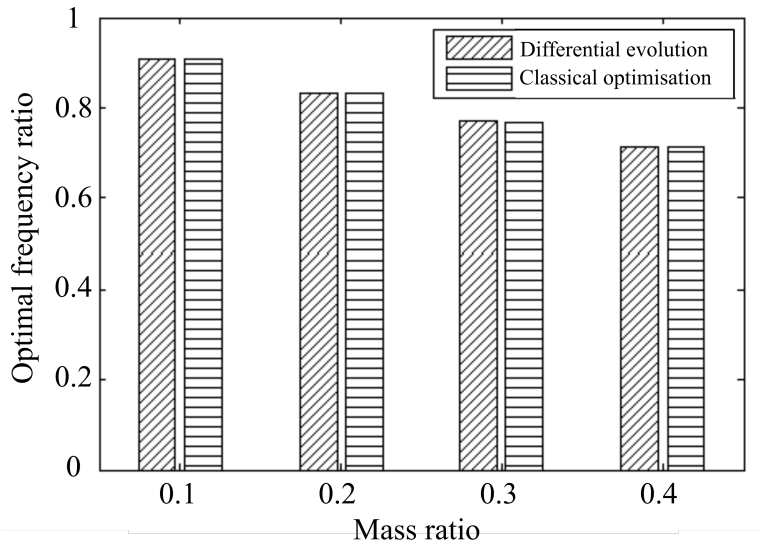

(a)

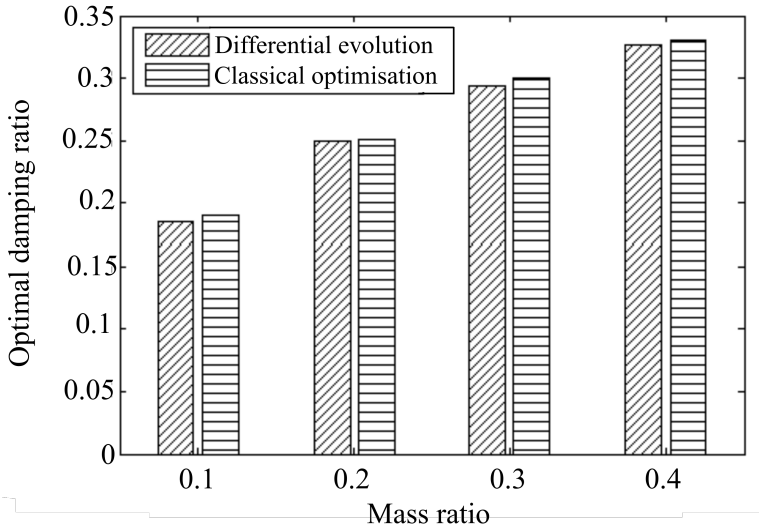

(b)

Figure 5.4: Comparison of optimal damping of TMD gained from DE and classic method (a) optimal frequency ratio (b) optimal damping

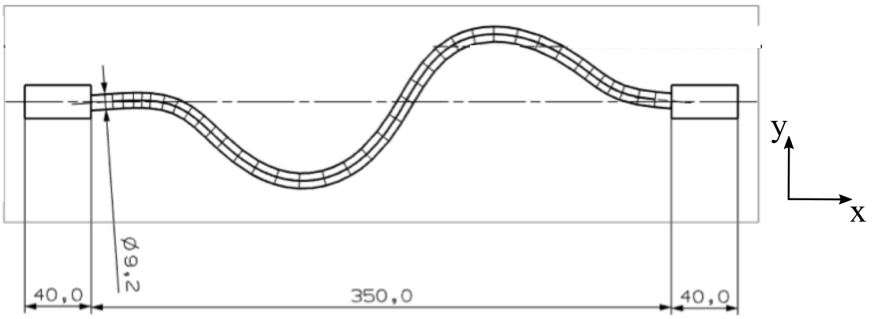

Figure 5.5: Schametic diagram of the curved pipe (unit: mm)

The inner diameter of the hollow pipe is approximately 7.9 mm. The shape of this pipe can be demonstrated as follow,

$$\begin{aligned} y =& 205.7\sin(0.004298x + 0.9456) + 25.1\sin(0.00694x - 2.359) \\ &+ 169.8\sin(0.001236x + 4.301) + 1.583\sin(0.01269x - 3.449) \end{aligned} \tag{5.2}$$

Using the experimental modal analysis, the modal properties of the first two bending mode can be obtained. The details of these natural frequencies, effective mass and modal damping ratio are shown in Table 5.1,

Mode	Natural frequency, Hz	Effective mass, kg	Modal damping ratio
1	316.9	0.340	1.02×10^{-3}
2	506.2	0.484	8.28×10^{-4}

Table 5.1: Structural dynamic parameters for the host structure

The maximum frequency responses of different modes do not occur at the same position on the pipe. In order to evaluate the maximum response for different modes, the simulation of main structure with TMDs for these two modes was carried out separately. Note that the TMD is located at the position that exhibits maximum displacement for the first mode. For the second mode, a scale factor, $\frac{1}{\phi_1^2\phi_2^2}$, was introduced to ascertain that the effect of mode shape would not disturb the design of the TMD. Note that $\phi_{\mathrm{i}}^{\mathrm{j}}$ represents the mode shape at the position i

for j^{th} mode. The mode shape of this curved pipe can be obtained from Blevins's work [109]. The mode shape vectors used in this section are listed as follows,

The DE algorithm provides an alternative way to obtain optimal TMDs. In this section, the following three design criteria for the TMD are introduced:

- Minimise the maximum displacement for the fundamental mode of the host structure referred to as 'classic'
- Minimise the highest displacement amplitude over the selected frequency range using the DE algorithm referred to as 'DE'
- Minimise the kinetic energy of the host structure referred to as 'min. KE'

To address the narrow bandwidth issue with the traditional TMD, a numerical approach was developed to minimise the highest displacement amplitude over the selected frequencies. In this simulation, the peak displacement amplitude at frequencies up to 1000Hz was used as the objective function. The alternative method for reducing the response over a broad frequency range is to minimise the kinetic energy of the host structure – a multiple DOF (MDOF) system. Often, impact and fatigue damage in a mechanical component is relevant to this vibratory energy. In this section of the work, expressions of optimal stiffness and damping ratio using the KE algorithm were developed according to the work by Warburton [55].

Comparisons of the displacement frequency response of a STMD-MDOF system using different parameter design strategies were carried out and the results are shown in Figure 5.6. The details of the optimal strategies are shown in Table 5.3

Note that X_1 refers to the frequency response of the host structure, F is the applied force spectrum, m_1 is the effective mass of the host structure, ν_{opt} is

1	position where the accelerometer is attached	$\phi_1^1 = 1.717$	$\phi_1^2 = 1.8025$
2	position where the TMD is attached	$\phi_2^1 = 1.050$	$\phi_2^2 = 1.967$

Table 5.2: Mode shape vectors at selected positions of the pipe

Strategy	Targeted mode	Objective function	Optimal parameters
DE	1^{st} & 2^{nd} modes	$\max\left[\frac{X_1}{F}\right]$	-
Classic	1^{st} mode	$\max\left[\frac{X_1}{F}\right]$	$\nu_{opt} = \frac{1}{\sqrt{1+\mu}}$ & $\zeta_{opt} = \sqrt{\frac{3\mu}{8(1+\mu)}}$
Min KE	1^{st} & 2^{nd} modes	$\frac{1}{2}\sum m_1\omega^2 X_1^2$	$\nu_{opt} = \frac{\sqrt{\mu}}{2}$ & $\zeta_{opt} = \frac{1}{\sqrt{1+\mu}}$

Table 5.3: Optimisation criteria of the dynamic vibration absorber

the optimal frequency ratio of the TMD and host structure, η_{opt} is the optimal damping ratio of the TMD and μ is the mass ratio.

Figure 5.6 shows that the classic TMD design works best among these three methods for the first mode while the minimisation of kinetic energy of the main system achieves the best performance for the second mode. Regarding the 'min. KE' strategy, the physical explanation is to minimise the maximum velocity of the host structure. The TMD designed using this strategy is made more sensitive to the resonances at high frequencies. With the TMD designed by the numerical searching method, balance was achieved in minimisation of the peak displacement magnitudes between the first mode and second mode. It can thus be concluded that this work demonstrated the advantages of DE method over other methods for TMD design.

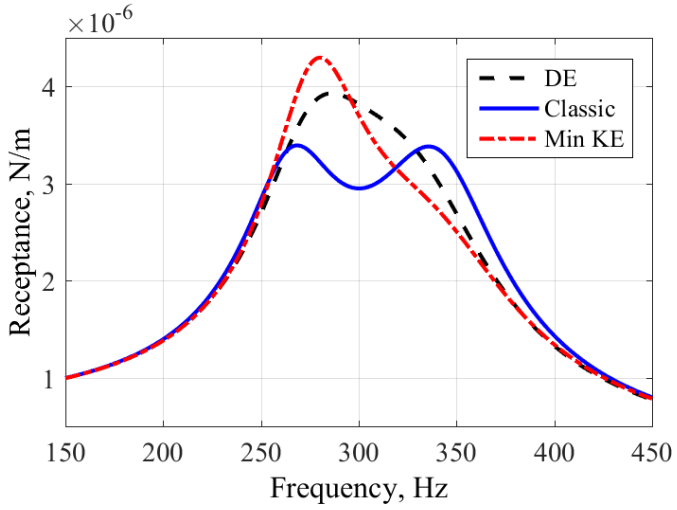

(a)

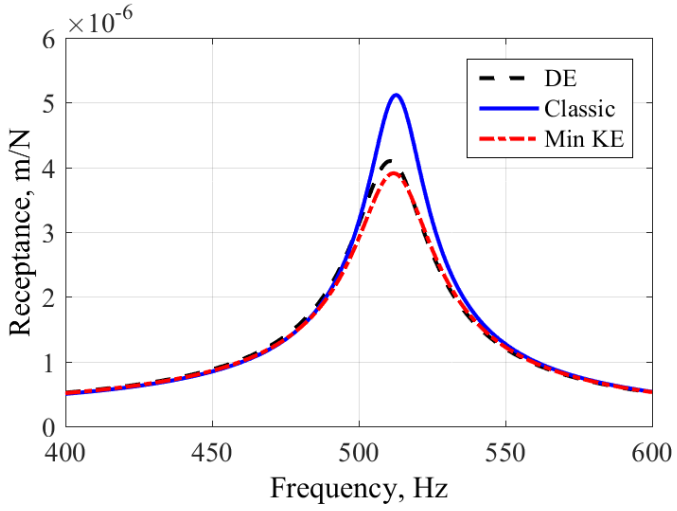

(b)

Figure 5.6: FRFs with TMDs designed by different methods for (a) the 1st mode (b) the 2nd mode (mass ratio of secondary oscillator and main mass = 0.1)

5.2.4 Using multiple TMDs for multiple mode vibration

One of the apparent strategies to reduce multi-mode vibration is to attach multiple TMDs on the vibrating structure. Previously, the lack of strategy for parametric optimisation has been a barrier to developing this kind of device. Since the DE algorithm is a numerical search method, it is much more flexible in dealing with these optimisations. In the following simulations, investigations of multiple TMDs (MTMDs) in the fundamental mode were carried out using different configurations of TMDs. Multiple paralleled TMDs, as shown in Figure 5.7, were then used for vibration suppression over a broad frequency range. Note that only one selected vibration mode was represented as the host structure in Figure 5.7. The objective function chosen in this section of the work is the peak displacement amplitude of the host structure at the selected frequencies.

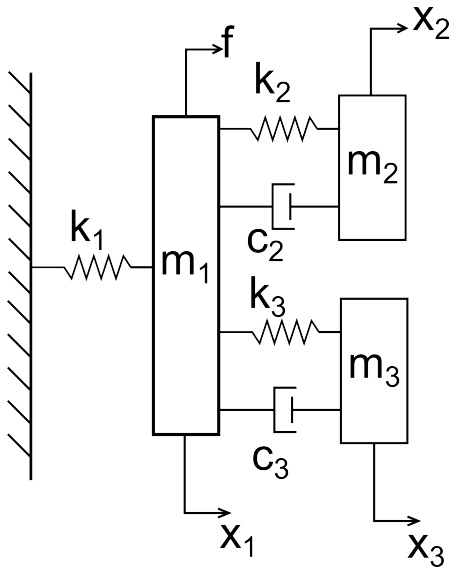

Figure 5.7: Typical MTMD configurations for vibration suppression

The displacement response of the main system for two different TMD configurations: a) SDOF-Two TMD system and b) SDOF-STMD system, is described in Figure 5.8. Only the fundamental mode of a flexible structure is considered here and the total mass for both TMD configurations remains the same. It should be

noted that the mass of the two TMDs is not necessarily equal. The cost function of this simulation is listed below,

$$\text{Objective function} = \max\left(\frac{X_1}{F}\right) \tag{5.3}$$

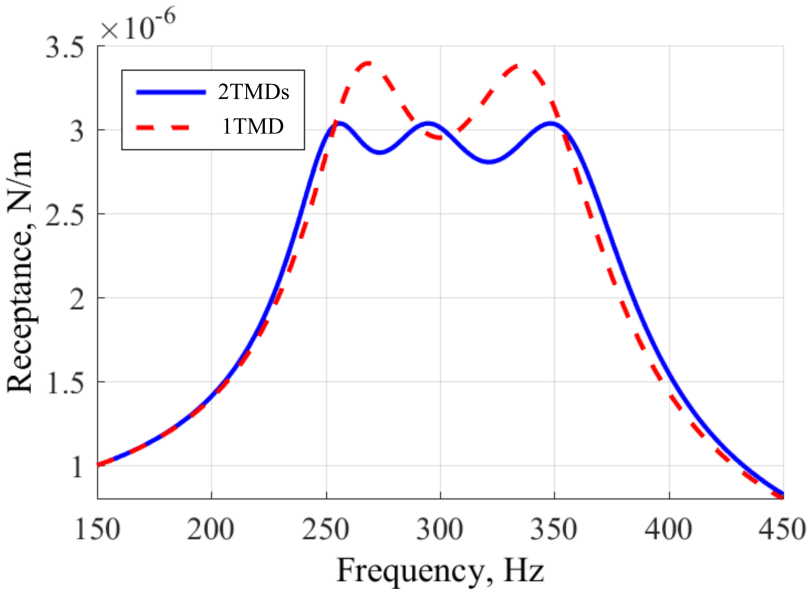

Figure 5.8: Comparison of FRF with 2 TMDs and 1 TMD for fundamental mode. (mass ratio of secondary oscillator and main mass = 0.1)

Figure 5.8 indicates that the SDOF-two TMD system performed slightly better than the optimal SDOF-STMD system. However, it is not usually realistic to use this configuration in a mechanical structure because of limitation space: for example, within the curved pipe insufficient space exists to add additional TMDs. A more realistic approach for designing multiple TMDs is to place them at different positions in a continuous system in order to suppress vibration over a wide frequency range. To optimise the dynamic parameters for different modes of this type of device, a TMD system, involving two parallel connected TMDs was used to suppress the first two bending modes of a curved pipe. In this case, the TMDs could be placed in positions that would exhibit the highest displacement for selected modes.

Three different strategies – two TMDs with equal mass, two TMDs with different mass, STMD – were utilised to suppress the vibration for two given modes of a engineering structures simultaneously, and all the parameters of TMDs were optimised using the DE algorithm. Note that the total mass of the TMDs used in these three strategies was equal. The peak displacement response at selected frequencies up to 1000Hz, as demonstrated in Equation 5.3, was still used as the performance indicator. The results of the simulation are shown in Figure 5.9.

From Figure 5.9, it can be seen that only slight improvements were achieved when multiple TMDs were used. One probable reason is the closeness of the resonances of the two selected modes. It has also been shown that the classic single TMD can suppress the vibration by 96%. There is, therefore, not much room to optimise these dampers. Nevertheless, it can be implied that using the DE algorithm is valid for designing multiple TMDs to suppress multiple mode vibration.

5.2.5 Summary

To conclude, the optimal TMDs designed using the DE algorithm were shown to be acceptable for vibration suppression over a broad frequency range. The key findings regarding TMD design using DE can be summarised as follows,

- The TMDs optimised using the DE algorithm can achieve similar performance for focused vibration mode to the classic TMD when the optimisation indicators are equal. For multiple mode vibration suppression, TMDs optimised using the DE algorithm can perform better than the classic type when the mass ratio of TMD and modal mass of host structure is small.
- Comparing the MTMD and STMD systems optimised using the DE algorithm, it was found that the performance of both systems was similar across the selected frequencies.

Although applying MTMDs is a straight forward algorithm for suppressing multi-mode vibration, the attachment of additional TMDs can significantly change

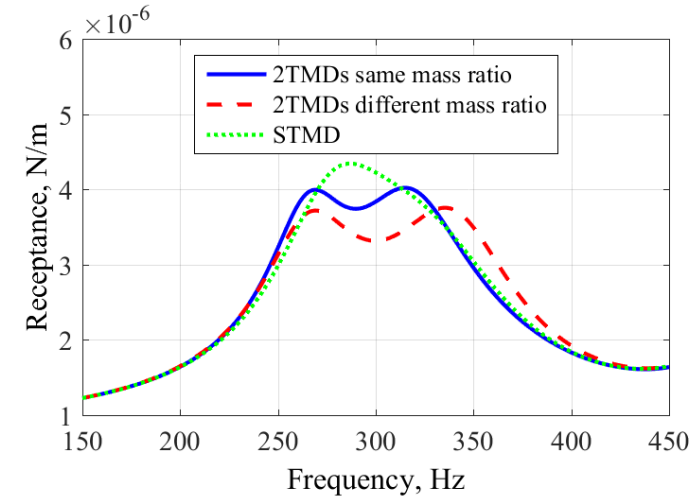

(a)

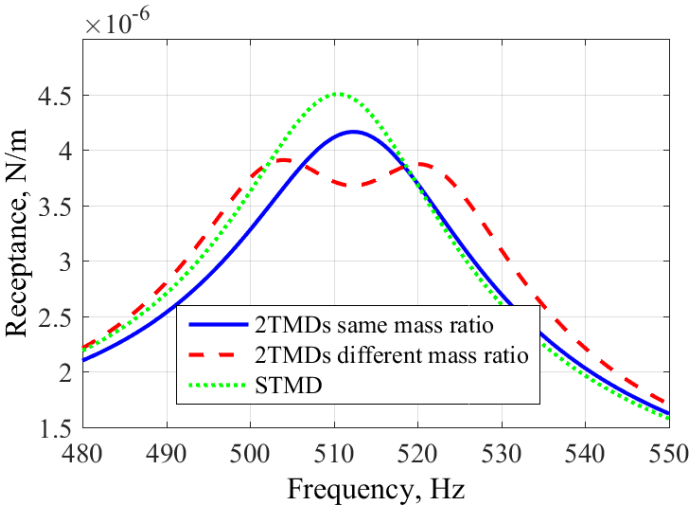

(b)

Figure 5.9: Comparisons of FRF with different TMD configurations optimised using DE algorithm for (a) the 1st mode (b) the 2nd mode (mass ratio of secondary oscillator and main mass = 0.1)

the deformation pattern of the host structure and thus the expected performance from attaching MTMDs might not be achieved. Meanwhile, attaching MTMDs increases the weight of the host structure massively. The alternative choice is to use a multi-mode TMD, such as a TMD incorporating O-rings or TMW particles. These devices have been demonstrated to suppress multiple vibrations effectively. Even with this type of structure, it has been shown that it is feasible to use the DE algorithm to design optimal TMDs.

Although the DE algorithm is useful in determining the minimum displacement for a linear and continuous structure, it cannot be applied directly in the TMD incorporating nonlinear elements. The reasons are as follows,

- The optimisation indicators for the DE algorithm depend on the frequency spectrum of the host structure. However, this method faces critical issues when applied to a TMD with nonlinear behaviour. The lack of well-developed methods to predict the frequency response limits its application. One possible solution is to simulate the system in the time domain, although it is computationally expensive to predict the steady-state time response and this increases the workload in applying the DE algorithm.

- Nonlinearity in a TMD brings about unpredictable responses from the main structure at selected frequencies. The simulation in a fixed period might not predict the entire behaviour of an MDOF-Nonlinear TMD system. The objective function based on this time domain simulation would lead to poor design of the optimal TMD.

To overcome these disadvantages, the harmonic power flow method was developed. In the case of a nonlinear TMD system, the power flow could be much more predictable than the displacement response. Therefore, the possibility exists to use power measurement when incorporating the DE algorithm in designing a nonlinear TMD.

5.3 Resonant power based optimisation for SDOF-TMD system

In this section, the novel TMD optimisation scheme using harmonic power flow method is introduced. The cross-coupling term between two oscillators is used to calculate the average power, which is the optimal indicator to evaluate the performance of the TMD for both vibrating structure and secondary system. The performance of this TMD is then assessed in relation to that of TMDs optimised by other strategies.

5.3.1 An introduction to vibratory power flow method

This section describes the relationship between vibration response and energy flow for a linear system. Both instantaneous and time-average power were used as indicators to demonstrate the amount of energy input to this vibrating system. To keep this section concise, only the SDOF-STMD system is explained here. The power flow equations for a basic SDOF system can be found in Appendix **??**.

Two different strategies, minimisation of absorbed power of the mass of the TMD at the resonant frequencies and minimisation of reactive power over whole frequency ranges, were considered for a linear SDOF-TMD system, as shown in Figure 5.10. The aim of these optimisation schemes was to determine the optimal TMD configurations in terms of gaining peak power from the host structure and a reasonable energy dissipation from damping elements in the TMD. Note that the damping of the host structure is assumed negligible in the following analysis.

It is important to know how the power flow is represented for this SDOF-TMD system. For this 2-DOF system, the Equation of Motion is represented as

$$\begin{bmatrix} m_1 & 0 \\ 0 & m_2 \end{bmatrix} \begin{bmatrix} \ddot{x}_1 \\ \ddot{x}_2 \end{bmatrix} + \begin{bmatrix} k_1 + k_2 & -k_2 \\ -k_2 & k_2 \end{bmatrix} \begin{bmatrix} x_1 \\ x_2 \end{bmatrix} + \begin{bmatrix} c_2 & -c_2 \\ -c_2 & c_2 \end{bmatrix} \begin{bmatrix} \dot{x}_1 \\ \dot{x}_2 \end{bmatrix} = \begin{bmatrix} f \\ 0 \end{bmatrix} \tag{5.4}$$

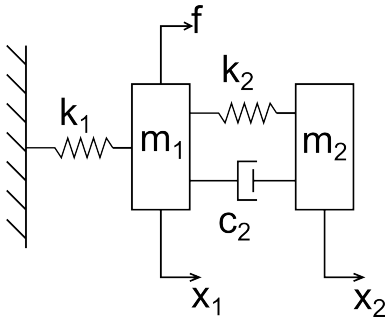

Figure 5.10: Theoretical SDOF-TMD model

From Equation 5.4, the energy equation for this 2-DOF system can be given by

$$\frac{1}{2}\left[m_1\dot{x}_1^2 + k_1x_1^2 + m_2\dot{x}_2^2 + k_2\left(x_1 - x_2\right)^2 + c_2\left(\dot{x}_1 - \dot{x}_2\right)^2\right] = fx_1 \tag{5.5}$$

It can be seen from Equation 5.5 that the energy flow between host structure and additional mass can be represented as $k_2\left(x_1 - x_2\right)^2 + c_2\left(\dot{x}_1 - \dot{x}_2\right)^2$. To simplify the derivation, the initial phase of secondary mass is assumed to be zero. The displacement of the secondary mass may be expressed as

$$x_2 = X_2 \sin\left(\omega t\right) \tag{5.6}$$

The displacement of the host structure may be given by

$$x_1 = X_1 \sin\left(\omega t - \phi\right) \tag{5.7}$$

The averaged energy per cycle for the secondary oscillator can be given by

$$E_{\text{TMD}} = \frac{\frac{1}{2}\int_0^{\frac{2\pi}{\omega}} k_2\left(x_1 - x_2\right)^2 + c_2\left(\dot{x}_1 - \dot{x}_2\right)^2 dt}{\frac{2\pi}{\omega}} \tag{5.8}$$

This time-averaged energy may also be obtained by substituting Equation 5.6 and 5.7 into Equation 5.8. After some reorganisation, this energy is given by,

$$\begin{aligned} E_{\text{TMD}} = \frac{1}{2}&\left(\frac{k_2X_1^2}{2} + \frac{k_2X_2^2}{2} - k_2X_1X_2\cos\phi\right) \\ &+ \frac{1}{2}\omega^2\left(\frac{c_2X_1^2}{2} + \frac{c_2X_2^2}{2} - c_2X_1X_2\cos\phi\right) \end{aligned} \tag{5.9}$$

To maximise the power transfer away from the main structure, both the strain energy and energy dissipation for this secondary system need to be pushed to the maxima. However, this condition can never be achieved because phase delay between the host structure and TMD blocks the energy transfer. To achieve balance in this contradictory situation, the absorbed instantaneous power can be introduced as an optimal indicator in this analysis because the responses of both primary and secondary mass are considered when using this expression. Physically, these terms demonstrate the amount of energy generated by the movement of the host structure that is input to the TMD and the energy dissipation involving the secondary oscillator. The free body diagram of this secondary system is shown in Figure 5.11.

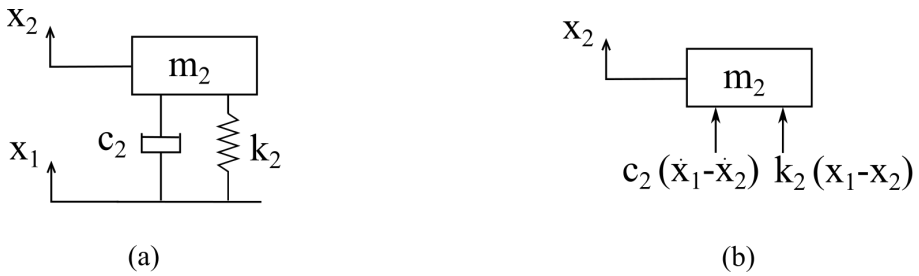

Figure 5.11: Schematic digram of the Tuned Mass Damper (a) loading arrangement (b) free body diagram

The power expression for the secondary mass of the TMD can be written as,

$$P(t) = \left[k_2 \left(x_1 - x_2\right) + c_2 \left(\dot{x_1} - \dot{x_2}\right)\right] \dot{x_2} \tag{5.10}$$

In this work, the objective of the TMD design is to transfer more power into the secondary system. Like the power flow method for the SDOF system, the complex power for the secondary mass is defined as

$$P\left(\omega\right) = \frac{1}{2} \left(k_2 + j\omega c_2\right) \left(X_1 - X_2\right) j\omega X_2 \tag{5.11}$$

5.3.2 Understanding the resonances of SDOF-TMD system

In general, a TMD is used in order to reduce the response of the host structure near resonances. The approach considered here is optimisation based on complex power at resonances.

5.3.2.1 Influences of the stiffness and damping on the resonance frequencies

Since the proposed strategy focuses on the resonance of the typical SDOF-TMD system, the effect of stiffness and damping of the TMD on these resonances was investigated using complex eigenvalue analysis.

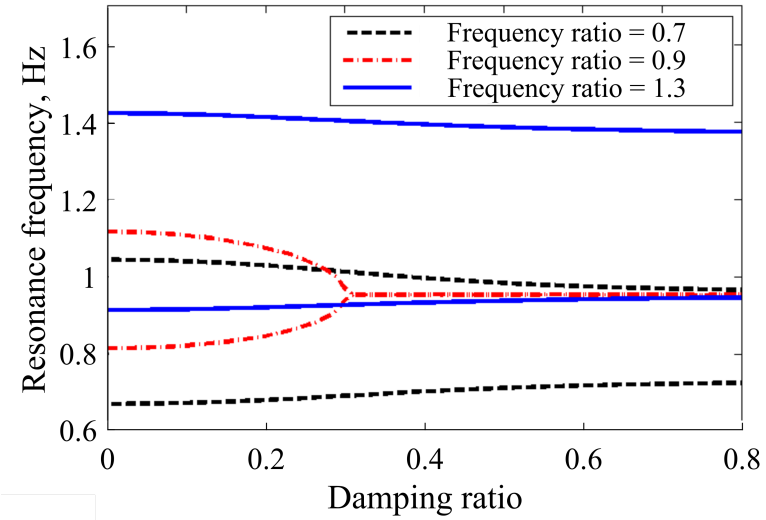

Figure 5.12: Resonance frequencies for SDOF-TMD system with different TMD damping ratios(dynamics parameters: $m_{\text{host structure}}$=1 kg, $f_{\text{host structure}}$=1 Hz, $M_{\text{secondary oscillator}}$=0.1 kg)

Figure 5.12 indicates that the two resonances of this 2DOF system tend to merge into one with the increase of damping, especially when the natural frequency

of the TMD is close to that of the host structure. When the inherent damping is low, there is very limited blocking of energy transfer, and therefore, this SDOF-TMD system still demonstrates the behaviour of a typical 2DOF system. With the increase of damping, the phase shift between the main system and secondary mass tends to zero. As a result, the two peaks in this frequency response merge into one and the energy dissipation of the secondary oscillator occupies a more important role than energy transfer. In the following analysis, the average of the power at resonances was used as a performance indicator.

Since the complex power linked both resonances for the host structure and the TMD, it is worth understanding the frequency difference between these two systems.

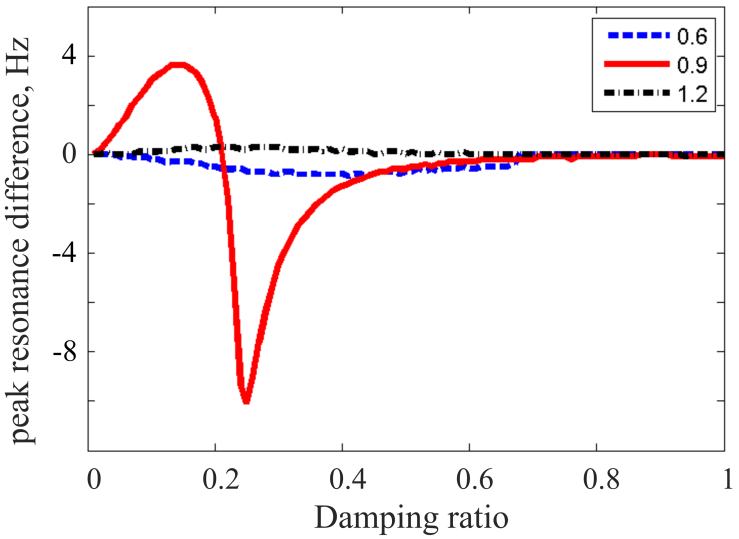

Figure 5.13: Resonance frequency difference between host structure and TMD against damping subject to different stiffness of the TMDs

Figure 5.13 shows the difference in resonance frequencies between the host structure and secondary system. It can be seen from this figure that the resonance frequency of the TMD coincides with that of the host structure, except in the situation where the natural frequency of the TMD is close to that of host structure. When the frequency ratio of host structure and TMD is close to one, a variation

from 4 Hz to 9 Hz occurs when damping of the TMD is approximately 0.2 to 0.4 due to the existence of two resonance peaks. The highest peak may not occur for the same vibration mode, and thus a sudden jump can be observed in Figure 5.13. Nevertheless, both the TMD and host structure still achieve their maximum displacements near the resonance of the host structure.

To evaluate the role of damping for the secondary system, the resonance phase difference between the host structure and TMD against damper stiffness was investigated. The result is shown in Figure 5.14.

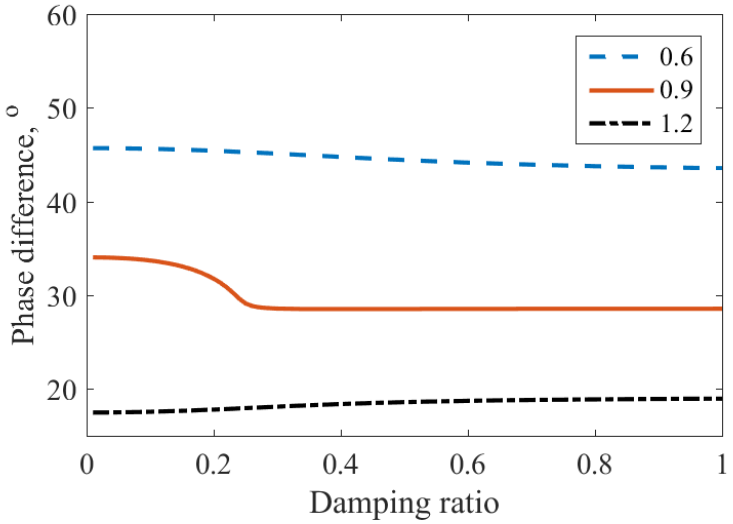

Figure 5.14: Phase difference between host structure and TMD against damping subject to different frequency ratio of TMD and host structure

It can be seen from Figure 5.14 that the energy dissipation of the TMD is much more sensitive to the natural frequencies than to the damping. With the increase of damping, the energy dissipation remains unchanged when the resonance frequency of the TMD is far away from that of the host structure. Meanwhile, an obvious transition can be observed in the phase difference-damping curves when the TMD is near its optimal frequency region. Physically, this transition is caused by the merging of two resonance peaks. Nevertheless, this phase difference is only up to 6° and can be negligible. It can be concluded that the damping of the

secondary system is less sensitive to the energy dissipation than the stiffness of this TMD.

5.3.2.2 Understanding the absorbed power at resonances

In this section, the physical meanings of the absorbed complex power at resonance is explained. The mechanics of the vibration suppression for a TMD-SDOF system is listed as follows:

- energy dissipation from the movement of the host structure,
- energy dissipation from the movement of the TMD,
- energy transfer from the host structure to the secondary mass,

Referring to Equation 5.11, the absorbed complex power represents the energy flow into the secondary system. Figure 5.14 indicates that variation in energy dissipation of the TMD at resonance is almost negligible for different levels of damping. With minimisation of power transferred from the secondary mass, the energy transfer from the movement of the main system becomes significant. Meanwhile, more power may flow into the secondary oscillator as the energy dissipation is partially restricted. Also, the instantaneous absorbed energy of the secondary system is only relevant to the TMD, while the power of the main structure is affected by both host structure and the TMDs. Therefore, the absorbed complex power at resonance is chosen as a performance indicator.

5.3.2.3 Optimisation results

In this section, the resonant power flow algorithm was applied to investigate the suitability of optimising the classic TMDs. Figure 5.15 shows complex power against damping ratio with TMDs of different frequencies. It is worth noting that an unexpected discontinuous point occurs when the frequency ratio for the TMD is near its optimal frequency because the highest peak moves from the out-of-phase

to in-phase mode with the increase of the damping ratio. This undesirable jump can be achieved only if the two resonances are close to equal height. To avoid this unwanted behaviour, the average active power of the two resonances when these peak exchanges appeared was used for calculating the effect of different mass ratio.

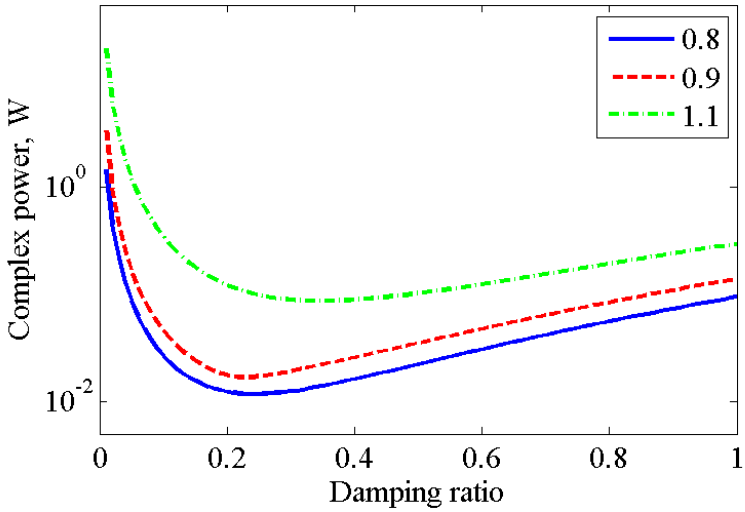

Figure 5.15: Complex power against damping subject to different frequency ratio (mass ratio = 0.1)

Results from Figure 5.15 indicate that a minima exists in all curves, which are the optimal frequency and damping ratio for TMD, respectively.

Figure 5.16 shows the typical complex power curve against different frequency ratios. It can be seen that minima still exist for these curves. It can be seen from Equation 5.11 that this indicator is proportional to ω. Thus, complex power is continuously increasing with TMD frequency. To remove that undesirable effect, this absorbed power is normalised by the frequency.

The iteration procedure shown in Figure 5.17 was used to identify the optimal damping and frequency for SDOF-TMD. The error tolerance ε was applied to determine whether damping and frequency ratio of TMD would be convergent for a given mass ratio. Since the power is sensitive to the peak amplitude of the host

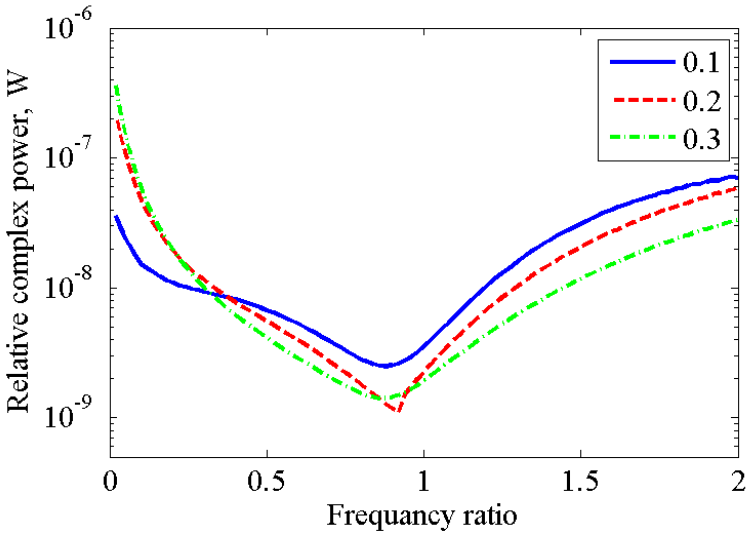

Figure 5.16: Normalised complex power against TMD frequency ratio for different damping ratios

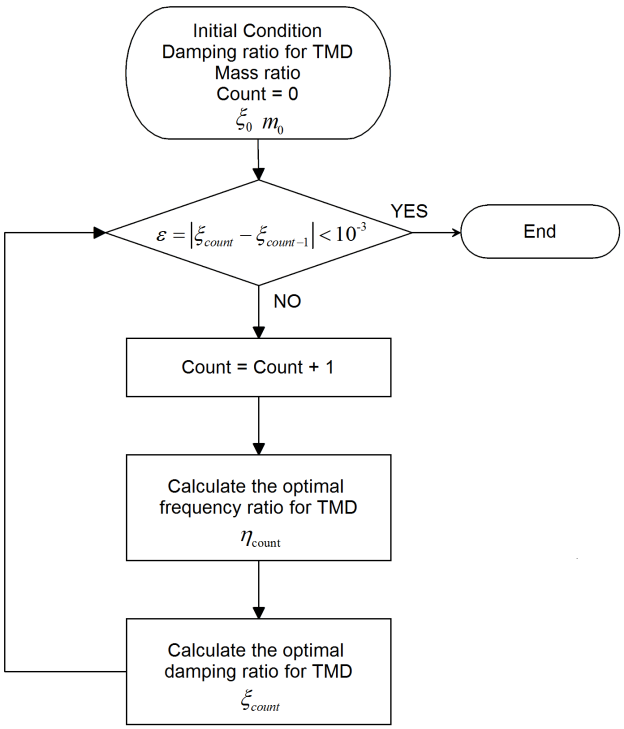

Figure 5.17: Flow chart of optimisation procedure

structure, the choice of the tolerance of optimal damping is closely related to the frequency resolution. Basic parameters for the iteration configuration are shown in Table 5.4.

Variables	Value
Excitation frequency resolution	0.01Hz
Damping resolution	0.001
Maximum damping	1
Frequency ratio resolution	0.001
Maximum frequency ratio	2
Error tolerance ϵ	0.001

Table 5.4: Iteration configurations

Comparisons of optimal TMD parameters between different optimal strategies, including minimisation of maximum displacement, minimisation of relative displacement and transient stability method, are demonstrated in Figure 5.18. The equations of the optimal parameters of the TMD subject to different mass ratio were demonstrated in Zilletti's work [56]. The responses for both the TMD and the host structure using different optimal strategies are shown in Figure 5.18. It should be noted that the mass ratio of the secondary system and host structure used here is 0.1 and all the receptances target minimising the performance indicator where the host structure is aimed at its peak resonance amplitude. It can be seen that almost no difference exists for the performance of the TMDs, designed by the proposed and classic TMD design method, for both host structure and secondary mass.

Table 5.5 and Figure 5.19 demonstrate the optimal parameters of the secondary structure in a SDOF-TMD system gained via the methods mentioned before.

Table 5.5 indicates that the stiffness of the optimal TMD for the different optimal methods is nearly the same. The reason is that the performance of the TMD is much more sensitive to the frequency ratio than the damping. From Figure 5.19, the optimal damping gained from resonance power method is slightly

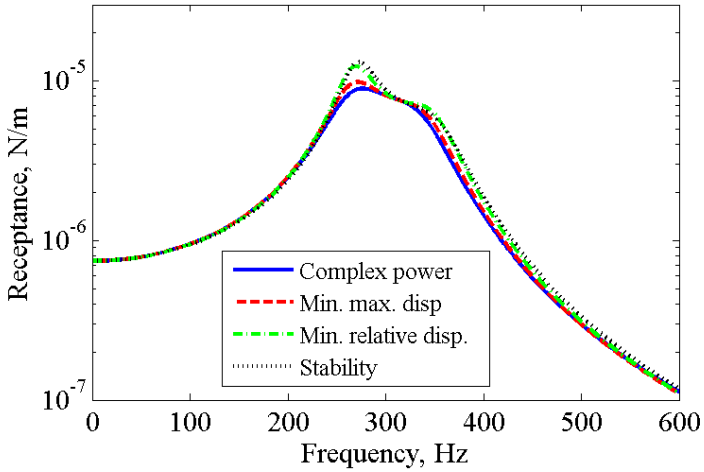

(a)

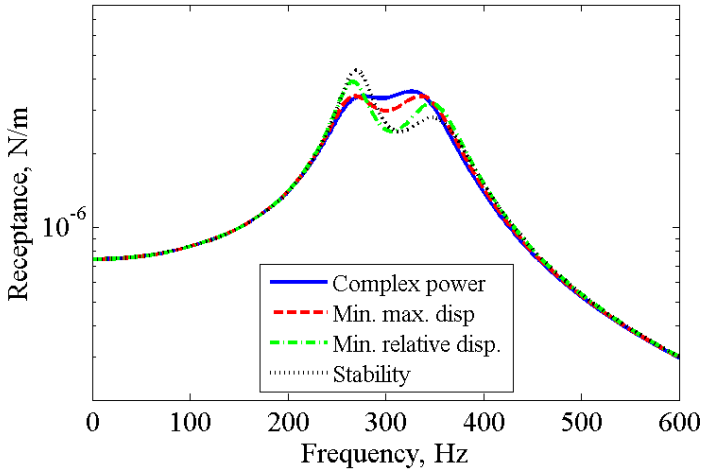

(b)

Figure 5.18: Comparison with different optimal strategies for (a)host structure and (b)secondary mass (mass ratio = 0.1)

Mass ratio	Optimal frequency ratio	
	(complex power)	(other strategies)
0.1	0.902	0.909
0.2	0.824	0.83
0.3	0.771	0.76
0.4	0.714	0.71
0.5	0.676	0.67

Table 5.5: Optimal TMD parameters gained via different strategies for frequency ratio

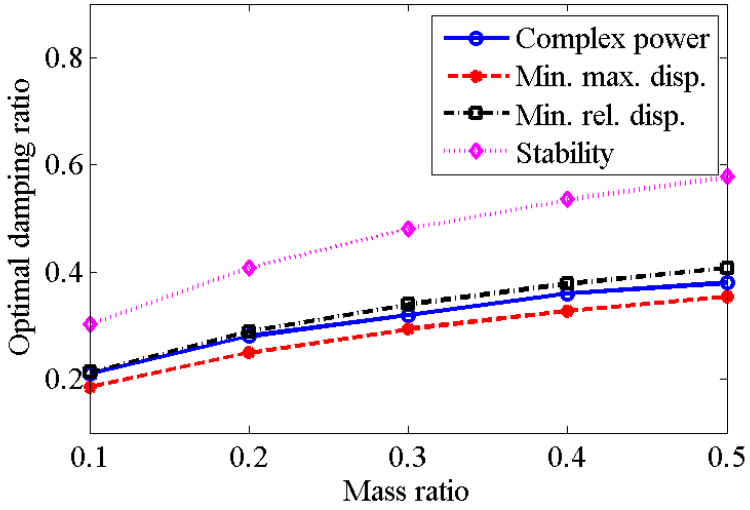

Figure 5.19: Optimal TMD parameters gained via different strategies for damping

lower than via other methods. One of the most apparent features from these results is that the difference in damping obtained between proposed method and traditional method is negligible.

The resonance power flow method uses the concept of absorbed power for the secondary system and the optimal TMD is achieved when more energy is transferred to the secondary system. It has been shown to work well for the linear TMD. The other advantage of this method is that it uses the power, as an indicator of energy, in summing different frequencies. For example, it can deal with the parameter design for TMDs subject to multi-frequency excitations. Traditionally, only numerical searching algorithms can be used to design TMDs, which is much more computationally expensive. Nonetheless, this strategy is still unable to design the TMD if any nonlinear components are incorporated into the SDOF-TMD system. To address this situation, an alternative, power spectrum based optimisation was introduced.

5.4 Power spectrum based optimisation for the SDOF-TMD system

Although resonance power based optimisation provides a strategy to design TMD for multiple excitations, it does not work well when nonlinear elements are incorporated into the SDOF-TMD system. For such systems, numerical simulation has normally been employed to achieve optimal performance. One of the critical issues for this procedure is that it is time-consuming. Also, in practice, in a TMD with multiple working modes, such as the TMD with O-rings, it is difficult to choose the resonance peaks for calculating the complex power. In this case, power spectrum based optimisation provides an alternative way to optimise the structure with TMDs. The advantage of this method is that it is not necessary to identify the resonances of the system, and therefore this strategy is much more suitable for the nonlinear system where the peak magnitude of the response spectrum is hard to predict.

5.4.1 Further developments of the power flow method

Referring to Section 5.3.1, the power relationship for the secondary system may be obtained by substituting Equations 5.6 and 5.7 into Equation 5.4 and multiplying it by $\dot{x}_2$

$$\begin{aligned}&\frac{1}{2}c_2X_2^2\omega^2 + \frac{1}{2}\omega X_2\left[\left(-\omega^2 m_2 + k_2\right)X_2\sin 2\omega t + c_2X_2\omega\cos 2\omega t\right]\\&\quad = \left[k_2X_1\sin\left(\omega t-\phi\right) + c_2X_1\omega\cos\left(\omega t-\phi\right)\right]X_2\omega\cos\omega t\end{aligned} \tag{5.12}$$

After some reorganisation, the right hand side of Equation 5.12 can also be given by

$$\frac{1}{2}\omega X_1X_2\left\{\left[k_2\sin\left(2\omega t+\phi\right) + c_2\omega\cos\left(2\omega t+\phi\right)\right] + \left[c_2\omega\cos\phi - k_2\sin\phi\right]\right\} \tag{5.13}$$

Substituting Equation 5.6 and 5.7 into the 2$^{\text{nd}}$ row of Equation 5.4, the internal force caused by the movement of host structure may be represented by

$$\begin{aligned}&X_1k_2\sin\left(\omega t-\phi\right) + X_1c_2\omega\cos\left(\omega t-\phi\right)\\&\qquad = \left(-\omega^2m_2 + k_2\right)X_2\sin\omega t + c_2X_2\omega\cos\omega t\end{aligned} \tag{5.14}$$

It is worth noting that Equation 5.14 stays unchanged at the time $2t$ as this relationship works at any instantaneous time t. Substituting $2t$ into Equation 5.14 and using the left hand side of Equation 5.12, the energy dissipation term may also be given by

$$\frac{1}{2}c_2X_2^2\omega^2 = \frac{1}{2}\omega X_1X_2\left(c_2\omega\cos\phi - k_2\sin\phi\right) \tag{5.15}$$

In this work, the objective of the TMD design is to transfer more power into the secondary system, and therefore, only power flow of the secondary system is considered. After some rearrangement, the complex power for secondary mass (as shown in Equation 5.11) is defined as

$$P\left(\omega\right) = \left(k_2X_1 + j\omega c_2X_1\right)j\omega X_2 - \left(k_2X_2 + j\omega c_2X_2\right)j\omega X_2 \tag{5.16}$$

It is worth to define the first term of this complex power,$\left(k_2X_1 + j\omega c_2X_1\right)j\omega X_2$, as the coupling term. Combining Equation 5.11 with the time domain solution

for the response of both host structure and secondary system, the coupling term of Equation 5.11 can be represented as

$$\omega X_1 X_2 \left(c_2\omega\cos\phi - k_2\sin\phi\right) + \frac{1}{2}j\omega X_1 X_2 \left(c_2\omega\sin\phi - k_2\cos\phi\right) \tag{5.17}$$

Combining with Equation 5.14 and 5.17, the real part of this term is given by

$$\Re\left(k_2X_1 + j\omega c_2 X_1 \omega X_2\right) = c_2 X_2^2\omega^2 \tag{5.18}$$

Taking the Fourier transform for the Equation of Motion of the secondary system in power form, the imaginary part of this term is given by

$$\Im\left(k_2X_1 + j\omega c_2 X_1 \omega X_2\right) = \Im\left\{\left[\left(-\omega^2 m_2 + k_2\right)X_2 + jc_2X_2\omega\right]j\omega X_2\right\} \tag{5.19}$$

After some transformations, Equation 5.19 can be expressed as,

$$\Im\left(k_2X_1 + j\omega c_2 X_1 \omega X_2\right) = \left(-\omega^2 m_2 + k_2\right)\omega|X_2|^2 \tag{5.20}$$

Substituting Equation 5.20 and 5.18 into Equation 5.16, the power flow of secondary system is represented as

$$P\left(\omega\right) = \frac{1}{2}\left[X_2^2 c_2\omega^2 + jX_2^2\omega\left(-m_2\omega^2 + k_2\right)\right] - \frac{1}{2}\left(k_2X_2 + j\omega c_2X_2\right)j\omega X_2 \tag{5.21}$$

After some transformations, the absorbed complex power can be obtained,

$$P\left(\omega\right) = X_2^2 c_2\omega^2 + \frac{1}{2}jX_2^2\omega\left(-m_2\omega^2\right) \tag{5.22}$$

Note that the imaginary part of complex power, $\frac{1}{2}X_2^2\omega\left(-m_2\omega^2\right)$, is defined as the reactive power in the following analysis. This term is used to identify the power transfer and dissipation of TMDs for different strategies.

5.4.2 Understanding of the reactive power over the selected frequency range

Since this optimisation method is based on the energy over the selected frequency range, the energy distribution of the whole system needs to be investigated first.

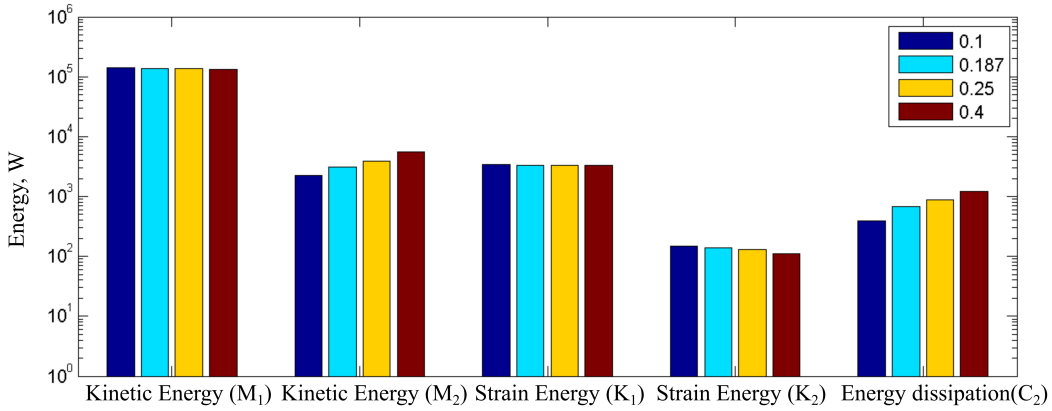

Figure 5.20: Energy distribution of TMD-SDOF subject to different damping ratios of TMD (mass ratio = 0.1 frequency ratio = 0.909)

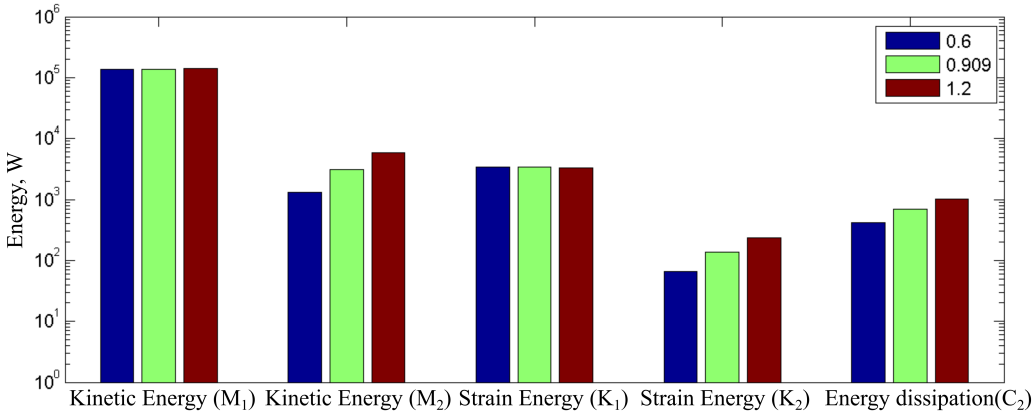

Figure 5.21: Energy distribution of TMD-SDOF subject to different frequency ratios of TMD (mass ratio = 0.1 damping ratio = 0.187)

From Figure 5.20 and 5.21, it can be seen that stiffness and damping of the TMD have much greater influence on the energy of the secondary system than that of the host structure. The sum of the kinetic and strain energy of host structure is almost the same over these frequencies subject to different stiffness and damping. The optimal TMD for the whole frequency range is achieved when most of the work done by external force is transferred to the secondary system. Therefore, this optimisation focuses on the energy distribution of the secondary system. Figure 5.20 also indicates that the variation of the damping for the TMD has limited effect on the power transfer subject to any selected stiffness of the device. Additionally, Figure 5.21 demonstrates that the stiffness of the TMD has a significant impact on both energy transfer and energy dissipation.

The reactive power over the whole frequency range can be used as a performance indicator in this situation. Physically, the reactive power of the secondary system refers to the kinetic energy KE_2, $\frac{1}{2}m_2\dot{x}_2^2$, for the secondary system. Using the conservation of the energy, the total energy for this system can be represented as,

$$E_{\text{total}} = \sum_{f_{\min}}^{f_{\max}} (\mathrm{KE}_1 + \mathrm{SE}_1 + \mathrm{KE}_2 + \mathrm{SE}_2 + \mathrm{DE}_2) \tag{5.23}$$

where E_{total} is the total energy, KE_1 is the kinetic energy of the host structure, SE_1 is the strain energy of the host structure and DE_2 is the energy dissipation caused by the damping of the TMD. Since the energy of the host structure does not vary appreciably with the parameters of the TMD - as shown in Figure 5.20 and Figure 5.21, the conservation of the energy distribution can be given by,

$$E_2 = \sum_{f_{\min}}^{f_{\max}} (\mathrm{KE}_2 + \mathrm{SE}_2 + \mathrm{DE}_2) \tag{5.24}$$

where E_2 is the energy involved in the oscillation of the secondary system. It is worth noting that the E_2 is equivalent to the work done by external force subtracting the energy for the host structure. This energy remains unchanged for the same external periodic force regardless the stiffness and damping of the TMD. To achieve the minimum of the reactive power, the strain energy and kinetic

energy need to be close to each other. Mathematically, this relationship can be given by,

$$\min\left(\text{reactive power}\right) = \sum_{f_{\min}}^{f_{\max}} \left(\frac{1}{2} m_2 \dot{x}_2^2\right) \rightarrow \varepsilon \tag{5.25}$$

where ε is a tiny number. Substituting Equation 5.24 into Equation 5.25, the minimisation of the reactive power can be represented as,

$$\mathrm{SE}_2 + \mathrm{DE}_2 - E_2 \rightarrow \varepsilon \tag{5.26}$$

Physically, the kinetic energy of the secondary system is the performance indicator in this situation. With the minimal kinetic energy, the strain energy and energy dissipation, and, therefore energy transfer and dissipation, were pushed to a high level, as shown in Equation 5.24. Since the displacement of the secondary mass reduces, the power flow into the secondary system is limited. Instead, more energy is dissipated during the relative motion between the two systems. This behaviour is understandable as the damping is the objective of this optimisation.

To conclude, the idea behind the proposed indicator is to minimise the kinetic energy of the secondary oscillator. The peak amplitude of the TMD is controllable and balance between the energy transfer and dissipation for the TMD is achieved through achieving the minimisation of this indicator.

5.4.3 Optimisation results

Figure 5.22 shows the typical reactive power curve for TMDs with different damping and stiffness. The mass ratio of the secondary system and host structure is chosen as 0.1 for both figures. Figure 5.22(a) shows that the optimal damping of the TMD remains with the increase of frequency of TMD. From Figure 5.22(b), it can be seen that the reactive power for the secondary system is highly affected by the damping of the secondary system. The local minima can be observed only if the damping of the TMD is relative low. In this case, a tiny kinetic energy of the secondary system can be achieved. As a result, the optimal indicator is much more sensitive to optimal damping than to stiffness of the TMD.

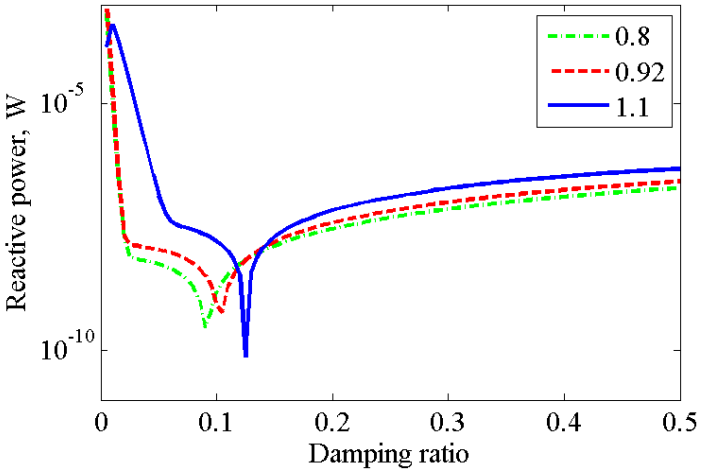

(a)

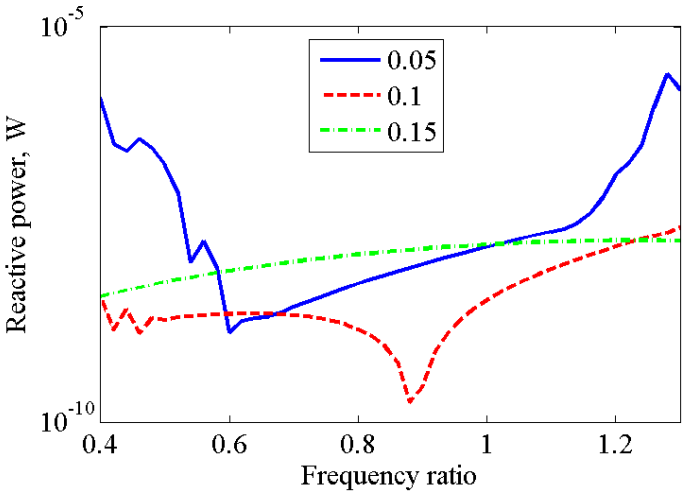

(b)

Figure 5.22: Typical reactive power against (a) damping ratios for different natural frequency of TMD and (b) frequency ratios subject to different damping ratios (mass ratio = 0.1)

Since the local minima of the reactive power may not exist for selected frequencies of the TMD, the normal iteration procedures are extremely time-consuming and convergence of these iterations may not be obtained. Differential Evolution, as mentioned in the previous section, was thus used to identify the optimal parameters using the reactive power over the selected frequency spectrum. The objective function could then be set as the sum of the frequency-normalised reactive power for the selected frequency range.

Comparisons of frequency response for host structure and secondary system are shown in Figure 5.23. Several methods, including minimisation of maximum displacement, minimisation of mean squared displacement and minimisation of kinetic energy of the host structure, were applied to design the optimal TMD. The mass ratio of the TMD and main structure was set as 0.1. From Figure 5.23, it can be seen that the reactive power optimisation performs slightly worse than the other optimisation strategies regarding the response of the host structure. Since the energy dissipation and the transfer was pushed into a high level, the balance between these two behaviours may not be achieved. As a result, more motions can be observed for both the main mass and secondary system. Nevertheless, the resonance-based reactive power still provides an alternative way to design the nonlinear TMD.

In this section, two different optimisation methods, active power at resonance and reactive power over frequency range, were used to identify the optimal parameters of the TMDs. Both methods were intended to transfer the unwanted strain energy from the host structure into the secondary system. For linear TMDs, determining the frequency spectrum of this device is relatively convenient, and therefore the complex power routine is always feasible, even for a multi-mode TMD and multiple TMDs on one host structure. To conclude, the proposed optimisation routine can be effective in developing any kind of linear TMD, including the adjustable TMD with O-rings.

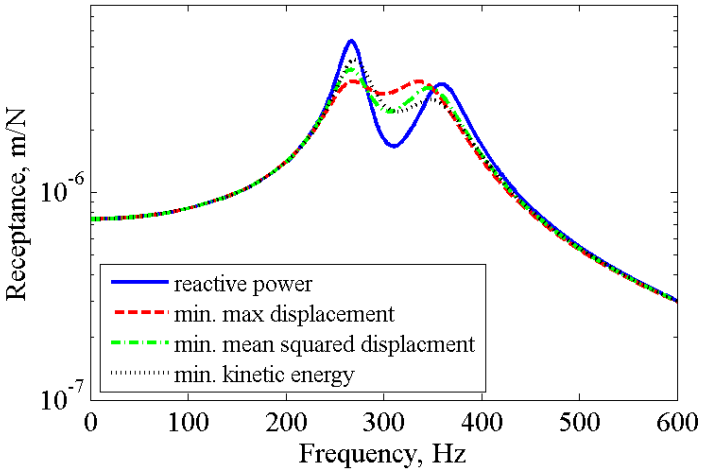

(a)

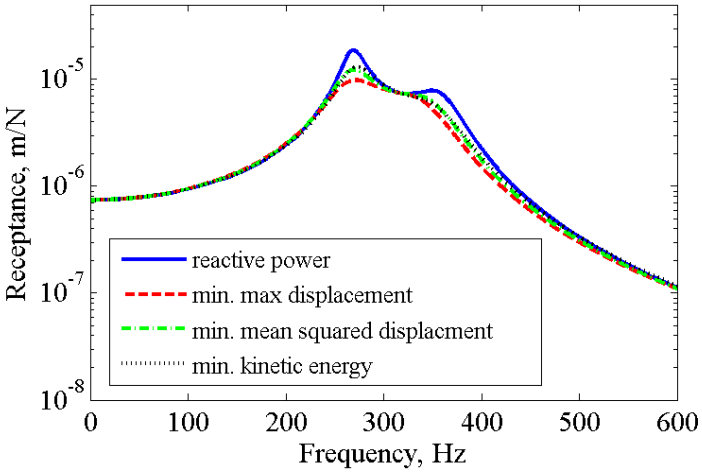

(b)

Figure 5.23: Comparison of different optimal strategies for (a)host structure and (b)secondary mass, (mass ratio = 0.1)

5.5 Extension of the power flow method to the nonlinear system: a preliminary study

When the TMD involves nonlinear components, for example, TMW particles, optimal performance is always difficult to achieve. Most TMDs are in practice based on the classic design rules for a linear TMD. However, the invariant points of receptances subject to different damping ratios no longer exist, and therefore, vibration suppression of the host structure cannot be guaranteed. In this case, application of the power flow method to the nonlinear system needs to be developed. In this section, a preliminary analysis was carried out to provide an alternative route to optimise this device. In this section, two nonlinear TMDs, one with cubic stiffness and the other with cubic damping, were employed to assess the performance of the developed method for a nonlinear TMD. A linear SDOF – nonlinear TMD (SDOF-NTMD) system, as shown in Figure 5.24, was used and the parameters of this simulation are shown in Table 5.6.

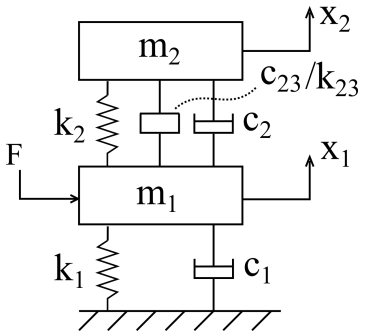

Figure 5.24: Schematic figures for a SDOF-NTMD model

	m_1, kg	k_1, N/m	k_{23}, N/m^3	c_1, N/ms	c_{23}, N/m^{3}s	F, N
Cubic stiffness - TMD	10	10	0.1	0.05	0	5
Cubic damping - TMD	10	10	0	0.05	0.1	5

Table 5.6: Parameters of the simulation for a SDOF-NTMD system

The optimal parameters of these TMDs are always the linear dynamic proper-

ties of the TMD. Since the nonlinear stiffness and damping are only dependent on the relative motion, the coordinate transformation is used and can be represented as,

$$y_1 = x_1 \qquad \text{and} \qquad y_2 = x_2 - x_1 \tag{5.27}$$

The Equation of Motion of this nonlinear system is then given by,

$$\begin{bmatrix} m_1 & 0 \\ m_2 & m_2 \end{bmatrix} \begin{bmatrix} \ddot{y}_1 \\ \ddot{y}_2 \end{bmatrix} + \begin{bmatrix} c_1 & -c_{21} \\ 0 & c_{21} \end{bmatrix} \begin{bmatrix} \dot{y}_1 \\ \dot{y}_2 \end{bmatrix} + \begin{bmatrix} 0 & -c_{23}\dot{y}_2^2 \\ 0 & c_{23}\dot{y}_2^2 \end{bmatrix} \begin{bmatrix} \dot{y}_1 \\ \dot{y}_2 \end{bmatrix} + \begin{bmatrix} k_1 & -k_{21} \\ 0 & k_{21} \end{bmatrix} \begin{bmatrix} y_1 \\ y_2 \end{bmatrix} + \begin{bmatrix} 0 & -k_{23}y_2^2 \\ 0 & k_{23}y_2^2 \end{bmatrix} \begin{bmatrix} y_1 \\ y_2 \end{bmatrix} = \begin{bmatrix} F\sin\omega t \\ 0 \end{bmatrix} \tag{5.28}$$

The harmonic balance method was introduced to convert the polynomial stiffness and damping into amplitude-dependent properties. Note that the high order terms were neglected in these simulations. The detailed derivations are shown in Elliott's paper - see reference [110].

$$K_{eqe} = \begin{bmatrix} 0 & -\frac{3}{4}k_{23}Y_2^2 \\ 0 & \frac{3}{4}k_{23}Y_2^2 \end{bmatrix} \tag{5.29}$$

$$C_{eqe} = \begin{bmatrix} 0 & -\frac{3}{4}c_{23}\dot{Y}_2^2 \\ 0 & \frac{3}{4}c_{23}\dot{Y}_2^2 \end{bmatrix} \tag{5.30}$$

By introducing the equivalent stiffness and damping matrices, shown in Equation 5.29 and 5.30, the quasi-linear EOM of this system can be obtained,

$$\begin{bmatrix} m_1 & 0 \\ m_2 & m_2 \end{bmatrix} \begin{bmatrix} \ddot{y}_1 \\ \ddot{y}_2 \end{bmatrix} + \begin{bmatrix} c_1 & -c_{21} - \frac{3}{4}c_{23}\dot{Y}_2^2 \\ 0 & c_{21} + \frac{3}{4}c_{23}\dot{Y}_2^2 \end{bmatrix} \begin{bmatrix} \dot{y}_1 \\ \dot{y}_2 \end{bmatrix} + \begin{bmatrix} k_1 & -k_{21} - \frac{3}{4}k_{23}Y_2^2 \\ 0 & k_{21} + \frac{3}{4}k_{23}Y_2^2 \end{bmatrix} \begin{bmatrix} y_1 \\ y_2 \end{bmatrix} = \begin{bmatrix} F\sin\omega t \\ 0 \end{bmatrix} \tag{5.31}$$

An iterative approach was adopted to identify the amplitude-dependent damping. The frequency response of the host structure could then be obtained. Once

the frequency response was obtained, the spectrum-based reactive power was used to identify the optimal parameters. Note that the frequency range calculated in this case is between 0 and 2 Hz. To speed up the whole procedure, the DE algorithm was introduced and three different criteria, minimum kinetic energy, reactive power flow and minimising the peak displacement, were set as indicators. Typical displacement responses of the host structure are shown in Figure 5.25

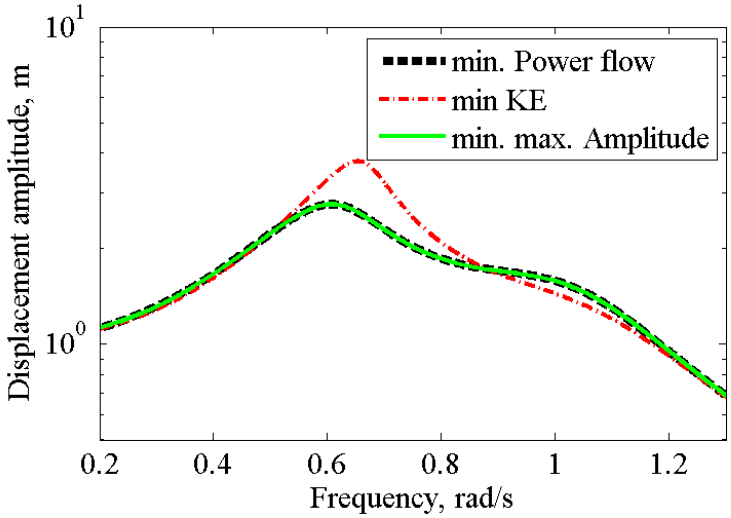

Figure 5.25: Typical displacement responses for the SDOF-NTMDs optimised using different strategies Note that nonlinear stiffness is employed in this simulation

A very good agreement was achieved for the TMD using power flow and minimisation of maximum amplitude strategies. Results from the kinetic energy scheme tend to have a high response because the optimisation indicator is proportional to the velocity. Excitation frequencies have a great impact on the optimisation. To verify these results, examination of responses of the host structure subject to different mass ratios was carried out. Two different nonlinear TMD systems, cubic stiffness and cubic damping, were used and the results are shown in Figure 5.26 and Figure 5.27.

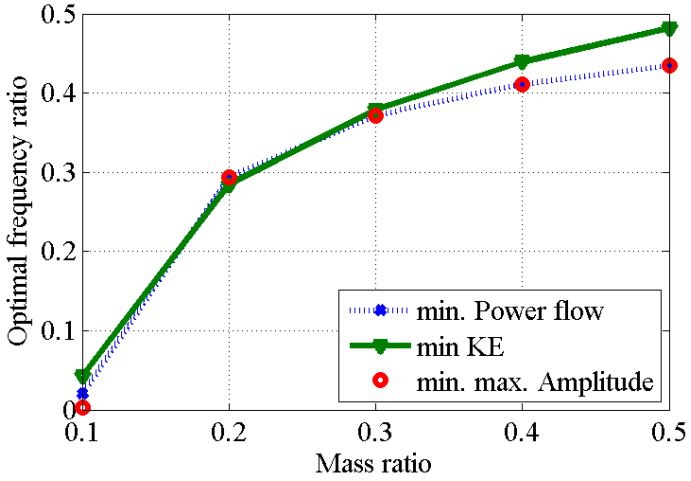

(a)

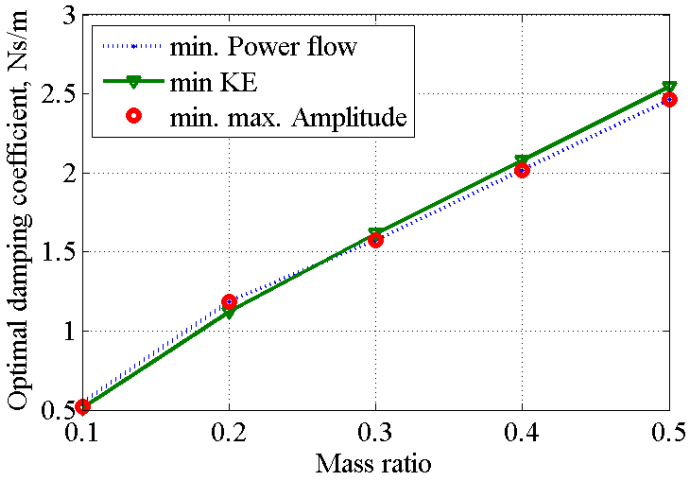

(b)

Figure 5.26: Optimal parameters of the cubic stiffness TMD against different mass ratio subject to different optimisation methods (a)stiffness and (b)damping.

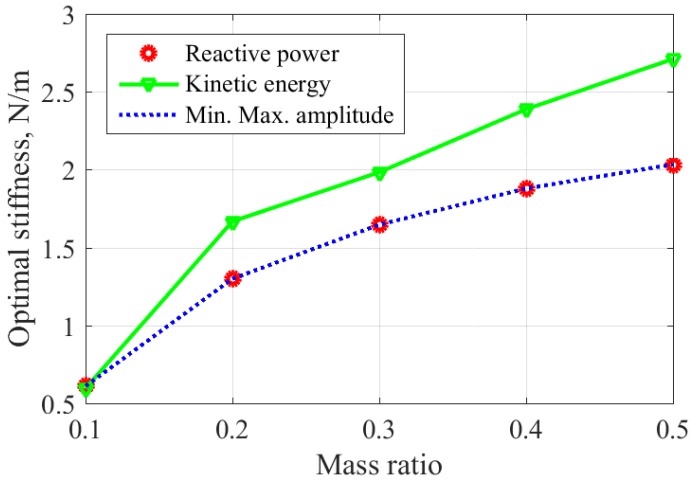

(a)

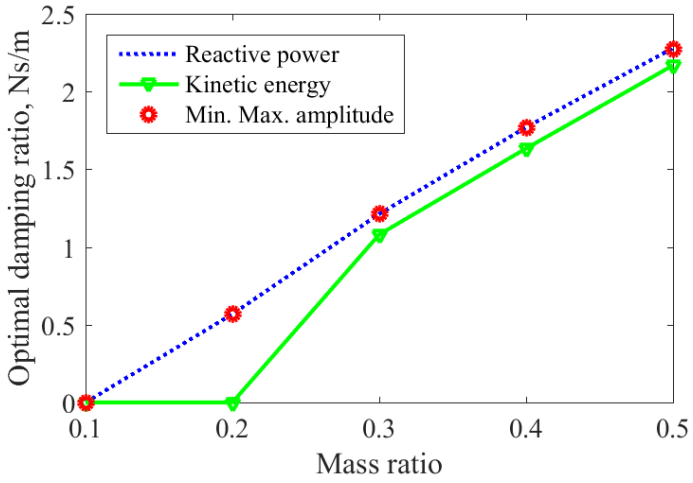

(b)

Figure 5.27: Optimal parameters of the cubic damping TMD against different mass ratio subject to different optimisation methods (a)stiffness and (b)damping.

Figures 5.26 and 5.27 indicates that this method has good capability to deal with the nonlinear TMD. However, the cubic stiffness and damping were fixed in these simulations. Further investigations need to be carried out to form a full picture of the feasibility of using this strategy for nonlinear components of TMDs.

5.6 Conclusion

In this chapter, the design criteria for the TMD were investigated. A numerical search method, the Differential Evoluation algorithm, was introduced to design multiple TMDs on a multiple Degree of Freedom (DOF) system. It has been shown that these multiple TMDs can only slightly improve the energy dissipation over a broad frequency range. However, this method is really time-consuming, especially when subjected to a nonlinear TMD. In this situation, a numerical finite difference method need to be introduced to gain the response of this dynamic system, and the performance of this TMD.

To overcome this problem, a new indicator, complex power, was applied to indicate the energy transfer between the host structure and the secondary oscillator. This novel TMD design criteria were developed using the power transfer in the linear Equation of Motion. When the TMD is minimising the power at resonances, the energy dissipation of the TMD is also minimised, and therefore the strain energy of the host structure tends to transfer to the TMDs. Compared with other optimisation strategies using resonance frequencies, the peak magnitudes for both main structure and secondary mass achieves similar performances. To conclude, resonant active power-based optimisation, aimed at speeding up the design targets for a system with multiple resonances. However, these resonance frequencies may be difficult to estimate for a practical mechanical system, especially when some nonlinearities were introduced.

Reactive power-based optimisation over a selected frequency range was employed to evaluate the host-TMD system that involved a nonlinear element. The minimisation of the reactive power at selected frequencies targets reducing the kinetic energy of the secondary oscillator. The balance between the energy transfer and dissipation for this TMD is the key feature to be optimised in this situation. This method is shown to be capable to suppress the motion of the host structure at selected mass of the damper, while it is worth to investigating the performance of this strategy for higher mass ratio. Nevertheless, this reactive power-based method still provides an alternative way to design a nonlinear TMD.

Since the static compression-dependent stiffness of the O-ring TMD primarily follows polynomial relationships, a nonlinear TMD incorporated either cubic stiffness or damping was introduced to show the feasibility of the proposed reactive power design criterion. The TMD designed by resonance reactive power-based optimisation showed a good agreement with that optimised by the minimisation of maximum displacement of the host structure.

Chapter 6

Conclusions and further work

The aim of this work was to provide an understanding of adjustable Tuned Mass Dampers (TMDs) based on passive, nonlinear material from which design guidelines could be produced for targeting vibration suppression over a wider frequency range. This has been achieved successfully.

6.1 Novelty of this research

The main contribution of this work are listed below,

- A novel adjustable (TMD) incorporating elastomeric O-rings has been presented. The main features of this device are: (a) use of motions in three different directions (b) use of static compression-dependent stiffness and relatively uniform damping. The frequency-altering ability of this novel TMD is significantly higher than that for currently available ones. Accurate analytical and numerical models of the O-rings, especially in the shear and tilting directions, have been established.
- An adjustable TMD using Tangled Metal Wire (TMW) particles that is aimed at high temperature mechanical structures has been invented. Its

effectiveness on suppressing the first two vibration modes of a box-section beam has been demonstrated. The semi-empirical analytical model, based on Neo-Hookean and low wave speed medium assumptions, has been established and able to predict the static compression-dependent and frequency-depedent elasticity and damping.

- Complex power based design strategies have been presented to provide alternative routes for designing nonlinear TMDs.

6.2 Main conclusions

The classic TMD is always limited by its narrow working frequency range. Meanwhile, this damper loses its effectiveness when the multi-directional vibration appears in the practical structures.

6.2.1 TMD incorporating elastomeric O-rings

One of the easiest way to extend the effective frequency range of a TMD was to make this device adjustable, using components with nonlinear load-deflection behaviour. In this situation, the elastomeric O-ring was introduced as the elastic and damping elements of an adjustable TMD. In the proposed device, three different working conditions including compression, shear and rocking modes identified for this TMD makes it suitable for an adjustable device.

When a mechanical structure experiences environmental vibration, the temperature, excitation frequencies and magnitudes are always changing. Thus, these factors as well as the type of elastomer and the static compressions were selected as the variables, which may affect the stiffness and damping of the elastomeric O-rings. It has been shown that the damping of this component is relatively uniform, while the stiffness, is strongly affected by the static compression and dynamic excitation levels. In operation, the dynamic strain on an O-ring in such a TMD, was significantly lower than the static strain used to set the stiffness. As a

result, only static compression-dependent stiffness was investigated and modelled in this study.

Analytical models were developed to describe the load-deflection behaviour of the O-rings. The temperature and frequency-dependent elasticities were explained by the elastic modulus of the elastomer. An existing model for axial compression was improved while new model is established for the shear and rocking deformations. The strain distributions of the O-rings in the contact regions was considered in the compressive model, which improves the accuracy, especially when subjected to low static compressions. With the increase of the static compression, expansions of the nominal diameter of the O-ring occupies an important role. In the current model, an empirical term was introduced to compensate this unwanted underestimations, while this term may not be guaranteed when different O-rings are employed. This effect need to be included in the further developments of this compressive load-deflection relationships.

Assuming the dynamic tilting angle and shear displacement is small, the corresponding stiffness model of the O-ring was developed. The deformed cross-sectional pattern of the O-ring was important for estimating rocking and shear stiffness, and therefore, the shape factor was introduced. As a result, reasonable accurate analytical expressions for stiffness and damping was developed. A experimental rig was developed to validate the rocking and compressive models without obtaining complicate interfacial boundary conditions between the O-rings and restricting plates. Since the rotational excitations are difficult to estimate for this system, the predictions of the damping in both directions are problematic. Fortunately, the viscoelasticity of the O-ring is assumed to be linear, and therefore, does not vary with different elements. Nevertheless, the resonance frequencies are still good indicators to validate the feasibilities of the stiffness models.

The O-rings with standard cross sections, may not provide the suitable stiffness ranges due to the restrictions of the sizes. The O-rings with irregular cross-section need to be introduced, and this element is very difficult to model analytically. Numerical models of these O-rings were then developed successfully using both finite strain and modal analysis.

Validation of the models was carried out using a specifically designed vibration tests. Evaluation of the performance of this device on a typical engineering structure was carried out and the feasibility of the proposed devices demonstrated. One of the most significant findings was the influence of the TMD on the mode shape of the host structure. The portion of the TMD that attached on the host structure was affected by the damping. For a relative heavy TMD, the mode shape of the host structure varies with different parametric configurations of the damper. As a result, the difficulty in designing this type of TMD increases. Additionally, the interracial frictions between the TMD and host structure may also shift the resonance frequency, which may cause the further trouble in using this type of device.

6.2.2 TMD incorporating the TMW particles

A TMD using TMW particles was invented for high temperature mechanical applications. It has been shown that this damper can achieve similar vibration suppression to the TMD using O-rings, while the additional weight was approximately 4 times smaller.

In order to estimate the stiffness and damping of the collections of the TMW particles, these properties for an individual TMW particle was investigated and results showed that the properties of these particles are sensitive to the strains applied. Meanwhile, the properties is not uniform for the particles with similar physical properties. One possible explanation is the difference in the micro-structure, and hence the contact status of the internal wires for different particles. To reduce the influences of these geometric uncertainties, the properties of a collection of particles was identified.

Some levels of randomisation for the stiffness and damping can still be observed for different collections of particles. Even for the particular collections of the particles, the performance tends to become stable after several trainings. Also, strong dynamic strain-dependent stiffness and damping can be found for this material, which increases the difficulties in the prediction of these properties when

incorporated in a practical TMD. Nevertheless, the static compression-dependent nonlinear stiffness can still be seen for any collection of particles. Hence, this type of material is able to used to develop an adjustable TMD.

Since the TMW particles are sensitive to micro-structures, careful calibrations of a specific TMW TMD need to be carried out before the damper is attached on a practical structure. This procedure is usually time-consuming, and therefore, the semi-empirical stiffness model, using hyperelastic material approach, was introduced. Using this analytical model, only single calibration test is required to estimate the equivalent shear modulus of particles for a specific TMW TMD. The approach to damping, however, is based on the assumption of internal resonances of the low-wave speed damping medium. The proposed model has been shown great accuracy for the stiffness, while it only worked for the damping at high static compressions.

6.2.3 Optimisation of the nonlinear TMD

The classic TMD design criterion is always based on the existence of two invariant points for different parametric configurations. These invariant points dismisses when the nonlinear elements are employed. Therefore, a numerical search method, the Differential Evoluation algorithm, was introduced to design the parameters of the TMDs on a multiple Degree of Freedom (DOF) system. This algorithm was shown to improve the efficiency of parametric designs for linear TMDs. However, it failed to speed up the design for the nonlinear TMD because it is time-consuming to estimate the time response of the nonlinear TMD using finite different algorithm.

A new indicator, complex power for secondary mass, was applied to represent the energy transfer between the host structure and the secondary oscillator. Physically, the power is a form of instantaneous energy, and therefore, these powers can be summed up over the selected frequency range. Two different optimal indicators, the complex power at resonances and reactive power over selected frequency ranges, were demonstrated their feasiblities in designing TMD. It has been shown

that this indicator worked reasonable well for the linear TMDs. However, the power at resonances is difficult to estimate for a nonlinear TMD, as the multiple resonances may appear when subjected to a harmonic excitation. Therefore, reactive power-based optimisation over a selected frequency range was employed to evaluate the host-TMD system that involved a nonlinear element. The TMD designed by resonance reactive power-based optimisation showed a good agreement with that optimised by the minimisation of maximum displacement of the host structure, when this nonlinear TMD incorporated either cubic stiffness or damping.

6.3 Further work

The adjustable TMD incorporating selected nonlinear components may still present a wide range of issues, from the material properties to the predictions of the stiffness and damping. Some important areas of research which emerge immediately from the work presented in this thesis are listed below,

- The degradation of the stiffness of the O-ring due to dynamic displacement amplitudes needs to be included in the analytical model of the O-rings in tensile-compressive direction.
- Since the interfacial friction between the TMD and the host structure may shift the resonance frequencies, investigations on the interfacial friction between the TMD and the host structure need to be carried out. This nonlinear frictional effect should be incorporated in the analytical model of an engineering structure with TMD.
- One issue relating to this TMD is the misalignment of the restricting blocks and eccentricity of the O-rings, as shown in Figure 6.1. To improve the setting-up of the O-rings in this TMD, a stepped restricting mass disc can substitute for the current flat one. This step constrains the movement of

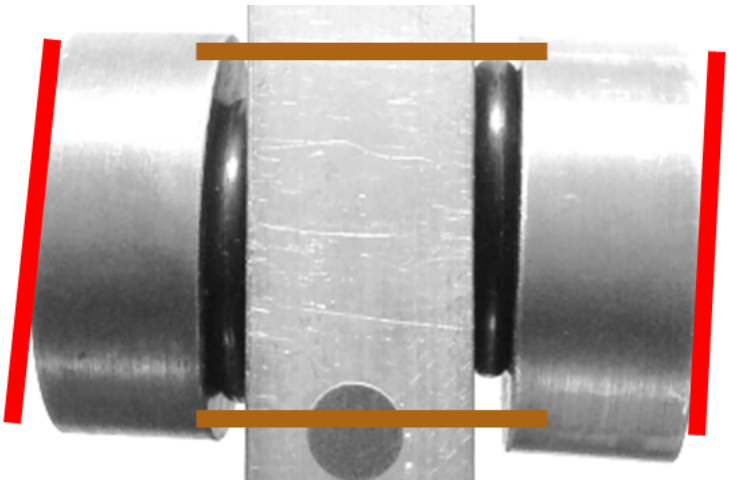

Figure 6.1: Poor positioning of the TMD

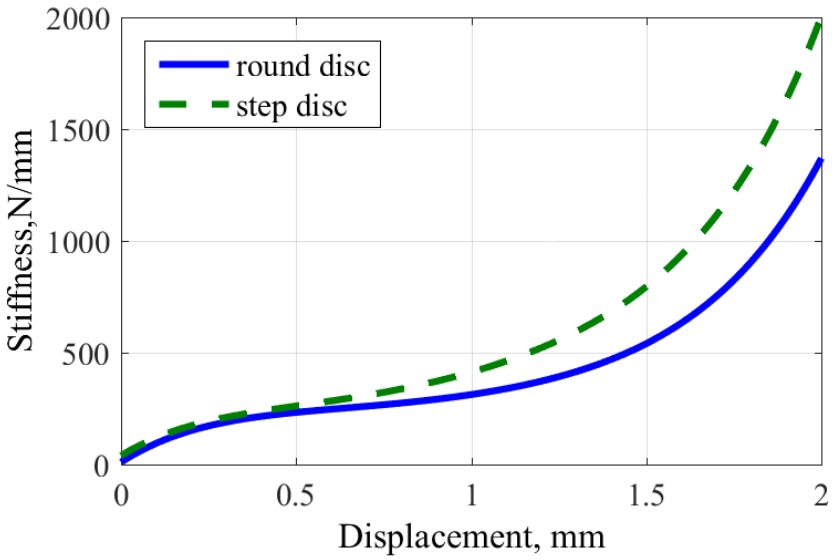

Figure 6.2: Effect of the step disc

the O-ring effectively. Static compression tests using the with and without disc step were carried out to evaluate this effect, as shown in Figure 6.2.

Figure 6.2 indicates that a considerable stiffening is observed due to the constraints of the expansions of the O-ring. Meanwhile, these constraints result in a high level of contacts and then introduce additional undesirable nonlinear stiffness and damping. The evaluation of this nonlinear damping needs to be investigated in future work.

- In the current structure of the TMD, the precise control of the static compression is also a critical issue. To address this problem, smart materials can be introduced. The O-rings can be manufactured using temperature-dependent shape memory or magnetic-dependent magnetorheological elastomers to control the static compressions. Once developed, a PID feedback control algorithm may be developed for an adaptive device.

- Statistical modelling can be employed to predict the average stiffness and damping of either the individual particle or a collection of particles.

- The repeatabilitiy of this high-temperature TMD with similar physical configurations of TMW particles needs to be evaluated.

- The semi-empirical model for the stiffness of the TMW particles needs to be validated using a greater number of the experiments. The relationship between the empirical scale factor and the static compression needs to be established as well.

- Since the dynamic displacement has a great influence on damping, the compensations of this effect on the proposed damping model of the TMW TMD needs to be evaluated.

- The performance of the resonance active power or reactive power optimisation algorithm for multiple TMDs on a discrete multiple DOF system for the selected frequency spectrum needs to be validated.

- A more complex frictional damping may be involved in the engineering structures. The feasibility of power-based design optimisation for a structure with highly nonlinear component (for example, TMW particles) need to be evaluated.

Bibliography

[1] C. Sun, R.P. Eason, S. Nagarajaiah, and A.J. Dick. Hardening düffing oscillator attenuation using a nonlinear tmd, a semi-active tmd and multiple tmd. *Journal of Sound and Vibration*, 332(4):674–686, 2013.

[2] M.A. Acar and C. Yilmaz. Design of an adaptive–passive dynamic vibration absorber composed of a string–mass system equipped with negative stiffness tension adjusting mechanism. *Journal of Sound and Vibration*, 332(2):231–245, 2013.

[3] R. Mohammadi-Ghazi, A.K. Ghorbani-Tanha, and M. Rahimian. Adaptive configuration tuned mass damper for mitigation of rotational vibrations. *Journal of Engineering Mechanics*, 138(8):934–944, 2012.

[4] P. Bonello, S. Rafique, and R. Shuttleworth. A theoretical study of a smart electromechanical tuned mass damper beam device. *Smart Materials and Structures*, 21(12):125004, 2012.

[5] J. Bae, J. Hwang, J. Roh, J. Kim, M. Yi, and J. Lim. Vibration suppression of a cantilever beam using magnetically tuned-mass-damper. *Journal of Sound and Vibration*, 331(26):5669–5684, 2012.

[6] B.P. Mann and N.D. Sims. Energy harvesting from the nonlinear oscillations of magnetic levitation. *Journal of Sound and Vibration*, 319(1):515–530, 2009.

[7] L. Wang and R.V.N. Melnik. Nonlinear dynamics of shape memory alloy oscillators in tuning structural vibration frequencies. *Mechatronics*, 22(8):1085–1096, 2012.

[8] Y Ma, Z. Liang, H. Wang, D. Zhang, and J. Hong. Theoretical and experimental steady-state rotordynamics of an adaptive air film damper with metal rubber. *Journal of Sound and Vibration*, 332(22):5710–5726, 2013.

[9] Y. Chevalier and J.V. Tuong. *Mechanical characterization of materials and wave dispersion*. John Wiley & Sons, 2013.

[10] G. Housner, L.A. Bergman, T.K. Caughey, A.G. Chassiakos, R.O. Claus, S.F. Masri, R.E. Skelton, T.T. Soong, B.F. Spencer, and J.T.P. Yao. Structural control: past, present, and future. *Journal of Engineering Mechanics*, 123(9):897–971, 1997.

[11] J.D. Ferry. *Viscoelastic Properties of Polymers*. John Wiley & Sons, 1980.

[12] D.E. Chegodayev. *The designing of components made of metal rubber*. Industry Publishing Company of National Defence, 2000.

[13] J. Hong, L. Chen, Y. Ma, G.R. Tomlinson, and J.A. Rongong. Hysteretic properties of metal rubber particles. *Proceedings of Institution of Mechanical Engineers Part C: Journal of Mechanical Engineering Science*, 227(4):693–702, 2013.

[14] J. A. Chandrasekhar, K.and Rongong and E.J. Cross. Frequency and amplitude dependent behaviour of tangled metal wire dampers. In *ISMA 2014 - International Conference on Noise and Vibration Engineering*, 2014.

[15] H. Yan, H. Y. Jiang, W. J. Liu, Z. D. Hao, and A. M. Ulannov. Analysis of acceleration response of metal rubber isolator under random vibration. *Acta Physica Sinica*, 59(6):4065–4070, 2010.

[16] S. Kwon and K. Park. Suppression of bridge flutter using tuned mass dampers based on robust performance design. *Journal of Wind Engineering and Industrial Aerodynamics*, 92(11):919–934, 2004.

[17] B. Farshi and A. Assadi. Development of a chaotic nonlinear tuned mass damper for optimal vibration response. *Communications in Nonlinear Science and Numerical Simulation*, 16(11):4514–4523, 2011.

[18] N.A. Alexander and F. Schilder. Exploring the performance of a nonlinear tuned mass damper. *Journal of Sound and Vibration*, 319(1):445–462, 2009.

[19] S. Deshpande, S. Mehta, and G. N. Jazar. Optimization of secondary suspension of piecewise linear vibration isolation systems. *International Journal of Mechanical Sciences*, 48(4):341–377, 2006.

[20] X. Gong, C. Peng, S. Xuan, Y. Xu, and Z. Xu. A pendulum-like tuned vibration absorber and its application to a multi-mode system. *Journal of Mechanical Science and Technology*, 26(11):3411–3422, 2012.

[21] T. Cheng and I. Oh. A current-flowing electromagnetic shunt damper for multi-mode vibration control of cantilever beams. *Smart Materials and Structures*, 18(9):095036, 2009.

[22] S. Neild, P.L. Green, K. Worden, K. Atallah, and N.D. Sims. The effect of duffing-type non-linearities and coulomb damping on the response of an energy harvester to random excitations. *Journal of Intelligent Material Systems and Structures*, 23(18):2039–2054, 2012.

[23] L.R.G. Treloar. *The Physics of Rubber Elasticity*. Oxford University Press, 1975.

[24] A.R. Payne and J.R. Scott. *Engineering Design with Rubber*. Maclaren et Sons, 1960.

[25] M. Mooney. A theory of large elastic deformation. *Journal of Applied Physics*, 11(9):582–592, 1940.

[26] R.S. Rivlin. Torsion of a rubber cylinder. In *Collected Papers of R.S. Rivlin*, pages 3–8. Springer, 1947.

[27] R.F. Boyer and R.L. Miller. Correlations involving the mooneyrivlin c2 constant and the number of chain atoms between physical entanglements, nc. *Polymer*, 28(3):399–407, 1987.

[28] O.H. Yeoh. Some forms of the strain energy function for rubber. *Rubber Chemistry and technology*, 66(5):754–771, 1993.

[29] A.N. Gent. A new constitutive relation for rubber. *Rubber Chemistry and Technology*, 69(1):59–61, 1996.

[30] E. Pucci and G. Saccomandi. A note on the gent model for rubber-like materials. *Rubber Chemistry and Technology*, 75(5):839–852, 2002.

[31] C.O. Horgan and G. Saccomandi. A molecular-statistical basis for the gent constitutive model of rubber elasticity. *Journal of Elasticity*, 68(1):167–176, 2002.

[32] E.M. Arruda and M.C. Boyce. A three-dimensional constitutive model for the large stretch behavior of rubber elastic materials. *Journal of the Mechanics and Physics of Solids*, 41(2):389–412, 1993.

[33] M.C. Boyce and E.M. Arruda. Constitutive models of rubber elasticity: a review. *Rubber Chemistry and Technology*, 73(3):504–523, 2000.

[34] P.B. Lindley. Compression characteristics of laterally-unrestrained rubber o-rings. *Journal of Institution of Rubber Industry*, 1(4):209–213, 1967.

[35] P.B. Lindley. Load-compression relationships of rubber units. *Journal of Strain Analysis*, 1(3):190–195, 1966.

[36] C. Zhao, H. E. Yue Jin, and H. Zhang. Application research of metal-rubber. *Noise and Vibration Control*, 2006.

[37] K. Chandrasekhar. *Mechanical and Microstructural Behaviour of Tangled Metal Wire Devices*. PhD thesis, University of Sheffield, 2016.

[38] D. Zhang, F. Scarpa, Y. Ma, K. Boba, J. Hong, and H. Lu. Compression mechanics of nickel-based superalloy metal rubber. *Materials Science and Engineering*, 580:305–312, 2013.

[39] D. Zhang, F. Scarpa, Y. Ma, J. Hong, and Y. Mahadik. Dynamic mechanical behavior of nickel-based superalloy metal rubber. *Materials & Design*, 56:69–77, 2014.

[40] Y. Ma, H. Wang, H. Li, and J. Hong. Study on metal rubber materials characteristics of damping and sound absorption. In *ASME Turbo Expo 2008: Power for Land, Sea, and Air*, pages 477–486. American Society of Mechanical Engineers, 2008.

[41] Y. Ma, F. Scarpa, D. Zhang, B. Zhu, L. Chen, and J. Hong. A nonlinear auxetic structural vibration damper with metal rubber particles. *Smart Materials and Structures*, 22(8):084012, 2013.

[42] J.P. Den Hartog and J. Ormondroyd. Theory of the dynamic vibration absorber. *Journal of Applied Mechanics*, 50(7):11–22, 1928.

[43] J.E. Brock. A note on the damped vibration absorber. *Journal of Applied Mechanics*, 13(4):A–284, 1946.

[44] H. Yamaguchi and N. Harnpornchai. Fundamental characteristics of multiple tuned mass dampers for suppressing harmonically forced oscillations. *Earthquake Engineering & Structural Dynamics*, 22(1):51–62, 1993.

[45] M. Abe and Y. Fujino. Dynamic characterization of multiple tuned mass dampers and some design formulas. *Earthquake Engineering & Structural Dynamics*, 23(8):813–835, 1994.

[46] R. Rana and T.T. Soong. Parametric study and simplified design of tuned mass dampers. *Engineering Structures*, 20(3):193–204, 1998.

[47] R.S. Jangid. Optimum multiple tuned mass dampers for base-excited undamped system. *Earthquake engineering & structural dynamics*, 28(9):1041–1049, 1999.

[48] C. Li and Y. Liu. Further characteristics for multiple tuned mass dampers. *Journal of Structural Engineering*, 128(10):1362–1365, 2002.

[49] L. Zuo and S.A. Nayfeh. Optimization of the individual stiffness and damping parameters in multiple-tuned-mass-damper systems. *Transactions of the ASME - Journal of Vibration and Acoustics*, 127(1):77–83, 2005.

[50] H. Li and X. Ni. Optimization of non-uniformly distributed multiple tuned mass damper. *Journal of Sound and Vibration*, 308(1):80–97, 2007.

[51] S. Krenk. Frequency analysis of the tuned mass damper. *Journal of Applied Mechanics*, 72(6):936–942, 2005.

[52] D. Miller, E. Crawley, and B. Ward. Inertial actuator design for maximum passive and active energy dissipation in flexible space structures. In *26th Conference on Structures, Structural Dynamics, and Materials*, page 777, 1985.

[53] H. Yamaguchi. Damping of transient vibration by a dynamic absorber. *Transactions of the Japan Society of Mechanical Engineers: Series C*, 54(499):561–568, 1988.

[54] Y. Iwata. On the construction of the dynamic vibration absorbers. *Preceedings of Japan Society of Mechanical Engineer*, (820-8):150–152, 1982.

[55] G.B. Warburton. Optimum absorber parameters for various combinations of response and excitation parameters. *Earthquake Engineering & Structural Dynamics*, 10(3):381–401, 1982.

[56] M. Zilletti, S.J. Elliott, and E. Rustighi. Optimisation of dynamic vibration absorbers to minimise kinetic energy and maximise internal power dissipation. *Journal of sound and vibration*, 331(18):4093–4100, 2012.

[57] A.D. Drozdov. *Mechanics of Viscoelastic Solids*. Wiley, 1998.

[58] M.T. Shaw and W.J. Mac knight. *Introduction to Polymer Viscoelasticity*. John Wiley & Sons, 2005.

[59] C. Henderson. The application of boltzmann's superposition theory to materials exhibiting reversible *beta* flow. In *Proceedings of the Royal Society of London Part A: Mathematical, Physical and Engineering Sciences*, volume 206, pages 72–86. The Royal Society, 1951.

[60] S. Arrhenius. Über die dissociationswärme und den einfluss der temperatur auf den dissociationsgrad der elektrolyte. *Zeitschrift für Physikalische Chemie*, 4(1):96–116, 1889.

[61] S. Arrhenius. Über die reaktionsgeschwindigkeit bei der inversion von rohrzucker durch säuren. *Zeitschrift für Physikalische Chemie*, 4:226–248, 1889.

[62] K.J. Laidler and P.S. Bunting. *The Chemical Kinetics of Enzyme Action*. Clarendon Press, 1973.

[63] H. Leaderman. *Elastic and creep properties of filamentous materials*. PhD thesis, Massachusetts Institute of Technology, 1941.

[64] M.L. Williams, R.F. Landel, and J.D. Ferry. The temperature dependence of relaxation mechanisms in amorphous polymers and other glass-forming liquids. *Journal of the American Chemical society*, 77(14):3701–3707, 1955.

[65] D.I.G. Jones. On temperature-frequency analysis of polymer dynamic mechanical behaviour. *Journal of Sound and Vibration*, 140(1):85–102, 1990.

[66] R. Christensen. *Theory of viscoelasticity: an introduction*. Elsevier, 2012.

[67] N.W. Tschoegl. *The phenomenological theory of linear viscoelastic behavior: an introduction*. Springer Science & Business Media, 2012.

[68] Y.W. Chan, S.O. Oyadiji, J.R. Wright, and G.R. Tomlinson. Predicting the vibration characteristics of antivibration mounts using the finite element method. *Journal of Vibration and Control*, 3(1):55–76, 1997.

[69] B. Darabi. *Dissipation of vibration energy using viscoelastic granular materials*. PhD thesis, University of Sheffield, 2013.

[70] J.A. Rongong and G.R. Tomlinson. Passive and active constrained layer damping of ring-type structures. In *Smart Structures and Materials*, pages 282–292. International Society for Optics and Photonics, 1997.

[71] R.O. Ebewele. *Polymer Science and Technology*, volume 1. CRC press, 2000.

[72] A.F. Blanchard and D. Parkinson. Breakage of carbon-rubber networks by applied stress. *Industrial & Engineering Chemistry*, 44(4):799–812, 1952.

[73] F. Bueche. Molecular basis for the mullins effect. *Journal of Applied Polymer Science*, 4(10):107–114, 1960.

[74] R. Houwink. Slipping of molecules during the deformation of reinforced rubber. *Rubber Chemistry and Technology*, 29(3):888–893, 1956.

[75] G. Kraus, C.W. Childers, and K.W. Rollmann. Stress softening in carbon black reinforced vulcanizates. strain rate and temperature effects. *Rubber Chemistry and Technology*, 39(5):1530–1543, 1966.

[76] L. Mullins. Softening of rubber by deformation. *Rubber Chemistry and Technology*, 42(1):339–362, 1969.

[77] D.E Hanson, M. Hawley, R. Houlton, K. Chitanvis, P. Rae, E.B. Orler, and D.A. Wrobleski. Stress softening experiments in silica-filled polydimethylsiloxane provide insight into a mechanism for the mullins effect. *Polymer*, 46(24):10989–10995, 2005.

[78] G. Marckmann, E. Verron, L. Gornet, G. Chagnon, P. Charrier, and P. Fort. A theory of network alteration for the mullins effect. *Journal of the Mechanics and Physics of Solids*, 50(9):2011–2028, 2002.

[79] A.R. Payne. The dynamic properties of carbon black-loaded natural rubber vulcanizates. part i. *Journal of Applied Polymer Science*, 6(19):57–63, 1962.

[80] A.N. Gent and P.B. Lindley. The compression of bonded rubber blocks. *Proceedings of the Institution of Mechanical Engineers*, 173(1):111–122, 1959.

[81] A.F. George, A. Strozzi, and J.I. Rich. Stress fields in a compressed unconstrained elastomeric o-ring seal and a comparison of computer predictions and experimental results. *Tribology International*, 20(5):237–247, 1987.

[82] K. L. Johnson. *Contact Mechanics*. Cambridge Univ. Press, 005 1985.

[83] B. Bhushan. *Modern Tribology Handbook*. CRC press, 2000.

[84] C.M. Blow, H.B. Demirli, and D.W. Southwart. Anisotropy in molded nitrile rubber. *Rubber Chemistry and Technology*, 48(2):236–245, 1975.

[85] A.R. Payne. Effect of compression on the shear modulus of rubber. *Rubber Chemistry and Technology*, 36(3):675–681, 1963.

[86] D.J. Mead. *Passive Vibration Control*. John Wiley & Sons Inc, 1999.

[87] P.A.L.S. Martins, R.M. Natal Jorge, and A.J.M. Ferreira. A comparative study of several material models for prediction of hyperelastic properties: Application to silicone-rubber and soft tissues. *Strain*, 42(3):135–147, 2006.

[88] B. Kim, S. Lee, J. Lee, S. Cho, H. Park, S. Yeom, and S. Park. A comparison among neo-hookean model, mooney-rivlin model, and ogden model for chloroprene rubber. *International Journal of Precision Engineering and Manufacturing*, 13(5):759–764, 2012.

[89] L. Meunier, G. Chagnon, D. Favier, L. Orgéas, and P. Vacher. Mechanical experimental characterisation and numerical modelling of an unfilled silicone rubber. *Polymer Testing*, 27(6):765–777, 2008.

[90] J.M. Hill and A.I. Lee. Large elastic compression of finite rectangular blocks of rubber. *The Quarterly Journal of Mechanics and Applied Mathematics*, 42(2):267–287, 1989.

[91] P.B. Lindley, K.N.G. Fuller, and A.H. Muhr. *Engineering Design with Natural Rubber*. Malaysian Rubber Producers' Research Association, 1984.

[92] P.H. Mott, J.R. Dorgan, and C.M. Roland. The bulk modulus and poisson's ratio of noncompressible materials. *Journal of Sound and Vibration*, 312(4):572–575, 2008.

[93] M Sekiguchi, H.and Kakiuchi, T. Morimoto, K. Fujimoto, and N. Yoshimura. Poisson's ratio for stretched vulcanized natural rubber. *Rubber Chemistry and Technology*, 42(2):547–556, 1969.

[94] V. Gonca and Y. Shvabs. Definition of poisson's ratio of elastomers. *Engineering for Rural Development*, 2011.

[95] E.L. Taylor and J.P. Szabo. From mechanics to acoustics: model ing polymer properties. Technical report, DREA Document, 1995.

[96] L. Meirovitch. *Analytical Methods in Vibrations*, volume 438. Macmillan New York, 1967.

[97] W.H. Press, S.A. Teukolsky, W.T. Vetterling, and B.P. Flannery. *Numerical Recipes in C: The Art of Scientific Computing (; Cambridge*. Cambridge Univ. Press, 1992.

[98] K.E. Brenan, S.L. Campbell, and L.R. Petzold. *Numerical solution of initial-value problems in differential-algebraic equations*. SIAM, 1995.

[99] M. Nagurka and S. Huang. A mass-spring-damper model of a bouncing ball. In *Proceedings of the American Control Conference*, pages 499–504 vol.1, 2004.

[100] W.J. Stronge. *Impact Mechanics*. Cambridge University Press, 2004.

[101] D.J. Wagg and S.R. Bishop. A note on modelling multi-degree of freedom vibro-impact systems using coefficient of restitution models. *Journal of Sound and vibration*, 236(1):176–184, 2000.

[102] C. X. Wong, M. C. Daniel, and J. A. Rongong. Energy dissipation prediction of particle dampers. *Journal of Sound and Vibration*, 319(1-2):91–118, 2009.

[103] B. Darabi, J.A. Rongong, and T. Zhang. Viscoelastic granular dampers under low-amplitude vibration. *Journal of Vibration and Control*, page 1077546316650098, 2016.

[104] J.A. Rongong and H. Abbas. Damping of hollow beams using metal swarf. In *ICEDYN 2013 - Proceedings of International Conference on Structural Dynamics*, 2013.

[105] E.E. Ungar and E.M. Kerwin. Plate damping due to thickness deformations in attached viscoelastic layers. *Journal of the Acoustical Society of America*, 36(2):386–392, 1964.

[106] K. Walton. The effective elastic moduli of a random packing of spheres. *Journal of the Mechanics and Physics of Solids*, 35(2):213–226, 1987.

[107] J.A. Rongong and G.R. Tomlinson. Vibration damping using granular viscoelastic materials. In *Proceedings of ISMA 2002: International Conference on Noise and Vibration Engineering*, volume 27, pages 431–44, 2002.

[108] J.P. Den Hartog. *Mechanical Vibrations*. Courier Corporation, 1985.

[109] R.D. Blevins and R. Plunkett. Formulas for natural frequency and mode shape. *Journal of Applied Mechanics*, 47:461, 1980.

[110] S.J. Elliott, M. G. Tehrani, and R.S. Langley. Nonlinear damping and quasi-linear modelling. *Philosophical Transactions of the Royal Society A*, 373(2051):20140402, 2015.

[111] A. Flamant. Sur la répartition des pressions dans un solide rectangulaire chargé transversalement. *Comptes Rendus Mathematique*, 114:1465–1468, 1892.

[112] S. Timoshenko. *Theory of Elasticity*. Mcgraw-Hill Book Company, New York, 1934.

[113] W.R. Hamilton. Essay on a general method in dynamics. *Philosophical transactions of the Royal Society of London*, 124:247–308, 1834.

[114] W.R. Hamilton. Second essay on a general method in dynamics. *Philosophical Transactions of the Royal Society of London*, 125:95–144, 1835.

[115] A. Ramos and J.A. Simoes. Tetrahedral versus hexahedral finite elements in numerical modelling of the proximal femur. *Medical Engineering & Physics*, 28(9):916–924, 2006.

[116] A.O. Cifuentes and A. Kalbag. A performance study of tetrahedral and hexahedral elements in 3-d finite element structural analysis. *Finite Elements in Analysis and Design*, 12(3-4):313–318, 1992.

[117] A.F. Bower. *Applied Mechanics of Solids*. CRC press, 2009.

[118] J. Barlow. Optimal stress locations in finite element models. *International Journal for Numerical Methods in Engineering*, 10(2):243–251, 1976.

[119] J. Robinson. Cre method of element testing and the jacobian shape parameters. *Engineering Computations*, 4(2):113–118, 1987.

Appendix A

Parameters for Prony series

In this Appendix, the Prony seris, which is used to construct the master curves in the commercial FE code, was presented. Using the fitting of the master curve of viscoelastic material, as shown in Figure 3.14, the empirical coefficients in Equation 3.8 are listed as follows,

n	Modulus E_n,Pa	Time constant τ_n,s	n	Modulus E_n,Pa	Time constant τ_n,s
1	5.13E+05	4.73E-02	16	1.79E+01	1.48E-01
2	7.66E+05	2.49E-02	17	1.02E+02	4.99E-02
3	5.09E+01	5.77E-01	18	3.15E+01	8.28E-01
4	1.04E+02	8.77E-01	19	9.46E+01	9.14E-01
5	4.88E+08	1.95E-10	20	9.75E+01	2.13E-01
6	1.94E+08	2.51E-07	21	1.49E+08	1.10E-06
7	3.24E+01	3.50E-01	22	1.84E+05	3.05E-02
8	4.25E+07	1.49E-05	23	2.41E+01	1.33E-01
9	1.57E+02	7.75E-01	24	3.30E+01	2.62E-01
10	6.82E+06	2.80E-03	25	2.70E+00	8.93E-01
11	1.53E+02	2.33E-01	26	1.76E+01	2.85E-01
12	1.14E+07	1.67E-04	27	9.82E+01	4.00E-01
13	9.62E+06	1.00E+00	28	7.77E+05	2.46E-02
14	1.54E+09	2.89E-09	29	1.24E+09	4.37E-08
15	6.09E+08	1.63E-11	30	1.30E+09	1.57E-01

Table A.1: Fitting coefficients for the Prony series

Appendix B

Compressive stiffness of the O-ring

The analytical model for the compressive stiffness of the O-ring was derived using Hertz contact mechanics. A schematic figure for the contact between the O-ring and the stiff plate is shown in Figure B.1

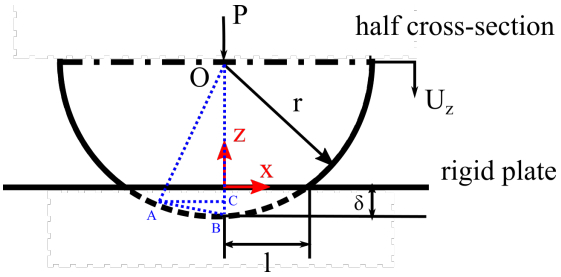

Figure B.1: Schematic contact configuration

The basic assumptions are listed as follows,

- The shape of the contact region is a ring. The cross-sections of O-rings can be regarded as elastic half planes and are loaded over these contact areas.
- Compared with the wire diameter, the contact half-width is negligible. This implies that the stress singularity at the edges of contact area does not influence the overall stress distribution of the elastic bodies.

- The local strain in the contact area is small enough to lie within the ranges of linear elasticity when the O-rings is subjected to low strain.
- The friction between two neighbouring surfaces is neglected, and thus, only the normal force can be observed in the contact region.

B.1 Load-deflection in the contact region

The local load-deflection relationship near the contact region was investigated at the first glance. To obtain the deflections alongside the contact, the geometric relationship, shown in Figure B.2 is used.

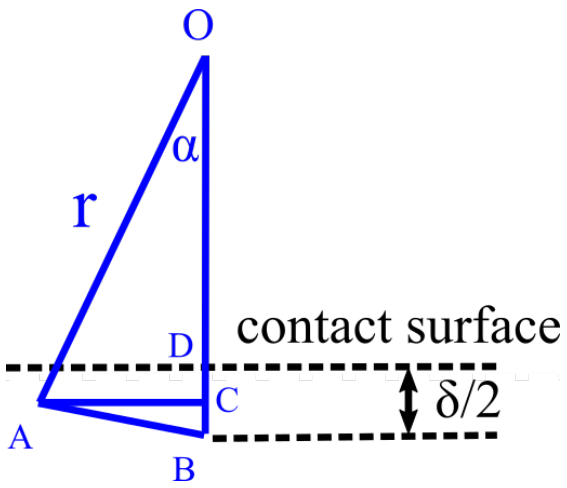

Figure B.2: Displacement at any point of contact

In this figure, the overall axial compression applied to the O-ring is 2δ. Note that the coordinate system is set-up in the middle of contact. At any point A located a distance x from the initial contact point, the axial deflection, $\overline{DC}$, caused by the applied load is given by,

$$U_z = \overline{DB} - \overline{BC} \tag{B.1}$$

where $\overline{DB}$ is the deflection in the middle of contact surface and denoted as δ. Noting that the triangle $\triangle OAB$ is equilateral and $\triangle ABC$ is right-angled, the

length $\overline{BC}$ can be represented using,

$$\overline{BC} = x \tan \frac{\alpha}{2} \tag{B.2}$$

As the triangle $\triangle OAC$ is also right-angled, this gives,

$$\alpha = \sin^{-1}\left(\frac{x}{r}\right) \tag{B.3}$$

where r is the radius of the cross-section. Combining Equations B.1,B.2 and B.3, the deflection at any point of contact is given by,

$$U_z = \delta - \frac{\frac{x}{r}}{1 + \sqrt{1 - \left(\frac{x}{r}\right)^2}} x \tag{B.4}$$

When $x \ll r$, Equation B.4 can be simplified to,

$$U_z = \delta - \frac{x^2}{2r} \tag{B.5}$$

The displacement in the contact regions can also be obtained using the elasticity of material. A schematic figure is shown in Figure B.3.

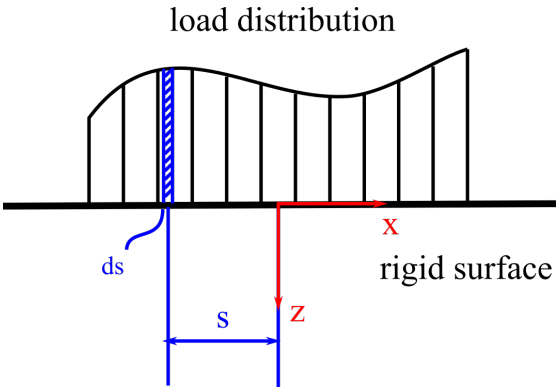

Figure B.3: Contact stress at any point of contact body

When contact loading is applied at any position on the rigid surface, Flamant [111] derives the stress distribution when point load applied to elastic half-space,

$$d\sigma_x = -\frac{2p(s)}{\pi} \frac{(x-s)^2}{(x-s)^2 + z^2} ds \tag{B.6}$$

$$d\sigma_z = -\frac{2p(s)}{\pi} \frac{z^3}{(x-s)^2 + z^2} ds \tag{B.7}$$

By integrating elementary stress over the contact half-width and introducing the generalised Hooke's law for plane strain, the strain in the rigid structure subject to distributed contact force is,

$$\varepsilon_z = \frac{1}{E}\left[(1-\nu^2)\sigma_z - \nu(1+\nu)\sigma_x\right] \tag{B.8}$$

where E is equivalent elastic modulus, ν is equivalent Possion's ratio. The equivalent material properties can be represented as,

$$E = \frac{1}{\frac{1}{E_1}+\frac{1}{E_2}} \tag{B.9}$$

$$\nu = \frac{1}{\frac{1}{\nu_1}+\frac{1}{\nu_2}} \tag{B.10}$$

in which E_1 and E_2 are the modulus of the walls and the rubber respectively, the ν_1 and ν_2 are the associate Poisson's ratios.

Using the definition of strain, the displacement along the tensile-compressive direction can be represented as,

$$U_z = \int \varepsilon_z dz \tag{B.11}$$

Combining Equation B.6,B.8 and B.11, the displacement of O-ring is,

$$U_z(x) = -\frac{2(1-\nu^2)}{E\pi}\int_{-l}^{l} p(s)\ln|x-s|\,ds \tag{B.12}$$

Substituting Equation B.12 into Equation B.5 and then differentiating for both equations, the pressure distribution can be given by,

$$p(x) = -\frac{E}{4r(1-\nu^2)}\frac{2x^2-l^2}{\sqrt{l^2-x^2}} + \frac{P}{\pi\sqrt{l^2-x^2}} \tag{B.13}$$

where P is applied load per unit depth of the O-ring cross-section. Note that the derivatives of $\int_{-l}^{l} p(s)\ln|x-s|\,ds$ is also called 'singular integral equations'. The solution procedures of this differential is out of the scope of this work. A full derivation from Equation B.12 to B.13 can be found in Johnson's book [82].

One interesting feature from Equation B.13 is that the stress tends to become infinity at the location where approaches to the edge of contact region, i.e. $x = l$. Since this phenomena is not possible physically, one more restricting condition, as shown in Equation B.14, is introduced.

$$P = \frac{\pi E l^2}{4r(1-\nu^2)} \tag{B.14}$$

Using Equation B.14, the stress on the edge is no longer infinity. After rearrangement of Equation B.14, the contact half-width subject to a given load is represented as,

$$l = \sqrt{\frac{4Pr(1-\nu^2)}{\pi E}} \tag{B.15}$$

B.2 Load-deflection of the O-ring

In the previous section, the contact pressure-displacement relations have been established. For elastomeric O-rings, a plane strain assumption can be made to estimate the corresponding deflection subject to given load. For the stress inside the centre cylinder, Timoshenko & Goodier [112] provides the simple equations,

$$\sigma_x = \sigma_z = \frac{P}{r\pi} \tag{B.16}$$

By considering both the contact and body elasticity, the stress occurring at any points inside cross-section can be represented as,

$$\sigma_x = \frac{P}{\pi}\left[\frac{1}{r} - \frac{2\sqrt{l^2+2z^2}}{l^2\sqrt{l^2+z^2}} + \frac{4z}{l^2}\right] \tag{B.17}$$

$$\sigma_z = \frac{P}{\pi}\left[\frac{1}{r} - \frac{2}{\sqrt{l^2+z^2}} + \frac{2}{2r-z}\right] \tag{B.18}$$

Combining Equation B.8, B.15 and B.17 and then making some rearrangements, the load-deflection relationship that allows for the geometric nonlinearity of the O-ring is,

$$\delta_z = \frac{2\left(1-\upsilon^2\right)}{E}\frac{P}{\pi}\left[\frac{1-2\nu}{1-\nu} - \frac{2\left(1-2\nu\right)}{1-\nu}A_1 - \frac{4\nu}{\left(1-\nu\right)l^2}A_2 + 2\ln 2 + A_3\right] \quad \text{(B.19)}$$

where A_1 refers to,

$$\ln\left(R+\sqrt{l^2+R^2}\right) - \ln\left(l\right) \quad \text{(B.20)}$$

A_2 is given by,

$$\frac{1}{2}R(l^2+R^2)^{1/2} - \frac{1}{2}l^2\ln\left[(l^2+R^2)^{1/2}+R\right] + \frac{1}{2}l^2\ln\left(l\right) \quad \text{(B.21)}$$

and A_3 is,

$$\frac{2\nu R^2}{l^2}\left(1-\nu\right) \quad \text{(B.22)}$$

The nonlinear stiffness sis given by

$$k_{\text{geo}} = \frac{\partial P}{\partial \delta_z} \quad \text{(B.23)}$$

B.3 Discussion

The analytic stiffness model for compressive loading of an O-ring has already been developed in Section 3.5. In the derivation, it was assumed that the contact half-width is far smaller than the wire diameter. This condition is not valid when the O-ring is subject to high compression. A full model, by replacing Equation B.5, can be established the displacement of cross-sections in compressive direction. To evaluate this difference, a comparison between two different models is carried out and this error function is given by,

$$\text{error} = \frac{U_{\text{simplified}} - U_{\text{full}}}{U_{\text{simplified}}} \quad \text{(B.24)}$$

Results of these comparisons are shown in Figure B.4

It can be seen from Figure B.4 that the difference is smaller than 3% when the static compression is up to 0.25. At high compression, the estimation loses its

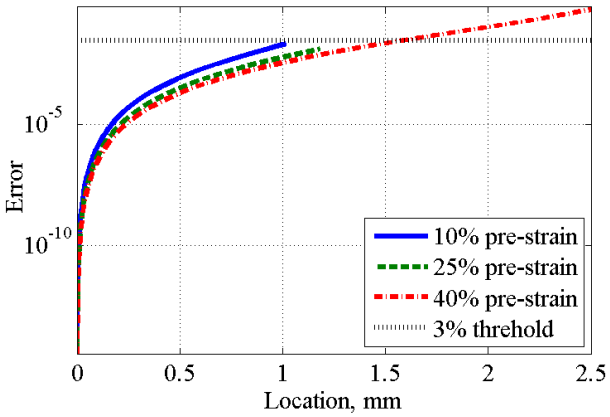

Figure B.4: Effect of small contact assumption

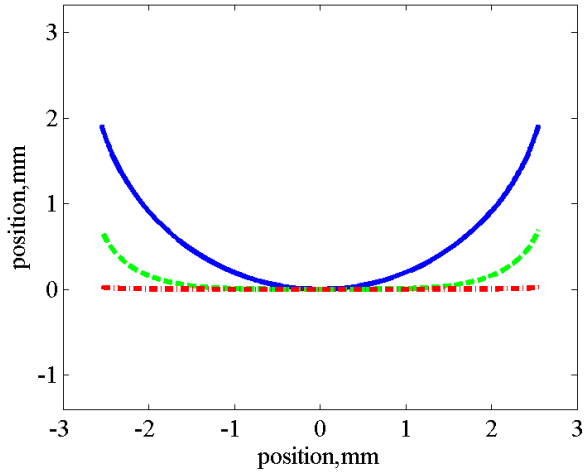

Figure B.5: Defomed cross-sections of O-ring subject to a static compression of 40% (blue solid: undeformed cross-section, green dash: full model, red chain: simplified model)

effectiveness and the error can exceed 70%. Close examinations of the deformed shapes estimated using these two models are shown in Figure B.5.

Figure B.5 shows that significant stiffening is to be expected for the simplified

model. However, this overestimation only affects the overall stiffness slightly as the stiffening caused by the material nonlinearity is likely to be much more significant. Therefore, the developed compressive stiffness model still works well for the proposed O-rings.

Appendix C

Rocking stiffness of the O-ring - supplemental information

In this appendix, the supplemental information is provided, which relates to the analysis of rotational behaviour of the O-rings.

C.1 Equivalent wire diameter of O-ring

The O-ring initially has a circular cross-section. Under axial pre-compression, flat sections appear where contact occurs. It is assumed that the rotational stiffness of the O-ring can be approximately by considering a ring with a rectangular cross-section of equal area. A schematic figure of the deformed cross-section of O-ring is shown in Figure C.1 Note that r_0 is the wire radius, $2t_0$ is the static compression and l is the contact radius. It is assumed that the deformed edges of O-rings follow a parabolic function. The coordinate system is set up, as shown in Figure C.1. The origin of this coordinate system is chosen as the centroid of the cross-section. The analytical formula for a curved edge is,

$$y(x) = \frac{l - r_0}{(t_0 - r_0)^2} x^2 + r_0 \tag{C.1}$$

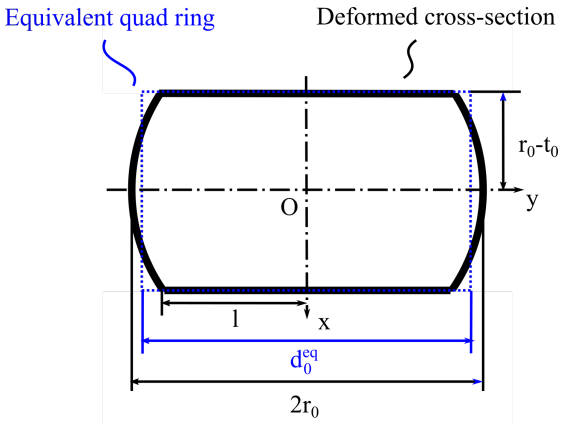

Figure C.1: Schematic cross-sections of deformed O-rings

The area of the cross-section is then given by,

$$\text{Area} = 4\int_0^{r_0-t_0} y(x)dx \tag{C.2}$$

Substituting Equation C.1 into Equation C.2, the area of cross-sections is also represented as,

$$\text{Area} = \frac{4}{3}(l+2r_0)(r_0-t_0) \tag{C.3}$$

The equivalent width of rectangular-section ring is then given by,

$$d_0^{\text{eq}} = \frac{\text{Area}}{2(r_0-t_0)} = \frac{2}{3}(l+2r_0) \tag{C.4}$$

C.2 Effect of eccentricity of O-ring

In the process of assembling the TMD,an O-ring may be located eccentrically. In this section, the effect of eccentricity is evaluated using an analytic model. A schematic figure showing the rotation of an O-ring is provided in Figure C.2.

Using the equivalence of the strain energy between the linear and rotational coordinate systems, the strain energy of the O-ring can be represented as,

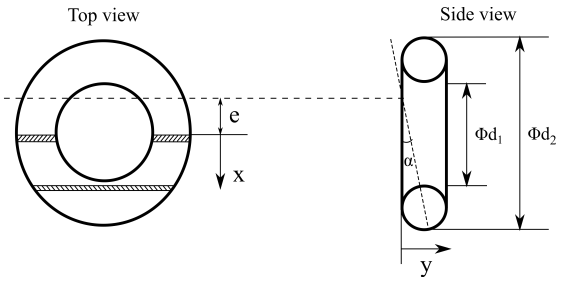

Figure C.2: Schematic rotational behaviours of the O-ring

$$\begin{aligned}\frac{1}{2}k_{rot}\alpha^2 = \int_{-\frac{d_1}{2}}^{\frac{d_1}{2}} k_{\text{eq}} \left(2\sqrt{\left(\frac{d_2}{2}^2 - x^2\right)} - 2\sqrt{\left(\frac{d_1}{2}^2 - x^2\right)}\right) \frac{1}{2}\alpha^2(x-e)^2 dx \\ + \int_{\frac{d_1}{2}}^{\frac{d_2}{2}} 2k_{\text{eq}}\sqrt{\left(\frac{d_2}{2}^2 - x^2\right)}\frac{1}{2}\alpha^2(x-e)^2 dx \\ + \int_{-\frac{d_2}{2}}^{-\frac{d_1}{2}} 2k_{\text{eq}}\sqrt{\left(\frac{d_2}{2}^2 - x^2\right)}\frac{1}{2}\alpha^2(x-e)^2 dx\end{aligned} \tag{C.5}$$

After some re-arrangements, the rocking stiffness of an O-ring with eccentricity can be given by,

$$k_{\text{eq}} = \left[\frac{\pi}{64}\left(d_2^4 - d_1^4\right) + \frac{\pi e^2}{8}\left(d_2^2 - d_1^2\right)\right] k_{\text{rot}} \tag{C.6}$$

Compared with the Equation 3.43, it is clear that the eccentricity stiffens the O-rings.

Appendix D

Numerical modelling approach - Finite element theory

In this appendix, the background of the Finite element approach is introduced. Efforts were focused on representing the stiffness and damping of elastomeric O-rings. Two different approaches, finite strain analysis and modal analysis, were used to identify the behaviours in the tensile-compressive and rotational direction respectively.

D.1 Finite Element theroy

D.1.1 Finite strain analysis

For each case considered, the load carried by specimens undergoing substantial deformation was calculated using the finite element (FE) method. The basis of this numerical model is discretisation of a continuous body into multiple 'individual' elements, which are formed by a grid and vertices. These vertices (and selected middle points between neighbouring vertices in this network) are also called as 'nodes'. The material properties, including density, elasticity and damping, are then assigned to each element. Within an element, the distribution of

displacement and hence strain, is defined by the specific 'shape function' used. The relationship between the strain and stress was defined by the material properties and shape functions. These shape functions and the matrix of elasticity are then assembled to form the global stiffness matrix. The restoring force vectors of the structure can then be predicted for a given nodal displacement, and vice versa. For a nonlinear analysis, Newton-Raphason iterations are introduced to obtain the load-deflection relations.

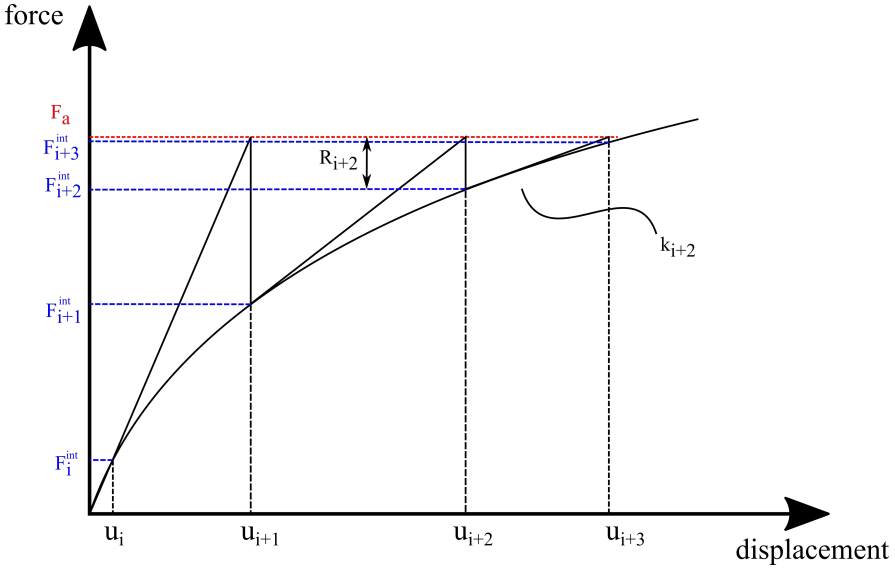

Figure D.1: A schematic diagram of solution strategy for commercial numerical package

For a nonlinear load-deflection model, the prediction of the nodal displacement is obtained using the balance of the given applied and restoring force vectors, as shown in Figure D.1. If the driving force is applied gradually, the whole procedure can be considered as linearisation of a nonlinear process. The mathematical expression of this iterative procedure can be represented as,

$$\left[K_i^T\right]\{\Delta u_i\} = \{F^a\} - \left\{F_i^{\text{int}}\right\} \tag{D.1}$$

$$\{\Delta u_i\} = \{u_{i+1}\} - \{u_i\} \tag{D.2}$$

where i refers to i^{th} equilibrium iterations. By updating the stiffness matrix $\left[K_i^T\right]$, the restoring force matrix $\left\{F_i^{\text{int}}\right\}$ is recalculated and compared with the

given external force $\{F^a\}$. If convergence is not achieved, the displacement vector $\{\Delta u_i\}$ is updated and passed to a new iteration $\{u_{i+1}\}$ using Equation D.1. These iterations are terminated when convergence is achieved. The index to evaluate convergence is selected as the residual force vector $\{R\}$.

$$\{R\} = \{F^a\} - \left\{F_i^{\text{int}}\right\} \tag{D.3}$$

The convergence criterion is shown in Equation D.4

$$\| \{R\} \| \leq \varepsilon_R R_{\text{ref}} \tag{D.4}$$

where $\| \{R\} \|$ refers to mean root square of vector $\{R\}$. ε_R is the tolerance for the error band and, for this work reported here, was set to 0.5%. R_{ref} is the out-of-balance residual force. The upper limit for this reference residual force was set to 0.01N for the analysis reported here.

D.1.2 Finite element modal analysis

The essence of a finite element analysis is the special case of the Rayleigh-Ritz method. Some restrictions of this finite element approach are shown as follows.

- All the nonlinear behaviour in the finite element models are neglected. For example, if a numerical model includes contact elements, the interfacial friction is ignored. The contact status never changes and keeps its original state.
- The mechanical behaviour of material can only be uniform or temperature-dependent. All of the other nonlinear material behaviour, for example frequency-dependent modulus, is neglected.

In the Rayleigh-Ritz method, the shape functions are chosen as components of assumed mode shapes. The vibration shape can be given by

$$\mathbf{u}\,(x, y, z, t) = \sum_{j=1}^{n} \lambda_j \boldsymbol{\phi}_j\,(x, y, z)\, q_j(t) \tag{D.5}$$

where λ_j is scale factor. $\boldsymbol{\phi}_j(x, y, z)$ is the shape function of j^{th} element. $q_j(t)$ is the time response.

According to Equation D.5, the shape function used in this numerical model is the sum of several individual piecewise linear functions.

The important features of each shape function, $\boldsymbol{\phi}_j$, are: (a) generally a triangular function; (b) unit peak magnitude; (c) unique node position of the peak magnitude. A high flexibility of this type of the mode shape is provided because the assumed shape function is not necessary to be continuous, especially when calculating the stiffness matrix of the structure with a complex boundary condition. The stiffness and mass matrices of this structure can be predicted using Hamilton principle [113, 114]. The algebraic eigenanalysis is then applied to obtain the natural frequencies and mode shapes of the selected structures.

D.1.3 Summary

For this work, the ANSYS implicit solver has been chosen because it is well versed in the estimation of elastic and frictional behaviours of the selected structure and can be worked for a relatively long simulation time.

D.2 Element formation

In this work reported here, an axisymmetric model was used to simulate the elastomeric O-ring in tension-compression. The cross-section was discretised with solid six-node triangle quadratic elements (PLANE182 in Ansys). Since an axisymmetric model is not able to present the rocking behaviour of the O-ring, a set of 20-node hexahedron-dominant elements (SOLID186) was selected in this work. To adapt the complex geometry, several 10-node tetrahedron, 13-node pyramid and 17-node prism elements was also employed. When choosing the quadratic element, several studies [115, 116] have shown that the accuracy of the numerical model using tetrahedral and hexahedral elements is similar while a lower amount

of element numbers is required for rapidly changing structures in the case that use tetrahedral elements. Therefore, all these elements can be represented the elastic behaviours of the O-rings in this work.

For a classic type of element, two of the most significant problems are volumetric and shear locking [117]. Shear locking refers to unexpected and unrealistic shear strain in an element subjected to bending because of poor prediction of the strain where nodes are not located. This shear locking can be avoided in the developed numerical model as most elements are quadratic. Volumetric locking is not relevant to the mesh and closely related to the interpolation of displacement for elements. When subject to the incompressible material, the finite element displacement at some nodes is very close to zero. Some estimated positions in the element can not provide a reasonable volume preserving strain field. Instead, a nonzero volumetric strain may lead to the displacement of elements due to the round-off error of stiffness matrix. To remove this effect for quadratic elements, a reduced integration scheme is recommended [117]. Although this strategy affects the accuracy of simulation, it can completely resolve volumetric locking. The errors from reduced integration schemes can be overcome when a fine mesh was applied.

The other important feature of this numerical model is the interfacial interaction between to O-ring and restricting plate. A zero-stiffness contact element, also called as contact pair, was used. Contact elements are made up of two mating surface elements referred to as CONTACT172 and TARG169 in Ansys. Tiny penetration is allowed for this pair of elements. The contact stiffness is represented as,

$$F_n = k_c x_p + \lambda \tag{D.6}$$

where F_n is the normal reaction force vector, k_c is contact stiffness matrix, x_p is normal penetration displacement and λ is the coefficient of the extra generalised coordinate that used to compensate the contact pressures in Lagrange equations. This additional term allows the normal stiffness to be less sensitive to the contact stiffness and promote the likelihood of the convergence. In this work, these

elements are capable of large displacements that make them ideal for frictional contact simulations, and therefore, is suitable to account for the geometric non-linearity caused by the local deformation of O-rings in contact regions.

D.3 Meshing

The node distribution and interpolation method of elements have been discussed in the previous section where is was also shown that the estimated stiffness in the node position is much more accurate than elsewhere. Therefore, a huge number of nodes in a structure increases the likelihood of achieving a reliable simulation. Also, significant amounts of the nodes in the contact regions bring a better likelihood of convergence for the finite strain analysis in the FE code used.

The errors of the numerical models mainly come from interpolation and round-off errors. Since the displacement matrix in the position other than nodes is estimated using the shape function, interpolation errors are introduced, especially for a low-order element. One serious consequence is that the stress estimation may be far away from exact value because the strain (and hence stress) is proportional to the first-order derivative of the displacement distribution. Barlow [118] has observed that the interpolation error can effectively be eliminated using quadratic elements. Therefore, limited errors are introduced for this work. The round-off errors, however, are a consequence of the singular stiffness matrix. This singularity is usually caused by a sudden change of constraints of geometry. To avoid these effects, a coarser mesh needs to be selected to avoid assigning nodes close to the singular points in the structure. Therefore, a proper quality of mesh is necessary to gain better simulation results. Following the recommendations from Robinson [119] , the skewness of element matrices for the selected flexible structure is set to smaller than 0.8, and the aspect ratio is below 4.

Appendix E

Test results from drop-rebound tests

In this appendix, results from the drop-rebound for the selected TMW particles are shown as follows,

Initial height	293.00	293.00	293.00	247.00	247.00	247.00	204.00	204.00	293.00	165.00
Start frame	50.00	134.00	98.00	397.00	16.00	78.00	120.00	56.00	312.00	246.00
End Frame	460.00	336.00	555.00	771.00	386.00	482.00	392.00	333.00	638.00	487.00
Frames number	410.00	202.00	457.00	374.00	370.00	404.00	272.00	277.00	326.00	241.00
Sampling rate	0.00	0.00	0.00	0.00	0.00	0.00	0.00	0.00	0.00	0.00
time	0.29	0.14	0.33	0.27	0.26	0.29	0.19	0.20	0.23	0.17
rotational start frame	59.00	137.00	137.00	436.00	73.00	114.00	164.00	124.00	341.00	262.00
rotational end frame	96.00	156.00	237.00	486.00	144.00	167.00	184.00	174.00	359.00	283.00
rotation time per radian	0.03	0.01	0.07	0.04	0.05	0.04	0.01	0.04	0.01	0.02
rotation speed (rps)	37.84	73.68	14.00	28.00	19.72	26.42	70.00	28.00	77.78	66.67
initial velocity	2.00	2.00	2.00	1.80	1.80	1.80	1.60	1.60	1.60	1.40
Coefficient of resisitution	0.60	0.30	0.67	0.60	0.59	0.64	0.48	0.49	0.48	0.47
Loss factor	0.16	0.36	0.13	0.16	0.17	0.14	0.23	0.22	0.23	0.23
Damping ratio	0.08	0.18	0.06	0.08	0.08	0.07	0.11	0.11	0.11	0.12

Initial height	165.00	165.00	130.00	130.00	130.00	100.00	100.00	100.00	73.00	73.00
Start frame	65.00	286.00	414.00	398.00	338.00	399.00	716.00	475.00	183.00	402.00
End Frame	404.00	633.00	642.00	599.00	568.00	463.00	824.00	543.00	337.00	518.00
Frames number	339.00	347.00	228.00	201.00	230.00	64.00	108.00	68.00	154.00	116.00
Sampling rate	0.00	0.00	0.00	0.00	0.00	0.00	0.00	0.00	0.00	0.00
time	0.24	0.25	0.16	0.14	0.16	0.05	0.08	0.05	0.11	0.08
rotational start frame	119.00	321.00	431.00	440.00	355.00	437.00	741.00	495.00	200.00	424.00
rotational end frame	168.00	385.00	497.00	471.00	406.00	452.00	761.00	511.00	260.00	446.00
rotation time per radian	0.04	0.05	0.05	0.02	0.04	0.01	0.01	0.01	0.04	0.02
rotation speed (rps)	28.57	21.88	21.21	45.16	27.45	93.33	70.00	87.50	23.33	63.64
initial velocity	1.40	1.20	1.20	1.20	1.20	1.00	1.00	1.00	0.80	0.80
Coefficient of resisitution	0.66	0.68	0.50	0.44	0.51	0.19	0.28	0.20	0.45	0.35
Loss factor	0.13	0.12	0.22	0.25	0.21	0.47	0.37	0.46	0.25	0.32
Damping ratio	0.07	0.06	0.11	0.13	0.11	0.23	0.19	0.23	0.12	0.16

Figure E.1: Test results from drop-rebound tests

Appendix F

Repeatability tests of the TMW TMD

In this appendix, results from the repeatability tests for the selected TMW TMS when subjected to different static compressions of the TMW particles are shown as follows,

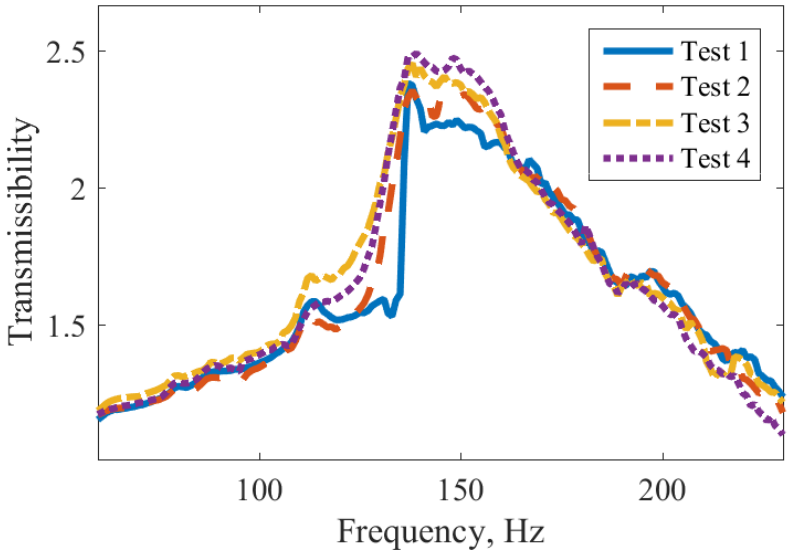

Figure G.1: Typical transmissibility curves for selected configurations of TMW TMD subject to different loading history (static compression of particles is 0 mm)

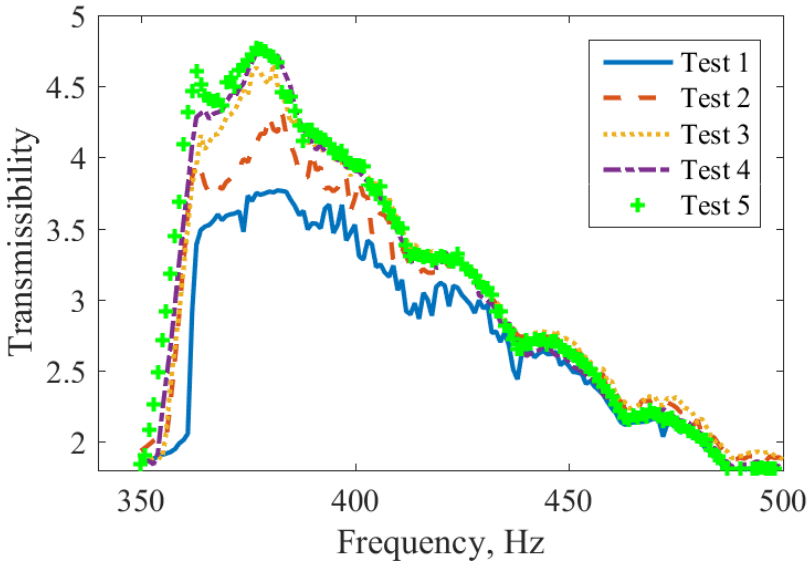

Figure G.2: Typical transmissibility curves for selected configurations of TMW TMD subject to different loading history (static compression of particles is 0.45 mm)

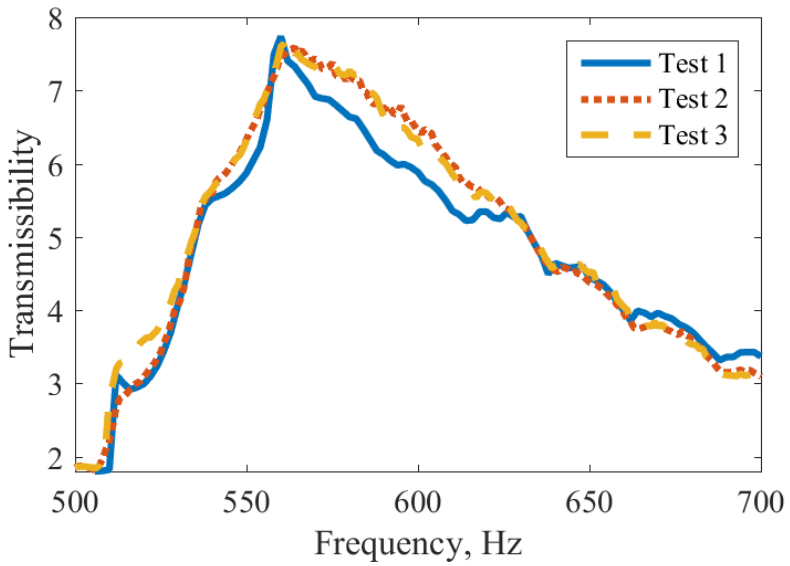

Figure G.3: Typical transmissibility curves for selected configurations of TMW TMD subject to different loading history (static compression of particles is 0.9 mm)